
A NUMERICAL INVESTIGATION OF
TRANSVERSELY-OSCILLATING CYLINDERS IN
TWO-DIMENSIONAL FLOW

BY JUSTIN LEONTINI

A THESIS SUBMITTED TO MONASH UNIVERSITY IN FULFILLMENT OF THE
REQUIREMENTS FOR THE DEGREE OF

DOCTOR OF PHILOSOPHY

Department of Mechanical Engineering

Monash University

January 2007

STATEMENT OF ORIGINALITY

This thesis contains no material that has been accepted for the award of a degree or diploma in this, or any other, university. To the best of the candidate's knowledge and belief, this thesis contains no material previously published or written by another person except where due reference is made in the text.

Justin Leontini

January, 2007

ABSTRACT

A numerical investigation of the two-dimensional flow past a circular cylinder oscillating transverse to the freestream direction at Reynolds numbers $Re \leq 300$ is presented. The cylinder motion is either decoupled from the fluid and driven externally, or allowed to respond to the flow by mounting the cylinder elastically. Wake modes, synchronisation and energy transfer are studied in the case of the externally-driven cylinder, whereas flow response regimes and their characteristics are identified for the elastically-mounted cylinder. The transition from two-dimensional to three-dimensional flow for the case of the externally-driven cylinder is investigated, as is the transition from steady to unsteady flow for the elastically-mounted cylinder.

A spectral-element method has been employed for all of the two-dimensional simulations of these flows. Domain size, and spatial and temporal resolution were all checked for the flows involved, and the results found to be resolved to an accuracy of 1% for the important flow parameters.

A dependence on Reynolds number exists for the synchronisation boundaries, value of energy transfer and wake mode for a sinusoidally-externally-driven cylinder. However, the maximum amplitude of oscillation for positive energy transfer (from the fluid to the cylinder) is approximately constant over the range $50 \leq Re \leq 300$, at $A^* = 0.6$, where A^* is the cylinder oscillation non-dimensionalised by the cylinder diameter. Conversely, the amplitude at which the wake undergoes a transition from one two-dimensional state (the $2S$ state) to another two-dimensional state (the $P + S$ state) is shown to be dependent on Reynolds number. Therefore this wake transition is not dependent on energy transfer. The asymmetric $P + S$ state can provide positive energy transfer, at least when $Re \geq 300$ and the flow is restricted to being two-dimensional.

Three distinct response regimes exist for the elastically-mounted cylinder. These are

the quasiperiodic, chaotic, and periodic regimes. Each of these regimes exists for a distinct range of reduced velocity, U^* . All three regimes exist for $Re \geq 70$, while only the periodic regime remains when $Re \leq 40$. While the three regimes are not immediately obvious from inspection of the peak amplitude of response, they are delineated through observation of the peak lift, frequency and phase response, and the behaviour in the phase plane described by the lift force and cylinder displacement.

Comparison of the sinusoidally-externally-driven cylinder results and the elastically-mounted cylinder results shows that sinusoidal driving performs well as a model of coupled vortex-induced vibration in the periodic regime. However, sinusoidal driving does not capture the flow dynamics in the chaotic regime. Externally-driven cylinder simulations, using a modulated driving function, result in peak lift coefficients that are much closer to those encountered in vortex-induced vibration in the chaotic regime.

The transition from two-dimensional flow to three-dimensional flow in the wake of the sinusoidally-externally-driven cylinder is investigated using Floquet stability analysis. When the two-dimensional base flow is in the $2S$ state, the same three-dimensional modes occur as for the fixed cylinder wake. However, for amplitudes $A^* > 0.3$, the order of inception of the modes is varied. For the $2S$ base state, the oscillation suppresses the three-dimensional transition, to a maximum Reynolds number of $Re = 280$.

With transition of the base flow to the $P + S$ state, two new three-dimensional modes arise. These modes are labelled modes SL and SS , and both are subharmonic. Either of these modes can lead the transition to three-dimensional flow, depending on the amplitude of oscillation. The $P + S$ base flow is shown to be inherently unstable to mode SL for $A^* < 0.67$, and the critical Reynolds number for the three-dimensional transition actually decreases with increasing amplitude of oscillation over this range. Considering both the $2S$ and $P + S$ base states, four modes can lead the transition to three-dimensional flow, depending on the amplitude of oscillation.

The transition from a steady to unsteady flow for the elastically-mounted cylinder was investigated using a Stuart-Landau model. A single equation model was deemed sufficient due to simulation results showing that a periodic, single-frequency response is the only unsteady response that occurs for Reynolds numbers in the vicinity of the transition. The unsteady transition occurs at significantly lower values of Reynolds number than the same

transition in the wake of a fixed cylinder, yet it remains supercritical. Evidence is presented that suggests this lowering of the critical Re may be due to a feedback between the elastically-mounted cylinder and an area of local absolute instability in the near wake.

ACKNOWLEDGEMENTS

Firstly, I would like to express my gratitude to my supervisors, Prof. Mark Thompson and Prof. Kerry Hourigan. Prof. Mark Thompson's ability to explain complicated concepts in a simple way, and Prof. Kerry Hourigan's sharp sense of logic and scientific method, have been integral in my development as a researcher and allowing me to write this thesis. For their guidance and teaching I am truly thankful.

Mention must be made also of the contribution of other academic staff of FLAIR. Prof. John Sheridan and A/Prof. Jon Hinwood provided many useful insights from their extensive backgrounds in vortex-induced vibration and fluid mechanics in general. To Drs. Greg Sheard and Kris Ryan, I extend my thanks for fielding many of my half-baked and ill-conceived enquiries. Also my thanks go to Mr. Andreas Fouras his perspective from an experimentalist's point of view.

For making my candidature such an enjoyable experience, I would like to thank all of my fellow post-graduate students in the Department of Mechanical Engineering, but especially my lab cohorts. In no particular order, my thanks go to Mr. Karlis Atvars, Mr. Aran Fitzgerald, Dr. Jon Dusting, Mr. Martin Griffith, Mr. Patrick Browne, Mr. Owen Gould, Mr. Anthony Buchanan, Ms. Bronwyn Stewart, Mr. Hyeok Lee and Mr. Joe Berry. Your company, good times and many critical discussions on topics that even occasionally related to fluid dynamics are greatly appreciated. Special mention needs to be made of Mr. Aran Fitzgerald for proof-reading parts of the thesis manuscript, and Mr. Karlis Atvars for sharing a lot of thoughts, a lot of laughs and not a lot of cubicle space with me over the last 18 months of my candidature.

PhD. research requires resources, and I would like to acknowledge the support of this work by the Department of Mechanical Engineering, and the financial support throughout my candidature in the form of a Monash Departmental Scholarship. Also, for the computa-

tional resources utilised for the simulations of this thesis, my acknowledgement goes to the Australian Partnership for Advanced Computing (APAC) and the Victorian Partnership for Advanced Computing (VPAC).

For the support of my family and friends I am indebted. Mum, dad, and Jarrod, without your constant support and belief in me over many years, I just would not have been capable of completing this thesis. To my brothers in all but blood, Mr. Benjamin “TV” Alpey and Mr. Mark “Bets” Bruin, my thanks for keeping my head high, and your advice on my “water and poles”.

Lastly, I must extend my gratitude to my partner, Hannah. Your love, support and understanding continue to astound me, and inspire me. Thank you.

A LIST OF PUBLICATIONS RELATING TO THIS THESIS

LEONTINI, J.S., THOMPSON, M.C. & HOURIGAN, K. 2006 Three-dimensional transition in the wake of a transversely oscillating cylinder *Journal of Fluid Mechanics* **In Press**.

LEONTINI, J.S., THOMPSON, M.C. & HOURIGAN, K. 2006 The beginning of branching behaviour of vortex-induced vibration during two-dimensional flow *Journal of Fluids & Structures* **22**, 857–864.

LEONTINI, J.S., STEWART, B.E., THOMPSON, M.C. & HOURIGAN, K. 2006 Wake state and energy transitions of an oscillating cylinder at low Reynolds number *Physics of Fluids* **18**, 067101.

LEONTINI, J.S., STEWART, B.E., THOMPSON, M.C. & HOURIGAN, K. 2006 Predicting vortex-induced vibration from driven oscillation results *Applied Mathematical Modelling* **30**, 1096–1102.

LEONTINI, J.S., THOMPSON, M.C. & HOURIGAN, K. 2005 The beginning of branching behaviour during vortex-induced vibration at 2-D Reynolds numbers *Proceedings of the International Conference on Bluff Body Wakes and Vortex Induced Vibrations 4 (BBVIV4)*, Santorini, Greece

LEONTINI, J.S., THOMPSON, M.C. & HOURIGAN, K. 2005 Modelling vortex-induced vibration with driven oscillation *Journal of the Australian and New Zealand Industrial and Applied Mathematics Society* **46**, C365–C378

LEONTINI, J.S., THOMPSON, M.C. & HOURIGAN, K. 2004 A numerical comparison of forced and free vibration of circular cylinders at low Reynolds number *15th Australasian Fluid Mechanics Conference, Sydney, Australia*

LEONTINI, J.S., THOMPSON, M.C. & HOURIGAN, K. 2004 Modelling vortex-induced vibration with multi-frequency oscillation at low Reynolds number *The 12th Biennial Computational Techniques and Applications Conference (CTAC2004), The University of Melbourne, Victoria, Australia*

STEWART, B.S., LEONTINI, J.S., HOURIGAN, K. & THOMPSON, M.C. 2005 A numerical survey of wake modes and energy transfers for an oscillating cylinder at $Re=200$ *Proceedings of the International Conference on Bluff Body Wakes and Vortex Induced Vibrations 4 (BBVIV4), Santorini, Greece*

STEWART, B.S., LEONTINI, J.S., HOURIGAN, K. & THOMPSON, M.C. 2005 Vortex wake and energy transitions of an oscillating cylinder at low Reynolds number *Journal of the Australian and New Zealand Industrial and Applied Mathematics Society* **46**, C181–C195

STEWART, B.S., LEONTINI, J.S., HOURIGAN, K. & THOMPSON, M.C. 2004 Vortex wake and energy transitions in an oscillating cylinder at low Reynolds number *15th Australasian Fluid Mechanics Conference, Sydney, Australia*

STEWART, B.S., LEONTINI, J.S., HOURIGAN, K. & THOMPSON, M.C. 2004 Energy and wake transitions of an oscillating cylinder in low Reynolds number flow *The 12th Biennial Computational Techniques and Applications Conference (CTAC2004), The University of Melbourne, Victoria, Australia*

HOURIGAN, K., THOMPSON, M.C., SHEARD, G.J., RYAN, K. & LEONTINI, J.S. 2006 Low Reynolds number instabilities and transitions in bluff body wakes *Second International Symposium on Instability and Bifurcations in Fluid Dynamics, Technical University of Denmark, Copenhagen, Denmark*

NOMENCLATURE

Symbol	Description
A	Generic amplitude variable of the Stuart-Landau model
A^*	Normalised oscillation amplitude, $ y/D $
A_{max}^*	Maximum normalised oscillation amplitude
Ar	Aspect ratio used in the study of tori
a	Index in the ξ -direction used for the weighting coefficients for Gauss-Legendre-Lobatto quadrature
b	Index in the η -direction used for the weighting coefficients for Gauss-Legendre-Lobatto quadrature
C_0	Symbol indicating continuity of the function across elemental boundaries, but not continuity of any derivatives
C_{bp}	Base pressure coefficient, pressure at the immediate rear of the cylinder normalised by $0.5\rho U^2$
C_E	Energy transfer coefficient, normalised energy transfer over one period of oscillation
C_L	Lift coefficient
C_{L_a}	Added mass force lift coefficient
$C_{L_{max}}$	Maximum instantaneous lift coefficient
C_{L_v}	Vortex force lift coefficient
c	Mechanical damping coefficient
c_{crit}	Critical mechanical damping coefficient, $4\pi m f_{Nvac}$
D	Cylinder diameter

Continued on next page \rightarrow

← Continued from previous page

Symbol	Description
El	Subscript denoting integration over a single element
f	Primary frequency of cylinder oscillation
f^*	Normalised oscillation frequency, fU/D
F_{lift}	Instantaneous lift force per unit length
$F_{lift_{max}}$	Maximum instantaneous lift force per unit length
f_m	Modulation frequency used in modulated oscillation experiments
f_N	Natural frequency of cylinder structure including added mass component, $f_{N_{vac}} \sqrt{\frac{1}{1+1/m^*}}$
f_N^*	Normalised natural frequency, $f_N D/U$
$f_{N_{vac}}$	Natural frequency of cylinder <i>in vacuo</i> , $\frac{1}{2\pi} \sqrt{\frac{k}{m}}$
f_{St}	Strouhal frequency, shedding frequency for a fixed cylinder
g	Index of the data points inside each element in the ξ -direction
h	Variable indicative of resolution of macro-element mesh
i	Index of the data point being considered during construction of the Lagrange polynomial in the ξ -direction
$\Im(\mu)$	Imaginary component of the complex quantity μ
\mathbf{J}	Jacobian operator for coordinate transformation
j	Data point index in computational space in η -direction
k	Spring stiffness coefficient
k^*	Spring stiffness divided by cylinder mass, k/m
L_2	The L_2 norm, or the RMS average of a variable
L_i	One-dimensional Lagrange polynomial component for point i
l_c	Coefficient of the cubic term in the Stuart-Landau model
Ma	Mach number, ratio of speed of sound to speed of fluid flow
$M1$	The first mesh used for the domain size study
$M2$	The second mesh used for the domain size study
$M3$	The third mesh used for the domain size study
$M4$	The fourth mesh used for the domain size study

Continued on next page →

← Continued from previous page

Symbol	Description
m	Cylinder mass per unit length
m^*	Mass ratio, mass of cylinder to mass of displaced fluid
\mathbf{N}	The non-linear convection term in the Navier–Stokes equations, $(\mathbf{V} \cdot \nabla)\mathbf{V}$
$N_{q,s}$	Two-dimensional tensor-product Lagrange polynomial component for point q, s
n	Timestep count to the current timestep
\mathbf{n}	Unit vector in the normal direction to a boundary
$O(2)$	Symmetry group consisting of spanwise translational and reflection invariance
p	Order of the Lagrange polynomials used as shape and weighting functions for the spectral-element method
p_f	Pressure
p'	Normalised perturbation pressure
P	Non-dimensional pressure, $p_f/\rho U^2$
P_{trial}	Trial solution for pressure
P_f	Power spectral density
q	Data point index in computational space in ξ -direction
\mathbf{R}	Residual formed when substituting trial solution into governing equations
$\Re(\mu)$	Real component of the complex quantity μ
Re	Reynolds number, UD/ν
r'	Symbol representing an arbitrary perturbation variable during Floquet stability analysis
St	Strouhal number, $f_{St}U/D$
s	Data point index in computational space in η -direction
T	Period of cylinder oscillation in non-dimensional units, τ
t	Time variable
U	Freestream velocity
U^*	Reduced velocity, $U/f_N D$
u	Normalised component of velocity in the x -direction

Continued on next page →

← Continued from previous page

Symbol	Description
\mathbf{u}	Velocity vector field
u'	The component of normalised perturbation velocity in the x -direction
\mathbf{V}	Non-dimensional velocity vector, \mathbf{u}/U
\mathbf{V}_{trial}	Trial solution for velocity
\mathbf{V}^*	Intermediate normalised velocity vector at the end of the advection sub-step
\mathbf{V}^{**}	Intermediate normalised velocity vector at the end of the pressure sub-step
\mathbf{V}_{cyl}	Transverse velocity of the cylinder, \mathbf{v}_{cyl}/U
$\mathbf{V}_{cyl}^{(n+1)\dagger}$	First approximation of \mathbf{V}_{cyl} at the end of the timestep during the elastically-mounted cylinder convection substep
$\mathbf{V}_{cyl}^{(n+1)\ddagger}$	Second approximation of \mathbf{V}_{cyl} at the end of the timestep during the elastically-mounted cylinder convection substep
$\mathbf{V}_{cyl}^{(n+1)'} $	Approximation of \mathbf{V}_{cyl} at the end of the timestep after relaxation during the elastically-mounted cylinder convection substep
$\mathbf{V}^{(n)}$	Normalised velocity vector at timestep n
$\mathbf{V}^{(n+1)}$	Normalised velocity vector at timestep $n + 1$
$\widehat{\mathbf{V}}^*$	Vector of \mathbf{V}^* at the node points
v	Normalised component of velocity in the y -direction
\mathbf{v}_{cyl}	Instantaneous transverse cylinder velocity
\mathbf{v}^*	Normalised transverse velocity at a point on the wake centreline
v'	The component of normalised perturbation velocity in the y -direction
\mathbf{v}'	Normalised perturbation velocity vector
$W_{a,b}$	Weighting coefficient associated with point a, b for Gauss-Legendre-Lobatto quadrature
w'	The component of normalised perturbation velocity in the z -direction
x	Cartesian coordinate in the freestream flow direction, positive downstream
y	Cartesian coordinate transverse to the flow direction and span direction
y_{cyl}	Transverse cylinder displacement

Continued on next page →

← Continued from previous page

Symbol	Description
$y_{cyl}^{(n+1)\dagger}$	A first approximation to y_{cyl} at the end of the timestep during the elastically-mounted cylinder convection substep
y_{max}	Peak cylinder transverse displacement
Z_2	Spatio-temporal symmetry group, consisting of evolution by half a period and reflection about the wake centreline
z	Cartesian coordinate in the spanwise direction
α	Coefficient determining the saturated amplitude of the periodic mode in the neighbourhood of the Hopf bifurcation
β	Eccentricity parameter used for elliptic instability theory
γ	Coefficient of the quintic term in the Stuart-Landau model
$\Delta \mathbf{V}_{cyl}$	Change in \mathbf{V}_{cyl} over one timestep
$\Delta \mathbf{V}_{cyl}^\dagger$	First approximation of change in \mathbf{V}_{cyl} over one timestep during the elastically-mounted cylinder convection substep
$\Delta \tau$	The non-dimensional timestep
ϵ	Under-relaxation parameter used during the elastically-mounted cylinder convection substep
ζ	Mechanical damping ratio
η	Coordinate axis in computational space
λ	Wavelength of Floquet mode in cylinder diameters
λ_{osc}	Normalised wavelength of cylinder oscillation, U/fD
μ	Floquet multiplier
μ_H	Floquet multiplier on the half-period flip map
μ_v	Dynamic viscosity
ν	Kinematic viscosity
ξ	Coordinate axis in computational space
ρ	Fluid density
σ	Power of exponential growth of a Floquet mode
σ_l	Coefficient of linear term in the Stuart-Landau model

Continued on next page →

← Continued from previous page

Symbol	Description
σ_y	Standard deviation of amplitude envelope of the elastically-mounted cylinder response
τ	Non-dimensional time, tU/D
ϕ	Phase lag of cylinder cross-flow displacement to lift force
ϕ_v	Phase between cylinder displacement and vortex lift
ϕ_p	Phase between cylinder displacement and pressure lift
θ	Angle of wave vector used during elliptic instability theory

CONTENTS

1	Preliminary remarks	1
2	A review of the literature	7
2.1	Flow past a fixed cylinder	7
2.1.1	Steady flow	8
	Creeping flow	8
	Separated flow	8
2.1.2	Unsteady flow	9
2.1.3	Three-dimensional flow	12
	Mode A	12
	Mode B	13
	Mode QP	15
2.1.4	Higher Reynolds number flow	16
2.2	Flow past an oscillating cylinder	17
2.2.1	Synchronisation	19
	The effect on wake frequency	19
	The effect on oscillation frequency during vortex-induced vibration	20
	The effect on oscillation amplitude	21
2.2.2	Phase, vortex-shedding timing and energy transfer	22
	Phase jumping	22
	Energy transfer	23
2.2.3	Wake modes	25
2.2.4	Mass-damping and response branches	28
	Mass-damping as a parameter	28

Branching of amplitude response	30
Discrepancies with the upper branch	32
Evidence for a two-dimensional upper branch	34
The critical mass ratio	35
2.2.5 Direct predictions of vortex-induced vibration from driven oscillations	36
Prediction from sinusoidal oscillation	36
Multi-frequency forcing	39
2.2.6 Analytical models of vortex-induced vibration	39
2.2.7 Effects of vibration on wake transitions	41
Delaying the onset of three-dimensionality with transverse oscillation	42
The inducement of unsteady flow by elastic mounting	44
2.2.8 Review summary and hypotheses	45
Hypothesis 1: Dependence on Re for two-dimensional flow	45
Hypothesis 2: Branching behaviour in two-dimensional flow	46
Hypothesis 3: Sinusoidal oscillation is not universally applicable	47
Hypothesis 4: Oscillation delays three-dimensional flow	48
Hypothesis 5: The primary Hopf bifurcation remains supercritical	49
3 Methodology and validation	53
3.1 Introduction	53
3.2 The governing equations: Navier–Stokes and continuity	54
3.3 Discretisation	55
3.3.1 Time-splitting	55
3.4 Integration of the substep equations	56
3.4.1 The convection substep: Externally-driven cylinder	56
3.4.2 The convection substep: Elastically-mounted cylinder	57
3.4.3 The pressure substep	60
3.4.4 The diffusion substep	61
3.5 Boundary conditions	61
3.6 The spectral-element method	62
3.7 Floquet stability analysis	66
3.8 Convergence and validation studies	69

3.8.1	Domain size	69
3.8.2	Grid resolution	72
3.8.3	Timestep dependence	72
3.8.4	Floquet analysis	73
3.8.5	Validation summary	77
4	Sinusoidal externally-driven oscillation	79
4.1	Introduction	79
4.2	Wake modes and variation with Reynolds number	80
4.3	Energy transfer	83
4.4	Phase between lift and displacement	87
4.5	Added mass and vortex force	89
4.6	Explicit dependence on Reynolds number	95
4.7	Sinusoidal oscillation summary	97
5	Vortex-induced vibration of an elastically-mounted cylinder	101
5.1	Introduction	101
5.2	The existence of three response regimes	103
5.2.1	An overview	103
5.2.2	Time history of cylinder response	107
5.2.3	Spectra of cylinder response	109
5.2.4	Phase space of cylinder and wake response	111
5.2.5	Wake structure in the different regimes	114
5.2.6	Chaotic behaviour at higher mass ratio	117
5.2.7	The dependence on Reynolds number of the chaotic regime	117
5.3	A comparison between elastically-mounted and driven oscillation	120
5.3.1	A comparison with sinusoidal driving	120
5.3.2	More complicated driving functions	123
5.4	Comparison with the upper branch at higher Re	126
5.5	Vortex-induced vibration summary	127

6	The transition to three-dimensional flow	131
6.1	Introduction	131
6.2	A definition of the problem studied	135
6.2.1	Geometry and oscillation history	135
6.2.2	The identification of critical values	135
6.3	Wake modes and three-dimensional transitions	136
6.4	Three-dimensional instabilities of the $2S$ base state	140
6.4.1	Mode A	141
6.4.2	Mode B	145
6.4.3	Mode QP	146
6.5	Three-dimensional instabilities of the $P + S$ base state	151
6.5.1	Mode SL : The first subharmonic mode	151
6.5.2	Mode SS : The second subharmonic mode	153
6.5.3	Behaviour of the subharmonic modes with increasing A^*	153
6.6	Floquet stability analysis summary	158
7	The primary Hopf bifurcation of an elastically-mounted cylinder	161
7.1	Introduction	161
7.2	A definition of the problem studied	165
7.3	The nature of the Hopf bifurcation	166
7.4	Determination of the critical Reynolds number	168
7.5	Hopf bifurcation summary	172
8	Conclusions	175

CHAPTER 1

PRELIMINARY REMARKS

Vibration and oscillation surround us. The phenomenon seems to infiltrate our world at every scale, from the Brownian motion of molecules to the orbits of planets. Living systems are practically synonymous with oscillations, and examples abound, such as beating hearts, growth cycles and predator-prey populations in ecosystems. Indeed, it seems a world without vibrations is a dead one.

Engineering has an interesting relationship with vibration and oscillatory systems. On the one hand, vibration is integral to our industrial and technological progress. Power generation from turbines and internal-combustion engines rely on the process of cyclic systems. On the other hand, vibrations can lead to catastrophic failure. Bridges can collapse, structural members fatigue and complex systems fail because of a lack of consideration, or the inability to eliminate, vibration. It has been generally the latter that has inspired research into flow-induced vibrations. Phenomena such as flutter, shell modes, and vortex-induced vibration are all examples of flow-induced vibration. Whole textbooks have been dedicated to the subject, including those from Naudascher & Rockwell (1994) and Blevins (1977).

Vortex-induced vibration, in particular, occurs in a plethora of circumstances. Generally, all that is required for its occurrence is a bluff structure immersed in a fluid stream. It is in this situation that vortex-shedding occurs, where vortices roll up and are shed alternately from either side of the bluff structure into its wake. The structure of the wake formed is often referred to as the Kármán vortex street. This wake structure is incredibly pervasive, existing in some form over a huge range of scales, occurring from bodies such

as very fine wires on the scale of millimetres as Aeolian tones Strouhal (1878), to bodies such as whole islands in atmospheric and oceanographic flows on the scale of kilometres (Chopra & Hubert, 1964). This alternating vortex shedding causes an alternating force on the submerged body.

An alternating, periodic force on a body that can oscillate can lead to the phenomenon of resonance. This occurs when the frequency of the forcing is close to a natural frequency of the body. Oscillating bodies are most receptive to frequencies close to their natural frequency and large oscillations can occur as the body resonates with the periodic forcing.

However, the situation is more complex during vortex-induced vibration. Not only does the body receptivity change depending on the frequency of forcing, but the frequency of forcing can become dependent on the body oscillation, as the body oscillation changes the flow, and therefore the frequency of the shedding vortices. This phenomenon is known as synchronisation, and is due to the coupling between the immersed structure oscillation responding to the flow, and the flow responding to the structural oscillation.

This leads to a very complicated dynamic system, that can involve non-linear coupling, turbulence, and effectively infinite degrees of freedom. To make any progress in understanding this problem, a reductionist approach needs to be taken. The system first needs to be reduced to its base concepts, and then to have its complexity increased one component at a time to gain some insight into what are the key parameters and features of the phenomena.

Probably the simplest system that bears any resemblance to this problem is that of a rigidly-mounted circular cylinder immersed in a uniform free stream. The cross-section has no sensitivity to alignment, and this system can be characterised by a single parameter, the Reynolds number, defined by

$$Re = \frac{UD}{\nu}, \tag{1.1}$$

where U is the freestream velocity, D is the cylinder diameter, and ν is the kinematic viscosity of the fluid involved. This quantity represents the ratio of inertial to viscous forces in the flow, and allows comparison across different scale flows. Even though there is no coupling in this system (due to the rigid cylinder mounting), increasing the Reynolds number sees the system move from steady flow, to periodic two-dimensional flow, to three-dimensional flow, and finally to fully-turbulent flow. From the transition to periodic two-

dimensional flow onwards, vortex shedding occurs. So, the simplest flow with some potential to act as the base case for an attack on vortex-induced vibration is two-dimensional vortex shedding.

To build on this base case, the following strategy has been employed in the work undertaken in this thesis. First, an externally-controlled transverse oscillation has been added, while keeping the flow two-dimensional. This configuration has a body motion that is uncoupled from the fluid flow, but does introduce the effect of oscillation on the flow. In this way, phenomena such as synchronisation and wake organisation can be investigated.

Next, the cylinder is allowed to oscillate freely in only one direction. This adds the complexity of coupling the body motion to the fluid flow. Comparison with the uncoupled externally-controlled cylinder can also elucidate the importance of allowing information to flow to and from the cylinder.

Finally, the transition from a purely two-dimensional flow to a three-dimensional flow, with variation along the span of the cylinder, is investigated in the wake of the externally-controlled cylinder. This overall strategy allows some insight into the physics behind the behaviour that is integral to vortex-induced vibration.

From a fundamental point of view, it is unfortunate that the majority of studies of vortex-induced vibration has been done for systems that are much more complex than this. Generally, the flow during experiments is at least three-dimensional, this being driven by direct engineering applications, particularly from marine engineering. This is clear from the literature review presented as part of this thesis. The flows encountered in marine engineering situations are generally very high Reynolds number, turbulent, shear flows. Incorporating all of these features in experiments, while valuable for empirical rules for engineering design, do not always allow the key physical phenomena involved to be clearly identified and quantified.

While a statement of the hypotheses tested in this thesis and the justification for them is given in the literature review of chapter 2, an outline of the structure of the thesis document is given here. First, the aforementioned literature review is presented. This review attempts to present the state of knowledge in the field of vortex-induced vibration, and to identify some of the key areas where knowledge is lacking. From these areas, hypotheses have been formed.

Chapter 4 then presents results from a series of two-dimensional direct numerical simulations (DNS) of an externally-driven cylinder. Chapter 5 presents results from two-dimensional DNS simulations of an elastically-mounted cylinder, and a comparison between these elastically-mounted results and the decoupled externally-driven results.

Following these chapters reporting on the classification of the flow in different regimes, two of the transitions between states of complexity are investigated. First chapter 6 looks at the transition between two-dimensional and three-dimensional flow, the first step on the path to fully-developed turbulence, in the wake of the externally-driven cylinder. This is done employing Floquet stability analysis. Chapter 7 then reports on the transition between steady and unsteady flow for the elastically-mounted cylinder. This transition is studied using a Stuart-Landau model. This is essentially a study of the nature of the beginning of vortex-induced vibration in the coupled fluid-structure system.

Finally, the overall conclusions of the thesis are presented. These focus on the most important findings, and how the results obtained relate to the hypotheses posed in chapter 2.

CHAPTER 2

A REVIEW OF THE LITERATURE

2.1 Flow past a fixed cylinder

For over a century, research has been conducted on the flow past a fixed circular cylinder. A primary reason for this is that the geometry is easy to describe, being defined by only the cylinder diameter and length. In the limit of two-dimensional flow, this description requires the definition of only one term, the diameter. Other shapes share this feature, such as squares and equilateral triangles, however, these shapes possess sharp corners, or discontinuities. This means that the angle of attack of the flow needs to be considered for these other cross-sections, whereas it is unimportant for a circular cylinder.

In fact, the geometrical simplicity of a circular cylinder immersed in a uniform stream of Newtonian fluid means it can be completely described by a single parameter. This parameter is the Reynolds number, $Re = UD/\nu$, which represents the ratio of inertial to viscous forces. Here, U is the freestream velocity, D is the cylinder diameter and ν is the kinematic viscosity. As Re is increased from zero to infinity, the flow around a circular cylinder does not vary linearly, but a series of distinct transitions do occur. The flow moves from a two-dimensional creeping flow, to a two-dimensional separated flow, then to an unsteady flow, a three-dimensional flow and finally a fully-turbulent flow. Summations of the characteristics of these different flow regimes, particularly those after the transition to unsteady flow, are given in Roshko (1993) and Williamson (1996*b*).

These different flow regimes provide a natural delineation when describing the flow

around a circular cylinder. Therefore, the following review of the literature pertaining to this flow is presented in sections relating to increasing Re .

2.1.1 Steady flow

Creeping flow

For very low values of Re (where $Re < 1$), viscous forces dominate the flow. The “stickiness” of the flow damps out any deviation of the flow quickly. The flow does not separate from the surface of the cylinder, but stays completely attached, and the flow streamlines appear identical upstream and downstream of the cylinder. An example of such a flow is shown in figure 2.1a.

This flow pattern of attached flow is also observed in analytical solutions of the flow past a cylinder arising from potential flow theory. Potential flows are governed only by Bernoulli’s equation and continuity, rather than the more complex Navier–Stokes equation.

While the flow pattern that potential flow theory renders looks very similar to that obtained with creeping flow, the solution leads to the conclusion that the cylinder should experience no drag force, a conclusion known as D’Alambert’s paradox (Roshko, 1993). This zero drag conclusion is far from true, as the drag coefficient, C_D , is at its highest when $Re \rightarrow 0$.

This problem was overcome by Stokes, whose equations considered viscous effects. Stokes’ treatment of the flow around a sphere analytically obtained the forces on a pendulum ball in creeping flow (Stokes, 1851). For this reason, such creeping flow is often referred to as Stokes flow. Stokes flows, being governed by a set of linear equations, have the property of being reversible, so that if the flow and external forces are reversed, the flow returns exactly to its original state.

Separated flow

Stokes flow around a circular cylinder persists only at very small values of Re , until the first of a series of transitions occurs. This is the transition to separated flow, when small regions of recirculating flow form at the rear of the cylinder. An example of this steady, separated flow is shown in figure 2.1b. This occurs for $Re \simeq 5$ (Taneda, 1956). The flow

is no longer reversible, and convective effects cannot be ignored. With increasing Re , the length of this recirculation region increases (Taneda, 1956; Roshko, 1993).

This trend continues until $Re \simeq 46$ (Taneda, 1956; Roshko, 1993; Dušek *et al.*, 1994; Williamson, 1996*b*; Le Gal *et al.*, 2001; Thompson & Le Gal, 2004). At this limit, the flow undergoes its second major transition, this time to an unsteady, time-periodic flow. This type of transition, from a steady flow to a time-periodic flow, is known as a Hopf bifurcation (Hopf, 1942; Seydel, 1994). Analysis shows that this transition obeys very closely the Stuart–Landau model (Stuart, 1958, 1960), and that this transition is supercritical (Provansal *et al.*, 1987).

2.1.2 Unsteady flow

The transition from a steady flow to a time-periodic one is probably the most important transition in cylinder wakes with respect to vortex-induced vibration. After this transition, laminar vortex shedding occurs, with vortices being shed in turn from alternate sides of the cylinder. This periodic shedding causes a periodic force on the cylinder, the transverse component of which is responsible for exciting crossflow oscillation of elastically-mounted cylinders. The vortices shed organise themselves into a two-row configuration, known as the Kármán or Bénard-von Kármán vortex street, so called because of the early observation of this street by Benard (1908) and the observation and analysis of the configuration by von Kármán (1911). A classic example of the Kármán vortex street is shown in figure 2.1c.

Papers from von Kármán (1911) and Robinson & Saffman (1982) analysed a series of point vortices in inviscid flow. The results showed that only a particular spacing of the rows in the street was stable, that spacing being when the ratio of the distance between the rows to the distance between consecutive vortices in the same row was 0.281. All other configurations (including a single row of vortices) was shown to be unstable to infinitesimal two-dimensional perturbations.

The frequency of this shedding, where the flow remains laminar and two-dimensional, is a unique function of the Reynolds number. Further, this frequency can be expressed as a non-dimensional quantity known as the Strouhal number $St = f_{St}D/U$, where f_{St} is the frequency of shedding, D is the cylinder diameter, and U is the freestream velocity. This dimensionless group was first suggested by Rayleigh (1879), to collapse the data presented

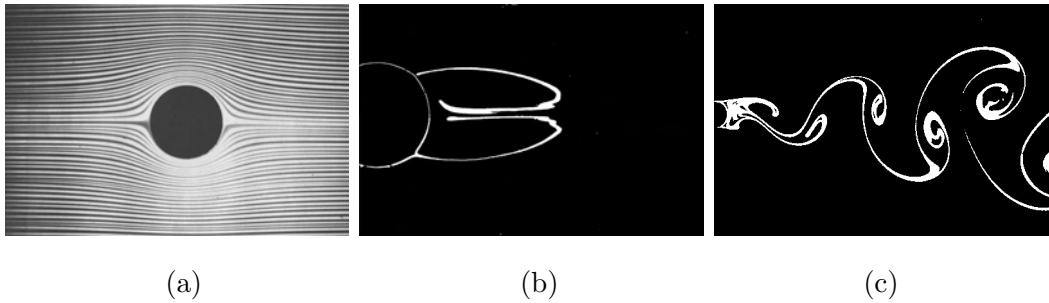


Figure 2.1: The regimes of flow past a fixed cylinder where the flow is two-dimensional. (a) Creeping flow, $Re \leq 5$. (b) Separated, steady flow, $5 \leq Re < 47$. (c) Two-dimensional vortex shedding, $47 \leq Re < 190$. Images taken from Van Dyke (1982).

by Strouhal (1878) in a study of Aeolian tones from cylindrical strings.

Roshko (1954) proposed a functional fit of St versus Re for $Re \leq 1000$. However, there was considerable spread in the data, especially for Re in the range of $90 < Re < 350$, and it was suggested by Tritton (1959, 1970) that there was a “low-speed” mode of shedding for $Re < 105$, and a “high-speed” mode for $Re > 80$. This suggestion was because of an apparent discontinuity in the St – Re curve at Re around 100. This observation was not made by all researchers (Gaster, 1969). This discrepancy was effectively resolved by the discovery of oblique shedding modes by Williamson (1989), where vortices are shed with their axes not parallel to the axis of the cylinder. Williamson (1989, 1992) showed that if the Strouhal number was corrected according to the angle of the oblique shedding, the Strouhal number data collapsed to a single curve.

This work on oblique shedding modes showed that careful manipulation of the end effects of the flow (such as end plates and base suction) could induce parallel shedding. Effectively, this was through decreasing the local stability in the near wake at the ends of the cylinder (Monkewitz, 1996). With the ability to induce parallel vortex shedding, and methods to correct the Strouhal number for oblique shedding effects, a new curve fit was suggested by Williamson & Brown (1998) based upon a series in $1/\sqrt{Re}$ extending up to at least $Re = 1000$. Very close fits could be obtained with the data, except over a range $190 \leq Re \leq 260$, which was attributable to the three-dimensional mode A (which is expanded upon in section 2.1.3). An example of such an St – Re plot is shown in figure 2.2.

Aside from just collapsing data, attempts have been made to link the value of St to

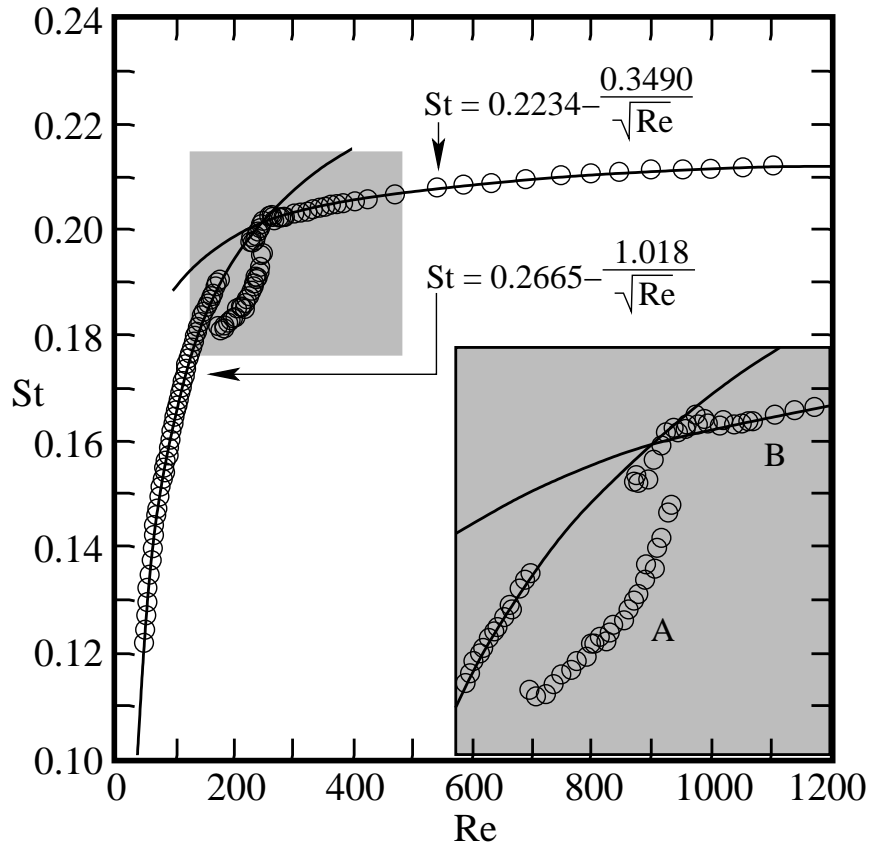


Figure 2.2: St - Re curve, taken from Williamson & Brown (1998). Data points are from experiments, solid lines are a fit of a series in $1/\sqrt{Re}$. The inset shows a close-up image of the discontinuity caused by the onset of three-dimensionality.

properties of the resulting flow, instead of just the dimensions of the geometry (Roshko, 1955; Williamson & Brown, 1998). This type of parameter was shown to collapse shedding data from a number of bluff bodies reasonably well, being based on a length scale representative of the wake width and the flow speed just outside the separation point. Such studies seemed to indicate that vortex shedding has little to do with the shape of the bluff body, and more to do with the configuration of the major wake structures.

It is clear that vortex shedding is usually quite a measurable property of bluff-body wakes. It is also very robust. While the shed vortices, and the shear and boundary layers eventually become turbulent with increasing Re evidence of vortex shedding persists up to values of at least $Re = 10^7$. This, of course, has ramifications for vortex-induced vibration, and reinforces the importance of the initial transition to unsteady flow in the cylinder wake.

The only region where the vortex shedding frequency seems to refuse to submit to a smooth function of Re (at least for $Re < 1000$) is over the range $190 \leq 260$. Various $St-Re$ curves (Williamson, 1992, 1996*b*), or plots of base suction coefficient (Roshko, 1993; Williamson, 1996*b*, 1997) display a discontinuity that begins somewhere around $Re = 190$, which is highlighted in the inset of figure 2.2. This discontinuity has long been documented, but has only relatively recently been attributed to the transition to three-dimensionality (Williamson & Roshko, 1988). This transition marks the start of the path to turbulence in the wake, and is the subject of the next section.

2.1.3 Three-dimensional flow

As noted previously, with the transition to three-dimensional flow in the cylinder wake, there is a marked discontinuous drop in St as energy is transferred to the three-dimensional mode. In fact, it can become quite difficult to define St in the neighbourhood of this transition, and it has been raised that the wake may not be perfectly periodic after the onset of the first three-dimensional mode of flow.

Mode A

The transition to three-dimensionality begins with the onset of mode A (Williamson, 1988). The mode is characterised by deformation of the vortex cores in the Kármán vortex street. The cores become wavy rather than straight, with a spatial wavelength of around 3.5 cylinder diameters. This waviness therefore turns some of the vorticity in the streamwise direction, and vortex loops are then drawn out in the high-strain region between the primary vortices (Henderson, 1997). The Reynolds number at which this transition occurs experimentally is scattered across the range $140 < Re < 194$ (Williamson, 1996*b*, 1997); however, this scatter has been attributed to end effects, and the “pure” transition is seen to occur very close to $Re = 190$ (Williamson, 1996*b*; Barkley & Henderson, 1996). The transition to mode A flow has been shown to occur through a subcritical transition (Henderson, 1997; Barkley *et al.*, 2000; Sheard *et al.*, 2003*a*), meaning the transition is hysteretic. Experimental and numerical examples of the structure of the saturated mode A are shown in figure 2.3.

The Floquet stability analysis of Barkley & Henderson (1996) provided predictions

of both critical wavelengths and Re for three-dimensional modes arising from the two-dimensional Kármán vortex street. That study found that the first Floquet mode became unstable at $Re = 188.5$, and possessed a spatial wavelength of $\lambda = 3.96D$, corresponding to mode A. This linear analysis also indicated that mode A was at its strongest in the vortex cores, agreeing with the experimental observation of vortex core waviness.

Leweke & Williamson (1998) investigated the character of the mode A instability. Following the work of Henderson (1997) marking mode A as primarily due to an elliptic instability, elliptical instability theory was applied utilising the methods of Landman & Saffman (1987) and Waleffe (1990). The analysis returned a predicted wavelength for the instability of $\simeq 3D$, in good agreement with the observed wavelength of mode A. Their analysis also indicated areas of the flow where the mode would be expected to grow. This was expanded in the work of Thompson *et al.* (2001), which showed that mode A was characterised as a cooperative elliptic instability. The mode was observed to originate in the forming vortex cores at the rear of the cylinder, and was then amplified in the high-strain region between vortices, after which a further elliptic instability of the shed vortices accentuated the mode.

The paper from Henderson (1997) covered many phenomena relating to the transition to three-dimensionality and mode A. The symmetry properties of the mode were reported, and an investigation to the effect of the span of the cylinder was made. It was reported that for long cylinder spans, mode A led to the development of spatio-temporal chaos, or a disordered pattern and a lack of periodicity in the wake. This was distinguished from strong turbulence that occurs with increasing Re and the reducing impact of dissipative viscous forces. This spatio-temporal chaos offered an explanation for the spread in the data of earlier $St-Re$ curves (Roshko, 1954).

Mode B

While mode A is the first three-dimensional mode to arise, it is not the most resilient. A second, finer-scaled mode arises with a modest increase in Re , logically named mode B (Williamson, 1988). This mode is characterised by a spatial wavelength $\lambda \simeq 0.8D$, and is more or less focused in the braid shear layer that links successive primary vortices in the Kármán vortex street. Examples of the saturated mode B are shown in figure 2.3.

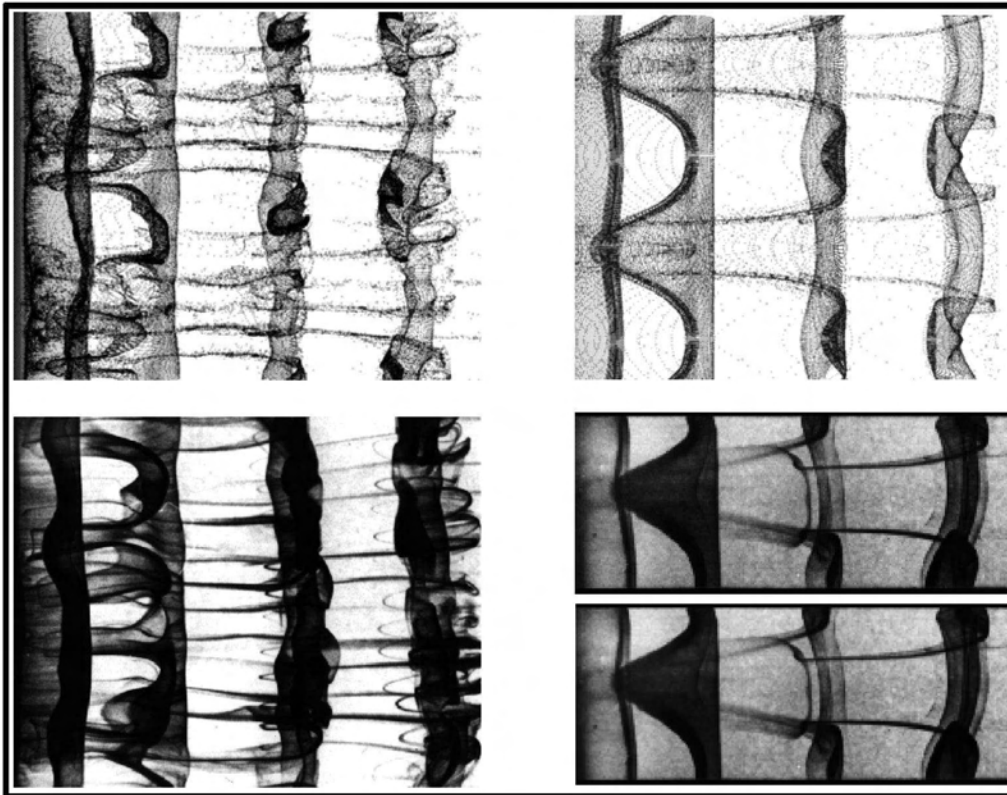


Figure 2.3: The saturated mode structure for mode B (left), and mode A (right). The bottom images were obtained through dye visualisation during experiments such as those by Williamson (1996*b*). The top images were obtained through particle tracking three-dimensional simulations such as those by Thompson *et al.* (1996). Both show the development of spanwise vortices. The wavyness of the vortex cores in mode A is clear, as is the finer-scale structure of mode B. Flow is from left to right. Reproduced from Thompson *et al.* (2006).

It has been indicated that mode B is a hyperbolic instability of the braid region (Henderson, 1997; Leweke & Williamson, 1998), but the findings are not as conclusive as that for the elliptic instability theory for mode A. It has also been proposed by Ryan *et al.* (2005) that mode B is caused by a centrifugal instability.

Floquet stability analysis by Barkley & Henderson (1996) predicted mode B to first become unstable at $Re = 259$, but experimentally mode B is first detected anywhere in the range $230 \leq Re \leq 250$ (Williamson, 1988, 1996a). This is because of the destabilising effect that mode A has on mode B (Barkley *et al.*, 2000). With the onset of mode B, energy is gradually passed from mode A to mode B, until by $Re \simeq 285$ there is effectively no evidence of mode A. Once mode B is established, it is very robust, with evidence of mode B still present in the wake at $Re = 1000$ (Wu *et al.*, 1996).

Early three-dimensional simulations by Karniadakis & Triantafyllou (1992) indicated that mode B was the primary three-dimensional transition, and that it led to a period-doubling cascade as the route to turbulence. However, later simulations from Zhang *et al.* (1995), and the extensive computations of Thompson *et al.* (1996) indicated that if a suitable spanwise domain was employed, mode A was resolved and the predicted period-doubling cascade did not occur, the route to turbulence instead being through spatio-temporal chaos. These findings highlighted that the suppression of particular three-dimensional modes could change the path to turbulence.

Mode QP

Following the discovery of modes A and B, and their effect on the path to turbulence, it seems natural to investigate what other types of modes are possible. As well as modes A and B, other modes have been shown to be theoretically possible. Marques *et al.* (2004) and Blackburn *et al.* (2005), using group theory (Rosen, 1995), showed that for flows possessing the symmetries of the Kármán wake, only three generic bifurcations can arise from the two-dimensional base flow: the first breaks only the spanwise translational symmetry, and corresponds to mode A; the second breaks the “space” part of the spatio-temporal symmetry in the original plane of the flow, and corresponds to mode B; and the third, and last, breaks the “time” part of the spatio-temporal symmetry, and is represented by a quasi-periodic mode, or a mode that has a different period to the two-dimensional base flow.

Such a quasi-periodic mode can be found numerically in the fixed cylinder wake (Blackburn & Lopez, 2003). It is predicted to occur around $Re = 377$, and so is not observed in experiments, as the base flow is far from two-dimensional by this stage. However, experiments by Zhang *et al.* (1995) with an upstream tripping wire excited a mode with a similar value of λ to this quasi-periodic mode, in the Reynolds number range $170 \leq Re \leq 270$.

The experiments of Zhang *et al.* (1995) and the restricted-domain simulations of Karniadakis & Triantafyllou (1992) demonstrated that relatively passive measures could be used to affect the inception order of the three-dimensional modes, even if there is only a small number of possible modes involved (Marques *et al.*, 2004; Blackburn *et al.*, 2005). It is therefore plausible that an oscillating cylinder, such as that which occurs during vortex-induced vibration, will have a different mode inception order and different path to wake turbulence than a fixed cylinder. Also, due to the coupled nature of the cylinder and the wake, the modes could have important ramifications for the vortex-induced vibration response.

The focus of this thesis is on low- Re vortex-induced vibration, and as such, the discussion of the relevant fixed cylinder wake characteristics is completed here. However, to complete the picture, the basic behaviours of the cylinder wake at higher Re are summarised in the following section.

2.1.4 Higher Reynolds number flow

As the Reynolds number is increased further, the disorder of the wake increases as full turbulence is approached. This occurs because of the presence of a series of fundamental instabilities of the shear flow. The first of these is an instability of the free shear layer, which is a Kelvin-Helmholtz instability, that causes the shear layers to become wavy. This phenomenon was well-described by Bloor (1964). The transition point from laminar to turbulent flow in the shear layer moves upstream toward the cylinder with increasing Re . The shear layers can also develop some three-dimensionality.

At $Re \geq 2 \times 10^5$, the so-called drag crisis is encountered, where the average drag force is suddenly reduced. This occurs due to the fact that a separation-reattachment bubble is formed by the shear layer. The reattached boundary layer then finally separates much further towards the rear of the cylinder, resulting in a narrow wake, hence lower form drag

(Williamson, 1996b) and a significantly lower base suction coefficient. The sudden drop in base suction is well-illustrated in figure 2.4a. The Re at which this occurs is classically referred to as *critical*, with subcritical flow comprising of no separation and reattachment, and supercritical flow occurring at Re higher than that where the separation-reattachment bubble is formed. However, vortex shedding is still present. An example is shown in figure 2.4b.

As Re is further increased, the forming boundary layers themselves become fully turbulent. It was originally envisaged that this would mark the end of any periodicity in the wake, as vortex shedding gave way to a completely turbulent wake fed by turbulent boundary layers. However, periodicity has been detected at Reynolds numbers above this limit, further emphasising the importance of this wake.

2.2 Flow past an oscillating cylinder

The focus of this thesis is on cylinders constrained to oscillate across the stream, either through vortex-induced vibration, or some external driving. Therefore, the following section of this literature review focuses on the primary phenomena that occur in such a flow. Many of these phenomena are observed in both the coupled problem of vortex-induced vibration, and the flows past externally-driven cylinders. For this reason, the literature pertaining to both of these flows is presented together, with a distinction made between vortex-induced vibration or driven cylinder studies when appropriate.

The reason for this is two-fold. First, as previously mentioned, many phenomena are observed in both flows, and it makes sense to focus on the aspects of the flow, rather than on the particular setup that generated them. Second, this allows an efficient comparison of the two systems. This is required as an aim of this thesis is to investigate the viability of modelling the more complex vortex-induced vibration problem with the decoupled driven oscillation. By being able to compare the two directly, the similarities and differences can be most easily highlighted.

Before considering the modelling of vortex-induced vibration, it is important to have a sound understanding of how the oscillation of a cylinder changes the behaviour of the flow from the limiting case of a fixed cylinder. Therefore, phenomena such as synchronisation,

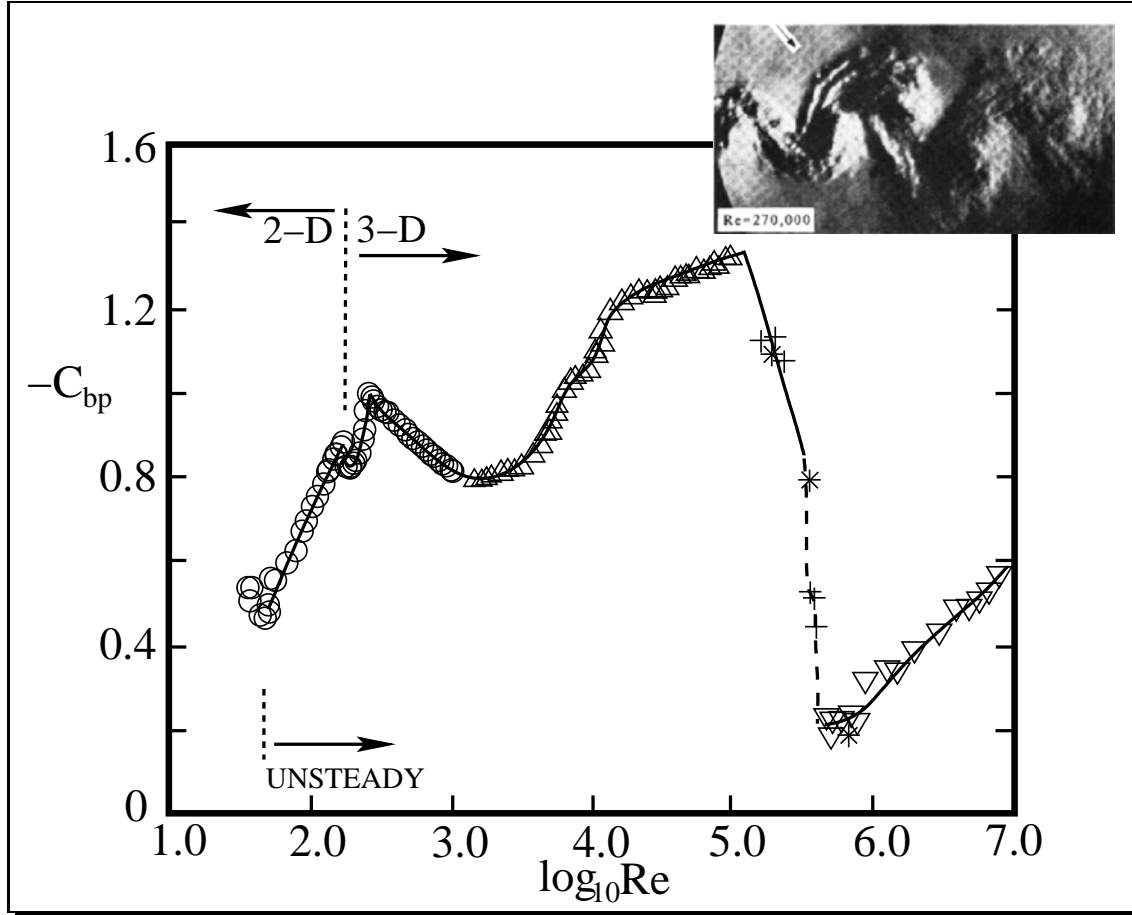


Figure 2.4: The base suction coefficient, expressed as negative base pressure coefficient, as a function of Re for a fixed cylinder. Note the sudden drop at the drag crisis that begins at $Re = 10^5$. Reproduced from Roshko (1993). Inset: A Schlieren photograph showing the presence of vortex shedding at $Re = 270000$, demonstrating the resilience of the instability. Reproduced from Williamson & Govardhan (2004), from Thomann (1959).

phase and timing of vortex shedding, energy transfer, wake modes, and effects on flow transitions will be presented. With these concepts established, oscillation-specific phenomena will be presented, such as amplitudes of response, the effects of mass and damping, and branching behaviour defining different regimes of response. Following this, work directly modelling vortex-induced vibration, and analytical models will be examined.

2.2.1 Synchronisation

The effect on wake frequency

One of the most profound effects of cylinder oscillation upon the cylinder wake is that of synchronisation, or lock-on. This is where the oscillation of the wake changes from its normal oscillation frequency, to match the oscillation frequency of the cylinder.

In driven cylinder experiments, the cylinder oscillation also has the effect, during synchronisation, of synchronising the moment (in time) of shedding along the span of the cylinder (Bearman, 1984), so that parallel vortex shedding is universally observed, with no oblique modes present. A finite amplitude is required to effect synchronisation, of around $0.05D$ (Koopman, 1967; Bearman, 1984). Amplitudes lower than this can only effect intermittent synchronisation at best (Blackburn & Melbourne, 1997).

Synchronisation has been noted by myriad papers, an early example of which is Bishop & Hassan (1964). In their experimental driven oscillation study, they found synchronisation occurred for driving frequencies close to, but both above and below, the shedding frequency. Therefore, a defining parameter was the ratio of the oscillation frequency to the Strouhal frequency, f/f_{St} . It was also noted that the range of synchronisation frequencies seemed to increase with increasing amplitude of oscillation.

This was systematically studied by Koopman (1967) with a series of low- Re experiments. It was shown as the amplitude of oscillation increased, so did the range of frequencies resulting in synchronisation. This range always encompassed the Strouhal frequency for a fixed cylinder, f_{St} , but extended further for frequencies below f_{St} than for frequencies above it. This synchronisation dependence on A^* has been confirmed through the experiments of Griffin (1971), Griffin & Ramberg (1974), Stansby (1976) and Williamson & Roshko (1988), and the simulations of Hurlout *et al.* (1982), Blackburn & Karniadakis (1993), and Meneghini & Bearman (1995) among others, at Re where the flow is both two- and three-

dimensional. The synchronisation boundaries defined during the experiments of Koopman (1967) are shown in figure 2.5a.

An aspect of synchronisation that has received relatively little attention is the effect of Re . The essentially two-dimensional flow experiments of Koopman (1967) and the three-dimensional experiments of Bishop & Hassan (1964) both reported some inverse dependence on Re for the range of synchronised oscillation frequencies. However, the later, detailed, study of Williamson & Roshko (1988) ignored the effect of Re , at least in the range of $300 \leq Re \leq 1000$, on the basis that St for a fixed cylinder is approximately constant over this range.

The effect on oscillation frequency during vortex-induced vibration

Synchronisation plays a major part in vortex-induced vibration. During vortex-induced vibration, the wake vortex shedding frequency also changes from the Strouhal frequency for a fixed cylinder to match the oscillation frequency of the cylinder. However, the oscillation frequency of the cylinder is set by the system, and not externally imposed. There is a coupling between the wake and cylinder. This effect is clear from the results of Govardhan & Williamson (2000) shown in figure 2.5b.

The parameter dictating synchronisation is not the oscillation frequency's proximity to the Strouhal frequency, but the proximity of the cylinder's natural frequency to the Strouhal frequency. The important parameter in this regard is f_N/f_{St} . However, the frequency of oscillation does not match the natural frequency, especially for low- m^* vortex-induced vibration. The exact frequency then depends heavily on the quantity of effective added mass, a concept further expanded on in section 2.2.4. It is only raised here to explain why the results for frequency of oscillation from Govardhan & Williamson (2000) presented in figure 2.5b do not converge to the natural frequency.

However, vortex-induced vibration results are usually presented using a parameter known as the reduced velocity, defined as $U^* = U/(f_N D)$. The use of this parameter arises from the fact that it is easier to vary the freestream velocity during an experiment than the natural frequency of the cylinder structure. It does lose the direct comparison with the Strouhal frequency, but if it is assumed St does not vary greatly from $St = 0.2$ over a large Re -range (White, 1999), then it should be expected to see synchronisation

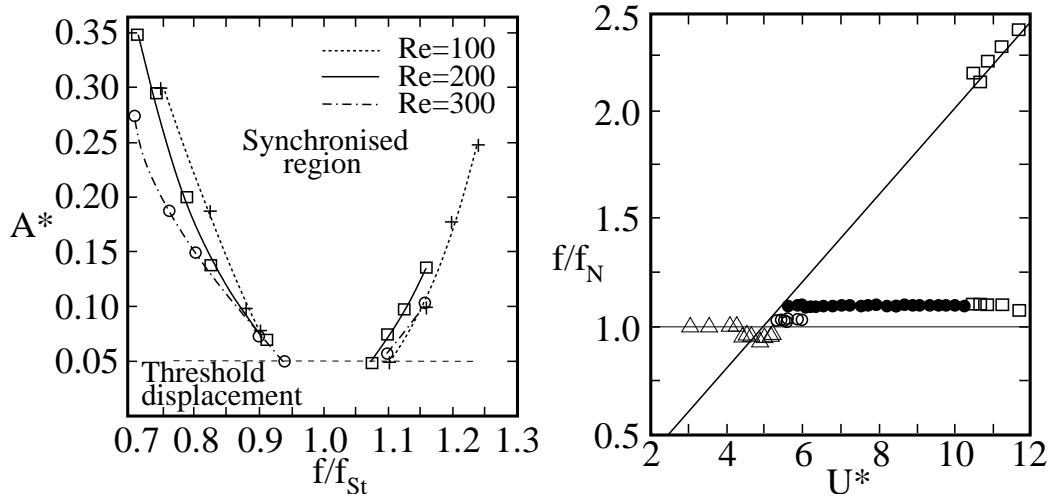


Figure 2.5: (a) Synchronisation boundaries during driven oscillation, reproduced from Koopman (1967). Note the increasing range of frequencies for synchronisation with increasing amplitude. (b) Frequency of oscillation results during vortex-induced vibration experiments, reproduced from Govardhan & Williamson (2000). In the synchronised regime, the flow moves away from the Strouhal frequency for a fixed cylinder (represented by the solid diagonal line) to a frequency close to the natural frequency of the cylinder structure.

effects somewhere in the vicinity of $U^* = 5$.

The effect on oscillation amplitude

Classical results illustrating synchronisation during vortex-induced vibration are found in the paper by Feng (1968). The results clearly show the effects of synchronisation over a range of $5 \leq U^* \leq 8$. The frequency of oscillation moves from the Strouhal frequency for a fixed cylinder, to close to the natural frequency of the cylinder structure. Also, as this occurs, the oscillation amplitude of the cylinder increases markedly. These vortex-induced vibration synchronisation features have been confirmed in many papers including Khalak & Williamson (1996, 1997, 1999) at higher Re , and Anagnostopoulos & Bearman (1992), Blackburn & Henderson (1996), and Blackburn *et al.* (2000) at lower Re where the flow is two-dimensional.

As well as the amplitude and frequency of oscillation, there is another parameter that is very important during vortex-induced vibration; the phase between the lift (cross-stream)

force and the cylinder displacement. This phase is related to the timing of vortex shedding. As it plays such an important role in the process, but is not expressly linked to synchronisation, it forms the topic of the next section.

2.2.2 Phase, vortex-shedding timing and energy transfer

“Phase”, with respect to vortex-induced vibration, can be slightly misleading. Using the term implies that the two signals being compared are of the same form, and perfectly periodic. It is easy to envisage that this is not the case for data obtained during vortex-induced vibration experiments. What is referred to as “phase” is actually the lag which gives the greatest correlation. However, for the sake of simplicity, the term “phase” is used here to describe this lag.

The importance of phase can be appreciated by considering a case where both the oscillation and lift force are sinusoidal. Under these assumptions, it can be shown that the direction of energy transfer is directly linked to the phase angle. For $0 \leq \phi \leq 180$, the energy transfer is positive (from the fluid to the cylinder); otherwise, the energy transfer is negative (from the cylinder to the fluid) (Carberry *et al.*, 2001; Carberry, 2001; Sarpkaya, 2004).

Phase jumping

The phase was observed by Bishop & Hassan (1964) to undergo a “jump” of approximately 180° at a frequency of oscillation just short of the Strouhal frequency, for a constant amplitude of oscillation. This phase jump was accompanied by a sudden jump in the peak lift force. Other, similar high-*Re* driven experiments have observed the same jump in phase and lift force (Carberry *et al.*, 2001; Gopalkrishnan, 1993). Zdravkovich (1982) presented photographs from a series of past papers, taken of both driven oscillation and vortex-induced vibration in both two-dimensional and three-dimensional flow, which showed that there were two variations to synchronised flow. The two variations were delineated by a difference in vortex shedding timing of half an oscillation cycle, or 180° . The photographs showed some early observations of the phase jump that had not been noticed at the time they were taken, such as in the experiments of Den Hartog (1932). Similar changes were observed by Griffin & Ramberg (1974).

Carberry *et al.* (2001) showed not only that there was a phase jump, but that it seemed possible to link this phase to a change in vortex-shedding timing *and* vortex organisation in the wake. With increasing frequency for a constant amplitude, it was observed that the wake switched from the $2P$ wake mode, consisting of two pairs of vortices shed each cycle of oscillation, to a $2S$ mode, consisting of two single vortices shed per cycle, similar to the conventional Kármán vortex street. Later studies as part of Carberry *et al.* (2003) showed that if the lift force was decomposed into “added mass” and “vortex” components, the vortex force underwent a phase jump slightly before the total force, giving an intermediate state. A similar decomposition was performed by Govardhan & Williamson (2000) for an elastically-mounted cylinder, showing that their upper branch of response also coincided with a phase jump with respect to the vortex force, but not the total force. The driven and elastically-mounted systems were directly compared in this regard by Carberry *et al.* (2002*a,b*). It was conjectured that the intermediate state found in the driven cylinder wake represented the upper branch in the elastically-mounted cylinder wake.

Interestingly, in both the driven and elastically-mounted systems, vortex phase (the phase between the vortex force and displacement) and total phase were observed to jump, or change by $\simeq 180^\circ$ over a very short range of frequencies or U^* (Sarpkaya, 2004). This is clearly demonstrated by the work of Khalak & Williamson (1996, 1997, 1999) for the elastically-mounted system. Data of phase against oscillation frequency, or reduced velocity, are shown in figure 2.6.

Energy transfer

While this characteristic compared well, the driven system was shown by Carberry *et al.* (2001, 2002*a*, 2003) to return values of phase that predicted negative net energy transfer, which is physically impossible in the elastically-mounted case. Blackburn & Henderson (1999) performed two-dimensional driven oscillation simulations and directly calculated the energy transfer per oscillation period. They showed a direct link between the jump in phase and a change in direction of energy transfer. They also showed evidence that the phase jump was dictated by a competition between vorticity production mechanisms, namely the acceleration of the oscillating cylinder, and the adverse pressure gradient in the boundary layer.

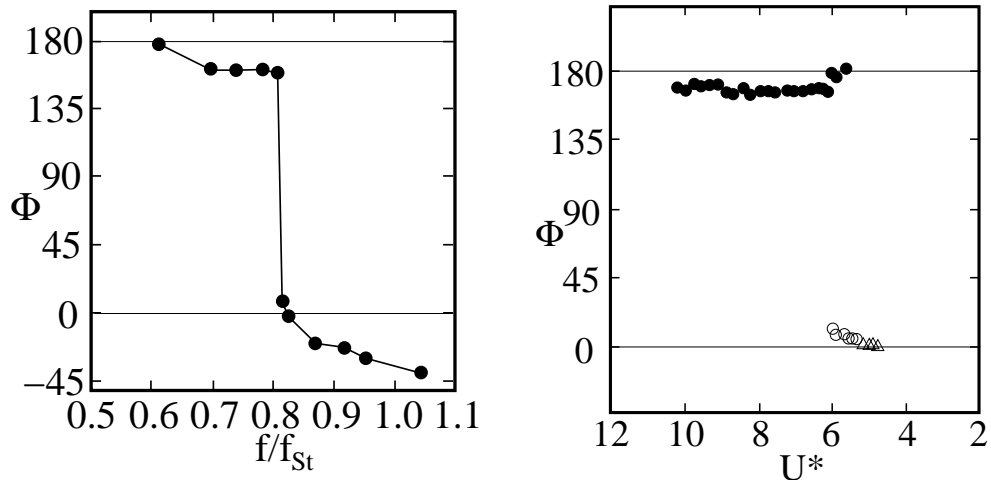


Figure 2.6: (a) Phase against frequency for driven oscillations, reproduced from Carberry *et al.* (2001). (b) Phase against reduced velocity during vortex-induced vibration. The data are taken from a Govardhan & Williamson (2000). Note the reversal of the U^* axis to allow a direct comparison with the driven oscillation results. Both systems show a distinct jump of close to 180° . However, the elastically-mounted system displays phase angles always between 0° and 180° , whereas the driven-oscillating cylinder renders phase angles outside this range.

Some differences were observed between the simulations and experiments that may be linked to this vorticity production. The simulations were two-dimensional, and low- Re , as opposed to the higher- Re and inherently three-dimensional experiments. Carberry *et al.* (2001) showed a link between the phase and the wake mode, where the wake mode is determined by the distribution of vortices, and therefore vorticity, in the wake. The study of Williamson & Roshko (1988) reported a difference in the wake modes obtained for $Re > 300$. Therefore, as the vorticity distribution is different, and phase is linked to vorticity production, it is not surprising that differences were observed in the phase behaviour.

This discussion also highlights the importance of wake modes. Therefore, the wake modes obtained during driven oscillation and vortex-induced vibration are presented in the following section.

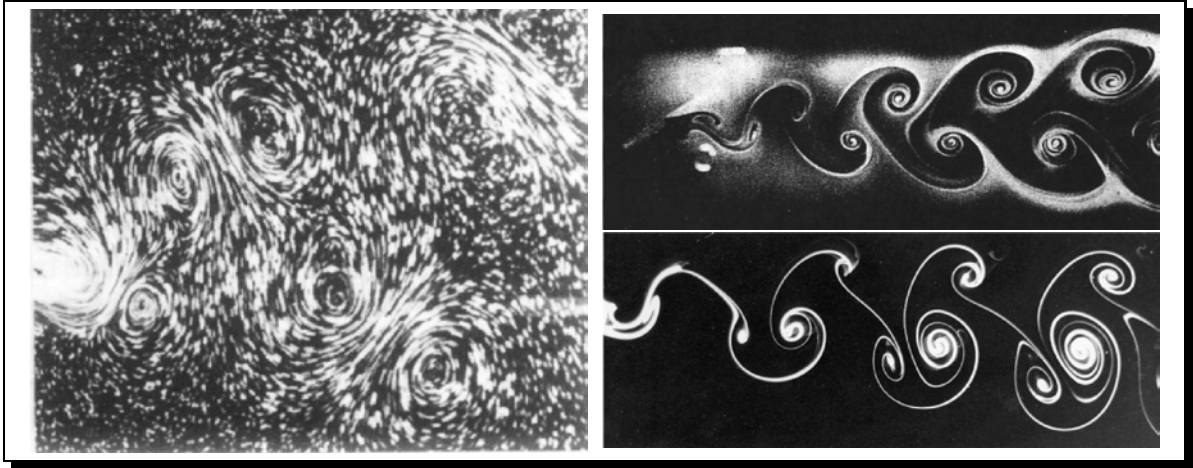


Figure 2.7: The major wake modes during synchronised vortex-induced vibration and driven oscillation. Left: the $2P$ mode (Williamson & Roshko, 1988). Top right: the $2S$ mode (Koopman, 1967). Bottom right: the $P + S$ mode (Williamson & Govardhan, 2004). Flow is from left to right in all images.

2.2.3 Wake modes

A systematic study of the wake modes of a driven oscillating cylinder was made by Williamson & Roshko (1988). In this study, the $A^*-\lambda_{osc}$ plane was covered by a series of experiments, and the wake modes for each classified. They were classified in terms of single vortices and pairs of vortices shed per oscillation cycle; i.e., the classic Kármán vortex street was designated the $2S$ mode, and a mode consisting of a pair of vortices shed each half-cycle was designated the $2P$ mode. In the regime of synchronisation, only the $2S$ and $2P$ modes were observed at amplitudes of relevance to vortex-induced vibration. Both of these modes possess a Z_2 spatio-temporal symmetry, which means if the flow is evolved forward by a half-period in time, and reflected about the wake centreline, the original flow pattern is recovered. Examples of the $2S$ and $2P$ mode, along with the asymmetric $P + S$ mode, are shown in figure 2.7. The wake mode map of Williamson & Roshko (1988) is reproduced in figure 2.8.

This wake-mode map was constructed for $300 \leq Re \leq 1000$. The Reynolds number was not held constant over the entire $A^*-\lambda_{osc}$ plane, it being argued that the Strouhal number for a fixed cylinder does not vary over this range. (However, significant changes do occur

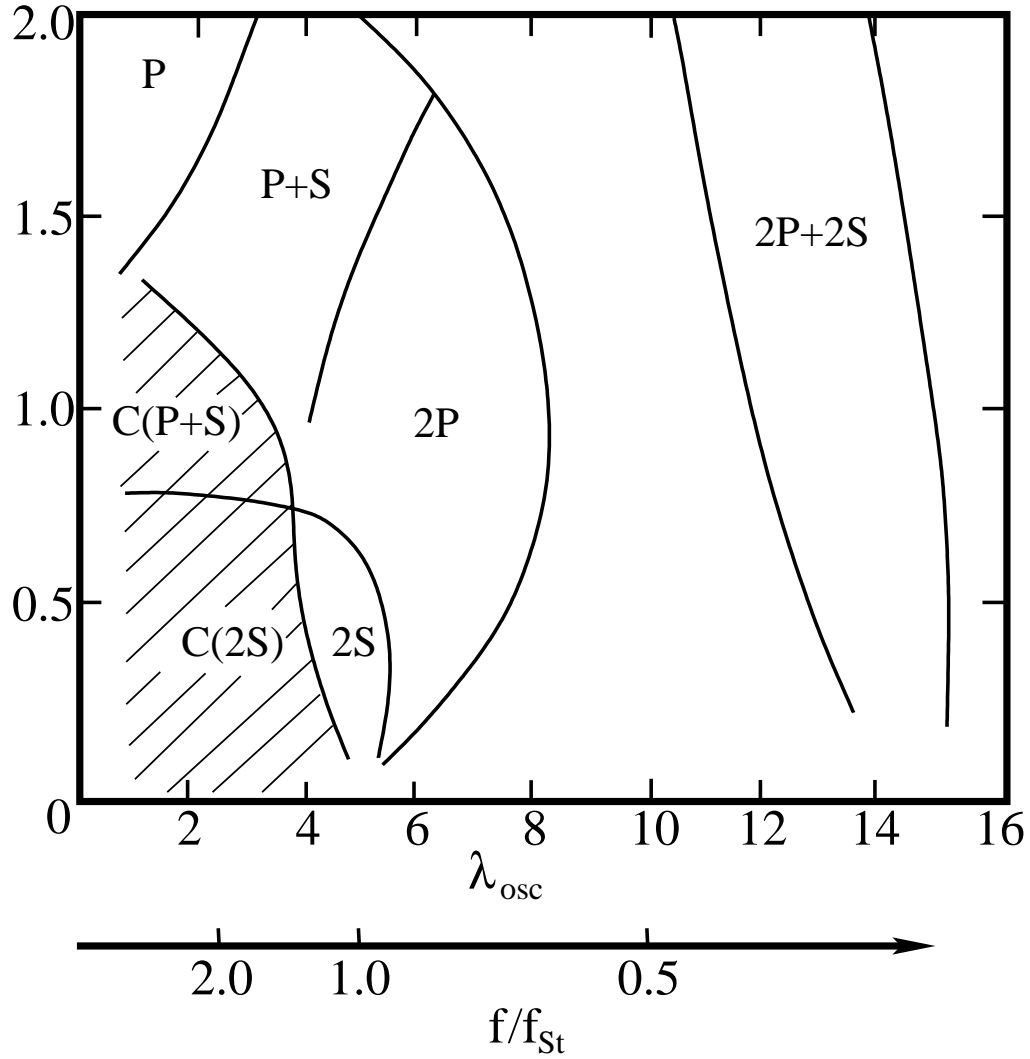


Figure 2.8: The wake mode map of Williamson & Roshko (1988). It is shown that in the region of primary synchronisation, only the $2S$ and $2P$ modes are found during three-dimensional flow, except at very high amplitudes.

over this range, such as decreasing base-suction coefficient and formation length (Roshko, 1993; Williamson, 1996*b*). Therefore, the boundaries shown on this plot may have some built-in bias. Regardless, the modes present seem universal, even if the boundaries are not completely fixed).

It was reported that the $2P$ mode was not observed in experiments at $Re < 300$. Here, the $2P$ mode was replaced by the $P + S$ mode, consisting of a pair and a single vortex shed per cycle. As such, this mode does not possess a Z_2 symmetry, the spatio-temporal symmetry being broken in a “spatial” sense. This loss of symmetry and the production of the $P + S$ mode is a dimensionality effect, as the mode occurs only during two-dimensional flow, even during two-dimensional simulations where Re is set to a value that would naturally lead to three-dimensional flow (Blackburn & Henderson, 1999). It has been observed in the low- Re experiments of Griffin & Ramberg (1974) and those reported in Williamson & Govardhan (2004), and in the simulations of Meneghini & Bearman (1995), Blackburn & Henderson (1996), Blackburn & Henderson (1999), and Ponta & Aref (2006). Based on the data of Meneghini & Bearman (1993, 1995), at $Re = 200$, Williamson & Govardhan (2004) produced a new map for two-dimensional flow, although inspection of the higher- Re data from Blackburn & Henderson (1999) shows that this map is far from universal for all two-dimensional flows.

These wake modes play an important role in vortex-induced vibration. It has been noted above that a relationship was established between a change in wake mode, and the phase jump in the wake of a driven oscillating cylinder (Carberry *et al.*, 2001, 2003). During vortex-induced vibration, all of the significant amplitude response occurs in the presence of a $2P$ wake (Brika & Laneville, 1993; Khalak & Williamson, 1996, 1999; Govardhan & Williamson, 2000). Due to the coupled nature of the fluid-structure system, it is unclear whether the $2P$ mode causes high- A^* oscillation, or if the high- A^* oscillation causes the $2P$ wake.

These vortex-induced vibration results, along with the driven oscillation results, do indicate that a relatively high amplitude is required to form the $2P$ wake. Results from Govardhan & Williamson (2001) show a significant increase in the periodic Reynolds stress when the $2P$ wake is present, as compared to the fixed cylinder Kármán wake. These results also show that the $2P$ wake does not consist of four vortical structures being shed

from the body; instead, one structure is shed per half-cycle that is then split into two under the influence of the high strain in the rear wake.

The influence of Reynolds stress goes some way to explaining the phenomenon of the $2P$ wake. However, the configuration is not observed in two-dimensional flow, where periodic Reynolds stresses still exist. So, it seems the exact mechanism is still unclear and open to investigation.

What is clear is that the $2P$ wake mode is a three-dimensional phenomenon, as it has never been observed during two-dimensional flow, including vortex-induced vibration. In fact, almost all two-dimensional vortex-induced vibration results in a $2S$ wake mode. Only one set of experimental data exists for two-dimensional vortex-induced vibration, and it does not include any flow visualisation (Anagnostopoulos & Bearman, 1992). Many simulations do exist, and all of these report the $2S$ wake during vortex-induced vibration (see, for example, Anagnostopoulos (1989); Blackburn & Karniadakis (1993); Blackburn & Henderson (1996); Shiels *et al.* (2001)). Blackburn *et al.* (2000) presented two-dimensional and three-dimensional simulations at the same Re , and showed that the $2P$ wake was present for the three-dimensional flow, and the $2S$ wake for two-dimensional flow. The only study that shows anything but the $2S$ wake for two-dimensional vortex-induced vibration is Singh & Mittal (2005), where the $P + S$ wake was realised. However, this only occurred for $Re > 300$ where the flow is assumed to be naturally three-dimensional, so that the assumption of the $2S$ wake being the only configuration for two-dimensional vortex-induced vibration still seems to hold. It therefore seems worthwhile investigating the conditions at which the two-dimensional assumption holds, which is an aim of this thesis.

2.2.4 Mass-damping and response branches

Mass-damping as a parameter

The complicating factor during vortex-induced vibration that inspires people to attempt to model it with driven oscillation is the fact that the oscillation frequency and amplitude are coupled. Adjusting the natural frequency of the cylinder system (or, inversely, U^*) can result in large changes in both of these response variables. It may also result in a complete change of character of the response, such as whether synchronisation is achieved, a phase jump occurs, or a sudden change in amplitude is realised.

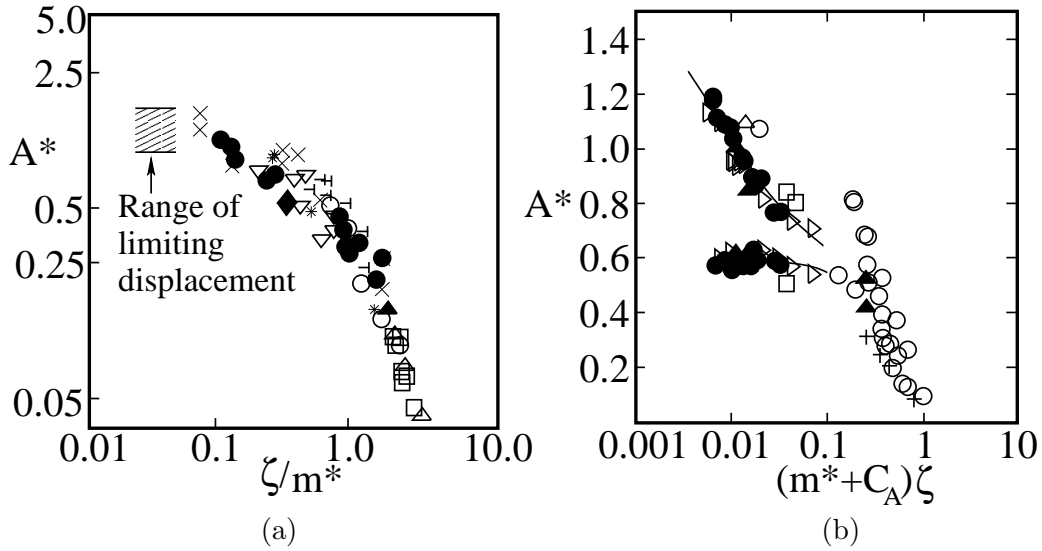


Figure 2.9: (a) The original log-scale Griffin plot of peak amplitude against a combined mass-damping parameter from Griffin (1980) with data from a variety of vibration systems, and (b) the linear-scale plot from Williamson & Govardhan (2004), using only data from elastically-mounted cylinders. The second plot clearly shows two separate trends for low mass-damping.

It is therefore sensible to try to classify these different types of response, and their dependence on some governing variable. In structural engineering applications, the primary variable of interest is often the amplitude of response. Griffin (1980) set out to do just this, plotting peak amplitudes of response against a parameter that grouped the effects of mass and damping. This plot (the style of which has become known colloquially as the “Griffin” plot) showed that as the mass and/or damping of the cylinder system was decreased, the peak amplitude increased, in a seemingly continuous fashion. An original Griffin plot, plotted on a log-scale is shown in figure 2.9a, alongside another on linear axes in figure 2.9b.

Sarpkaya (1979) presented similar plots, yet warned against the use of a combined mass-damping parameter as the magnitude of such a parameter became small based on an analytical argument. However, later work such as that presented in Naudascher & Rockwell (1994) showed that the application of a combined mass-damping parameter down to very low values still gleaned useful results.

Branching of amplitude response

Early work by Feng (1968) held the cylinder mass and damping constant, and instead varied U^* by changing the flow speed of the wind tunnel employed (this also changed Re , but the effect of Re was deemed negligible). A resonance-type effect was found, with high amplitudes occurring when the Strouhal frequency and the natural frequency were close. During these large amplitudes of oscillation, it was shown that the frequency of shedding moved away from the Strouhal frequency to match the natural frequency of the cylinder, resulting in synchronisation.

The synchronisation region consisted of two sections; one where A^* increased with increasing U^* , and another, at higher U^* , where A^* decreased with increasing U^* . The transition between these two “branches” exhibited some hysteresis.

A significant addition to the classification of vortex-induced vibration response was made by a series of papers from Khalak & Williamson (1996, 1997, 1999). These studies suggested that there were not two, but three branches of response, with the third only present at very low values of mass-damping. This was similar to the observations made of a vibrating cable by Brika & Laneville (1993). They termed these the initial, upper, and lower branch, in order of increasing U^* . The data of Feng (1968), for high mass-damping, are shown in figure 2.10, along with the low mass-damping data from Khalak & Williamson (1999). Many studies since have been based around this picture of branching vortex-induced vibration response, and as such these branches need to be described.

The initial branch exhibits moderate peak amplitude of oscillation, and frequencies of oscillation close to the Strouhal frequency for a fixed cylinder. Khalak & Williamson (1999) claim that it can be periodic; inspection of their spectra do not show definitive spikes, but rather energy spread over a range centred on a frequency close to (but slightly below) the natural frequency of the cylinder. The assumption of periodicity allows phase to be estimated. Throughout the initial branch, the phase is close to but greater than zero. When the initial branch is not periodic, it is quasi-periodic, with contributions from both the Strouhal and natural frequencies. It should be noted that these papers generally quote natural frequency that includes an added mass term, the added mass being equal to the inviscid added mass obtained using potential flow theory. For a cylinder, this is equal to the mass of displaced fluid.

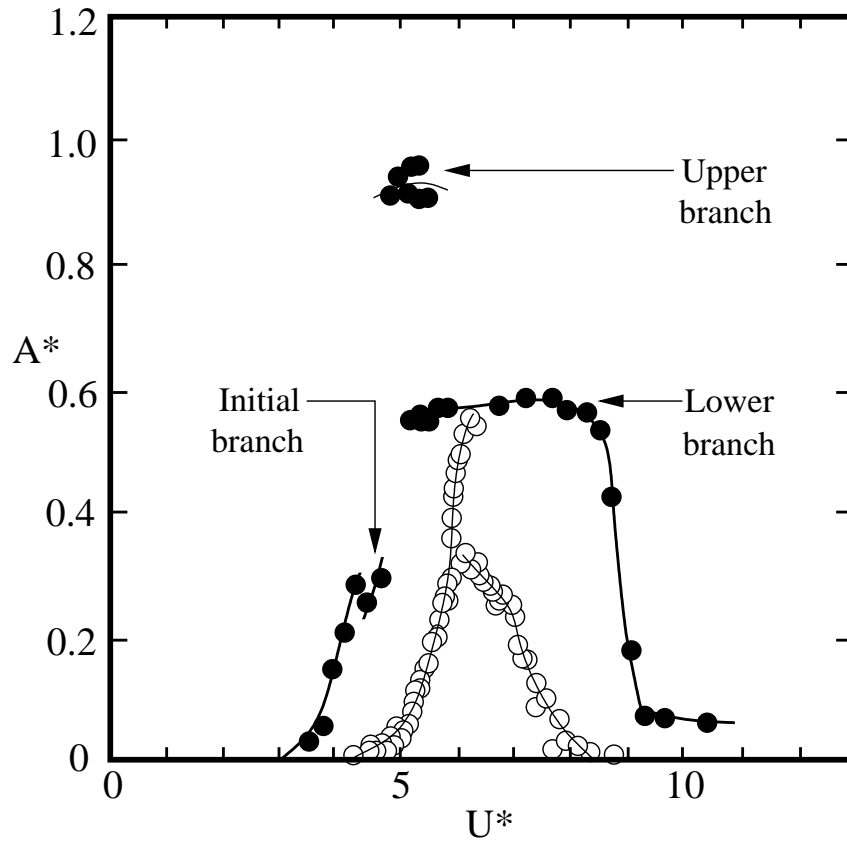


Figure 2.10: Examples of high (\circ) and low (\bullet) mass-damping peak amplitude response against U^* (Feng, 1968; Khalak & Williamson, 1999). The high mass-damping seemingly consists of only an initial and a lower branch, whereas the low mass-damping has initial, upper and lower branches.

With increasing U^* , the initial branch gives way to the upper branch. This transition is hysteretic. The upper branch is characterised by very large maximum amplitudes (up to $1.2D$ for very light cylinders), hence the name “upper”. Again Khalak & Williamson (1999), and later work from Govardhan & Williamson (2000, 2001) present this mode as essentially periodic and organised. It is reported to display a $2P$ wake, where the minor vortex of each pair is very weak. The overall phase in this branch is close to 0^0 , but the phase between vortex force and displacement jumps to close to 180^0 . The peak value of the oscillating lift force is generally at its highest in this branch. This description gives the impression of a settled, well organised mode, but there is evidence that this is not the case. This topic will be returned to after a description of the lower branch.

The lower branch exhibits lower amplitudes of oscillation than the upper branch. With transition to the lower branch, the total phase is seen to jump to close to 180^0 , and a stable $2P$ wake is formed. The transition from the upper to lower branch consists of intermittent switching between the two modes, with the flow gradually spending longer and longer periods of time in the lower branch with increasing U^* , before finally remaining on that branch indefinitely. The lower branch appears very stable, and there seems little discrepancy in the literature regarding its behaviour. This is in contrast with the upper branch, which has some seemingly contradictory behaviours reported.

Discrepancies with the upper branch

Even the results directly obtained by Khalak & Williamson (1996, 1999) that went so far in defining this branch show that the amplitude of oscillation is far from constant in this branch. This could be interpreted as either the upper branch has a variable amplitude, or that it has constant amplitude but occurs only in short bursts interspersed among lower branch response. Neither of these seems particularly satisfying when claiming that the branch is periodic, and that a single value of phase can be assigned to it.

The studies of Hover *et al.* (1998, 2004), using a computer-controlled water-channel setup, investigated the spanwise correlation in the synchronisation range of U^* . They found that during upper branch oscillation, the correlation coefficient of the forces near each end of their cylinder was near zero. The correlation coefficient plotted against U^* is shown in figure 2.11. Another study from the same authors (Hover *et al.*, 2001) investigated

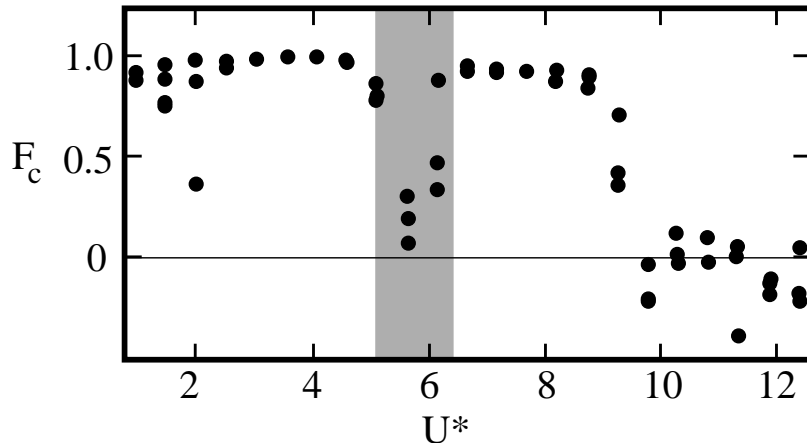


Figure 2.11: Correlation coefficient between the lift force signals at either end of the cylinder against U^* . The very low correlation in the shaded region corresponds to the upper branch, suggesting that through the upper branch, the flow is very disordered. Reproduced from Hover *et al.* (2001)

the effect of adding tripping wires to the surface of the cylinder to improve the correlation. The tripping wires had the effect of significantly reducing the peak amplitude of the upper branch. While this is not conclusive, it indicates that the upper branch consists of highly irregular flow, and that this regime could be chaotic by nature, rather than a high-amplitude periodic branch.

The issue is possibly further confused by consideration of a “critical” added mass (Govardhan & Williamson, 2000, 2002). These studies indicate that for very low mass ratios, the oscillation will never transit to the lower branch, but will remain in the upper branch indefinitely, and that synchronisation will be held for infinitely large values of U^* . However, their concept of an “operating point” shows the preferred oscillation at infinite U^* (realised by the removal of all spring force from the system, giving $f_N = 0$) sits somewhere very close to the start of the lower branch, and at slightly lower amplitudes than “classical” upper branch oscillation. This additional information seems to make the upper branch even more difficult to define.

Considering this, it seems natural to try and further simplify the system, limiting it to two-dimensional flow, and to closely examine the flow physics. However, this appears to over-simplify the situation, and avoids the formation of the upper branch altogether.

Govardhan & Williamson (2000) and Williamson & Govardhan (2004) presented Griffin plots plotted on linear, as opposed to logarithmic axes, and found considerable spread in the data for peak amplitude of response, particularly at low mass-damping. In particular, they found two separate trends, with some data collapsing to a curve for maximum amplitude around $A^* = 0.6$, and another with A^* increasing with decreasing mass-damping. These two trends were attributed to the upper and lower branches found in the plots of peak amplitude against U^* . Many of the data on the lower branch of the Griffin plot were from low- Re experiments and simulations, where the flow is naturally, or by imposition, two-dimensional. It was therefore concluded that the upper branch is not formed in two-dimensional flow. Observation of plots such as the high- m^* data of Feng (1968) led some authors to conclude that the upper branch is not seen for high- m^* flow either.

Evidence for a two-dimensional upper branch

The conclusion of there existing no upper branch for two-dimensional flow seems to be based purely upon observation of the peak amplitude, which does not exceed $A^* \simeq 0.6$ for two-dimensional flow (Anagnostopoulos & Bearman, 1992; Blackburn & Henderson, 1996; Shiels *et al.*, 2001), whereas A^* can exceed 1.2 in the upper branch for three-dimensional flow. However, the study of Blackburn & Henderson (1996) also showed that there was a range of U^* that resulted in effectively chaotic flow. In this range, peak amplitudes were significant, and peak lift forces were at their highest. Blackburn & Henderson (1996) also noted that the behaviour over this regime seemed characterised by intermittent lock-in (synchronisation). This range of U^* coincided with that at which the upper branch is found in three-dimensional flow. Singh & Mittal (2005), in two-dimensional simulations at $Re = 375$, found a regime that was disordered, but produced the $P + S$ wake configuration intermittently. This occurred at U^* lower than those at which full synchronisation and periodic flow occurred. Taken together with the findings of Hover *et al.* (1998, 2004) that the flow is quite disordered in the upper branch, a re-examination of these phenomena in two-dimensional flow is justified.

The critical mass ratio

Other studies have shown that similarities do exist between two-dimensional and three-dimensional vortex-induced vibration. The interesting phenomena of a “critical” mass ratio exists in both situations (Govardhan & Williamson, 2000; Shiels *et al.*, 2001), although the value obtained is different. “Critical” is used here in the sense of a mass ratio below which synchronisation is obtained at all values of U^* .

It could be expected that in the limit of a cylinder with zero mass, the cylinder oscillation and wake would synchronise at frequencies slightly below the Strouhal frequency for a fixed cylinder, regardless of U^* . Synchronisation would occur as the massless cylinder would respond instantly to any fluid force, and the frequency would be slightly lowered due to the mean widening of the wake caused by the oscillation (see Roshko (1954) for the correlation of Strouhal frequency with wake width). For this to happen for a finite mass cylinder, there needs to be another force that is exactly out of phase with the mass force to offset it to some degree. This force is often referred to as an effective added mass force. The “critical” mass will then be the mass at which the sum of the forces attributable to mass and to the effective added mass is zero.

Khalak & Williamson (1999) derived an expression for effective added mass based on a linear analysis of the equations of motion of the cylinder. Govardhan & Williamson (2000) then measured this parameter for lower branch response and deduced it to be approximately -0.54 over the entire lower branch. Interestingly, this is close to the value of -0.60 obtained during driven oscillation by Gopalkrishnan (1993).

Experiments with mass ratios either side of the value $m^* = 0.54$ showed distinctly different response, with mass ratios below this remaining synchronised to very high values of U^* . In experiments where the springs were removed, resulting in a situation with effectively an infinite U^* , Govardhan & Williamson (2002) showed high-amplitude response only for mass ratios below this critical value.

The use of such a linear analysis has come under criticism (Sarpkaya, 2004). Such criticisms are based upon the rather arbitrary grouping of parameters that make up the effective added mass coefficient in the paper by Khalak & Williamson (1999), and the assumption of applicability of an inviscid added mass. Results can be found that show the added mass deviates considerably from the value obtained with potential flow theory for

certain flow conditions (Sarpkaya, 2004; Hurlout *et al.*, 1982). Also, the results of Branković (2004), following the analysis of Govardhan & Williamson (2000) gave a critical mass of $m^* = 0.4$, a discrepancy of around 20%.

Still, even if the analytical derivation of such a parameter still needs some tuning, the experimental results do indicate that a critical mass exists.

2.2.5 Direct predictions of vortex-induced vibration from driven oscillations

Prediction from sinusoidal oscillation

The sensitivity of the elastically-mounted cylinder to reduced velocity, taken together with the observation that the majority of synchronised response is approximately sinusoidal in experiments and simulations (Khalak & Williamson, 1999; Shiels *et al.*, 2001), has led many researchers to attempt to directly model vortex-induced vibration using driven oscillations. Often, this consists of taking force measurements during driven oscillation experiments, deriving a transfer function from a linear analysis, and predicting amplitudes of response (Sarpkaya, 1978; Staubli, 1983).

One such study is that of Staubli (1983). From measurements of lift coefficient on a harmonically-driven cylinder, and assuming simple harmonic motion, oscillation amplitude and phase was calculated for an elastically-mounted cylinder with the same mechanical properties as that used by Feng (1968). Comparison of the calculated and experimental data showed while peak amplitude was predicted relatively closely, major discrepancies existed over the majority of the parameter space. Plots comparing the predictions with the data of Feng (1968) are shown in figure 2.12.

More recent studies have focused on the energy transfer, which must be positive in vortex-induced vibration (in fact, undamped, constant amplitude vortex-induced vibration should result in zero net energy transfer over a cycle of oscillation. If this does not occur, the amplitude should grow or decay until it does). The studies of Carberry *et al.* (2001, 2002*a,b*) of a driven cylinder all show results that indicate negative energy transfer for frequencies after the phase jump, that should coincide with the lower branch in vortex-induced vibration. This effectively means no vortex-induced vibration is predicted by the driven oscillations over the majority of the synchronisation region. This is despite the

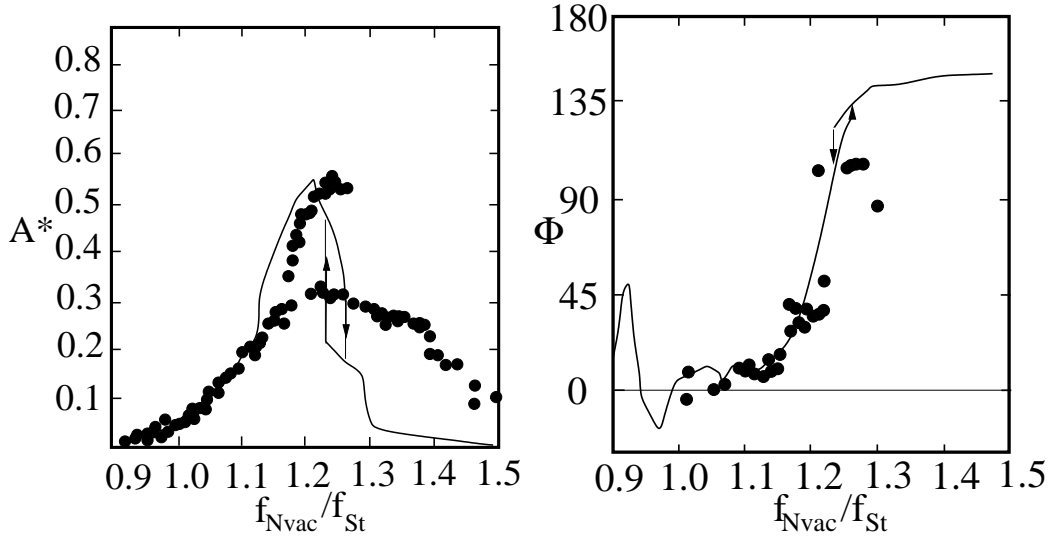


Figure 2.12: Predictions of amplitude and phase during vortex-induced vibration using data from driven oscillations. The solid lines (—) are the predictions from Staubli (1983), the points (•) are data from Feng (1968). There is a large discrepancy over most of the parameter space that corresponds to the lower branch.

direct comparison between the elastically-mounted and driven systems of Carberry *et al.* (2002a) showing a close match in the wake modes.

Hover *et al.* (1998) produced contour plots of the lift coefficient in phase with velocity (the only component that contributes to vortex-induced vibration in transverse-only oscillation), from a series of driven oscillation experiments. These contours were in the amplitude-frequency plane. Peak amplitudes from subsequent elastically-mounted experiments were then plotted over these contours. This plot is reproduced in figure 2.13. It can be seen that the peak vortex-induced vibration amplitudes follow the zero contour fairly closely. However, most of the lower branch response falls in regions where the contours are negative, which should be impossible during vortex-induced vibration. The later work of Carberry *et al.* (2001) found the same discrepancy.

The reviews of Sarpkaya (1979) and Bearman (1984) both comment on the fact that the flow during vortex-induced vibration is most likely history dependent, and that this fact precludes driven oscillation from accurately representing vortex-induced vibration. However, it is obvious that this has not stopped research into this comparison, and the later review of Sarpkaya (2004) points out that the value of this research is not decided on

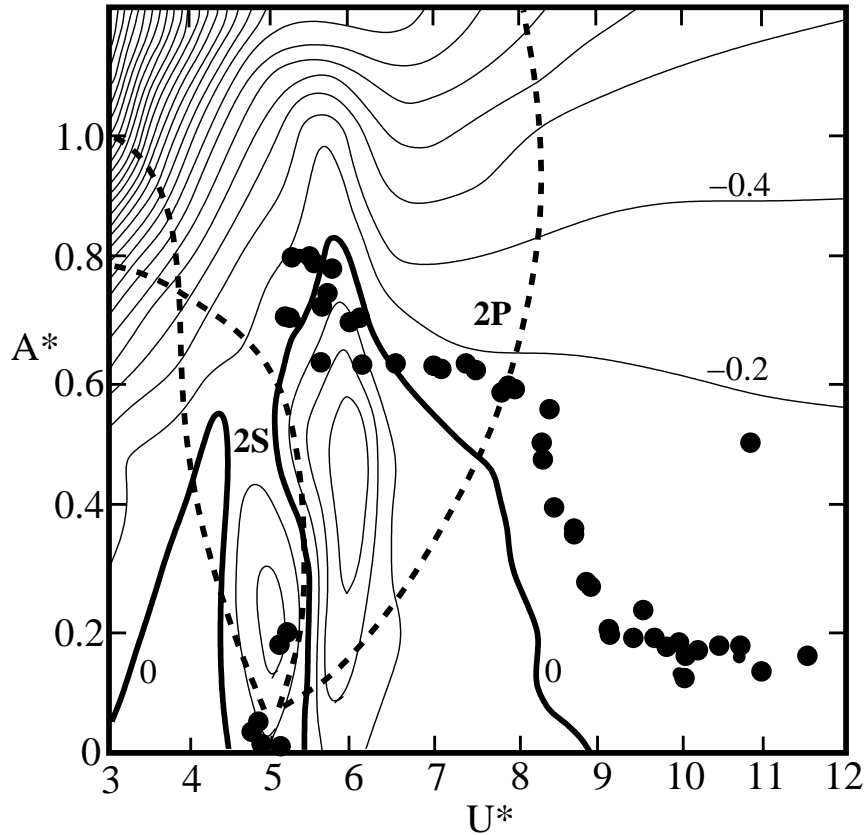


Figure 2.13: Contours of lift coefficient in phase with velocity (the only component that contributes to energy transfer for transverse oscillations), reproduced from Hover *et al.* (1998). Points (\bullet) are peak amplitudes from vortex-induced vibration experiments from the same authors. While the points lie close to the zero contour (highlighted by a bold solid line), most of the lower branch response falls in areas where the contours are negative. This is not possible for vortex-induced vibration. Dotted lines mark the wake mode boundaries found by Williamson & Roshko (1988).

whether the two systems are identical, but whether they are sufficiently similar. The review of Williamson & Govardhan (2004) left it as an open question whether sinusoidal driven oscillations could be used universally to predict vortex-induced vibration successfully. The compilation of studies presented here seems to suggest that it cannot.

Multi-frequency forcing

Limited studies have been performed using driving histories that are not purely sinusoidal. Nakano & Rockwell (1993) performed experiments at low Re , to investigate the effect of modulation. They found that for a nominal frequency equal to the Strouhal frequency, modulation had little effect on synchronisation. However, for a nominal frequency that was slightly detuned from the Strouhal frequency, different states of organisation could be obtained depending on the modulation frequency, including a period-doubled mode. A plot of the various synchronisation modes obtained by Nakano & Rockwell (1993) for a slightly detuned nominal frequency, is shown in figure 2.14. Such non-sinusoidal driving may go some way to addressing the inadequacies of modelling vortex-induced vibration with sinusoidal oscillations raised above.

2.2.6 Analytical models of vortex-induced vibration

To this point, all the models used to study vortex-induced vibration have been experimental (either using “real” experiments or numerical simulations), whether elastically-mounted or driven. However, due to the persistence of the wake oscillation behind a fixed cylinder, and the periodicity of the wake over a large range of Re , semi-empirical models have been developed that are based on coupled oscillators. These models use a harmonic oscillator for the cylinder structure, and treat the wake as some type of non-linear oscillator that is characterised by a single variable. In this way, the degrees of freedom of the wake are reduced from practically infinite to one.

While not a primary focus of this thesis, consideration of these models will be made here, at least to point out these models’ relative strengths and weaknesses. A review of these types of models is included in Gabbai & Benaroya (2005).

An early example of this type of model, commonly referred to as phenomenological models, is that proposed by Hartlen & Currie (1970). In this study, the ground rules for

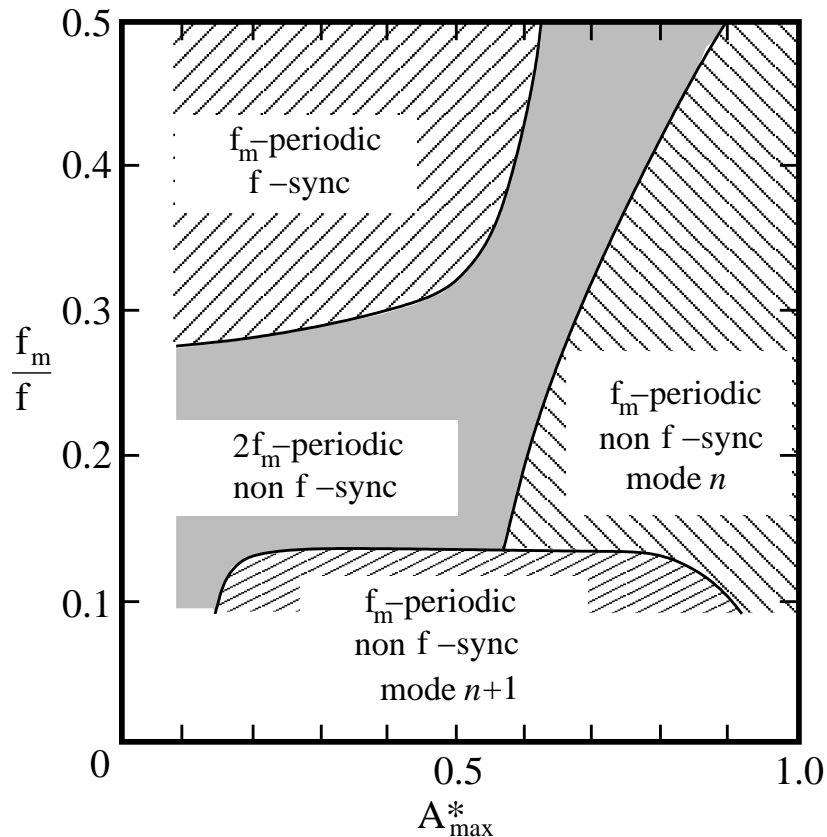


Figure 2.14: Synchronisation modes as a function of peak amplitude and the ratio of modulation frequency, f_m , to primary frequency, f , for modulated-amplitude oscillation experiments, reproduced from Nakano & Rockwell (1993). The primary oscillation frequency for this data was $0.95f_{St}$. Different synchronised responses become possible, such as period-doubled synchronisation.

any oscillator used to model the wake are laid out. These are that the oscillator must be self-exciting and self-limiting (as saturated-amplitude oscillations occur naturally in the fixed-cylinder wake), that the natural frequency of the oscillator must be proportional to freestream velocity (similar to the Strouhal number), and that there must be some force coupling between the wake and cylinder oscillator.

Following these rules, Hartlen & Currie (1970) then derived a model based upon a van der Pol oscillator for the wake and a standard harmonic oscillator for the cylinder. The van der Pol oscillator was used for the wake as it satisfies the self-exciting and self-limiting rule through a non-linear damping term (Rao, 1995). The two oscillators were coupled

through their respective external forcing terms, that were proportional to the cylinder transverse velocity. The coefficients of the wake oscillator equation were determined from driven oscillation or fixed-cylinder experiments. This relatively simple model displayed traits such as synchronisation, varying amplitudes of oscillation and a shift in phase over the synchronisation region, similar to vortex-induced vibration experiments. While there was a reasonable qualitative match, quantitatively the model did not match the experiments over large regions of parameter space.

More recently, a similar model was used by Krenk & Nielsen (1999). The coupling term was modified based upon an energy transfer direction argument, noting that energy must flow from the fluid to the cylinder for vortex-induced vibration to occur. Again, aspects of real vortex-induced vibration were represented qualitatively, with the added effect of hysteresis in the synchronisation onset, and a stronger and hysteretic jump in phase that was not rendered in the earlier model from Hartlen & Currie (1970).

Facchinetti *et al.* (2004) investigated the effects of changing the force-coupling terms. This study investigated the behaviour of the same basic model as the Hartlen & Currie (1970) and Krenk & Nielsen (1999) studies, but used a coupling term that scaled with cylinder displacement, velocity or acceleration in turn. They found that an acceleration coupling returned results closest to the true vortex-induced vibration response. A physical explanation was given for the lack of success of displacement and velocity couplings. It was stated that a different displacement did not affect the fluctuation of the wake at all, and that a constant velocity would affect only the approach angle of the flow, so the only dynamic term left was acceleration. While the match with experimental results was better, it still failed to capture important features, such as high-amplitude oscillation for low mass-ratio cylinders.

2.2.7 Effects of vibration on wake transitions

It is clear from the preceding discussion that the oscillation of a cylinder, be it through vortex-induced vibration or external driving, can have a significant impact upon the structure of the wake. It is also clear that there are differences in some aspects of the flow when considering flows that are two-dimensional or three-dimensional. It therefore seems natural to consider the effects that the oscillation has upon the transitions of the wake, especially

the transition from two-dimensional to three-dimensional flow.

Delaying the onset of three-dimensionality with transverse oscillation

Berger (1967), experimenting with an elongated cylinder reported that suitable oscillations could delay the onset of three-dimensionality in the wake until $Re \simeq 350$. Griffin (1971) and Koopman (1967) both performed driven oscillation experiments at $Re = 200$ with the assumption that their experiments were effectively two-dimensional. The flow visualisation of Koopman (1967) taken from above the cylinder show vortices being shed parallel to the cylinder, with no deformation in the spanwise direction (away from end effects). It has been discussed previously that the transition to three-dimensionality has already occurred at this Re in the wake of a fixed cylinder (Williamson, 1996*a*).

Aside from these and other similar observations, little work has been done on establishing the nature of the transition to three-dimensionality in the wake of an transversely oscillating cylinder. However, fully three-dimensional simulations by Poncet (2002) showed that a rotational oscillation could arrest and suppress mode B, reverting the flow to two-dimensional in the near wake, at $Re = 500$. This effect is well highlighted in the flow visualisation reproduced in figure 2.15.

Ryan *et al.* (2005) performed Floquet stability analysis on the wakes of elongated cylinders with an aerodynamic leading edge. It was shown that while three-dimensional modes similar to those in the wake of a cylinder were present, critical wavelengths and the order of inception of the modes were not always the same. While this work is not focused on the effects of any oscillation, it does highlight the effect of the scale of flow structures in the wake, such as shear layer thickness and vortex ellipticity. It is envisaged that oscillation of a cylinder will also affect these scales, implying changes to the three-dimensional modes.

Similarly, Sheard *et al.* (2003*b*) used Floquet stability analysis to investigate the transition to three-dimensionality in the wakes of rings. While locally the ring geometry resembles a circular cylinder, the Z_2 symmetry is broken due to the acceleration of the fluid through the centre of the ring (a Z_2 symmetry refers to the combination of a temporal evolution of half a period, plus a spatial reflection, here about the wake centreline). This break in symmetry allowed subharmonic modes to arise, where the three-dimensional structure repeated over two base flow cycles. Visualisation of the subharmonic mode found in the

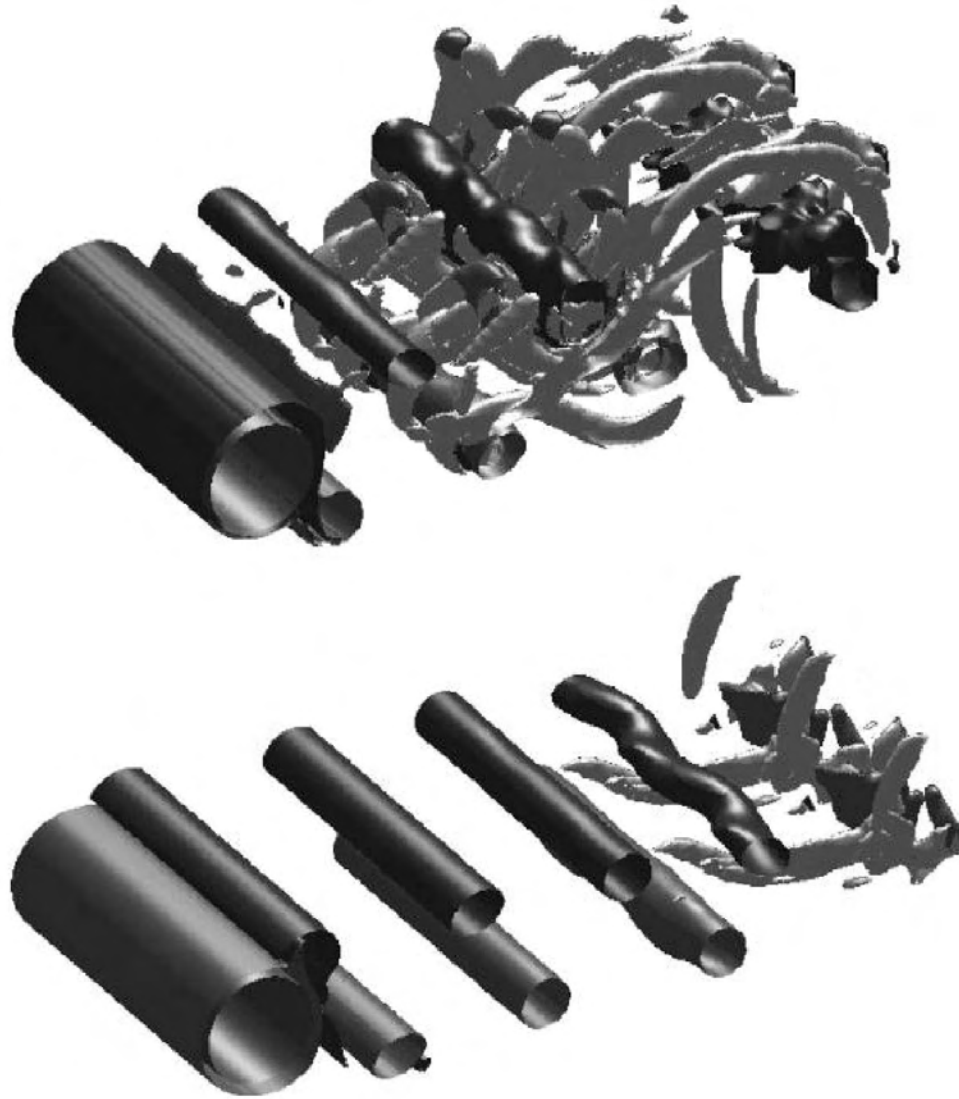


Figure 2.15: Contours of overall vorticity for a normal fixed cylinder (top), and after the beginning of rotational oscillation (bottom). Images reproduced from Poncet (2002). The effect of rotational oscillation at $Re = 500$ is to suppress the development of mode B, and revert the wake to a two-dimensional state.

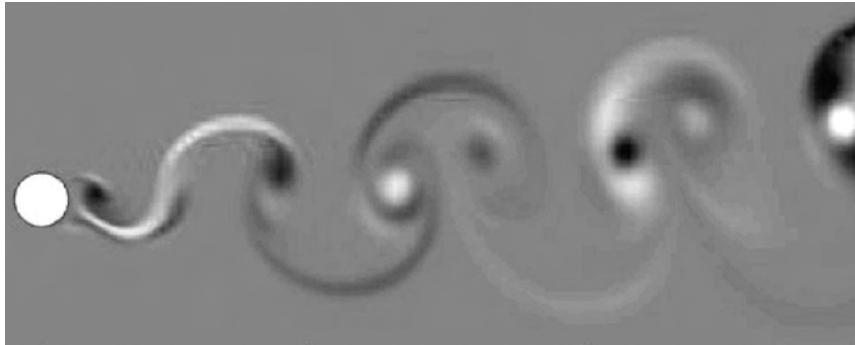


Figure 2.16: Streamwise vorticity of the subharmonic mode in the wake of tori, from Sheard *et al.* (2003*b*). The subharmonic nature of the mode can be observed from the change in colour indicating a change in sign every full shedding cycle.

wake of tori is reproduced in figure 2.16. Such subharmonic modes have been shown to be highly unlikely for wakes that possess Z_2 symmetry (Marques *et al.*, 2004; Blackburn *et al.*, 2005). These findings have repercussions for the wake of an oscillating cylinder, as it has already been shown that the $P+S$ wake replaces the $2P$ wake for a driven oscillation when the flow is two-dimensional. The $P+S$ wake also breaks Z_2 symmetry, and as such may allow other three-dimensional modes to arise than those observed in the wake of a fixed cylinder.

The inducement of unsteady flow by elastic mounting

As well as the transition to three-dimensionality, the primary Hopf transition (the transition from steady to periodic flow) has received recent attention. Mittal & Singh (2005) ran simulations of an elastically-mounted cylinder, and found they could achieve synchronised vortex-induced vibration for Re as low as 20, well below the $Re \simeq 47$ required for the transition to periodic flow in the wake of a fixed cylinder. Visualisation of a periodic vortex street at $Re = 26$ is shown in figure 2.17.

Using a Ginzburg-Landau model, Chomaz *et al.* (1988) demonstrated a series of bifurcations to local and global modes in the wake of a fixed cylinder. It was shown that before the onset of a global absolute instability, a local absolute instability exists. It was stated that this local absolute instability is essential, but not sufficient, for the eventual global instability to arise. Monkewitz (1988) found a similar local absolute instability from an

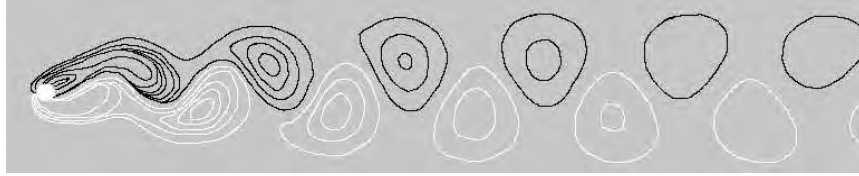


Figure 2.17: The periodic vortex street resulting from vortex-induced vibration at $Re = 26$, from Mittal & Singh (2005). This is well below the Re required for a periodic wake behind a fixed cylinder.

analysis of wake profiles. This local instability occurred at $Re \simeq 25$. It is interesting to note the similarity between this Re and that found for the Hopf bifurcation for an elastically-mounted cylinder by Mittal & Singh (2005). However, no work has been done to show a link between these two particular phenomena.

Work that has gone some way to linking the findings of Landau modelling to the wake of an oscillating cylinder has been performed by Le Gal *et al.* (2001) and Thompson & Le Gal (2004). Both of these papers investigated the wake behind a driven oscillating cylinder, using numerical simulations and a forced Stuart–Landau model. While the forced Stuart–Landau model indicated a hysteretic transition between non-shedding and vortex-shedding wakes with respect to Re , the simulations showed no such hysteresis. An explanation of this discrepancy was given, explaining that phase differences in the growth of the instability along the centreline of the wake effectively smooth out any hysteretic tendency.

2.2.8 Review summary and hypotheses

The preceding review of literature has established that while some very useful findings have been made in the field of vortex-induced vibration, and in the understanding of oscillating cylinder wakes in general, there still exist gaps in the knowledge base. From the findings surrounding these gaps, hypotheses have been formed, the investigation of which will go some way to bridging these gaps.

Hypothesis 1: Dependence on Re for two-dimensional flow

It is clear that the majority of the data on this problem is drawn from experiments where the flow is three-dimensional by nature. This is a complicating factor, even in the decoupled

problem of a externally-driven cylinder. Williamson & Roshko (1988) mentioned that the wake modes present change for $Re < 300$, presumably due to the two-dimensional flow at these lower Re . The experiments of Koopman (1967) established a basic shape for boundaries of synchronisation, that have been partly validated in many studies, including those of Griffin (1971); Griffin & Ramberg (1974); Blackburn & Karniadakis (1993) and Meneghini & Bearman (1995). However, no single study has established simultaneously the synchronisation boundaries, along with the map of wake mode transitions and energy transfer characteristics. Also, no study since those early experiments of Koopman (1967) has systematically investigated the effect of Re on any of these phenomena.

The lower Re of two-dimensional flow suggests that the balance of inertial to viscous force will be more sensitive, a problem most likely compounded by the removal of Reynolds stresses that are present in the three-dimensional flow. This fact, coupled with the observations of the studies above, leads to the first hypothesis of this thesis:

- Hypothesis 1: *Wake modes, transitions and energy transfer characteristics are dependent on Re , for Re where the wake of an oscillating cylinder is two-dimensional.*

The test of this hypothesis will be to perform simulations covering the $A^*-\lambda_{osc}$ plane, while holding Re constant. Synchronisation, wake modes and energy transfer can all be established simultaneously. The Reynolds number can then be changed and the process repeated, and the results compared across different Re .

The specific aims of this research are to establish maps of synchronisation, wake modes and energy transfer for different Re and establish any dependence on Re . This will also allow the identification of any correlation between a change in wake mode and a change in direction of energy transfer, as was discovered in high- Re flow by Carberry *et al.* (2001).

Hypothesis 2: Branching behaviour in two-dimensional flow

The specific problem of vortex-induced vibration of an elastically-mounted cylinder seems to be well-documented and quantified. In particular, there appear to be three well-defined regimes of response for low mass-damping situations, namely the initial, upper and lower branches. However, data from Khalak & Williamson (1999) and Govardhan & Williamson (2000, 2002) indicate that the upper branch in particular is very difficult to see as an

isolated periodic mode. Experiments from Hover *et al.* (1998, 2004), and the simulations from Lucor *et al.* (2005) demonstrate that the upper branch is very disordered in the spanwise direction, regardless of the high peak amplitude.

Until now, the upper branch has effectively been solely defined by this high peak amplitude, hence the name “upper”. These high peak amplitudes are not observed during two-dimensional flow. However, Blackburn & Henderson (1996) have observed a regime for similar ranges of U^* to those for the upper branch where the cylinder response appears chaotic during two-dimensional flow. The observation of this similarity leads to the following hypothesis:

- Hypothesis 2: *The origin of branching behaviour for three-dimensional vortex-induced vibration has its genesis in two-dimensional flow.*

It seems that this similarity has been overlooked due to the large differences in peak amplitude, a parameter that has dominated interest because of its engineering implications. The hypothesis will be tested by running a series of two-dimensional simulations of an elastically-mounted cylinder.

The main aims of this research will be to establish any branches or regimes present in the two-dimensional flow with relation to U^* and the mass ratio, m^* . It will also allow the study of the effect of Re on vortex-induced vibration, thereby extending the study of dependence on Re in the wake of a driven cylinder. Arising from the hypothesis that an upper-type branch can be established for two-dimensional flow, it will be established whether this branch is truly chaotic.

Hypothesis 3: Sinusoidal oscillation is not universally applicable

As previously mentioned, nearly all major reviews of vortex-induced vibration (Sarpkaya, 1979, 2004; Williamson & Govardhan, 2004) state that the question of whether purely sinusoidal driven motion can model vortex-induced vibration is still open. After decades of research into this very question, it seems safe to conclude that if this question is asked universally, then the answer is in the negative. However, experiments and simulations show that lower branch oscillations are quite periodic, with a stable amplitude (Khalak & Williamson, 1999; Govardhan & Williamson, 2000; Lucor *et al.*, 2005). The upper branch

does not display such periodicity, the amplitude can vary, and the oscillation becomes more disordered, as may be expected if the flow is not fully synchronised. The modulated-oscillation study of Nakano & Rockwell (1993) showed modulated oscillations could have a significant impact upon synchronisation, especially when the primary frequency of oscillation was slightly detuned from the Strouhal frequency for a fixed cylinder. These observations lead to the following hypotheses:

- Hypothesis 3A: *Pure sinusoidal oscillation is a valid approximation in the lower branch;*
- Hypothesis 3B: *Modulated oscillation can capture major flow features relating to force in the upper branch.*

These two hypotheses will be tested by first comparing the elastically-mounted cylinder response with the parameter space maps built from the simulations run in testing hypothesis 1. Fine-tuning will be done by running driven oscillation simulations that use amplitude and frequency data gained from elastically-mounted simulations.

The aims of this research are to establish that the lower branch, at least in two-dimensional flow, results in sinusoidal response and that a sinusoidal driven oscillation successfully captures flow characteristics such as vorticity distribution, lift force, phase of shedding and energy transfer. It will also be shown that the same is not true in the upper branch.

Since the experimental study of Berger (1967), little research has gone into the study of the transition to three-dimensionality in the wake of an oscillating cylinder. The direct comparisons in Blackburn *et al.* (2000) and Williamson & Govardhan (2004) show that following this transition, much larger peak amplitudes of response can be obtained during vortex-induced vibration. It therefore seems important to gain some insight into the nature of this transition.

Hypothesis 4: Oscillation delays three-dimensional flow

While the transition in the wake of a fixed cylinder is relatively well-understood (see the experiments of Williamson (1988, 1996*b*), and the stability analysis and simulations of Barkley & Henderson (1996), Thompson *et al.* (1996) and Blackburn *et al.* (2005)), it

cannot be assumed that the transition will be the same for an oscillating cylinder. Poncet (2002) reported that rotational oscillation could suppress three-dimensionality, and Sheard *et al.* (2003b) and Ryan *et al.* (2005) have shown that geometry that slightly changes the wake structure scales can change the mode inception order or give rise to new modes altogether. This leads to the following hypothesis:

- Hypothesis 4: *Transverse oscillation will change the nature of the transition to three-dimensionality in the wake of a cylinder*

This hypothesis will be tested using Floquet stability analysis of driven oscillation wakes, to attain when the nominally two-dimensional base flow becomes unstable to three-dimensional perturbations.

The aims of these tests are as follows. The modes present and any dependence on amplitude of their inception will be established. This will clearly define the transition Re for a given amplitude. Any new modes present will also be reported. This is most likely to occur for the $P + S$ base flow, due to the different symmetry properties of this wake.

Hypothesis 5: The primary Hopf bifurcation remains supercritical

The transition to a periodic wake has obvious importance to vortex-induced vibration. Mittal & Singh (2005) showed that an elastically-mounted cylinder undergoes this transition at much lower Re than the wake of fixed cylinder. Analysis of wake profiles by Monkewitz (1988) showed that a local absolute instability arises in the wake of a fixed cylinder before the onset of vortex shedding. Studies such as Provansal *et al.* (1987) established that the transition to vortex shedding for a fixed cylinder wake is supercritical (implying that no hysteresis is present). Also, Le Gal *et al.* (2001), and Thompson & Le Gal (2004) showed that while Landau modelling indicates that the transition from steady flow to vortex shedding in the wake of a driven cylinder should be hysteretic, simulations of the flow show no hysteresis. Based on these observations, the following hypothesis has been formed:

- Hypothesis 5: *Regardless of the lowering of Re at transition, the transition to unsteady flow in the wake of an elastically-mounted cylinder remains supercritical*

This hypothesis will be tested by running a series of simulations of an elastically-mounted cylinder spanning this transition in Re . These simulations will then be used to build a Landau model of the system.

The primary aim of this research is to establish the criticality of the primary Hopf transition in the wake of an elastically-mounted cylinder. As the focus of the study is the effect of Re , parameters such as m^* and the ratio of the cylinder natural frequency, f_N , to the fixed cylinder Strouhal frequency, f_{St} (where f_{St} is established by extrapolation), will be held constant.

CHAPTER 3

METHODOLOGY AND VALIDATION

3.1 Introduction

This chapter presents a basic overview of the computational methods used for the simulations conducted for this thesis. The overview given here is not exhaustive, and it should be noted that the focus of this thesis was not the development of computational methods, but the fluid mechanics of vortex-induced vibration.

The treatment given here is as follows. First, an overview of the equations solved is presented. This is followed by a discussion of the discretisation of these equations to allow their numerical solution. The methods of temporal and spatial discretisation are presented, along with the methods of formation of the final matrix equation set.

With this established, the methods employed for Floquet stability analysis are described. This description is focused around the formation of the equations to be solved, as the discretisation and solution methods are essentially the same as those for simulation of the flow presented in foregoing sections.

Following these method sections, the results from a series of validation studies are presented. Results confirming the accuracy of the solutions gained in both space and time are presented. These tests provide confidence in the predictions of this thesis.

3.2 The governing equations: Navier–Stokes and continuity

Central to any numerical simulation are the assumptions made. The key assumptions made regarding the fluid involved in the systems considered in this thesis follow.

First, the fluid is assumed to be a continuum, which makes it possible to consider a differential element of fluid that is infinitesimally small for the formation of differential equations. This assumption only becomes invalid in micro- and nano-fluidics, where the primary length scale of the flow approaches the same order as that of the fluid molecules.

Second, it is assumed that the fluid is incompressible; i.e., that the density is constant. This avoids the need to consider acoustic wave propagation in the flow. This assumption is typically valid for flows where the Mach number, $Ma < 0.3$. The Mach number represents the ratio of the speed of sound to the speed of the fluid flow, and density variations typically scale as the square of the Mach number – hence the Mach number cutoff. This condition is applicable in the majority of current engineering applications, especially to those in water. Also, the fluid is assumed to be isothermal, so that density gradients play no part in the flow dynamics.

Third, it is assumed that the fluid is what is known as a Newtonian fluid. This means that the shear stress is directly proportional to the strain rate. The constant of proportionality that relates the two is the fluid property known as dynamic viscosity. These are standard assumptions, and further details can be found in many texts, such as White (1999).

The equations that govern the behaviour of such Newtonian, incompressible flows are the Navier–Stokes equations,

$$\frac{\partial \mathbf{u}}{\partial t} + (\mathbf{u} \cdot \nabla) \mathbf{u} = -\frac{\nabla p_f}{\rho} + \frac{\mu_v}{\rho} (\nabla^2 \mathbf{u}) , \quad (3.1)$$

and continuity,

$$\nabla \cdot \mathbf{u} = 0 . \quad (3.2)$$

Here, \mathbf{u} is the velocity vector field, t is the time variable, p_f is the pressure field, ρ is the fluid density, and μ_v is the dynamic viscosity. The left-hand side of the Navier–Stokes equation as presented in equation 3.1 represents the inertial forces, and the terms on the right represent the pressure and viscous forces, respectively. The continuity equation specifies that the net mass flux into a given fluid element is zero.

For generality, these equations can be non-dimensionalised. For bluff-body wake flows, this non-dimensionalisation is performed using the cylinder diameter D , and the freestream velocity, U . It is also useful to move all the spatial derivative terms to the right-hand side of the equation. For the problem studied here, the equations are modified to be solved in an accelerating frame of reference attached to the cylinder. This involves adding an extra term to the Navier–Stokes equations, that is effectively the acceleration of the cylinder. This renders the equation set as

$$\frac{\partial \mathbf{V}}{\partial \tau} = -\nabla P + \frac{1}{Re}(\nabla^2 \mathbf{V}) - (\mathbf{V} \cdot \nabla) \mathbf{V} + \frac{d\mathbf{V}_{cyl}}{d\tau}, \quad (3.3)$$

$$\nabla \cdot \mathbf{V} = 0. \quad (3.4)$$

Here, $\mathbf{V} = \mathbf{u}/U$, $\tau = tU/D$, $P = p_f/(\rho U^2)$, $Re = \rho U D/(\mu_v)$, and $\mathbf{V}_{cyl} = \mathbf{v}_{cyl}/U$, where \mathbf{v}_{cyl} is the cylinder velocity. The acceleration term, $\frac{d\mathbf{V}_{cyl}}{d\tau}$, was explicitly stated in the case of the externally-driven cylinder; for the case of the elastically-mounted cylinder, it was found by coupling the Navier–Stokes equations with the differential equation describing the dynamics of the cylinder system. This was the equation for a damped linear oscillator,

$$\frac{\ddot{y}_{cyl}}{D} + 2\zeta\sqrt{k^*}\frac{\dot{y}_{cyl}}{D} + k^*\frac{y_{cyl}}{D} = \frac{\pi C_L}{2 m^*}, \quad (3.5)$$

where $\zeta = c/c_{crit}$, $k^* = kD^2/mU^2$ and $C_L = F_{lift}/(0.5\rho U^2 D)$. Here, C_L is the lift coefficient per unit length of the cylinder, y_{cyl} is the transverse displacement of the cylinder, D is the cylinder diameter, c is the damping coefficient, c_{crit} is the critical damping coefficient, k is the spring constant and m is the mass per unit length of the cylinder.

3.3 Discretisation

3.3.1 Time-splitting

To solve equations 3.3 and 3.4 (and equation 3.5 for the elastically-mounted cylinder), it was necessary to discretise the problem in both space and time. The temporal discretisation method used for this study was three-step time-splitting. The method is known as time-splitting (or a fractional step method) because each of the terms on the right-hand side of the Navier–Stokes equations is integrated separately, which results in the overall integration

over one timestep being split into three substeps. This process defines the equations that are actually solved numerically to approximate the solution to the Navier–Stokes equations.

The method proceeds as follows. The non-linear term accounting for convection (and, in this case, the cylinder acceleration) is first integrated over the whole timestep, providing a primary intermediate velocity field. This field is then used as the starting condition for the integration of the pressure step, which results in a secondary intermediate velocity field. This field is used as the starting condition for the integration of the diffusion term, which results in the final velocity field at the end of the timestep. This process results in three semi-discretised substep equations

$$\mathbf{V}^* - \mathbf{V}^{(n)} - \Delta \mathbf{V}_{cyl} = \int_{\tau}^{\tau+\Delta\tau} (\mathbf{V} \cdot \nabla) \mathbf{V} d\tau \quad (3.6)$$

$$\mathbf{V}^{**} - \mathbf{V}^* = - \int_{\tau}^{\tau+\Delta\tau} \nabla P d\tau \quad (3.7)$$

$$\mathbf{V}^{(n+1)} - \mathbf{V}^{**} = \frac{1}{Re} \int_{\tau}^{\tau+\Delta\tau} \nabla^2 \mathbf{V} d\tau, \quad (3.8)$$

where n represents the current timestep, and \mathbf{V}^* and \mathbf{V}^{**} are the intermediate velocity fields at the end of the convection and pressure substeps respectively. Here, $\Delta \mathbf{V}_{cyl} = \int_{\tau}^{\tau+\Delta\tau} \frac{d\mathbf{V}_{cyl}}{d\tau} d\tau$, which is the change in cylinder velocity over a timestep. The addition of these three substep equations results in the integrated form of the Navier–Stokes equations described in equation 3.3. The time-stepping methods employed in the solution of these equations are explained in section 3.4.

3.4 Integration of the substep equations

3.4.1 The convection substep: Externally-driven cylinder

To solve the convection substep equation set out in equation 3.6 for the externally-driven cylinder, a third-order Adams-Bashforth scheme was employed. This provided high temporal accuracy while still allowing a reasonable timestep. Because an explicit method was used, the timestep was controlled by a Courant condition (Canuto, 1988). The explicit method was used because the equation is non-linear. The cylinder motion could easily be added as a known quantity, directly calculated from the prescribed driving function. This

process rendered the equation to be solved for \mathbf{V}^* as

$$\frac{\mathbf{V}^* - \mathbf{V}^{(n)} - \Delta \mathbf{V}_{cyl}}{\Delta \tau} = \frac{1}{12} (23\mathbf{N}(\mathbf{V})^{(n)} - 16\mathbf{N}(\mathbf{V})^{(n-1)} + 5\mathbf{N}(\mathbf{V})^{(n-2)}), \quad (3.9)$$

where $\mathbf{N}(\mathbf{V})^{(n)}$ represents the non-linear term $(\mathbf{V}^{(n)} \cdot \nabla) \mathbf{V}^{(n)}$, and n represents the timestep.

3.4.2 The convection substep: Elastically-mounted cylinder

The same process could not be applied without modification for the elastically-mounted cylinder case, as the change in cylinder velocity, $\Delta \mathbf{V}_{cyl}$, was not known explicitly at each timestep. Instead, the coupled differential equation describing the cylinder dynamics, equation 3.5, needed to be solved at each timestep.

To proceed with the solution of the coupled equations, an iterative predictor-corrector method was employed. The first step was to obtain estimates of all the quantities involved in the integration. This is the ‘‘predictor’’ component of the method. An initial estimate of $\Delta \mathbf{V}_{cyl}$ was found using quadratic extrapolation from the values of \mathbf{V}_{cyl} at the three previous timesteps. This process resulted in the non-dynamical approximation

$$\mathbf{V}_{cyl}^{(n+1)\dagger} = 3\mathbf{V}_{cyl}^{(n)} - 3\mathbf{V}_{cyl}^{(n-1)} + \mathbf{V}_{cyl}^{(n-2)}, \quad (3.10)$$

where the dagger (\dagger) denotes that the value of $\mathbf{V}_{cyl}^{(n+1)\dagger}$ is an initial approximation. From this, $\Delta \mathbf{V}_{cyl}^\dagger$ was found by simply subtracting the value at the current timestep from the approximation at the end of the timestep.

The approximate cylinder position at the next timestep could then be estimated by integrating the cylinder velocity over the timestep. This was done using a third-order Adams-Moulton method. The final equation for the body position was

$$\frac{y_{cyl}^{(n+1)\dagger} - y_{cyl}^{(n)}}{\Delta \tau} = \frac{1}{12} (5\mathbf{V}_{cyl}^{(n+1)\dagger} + 8\mathbf{V}_{cyl}^{(n)} - \mathbf{V}_{cyl}^{(n-1)}), \quad (3.11)$$

where y_{cyl} denotes the cylinder’s transverse displacement, and again, the dagger superscript denotes an initial approximation.

With these approximate quantities calculated, it was possible to proceed with the solution of equation 3.6 to approximate \mathbf{V}^* . This was done in a similar manner to the solution of equation 3.6 for the driven cylinder. A third-order Adams-Bashforth scheme, using the approximation of equation 3.10 for $\Delta \mathbf{V}_{cyl}^\dagger$, was employed, giving the equation

$$\frac{\mathbf{V}^* - \mathbf{V}^{(n)} - \Delta \mathbf{V}_{cyl}^\dagger}{\Delta \tau} = \frac{1}{12} (23\mathbf{N}(\mathbf{V})^{(n)} - 16\mathbf{N}(\mathbf{V})^{(n-1)} + 5\mathbf{N}(\mathbf{V})^{(n-2)}). \quad (3.12)$$

This equation was solved for the first approximation of \mathbf{V}^* . It should be noted that this explicit integration method was only employed for the first approximation, with all subsequent iterations for \mathbf{V}^* employing a semi-implicit method, as explained below.

Following this, the remaining two substep equations were solved, to obtain the first estimate of $\mathbf{V}^{(n+1)\dagger}$, to complete the predictor cycle of the predictor-corrector method.

The ‘‘corrector’’ process was then initiated. This commenced by updating the cylinder velocity approximation, $\Delta\mathbf{V}_{cyl}^\dagger$. This was done by calculating the forces on the body from the approximation for the velocity field at the end of the timestep, $\mathbf{V}^{(n+1)\dagger}$. These forces, along with the approximation for the cylinder displacement, $y^{(n+1)\dagger}$, were then substituted into the equation of motion of the cylinder (see equation 3.5), which could then be solved for the cylinder acceleration. This acceleration was then integrated over the timestep to obtain a corrected value of the approximation of the cylinder velocity, \mathbf{V}_{cyl}^\dagger . The integration scheme used was

$$\frac{\mathbf{V}_{cyl}^{(n+1)\dagger} - \mathbf{V}_{cyl}^{(n)}}{\Delta\tau} = \frac{1}{24}(25\ddot{y}_{cyl}^{(n+1)} - 2\ddot{y}_{cyl}^{(n)} + \ddot{y}_{cyl}^{(n-1)}) . \quad (3.13)$$

With $\mathbf{V}_{cyl}^{(n+1)\dagger}$ recalculated, $\Delta\mathbf{V}_{cyl}^\dagger$ could be updated. The cylinder position was also updated by integrating this velocity over the timestep. For the first correction cycle, the integration scheme used was

$$\frac{y^{(n+1)\dagger} - y^{(n)}}{\Delta\tau} = \frac{1}{12}(5\mathbf{V}_{cyl}^{(n+1)\dagger} + 8\mathbf{V}_{cyl}^{(n)} - \mathbf{V}_{cyl}^{(n-1)}) , \quad (3.14)$$

which is a third-order Adams-Moulton method, rendered explicit in this instance because the velocity at the end of the timestep, $\mathbf{V}_{cyl}^{(n+1)\dagger}$, was already estimated. This completed the first iteration of the predictor-corrector method.

Subsequent iterations proceeded in a similar manner, with some slight modifications to improve the numerical stability of the scheme, and to take advantage of the information already gained from approximations made by previous iterations at the next timestep. First, as approximations for $\Delta\mathbf{V}_{cyl}^\dagger$ and $\mathbf{V}^{(n+1)\dagger}$ were available, further iterative correction steps employed a third-order Adams-Moulton method,

$$\frac{\mathbf{V}^* - \mathbf{V}^{(n)} - \Delta\mathbf{V}_{cyl}^\dagger}{\Delta\tau} = \frac{1}{12}(5\mathbf{N}(\mathbf{V})^{(n+1)\dagger} + 8\mathbf{N}(\mathbf{V})^{(n)} - \mathbf{N}(\mathbf{V})^{(n-1)}) . \quad (3.15)$$

As in the first iteration, the two remaining substeps were then solved for an new estimate of $\mathbf{V}^{(n+1)\dagger}$.

The correction then proceeded by first employing equation 3.13, as for the first correction step, to obtain a second estimate of the cylinder velocity, $\mathbf{V}_{cyl}^{(n+1)\ddagger}$. However, before utilising equation 3.14, a relaxation equation was employed for the velocity of the cylinder, because the equations are quite stiff. This equation was

$$\mathbf{V}_{cyl}^{(n+1)'} = \mathbf{V}_{cyl}^{(n+1)\ddagger} + \epsilon(\mathbf{V}_{cyl}^{(n+1)\ddagger} - \mathbf{V}_{cyl}^{(n+1)\dagger}), \quad (3.16)$$

where $\mathbf{V}_{cyl}^{(n+1)\ddagger}$ and $\mathbf{V}_{cyl}^{(n+1)\dagger}$ represent the most recent and previous approximations respectively, and ϵ represents an under-relaxation parameter, which effectively controls the proportion of the correction that is considered each iteration. $\mathbf{V}_{cyl}^{(n+1)'}$ represents the eventual approximation at the end of the relaxation process that was used in equation 3.14, completing the correction cycle and therefore the iteration.

Iteration continued until the cylinder lift force, cylinder velocity and fluid velocity field had all converged to within specified error criteria. These criteria were determined through a series of convergence studies (Pregalato, 2003). Typically, only 3–4 iterations were required for each timestep, and only very rarely did the iteration count exceed 10.

To recap, the solution procedure for \mathbf{V}^* (the velocity field at the end of the convection substep) for the freely-oscillating cylinder was as follows. A primary predictor cycle was first employed. This progressed by obtaining an approximation for $\Delta\mathbf{V}_{cyl}$, calculated using equation 3.10, which could then be used to approximate the cylinder position using equation 3.11. Next, \mathbf{V}^* was approximated by solving the substep equation with an explicit Adams-Bashforth method, as set out in equation 3.12. The remaining substep equations were then solved to arrive at a first approximation of $\mathbf{V}^{(n+1)}$, completing the predictor cycle.

A primary corrector step was then applied. This consisted of calculating the forces on the cylinder from the current approximation of $\mathbf{V}^{(n+1)}$, and using these forces and the current approximations of cylinder velocity and cylinder displacement in the cylinder equation of motion (equation 3.5) to obtain an approximation of the cylinder acceleration at the end of the timestep. This acceleration was then integrated over the timestep using equation 3.13 to obtain a corrected approximation of $\Delta\mathbf{V}_{cyl}$. This approximation was then used to integrate velocity over the timestep to obtain a corrected approximation of $y_{cyl}^{(n+1)}$ using equation 3.14. This completed the primary corrector process and the primary iteration.

All subsequent iterations employed the predictions from the previous iteration to solve the convection substep equation for \mathbf{V}^* , using a third-order Adams-Moulton method, as outlined in equation 3.15. The remaining substep equations were then solved to update the prediction of $\mathbf{V}^{(n+1)}$. Next, the predictions of $\mathbf{V}^{(n+1)}$, $\Delta\mathbf{V}_{cyl}$ and $y_{cyl}^{(n+1)}$ were used to update the prediction of the cylinder acceleration using the equation of motion set out in equation 3.5. This was then used to integrate the cylinder acceleration over the timestep to update the prediction of the cylinder velocity, and therefore $\Delta\mathbf{V}_{cyl}$, using equation 3.13. This prediction was then under-relaxed by applying equation 3.16. This under-relaxed prediction of $\Delta\mathbf{V}_{cyl}$ was then utilised with equation 3.14, to update the cylinder displacement, completing the corrector iteration process.

The use of the iterative predictor-corrector scheme, using the Adams-Moulton scheme outlined in equation 3.15, relaxed the stability restriction on the timestep, meaning that the requirement for internal iterations each timestep could be offset by using larger timesteps. However, this also required that the results obtained be verified for temporal convergence to a physically correct solution. The results of this temporal resolution study are presented in section 3.8.3.

3.4.3 The pressure substep

Regardless of the method employed for the convection substep, the pressure and diffusion substeps were treated in the same manner for both the externally-driven and elastically-mounted cylinder. The pressure equation was dealt with in two parts to deal with the two unknowns in the equation, namely the pressure field and the velocity field at the end of the substep.

First, the integration of the pressure substep, equation 3.7, was formulated in terms of a second-order Adams-Moulton method, giving

$$\frac{\mathbf{V}^{**} - \mathbf{V}^*}{\Delta\tau} = -\frac{1}{2}(\nabla P^{(n+1)} + \nabla P^{(n)}) . \quad (3.17)$$

This equation can be further simplified by considering the right-hand side as equal (to second-order accuracy) to $\nabla P^{(n+1/2)}$. Next, the divergence of equation 3.17 taken. Continuity was also enforced for the velocity field at the end of the substep (using equation 3.4),

resulting in a Poisson equation for the pressure of the form

$$\nabla^2 P^{(n+\frac{1}{2})} = \frac{1}{\Delta\tau} \nabla \cdot \mathbf{V}^* , \quad (3.18)$$

which could be solved for the pressure field at the middle of the timestep. This pressure field could then be substituted back into equation 3.17, along with the simplification of the right-hand side, to solve for the velocity field at the end of the substep, \mathbf{V}^{**} .

3.4.4 The diffusion substep

Even though the equation for the diffusion substep is linear, numerical stability of a solution scheme needs to be considered when selecting the numerical approximation. Therefore, an implicit second-order Adams-Moulton method was employed (i.e., the Crank-Nicholson method), which is unconditionally numerically stable. This rendered equation 3.8 as

$$\frac{\mathbf{V}^{(n+1)} - \mathbf{V}^{**}}{\Delta\tau} = \frac{1}{2Re} (\nabla^2 \mathbf{V}^{(n+1)} + \nabla^2 \mathbf{V}^{(n)}) . \quad (3.19)$$

The solution of this equation for $\mathbf{V}^{(n+1)}$ completed the integration over the timestep, and therefore the time-stepping scheme.

3.5 Boundary conditions

Common boundary conditions were applied for all of the simulations performed, regardless of the mesh employed. A no-slip condition was applied at the cylinder surface. This implies that all velocity components must go to zero at the cylinder surface. The velocity at the upstream boundary of the cylinder, and those to either side, was prescribed to be equal to the freestream velocity in the freestream direction, and equal to the negative of the cylinder motion in the transverse direction, to account for the accelerating frame of reference attached to the cylinder. The transverse velocity was solved for during the simulation, as explained in the sections 3.4.1 and 3.4.2. As these boundaries had specified values of the velocity, \mathbf{V} , they are generally referred to as Dirichlet boundary conditions (Kreyzig, 1999).

At the boundary downstream of the cylinder, it was imposed that $\frac{\partial \mathbf{V}}{\partial \mathbf{n}} = 0$, where \mathbf{n} is the unit normal vector. This effectively makes the assumption that the flow does not evolve spatially while exiting the domain. While this assumption is not completely physical, as

long as the outflow boundary is sufficiently far from the body, and the Reynolds number is low enough so that vortex structures can exit the domain, this does not pose a significant problem. A domain size study (the subject of section 3.8.1) was performed to ensure that this did not affect the results of this thesis.

First-order (in time) boundary conditions were derived for the pressure at the cylinder surface and freestream boundaries. The result of this derivation was a condition on the gradient of the pressure normal to the boundary. To obtain this boundary condition, the basic process was to take the dot product of the unit normal vector and the Navier–Stokes equations, and then to transpose the result to solve for the gradient of the pressure in the normal direction. This process was implemented using the following steps.

The substep equations shown in equations 3.6–3.8 were approximated to first-order time accuracy, using an explicit scheme for the convection step and an implicit scheme for the diffusion step. The linear diffusion term was decomposed into a divergence-free component and an irrotational component. After discounting terms that go to zero, the substep equations were summed to result in the integrated form of the discretised Navier–Stokes equations. The dot product of this vector equation with the unit normal vector was taken. The result was then transposed to form an expression for the gradient of the pressure in the normal direction. The form of this expression is

$$\frac{\partial P^{(n+\frac{1}{2})}}{\partial \mathbf{n}} = \mathbf{n} \cdot [\mathbf{N}(\mathbf{V})^{(n)} + \frac{1}{Re}(\nabla \times (\nabla \times \mathbf{V})^{(n)})], \quad (3.20)$$

where \mathbf{n} is the unit normal vector. The use of this first-order accurate condition for the pressure resulted in second-order accuracy for the velocity. Details of this scheme and its derivation can be found in Karniadakis *et al.* (1991). The boundary conditions were completed by imposing a constant pressure across the domain at the outflow boundary.

3.6 The spectral-element method

The spatial discretisation, and eventual formation of matrix equations from the series of equations set out in section 3.4, was implemented using a nodal-based spectral-element method. This is a method from the finite-element class, where the computational domain is divided into a series of macro-elements, and a continuous solution is obtained over each element. The macro-element mesh can be refined in areas of the domain that experience

high gradients. This is known as h -refinement. For the method employed here, it was also necessary that all elements were quadrilateral, although they were free to have curved sides.

The solution process began by calculating the residual, \mathbf{R} . To form the residual, all terms of the governing equations (in this case, the Navier–Stokes equations of equation 3.3) were moved to the left-hand side. This results in the expression

$$\frac{\partial \mathbf{V}}{\partial \tau} + \nabla P - \frac{1}{Re}(\nabla^2 \mathbf{V}) + (\mathbf{V} \cdot \nabla) \mathbf{V} - \frac{d\mathbf{V}_{cyl}}{d\tau} = 0 . \quad (3.21)$$

Next, a trial solution was substituted into equation 3.21. If the trial solution is an exact solution of the equation, the right-hand side will remain equal to zero. However, if the trial solution is an approximation to the exact solution (as is the case in general), then the right-hand side will not be zero, and a residual, \mathbf{R} , will be formed, defined by

$$\frac{\partial \mathbf{V}_{trial}}{\partial \tau} + \nabla P_{trial} - \frac{1}{Re}(\nabla^2 \mathbf{V}_{trial}) + (\mathbf{V}_{trial} \cdot \nabla) \mathbf{V}_{trial} - \frac{d\mathbf{V}_{cyl}}{d\tau} = \mathbf{R} , \quad (3.22)$$

where \mathbf{V}_{trial} and P_{trial} are the trial solutions for the velocity and pressure fields. The residual, \mathbf{R} , is effectively an error term introduced through the use of the trial functions. It is shown in equation 3.22 that \mathbf{R} is defined as the original governing equation with the trial solution substituted for the true solution.

The next step was to weight the residual, effectively distributing the introduced error over the domain, to minimise the maximum local error. This was done by taking the inner product of the residual with a series of weighting functions. The inner product is the integral of the product of the weighting functions and the residual. This leads to the method employed being referred to as a method of weighted residuals (MWR). This inner product is set to zero.

For the simulations conducted for this thesis, the interpolating trial functions and weighting functions were both tensor-product Lagrange polynomials. The order of these polynomials, p , could be varied from 2 to 14, further improving the grid resolution. This is known as p -refinement. This, coupled with h -refinement, leads to a so-called h - p method (Karniadakis & Sherwin, 2005). As the same family of functions was utilised for both the trial and weighting functions, the method used can be referred to as a Galerkin method. Further details of MWRs and Galerkin methods can be found in Fletcher (1984, 1991), and an in-depth presentation of spectral-element/ h - p methods found in Karniadakis & Sherwin (2005).

Lagrange polynomials are defined as

$$L_i(\xi) = \prod_{\substack{g=1 \\ g \neq i}}^{p+1} \frac{(\xi - \xi_g)}{(\xi_i - \xi_g)} \quad (3.23)$$

where ξ is the spatial coordinate, i and g are the indices of the data points, and $p+1$ is the number of data points. Lagrange polynomials have the property of being equal to unity at the point i , and zero at all other points (but not in-between). Therefore, multiplying L_i by the velocity at point i , and summing over all points, gives a continuous polynomial that matches the velocity at the node points exactly. Tensor-product Lagrange polynomials in two dimensions, $N_{q,s}(\xi, \eta)$, are simply the product of the Lagrange polynomial in one direction, $L_q(\xi)$, with that in the other direction, $L_s(\eta)$.

The basic solution procedure is as follows. First, the inner product of the residual and the tensor-product Lagrange polynomial weighting function is formed. This is the integral

$$\int \int_{\Omega} N_{k,m}(\xi, \eta) \cdot \left[\frac{\partial \mathbf{V}_{trial}}{\partial \tau} + \nabla P_{trial} - \frac{1}{Re} (\nabla^2 \mathbf{V}_{trial}) + (\mathbf{V}_{trial} \cdot \nabla) \mathbf{V}_{trial} - \frac{d\mathbf{V}_{cyl}}{d\tau} \right] dx dy = 0, \quad (3.24)$$

where Ω represents the computational domain. The weighting function $N_{q,s}(\xi, \eta)$ is defined in computational space. The definition of this space is given following the description of the treatment of equation 3.24.

From the definition of the inner product in equation 3.24, it is shown that each term in the equation is multiplied by the weighting function. Therefore, this integral can be split up into components, and the process can be performed on each of the substep equations defined in equations 3.6–3.8. Also, it can be applied to the integration scheme used to solve each of the substep equations. For instance, the discretised equation to be solved for the convection step for the driven cylinder, defined as equation 3.9, becomes

$$\begin{aligned} & \frac{1}{\Delta \tau} \int \int_{\Omega} N_{q,s}(\xi, \eta) \cdot (\mathbf{V}_{trial}^* - \mathbf{V}_{trial}^{(n)} - \Delta \mathbf{V}_{cyl}) dx dy = \\ & \int \int_{\Omega} N_{q,s}(\xi, \eta) \cdot \left(\frac{1}{12} (23\mathbf{N}(\mathbf{V}_{trial})^{(n)} - 16\mathbf{N}(\mathbf{V}_{trial})^{(n-1)} + 5\mathbf{N}(\mathbf{V}_{trial})^{(n-2)}) \right) dx dy. \end{aligned} \quad (3.25)$$

Again, this integral can be broken up into components, and each component dealt with separately. For instance, the first of the three terms on the left-hand side in equation 3.25 is defined as

$$\int \int_{\Omega} \mathbf{V}_{trial}^* N_{q,s}(\xi, \eta) dx dy. \quad (3.26)$$

This term will be used to illustrate the process of solution using a spectral-element method.

To calculate the integral of equation 3.26 over the entire computational domain, it is evaluated over each element separately, and then the elemental contributions are summed together. Each quadrilateral element is mapped to a square defined over the range $-1, 1$ in both directions. The computational coordinates ξ and η are just the orthogonal coordinates of this square. The internal node points in each element are then defined at the Gauss-Lobatto-Legendre (GLL) quadrature points of this unit square, which simplifies the approximation of the integral.

This coordinate transformation introduces a Jacobian into the inner product integral, and the integral over each element becomes

$$\int \int_{El} \mathbf{V}^* N_{q,s}(\xi, \eta) \mathbf{J}(\xi, \eta) d\xi d\eta , \quad (3.27)$$

where \mathbf{J} represents the Jacobian, and the subscript El denotes that the integration is performed over a single element. Expanding the solution \mathbf{V}_{trial}^* of equation 3.27 as a summation of Lagrange polynomial components and expressing the tensor-product Lagrange polynomials representing the weighting functions as components in each of the directions ξ and η allows equation 3.27 to be written as

$$\int \int_{El} \sum_{i,j} \widehat{\mathbf{V}}^* L_i(\xi) L_j(\eta) L_q(\xi) L_s(\eta) \mathbf{J}(\xi, \eta) d\xi d\eta , \quad (3.28)$$

where $\widehat{\mathbf{V}}^*$ represents the velocity field at the node points, L represents a one-dimensional Lagrange polynomial, i represents the node location in the ξ direction, and j represents the node location in the η direction.

The integral defined in equation 3.28 can be approximated using GLL quadrature, taking advantage of the definition of the location of the internal points in computational space. This leads to the integral of equation 3.28 being approximated as

$$\sum_{a,b} W_{a,b} \sum_{i,j} \widehat{\mathbf{V}}^*_{i,j} L_i(\xi_a) L_j(\eta_b) L_q(\xi_a) L_s(\eta_b) \mathbf{J}(\xi_a, \eta_b) , \quad (3.29)$$

where $W_{a,b}$ represents the weighting coefficients for GLL quadrature, a represents the node position in the ξ direction and b represents the node location in the η direction.

While equation 3.29 appears daunting, the expression simplifies considerably. Because the system is discrete, and only the values at the node points are of concern, the use of

Lagrange polynomials allows the substitution

$$L_i(\xi_a) = \delta_{ia} = \begin{cases} 1 & i = a \\ 0 & i \neq a \end{cases}, \quad (3.30)$$

where δ_{ia} is the Kronecker delta. This significantly reduces the number of non-zero terms in the summation, and allows a much simpler expression. For the example considered here based on the \mathbf{V}^* term in the convection substep equation, only a single term remains, namely

$$W_{q,s} \mathbf{J}(\xi_q, \eta_s) \widehat{\mathbf{V}}_{q,s}^*. \quad (3.31)$$

Similar simplifications can be made for all terms in the governing equations, and this process repeated over all elements. The elemental contributions can then be collected and assembled into a global matrix system that can be solved for the unknown velocity and pressure fields at the nodal points.

Although the shape functions are high-order polynomials within each element, only continuity of the function is required across element boundaries, with no condition imposed on the gradient (this condition is known as C_0 continuity). It can be shown that the method achieves global exponential convergence (Karniadakis & Sherwin, 2005). The implementation used for this thesis has been demonstrated to give exponential spatial convergence as the number of internal nodes per element is increased (Thompson *et al.*, 1996).

3.7 Floquet stability analysis

Floquet stability analysis is a method for determining the linear stability of periodic solutions. It has been successfully employed in the wakes of various bluff bodies to predict flow transitions, including cylinders (Barkley & Henderson, 1996; Blackburn *et al.*, 2005), perpendicular plates (Julien *et al.*, 2004), tori (Sheard *et al.*, 2003b) and elliptical leading-edge plates (Ryan *et al.*, 2005). The implementation used for this thesis has been validated by Thompson *et al.* (2001), Sheard *et al.* (2003b) and Ryan *et al.* (2005). Explanations of the basic method can be found in Iooss & Joseph (1990), and Seydel (1994).

In effect, the approach is as follows. Equations are formed that describe the perturbation field, by substituting $\mathbf{V}(x, y, \tau) + \mathbf{v}'(x, y, z, \tau)$ for \mathbf{V} in the Navier–Stokes equations,

where \mathbf{V} is the two-dimensional, periodic base flow velocity and \mathbf{v}' is the three-dimensional perturbation velocity. A similar expansion is followed for the pressure. The original equations describing the two-dimensional base flow are then subtracted, and what is left are equations describing the evolution of the perturbation field. The equations are then linearised, since perturbations must grow from low amplitudes, where non-linear terms are negligible. Even though the resulting linear equations describe the perturbation field evolution only, these equations still rely on the base flow fields. The final linearised equation system, after non-dimensionalisation similar to that for equation 3.3, can be expressed as

$$\frac{\partial u'}{\partial \tau} = -\frac{\partial p'}{\partial x} + \frac{1}{Re} \left(\frac{\partial^2 u'}{\partial x^2} + \frac{\partial^2 u'}{\partial y^2} + \frac{\partial^2 u'}{\partial z^2} \right) - u \frac{\partial u'}{\partial x} - u' \frac{\partial u}{\partial x} - v \frac{\partial u'}{\partial y} - v' \frac{\partial u}{\partial y} \quad (3.32)$$

$$\frac{\partial v'}{\partial \tau} = -\frac{\partial p'}{\partial y} + \frac{1}{Re} \left(\frac{\partial^2 v'}{\partial x^2} + \frac{\partial^2 v'}{\partial y^2} + \frac{\partial^2 v'}{\partial z^2} \right) - u \frac{\partial v'}{\partial x} - u' \frac{\partial v}{\partial x} - v \frac{\partial v'}{\partial y} - v' \frac{\partial v}{\partial y} \quad (3.33)$$

$$\frac{\partial w'}{\partial \tau} = -\frac{\partial p'}{\partial z} + \frac{1}{Re} \left(\frac{\partial^2 w'}{\partial x^2} + \frac{\partial^2 w'}{\partial y^2} + \frac{\partial^2 w'}{\partial z^2} \right) - u \frac{\partial w'}{\partial x} - v \frac{\partial w'}{\partial y} \quad (3.34)$$

$$\frac{\partial u'}{\partial x} + \frac{\partial v'}{\partial y} + \frac{\partial w'}{\partial z} = 0 \quad (3.35)$$

where the primed variables describe the perturbation field and the unprimed variables describe the base flow. The equations have been written out in full to show that the equation in the third dimension (the z -direction) is slightly different in form to the others, as the base flow velocity components are zero in that direction.

These linear perturbation equations can be solved in all three spatial dimensions directly; however, the partial differential equations are linear and have constant coefficients with respect to z , and hence the z (spanwise) dependent terms (such as $\frac{\partial^2 u}{\partial z^2}$) for each perturbation field can be expressed as a sum of Fourier modes. Moreover, because of linearity, the solution corresponding to each Fourier mode can be calculated independently.

Floquet theory then looks for solutions of the (two-dimensional) perturbation fields for each spanwise wavelength, λ , in the form

$$r'(\tau + T, x, y) = \exp(\sigma T) r'(\tau, x, y). \quad (3.36)$$

Here, r' represents any of the perturbation variables, τ is time and T is the period of the base flow. A Floquet mode is effectively a solution of the perturbation equations with the prescribed spatial wavelength in the z -direction. As the reduced differential equation set

presents an eigenvalue problem, there are infinitely many modes of the form of equation 3.36 that may exist for a given spatial wavelength. However, physically, the mode that grows fastest is of most interest, as it is this mode that will come to dominate the solution over time. The exponential coefficient in equation 3.36 can alternatively be written as $\mu = \exp(\sigma T)$, where μ is termed the *Floquet multiplier*. If $|\mu| > 1$, the corresponding perturbation field grows exponentially from one period to the next, hence the base flow is linearly unstable to perturbations of the selected spatial wavelength in the z -direction.

To implement this scheme numerically, the following steps were taken. An initial perturbation field was constructed consisting of random noise, for a selected spanwise wavelength. From these initial conditions, the perturbation equations were integrated forward in parallel with the base flow equations. The spatial discretisation and time integration schemes used were essentially the same as those employed for the base flow calculations. To obtain a measure of the Floquet multiplier, μ , the L_2 norm of a perturbation field (any of the fields will suffice) was taken, and the perturbation field then normalised by this value. The base flow and perturbation equations were then integrated forward one base flow period, T , the L_2 norm evaluated again, and the perturbation field again renormalised. The L_2 norm was the ratio of the perturbation solution magnitude from one period to the next. After many base flow periods, only the fastest growing (or slowest decaying) Floquet mode remained, and at this stage, the L_2 norm corresponded to the magnitude of the largest Floquet multiplier for the selected wavelength. For the results of this thesis, convergence of the Floquet multiplier, to three significant figures, was obtained within anywhere from 10 to 60 base flow periods.

The method described above works very effectively for Floquet modes that have the same period as the base flow, or a period that is a multiple of the base flow (Robichaux *et al.*, 1999; Thompson *et al.*, 2001; Sheard *et al.*, 2003b). However, modes can exist that have periods that are incommensurate with the base flow period. These are called quasi-periodic modes, and have been found to occur in the wakes of bluff bodies and other fluid flows (Blackburn & Lopez, 2003; Blackburn *et al.*, 2005; Marques *et al.*, 2004). For these modes, the true Floquet multiplier will be a complex quantity. The imaginary component of this multiplier is not directly resolved by the method described above. However, the imaginary component of the Floquet mode causes an underlying sinusoidal time variation

of the perturbation field, and hence the L_2 norm also oscillates in time. Therefore, with inspection of the history of the Floquet multiplier, and careful inspection of the perturbation fields, the existence of quasi-periodic modes can be deduced. It has also been shown by Blackburn & Lopez (2003) that the magnitude of the complex Floquet multiplier is the mean value over time of the quantity returned using the L_2 norm “power” method employed for this thesis.

3.8 Convergence and validation studies

This section presents validation results of the code used. Tests were conducted to ensure adequate domain sizes, and spatial and temporal resolutions, were used.

For comparison, validation simulations were performed using a fixed cylinder, where well-established experimental and numerical data exist. The parameter monitored for these studies was the Strouhal number, St . The lift and drag coefficients were also used, as they are known to be sensitive to domain size due to blockage effects, and spatial and time resolution. They are also global parameters, and as such somewhat account for the accuracy of the solution over the whole domain.

3.8.1 Domain size

Almost all of the two-dimensional simulations that contributed to the results of this thesis were run on the same mesh. The domain covered by this mesh extended $25D$ downstream, and $15D$ to either side of the cylinder and upstream. This mesh is referred to throughout this section as $M1$. The validity of this domain was checked by computing simulations on three other meshes: one the same length but narrower ($M2$); another the same length but wider ($M3$); and a third the same width but longer ($M4$). Images of all these meshes are shown in figure 3.1. For this domain size study, a polynomial order $p = 7$ was used.

Fixed cylinder simulations were run on each of these meshes at $Re = 200$ and St calculated. The value $Re = 200$ was used as it is close to the highest value of Re where two-dimensional vortex shedding is observed for a fixed cylinder. The values of St acquired were then compared to the value gained using the three-term fit given by Williamson & Brown (1998). The results of this comparison are plotted in figure 3.2a. This figure shows

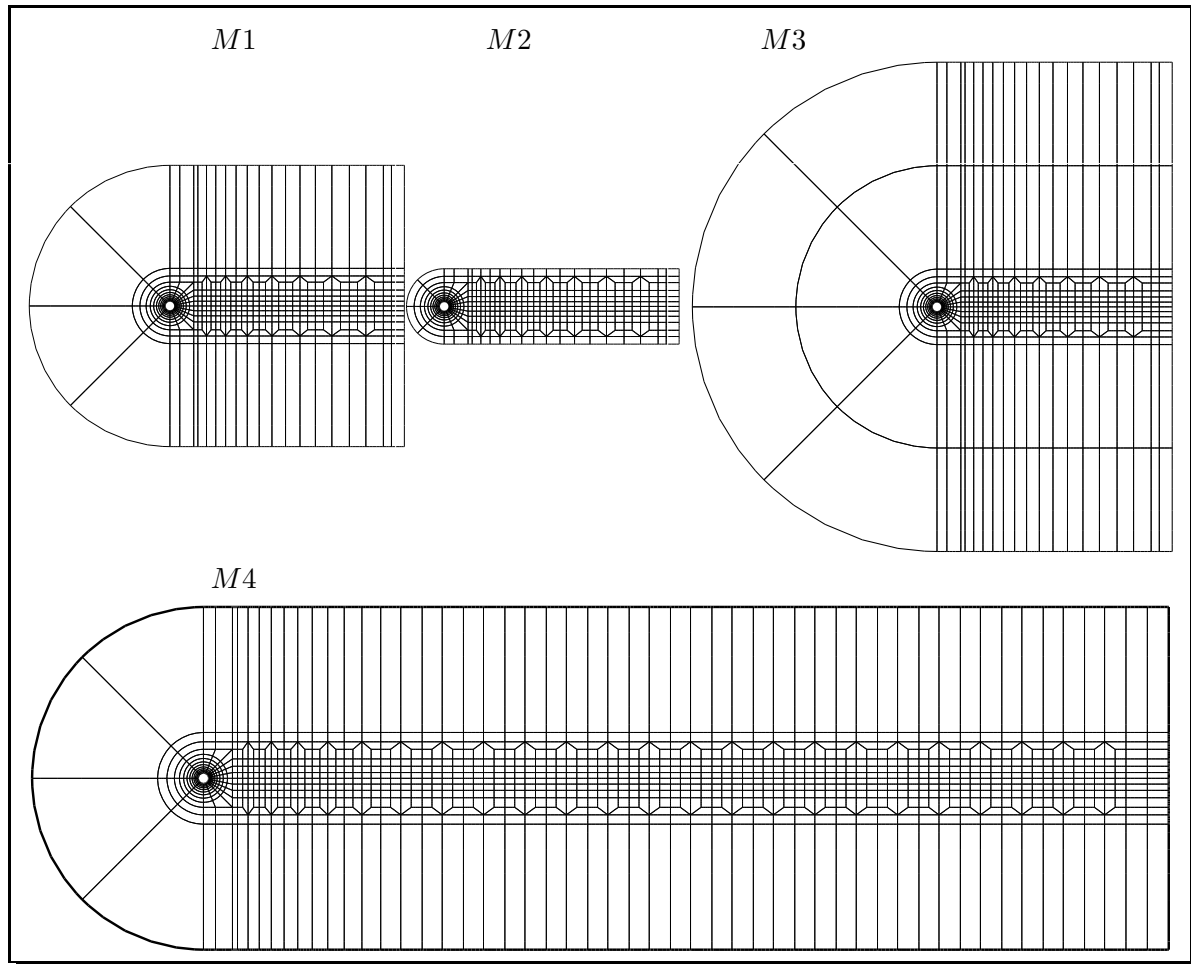


Figure 3.1: Top, from left to right: mesh $M1$, extending $25D$ downstream and $15D$ to either side and upstream; mesh $M2$, extending $25D$ downstream and $\sim 4.5D$ to either side and upstream; mesh $M3$, extending $25D$ downstream, and $\sim 25D$ to either side and upstream. Bottom: mesh $M4$, extending $80D$ downstream and $15D$ to either side and upstream.

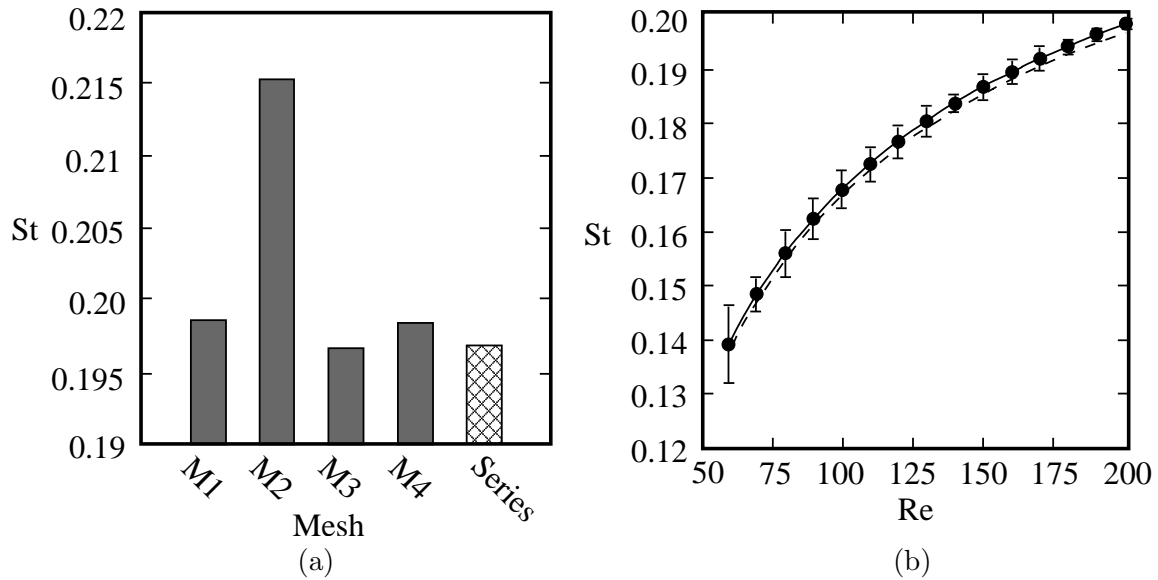


Figure 3.2: (a) The Strouhal number St for the four meshes at $Re = 200$, compared with the value obtained with the three-term series from Williamson & Brown (1998). (b) St versus Re on mesh $M1$. The solid line indicates a three-term fit to this data, and the dashed line represents the three-term fit to numerical data in Williamson & Brown (1998).

that mesh $M2$ produces an unacceptable error, whereas meshes $M1$, $M3$, and $M4$ are all close to the value predicted by the series of Williamson & Brown (1998).

Comparison of the value of St for meshes $M1$ and $M4$ shows that the increased domain length has a negligible effect, yet $M4$ is much more computationally expensive. For this reason, $M4$ was not considered for use.

Mesh $M3$ results in a value of St closer to the value predicted by the series than $M1$. However, the value predicted by $M1$ is within 1% of the series value. This is an acceptable level of accuracy, and it was decided that the increased accuracy afforded by mesh $M3$ was not worth the computational expense of a larger mesh.

The accuracy of mesh $M1$ across a range of Re was also checked. Fixed cylinder simulations were run over $50 < Re < 200$ in Re -increments of 10. The resulting St - Re curve produced is shown in figure 3.2b. The results are again compared to the three-term fit given by Williamson & Brown (1998).

It is shown that mesh $M1$ predicts the relationship between St and Re very well. It is also shown that the trend predicted follows very closely that of Williamson & Brown

(1998), and that this trend is within the error bounds of the data. The frequencies used to calculate St were obtained by measuring the period of the lift force on the cylinder. This period was deemed to be the time between two consecutive times where the lift force was equal to zero, and changed from negative to positive. The error bars on St for all of these validation studies were obtained by assuming second-order accuracy in determining where the lift force was equal to zero.

3.8.2 Grid resolution

To ensure that the results gained were mesh-independent, a grid resolution study was undertaken. This was done by varying the interpolation polynomial order (p -refinement), while keeping the macro-element layout the same. The macro-element mesh employed was mesh $M1$. Again, St was monitored as an indication of accuracy. Results of St for polynomials of order $2 \leq p \leq 14$ are presented in figure 3.3a. This figure shows that St has effectively converged by $p = 5$.

Simulations for an oscillating cylinder at $Re = 200$, with $A^* = 0.5$ and $f^* = 0.20$, were also performed to ensure the mesh resolution was adequate to resolve the finer-scale structures expected in the wake of the oscillating cylinder, due to the high strain induced by the oscillation. Here, $A^* = A/D$ and $f^* = fD/U$, where A is the amplitude of oscillation and f is the frequency of oscillation. Due to the phenomenon of synchronisation, St is not a suitable parameter to use as a convergence check in this case. Therefore, the peak drag coefficient amplitude was compared between resolutions. These results are presented in figure 3.3b. Again, it is clear that the results are converged by $p = 7$. Therefore, polynomial order $p = 7$ was employed for the simulations for this thesis.

3.8.3 Timestep dependence

As an implicit time-stepping method was employed for the elastically-mounted cylinder simulations, it was necessary to establish that the solution generated was not timestep dependent. This is an issue for implicit methods as the increased stability of the numerical scheme can result in a converging solution, even though the timestep is too coarse to resolve the timescale of the flow. This is not such an issue for explicit methods, due to the strong timestep restriction imposed by the Courant condition.

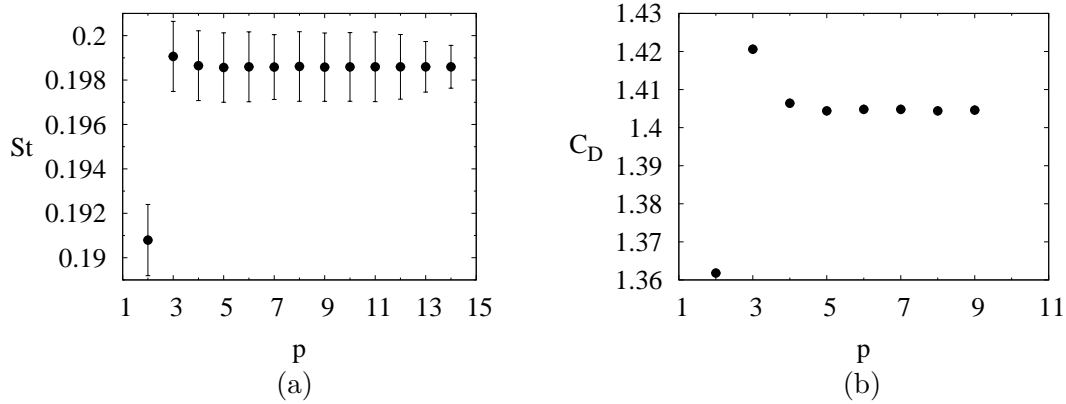


Figure 3.3: (a) The Strouhal number St with varying polynomial order for a fixed cylinder, $Re = 200$. The solution is converged for $p \geq 5$. (b) Peak drag coefficient amplitude with varying polynomial order for an oscillating cylinder, $Re = 200$, $A^* = 0.5$, $f^* = 0.2$. The solution is converged for $p \geq 7$.

Simulations were performed at a series of timesteps for an elastically-mounted cylinder where $Re = 200$, $m^* = 10$, $U^* = 5$ and $\zeta = 0$. Here, m^* is the mass ratio, $U^* = U/f_N D$ is the reduced velocity and ζ is the damping ratio. These parameters were expected to result in synchronisation, but where the system was free to select the frequency of oscillation. Therefore, the frequency of oscillation, f^* was monitored, as was the peak lift coefficient. The results of these simulations are presented in figure 3.4.

The results from these simulations show that the variation across the range of timesteps is minimal. From these results, it was deduced that a timestep of $\Delta\tau = 0.01$ was sufficient to capture all of the flow features accurately.

3.8.4 Floquet analysis

To ensure the accuracy of the Floquet method employed, a validation study was undertaken on the wake of a fixed cylinder.

Simulations were run at $Re = 190$, and the stability of a mode with $\lambda = 4.0$ was tested. These values are very close to the critical values for mode A reported by Barkley & Henderson (1996) of $Re = 188.5$ and $\lambda = 3.96$. A Floquet multiplier of $\mu = 1.0155$ was calculated, indicating that the mode was only just supercritical, as expected.

Similarly, simulations were run for $Re = 260$, and a mode with $\lambda = 0.8$ was tested

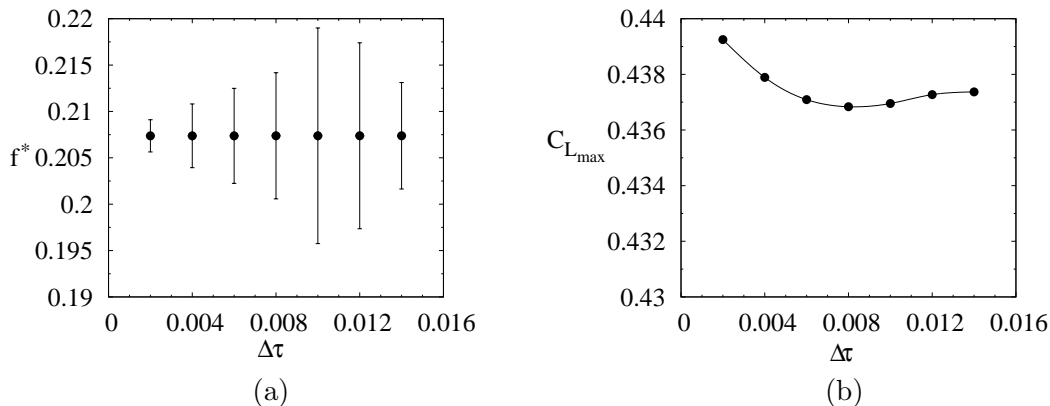


Figure 3.4: (a) Frequency of oscillation versus timestep, for an elastically-mounted cylinder, $Re = 200$, $m^* = 10$, $U^* = 5$, $\zeta = 0$. The variation of oscillation frequency over the range of $\Delta\tau$ tested is $< 0.1\%$. (b) Peak lift coefficient versus timestep for the same conditions. While some variation is observed, the variation of $C_{L_{max}}$ over the range of timesteps tested is $< 1\%$.

for stability. The critical values for mode B are $Re = 259$ and $\lambda = 0.822$ (Barkley & Henderson, 1996). Using these values, a Floquet multiplier of $\mu = 1.0336$ was obtained, confirming that the method employed also correctly resolved this finer-scale mode.

Images of the streamwise perturbation vorticity for these two modes is shown in figure 3.5. They compare very favourably to the images for mode A and B in Barkley & Henderson (1996). The similarity of these results to the published data gives a high level of confidence that the solution is converged.

To ensure the method could also predict accurate critical values for quasi-periodic modes, simulations were run to establish the critical Re and λ values for mode QP for a fixed cylinder wake. While the method used does not automatically return the total complex Floquet multiplier, it has been shown that the magnitude of μ is equal to the mean value returned over a number of base flow periods (Blackburn & Lopez, 2003). Using this method, Floquet runs were performed over a wavelength range $1.5 \leq \lambda \leq 2.0$, and a Reynolds number range $370 \leq Re \leq 380$. From these results, the critical Re for mode QP was estimated to be $Re \simeq 377$, and the critical $\lambda \simeq 1.8$. These values are the same as those reported by Blackburn *et al.* (2005). It is therefore concluded that if care is taken in the interpretation of results, the method utilised can resolve quasi-periodic modes, and

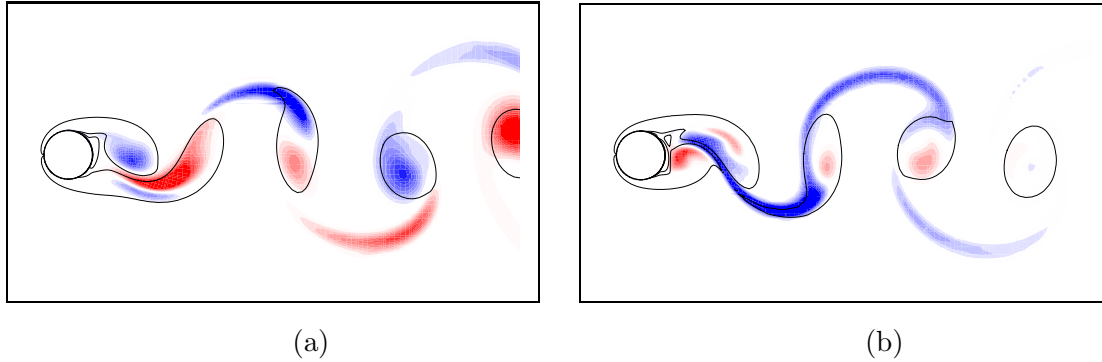


Figure 3.5: (a) Streamwise perturbation vorticity corresponding to mode A at $Re = 190$, $\lambda = 4.0$. (b) Streamwise perturbation vorticity corresponding to mode B at $Re = 260$, $\lambda = 0.8$. For these conditions, both modes were found to be just supercritical.

distinguish them from true subharmonic modes.

Confirmation of this close match was also found by extracting the frequency of the perturbation field by measuring the perturbation velocity at a point in the wake. This frequency and the amplitude of the Floquet multiplier could then be used to reconstruct an approximation of the full complex Floquet multiplier. This was done by noting that the angle in the complex plane was equal to the ratio of the mode frequency to the base flow frequency multiplied by 2π .

Multipliers constructed in this way are presented in figure 3.6. They are plotted alongside results from Blackburn *et al.* (2005), and both are presented on the half-period flip map, rather than the traditional Poincaré map. Floquet multipliers in the half-period flip map, μ_H , are constructed by taking advantage of the spatio-temporal symmetry of the flow, and therefore assuming that

$$r'(\tau + T/2, x, y) = \exp(\sigma T)r'(\tau, x, -y). \quad (3.37)$$

so that

$$\mu_H = \exp(\sigma T). \quad (3.38)$$

From this definition, and that of the standard Floquet multiplier, μ , based on the Poincaré map given in equation 3.36, the relationship between the two can be shown to be

$$\mu_H^2 = \mu. \quad (3.39)$$

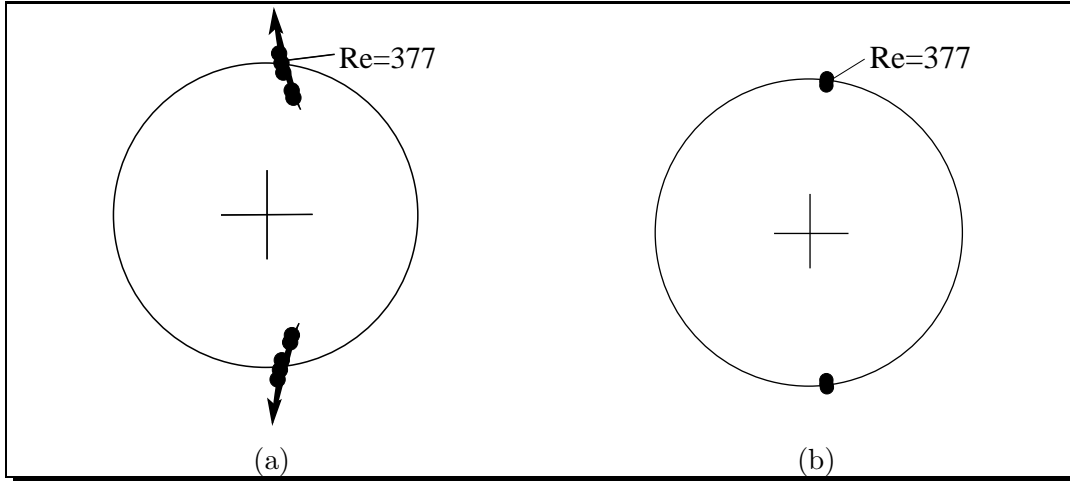


Figure 3.6: Floquet multipliers for mode QP presented on the half-period flip map unit circle. (a) Results from Blackburn *et al.* (2005) that resolved the complex multiplier directly. (b) Results from simulations where the complex component was reconstructed by measuring the wake perturbation velocity at a point in the wake to extract frequency. There is a close match, and the magnitudes of the multipliers are almost identical. This gives an indication that the simulations were accurately resolving quasiperiodic modes.

The comparison between the results presented in this way of Blackburn *et al.* (2005) and those from the simulations from this thesis presented in figure 3.6 shows that the method employs returns accurate results of these quasiperiodic modes, if care is taken in inspection of the history of μ and the perturbation field.

For the high oscillation amplitude Floquet simulations, a second mesh was employed with higher h -refinement near the rear of the cylinder. This was necessary to accurately resolve the finer-scale structures of the perturbation field. Convergence was tested on this mesh, using p -refinement. For an oscillation amplitude of $A^* = 0.70$, varying the polynomial order from 7 to 9 saw the value of the Floquet multiplier μ vary by less than 0.1%. It was therefore concluded that seventh-order tensor-product polynomials were adequate on this macro mesh. The macro-element mesh used for the high-amplitude simulations is shown in figure 3.7.

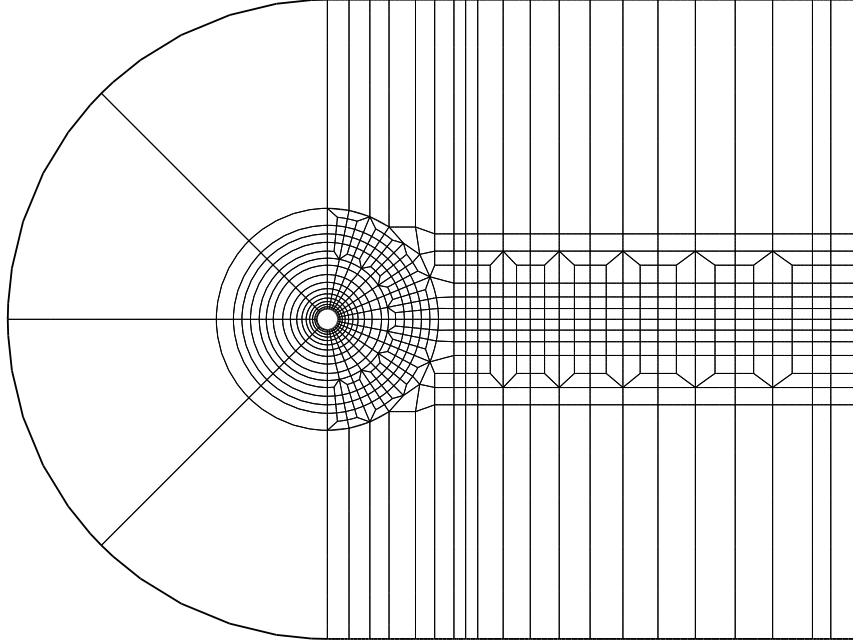


Figure 3.7: The macro-element mesh employed for high-amplitude Floquet simulations. Note the higher h -refinement compared to mesh $M1$ (see figure 3.1)

3.8.5 Validation summary

It has been shown that the primary mesh employed (mesh $M1$), with a polynomial order $p = 7$, accurately captures the flow physics of a fixed cylinder wake flow. It has also been shown that the same mesh resolves the characteristics for an externally-driven sinusoidally-oscillating cylinder. Extending from this, it has been shown that converged results are obtained on this mesh with a timestep of $\Delta\tau = 0.01$, using a semi-implicit algorithm, for elastically-mounted cylinder simulations. The same mesh also returns accurate results of the Floquet multiplier, μ , when compared to previously-known fixed cylinder results. This gives a high level of confidence that the converged results obtained for an oscillating cylinder are accurate.

A second mesh, with higher p -refinement, has also been shown to return converged results of Floquet simulations for high oscillation amplitudes. It is therefore concluded that the results of this thesis can be confidently assumed to be accurate.

CHAPTER 4

SINUSOIDAL EXTERNALLY-DRIVEN OSCILLATION

4.1 Introduction

This chapter contains results and discussion pertaining to the first hypothesis of this thesis. This centres around demonstrating the dependence on Reynolds number, Re , of the wake modes, transitions and energy transfer characteristics during sinusoidal driven oscillation.

A description of the wake modes obtained in general is given. This is followed by results demonstrating that the amplitude and frequency of oscillation at which the transition between these wake modes occurs is dependent on Re . As well as the transition, it is also demonstrated that synchronisation boundaries show some dependence on Re .

The upper amplitude of oscillation for positive energy transfer (from the fluid to the cylinder) is shown to be effectively independent of Re . As the wake mode transition is dependent on Re , and the change in sign of energy transfer has an approximately constant upper value of amplitude with varying Re , it is concluded that the change in wake mode is not linked to the direction of energy transfer.

Expanding on energy transfer, it is shown that regardless of Re , energy transfer is predominantly dependent of the frequency of oscillation at low amplitudes, but predominantly dependent on the amplitude of oscillation at higher amplitudes. This is explained in terms of the varying relationship between flow forces with increasing amplitude.

Following this, the phase between the lift force and cylinder displacement, and its relation to energy transfer is investigated. This is also expanded upon by decomposing the lift force into added mass and vortex components, and investigating the effect of the phase of the vortex lift.

4.2 Wake modes and variation with Reynolds number

To investigate the predicted wake modes, wake mode maps have been constructed in the A^*-f/f_{St} plane, following the lead of Williamson & Roshko (1988). Here, $A^* = y_{max}/D$, f is the frequency of oscillation and f_{St} is the Strouhal frequency for a fixed cylinder. To allow an easy comparison between these results and those of previous studies presented in terms of oscillation wavelength λ_{osc} , the f/f_{St} axis has been reversed. In contrast to previous studies, these maps have been constructed at a single Re . Here, $Re = UD/\nu$, where U is the freestream velocity, D is the diameter and ν is the kinematic viscosity. The frequency variable f/f_{St} has been used to facilitate a direct comparison across different Re . Two such maps are shown in figure 4.1, one at $Re = 100$, and another at $Re = 300$. These maps were constructed by running simulations with parameters that spanned the space. The maximum increment of A^* used was 0.1, and the maximum increment of f/f_{St} was 0.06. Some of the general features of these maps are the same, while other features differ. The similarities will be discussed first.

Only two wake modes occur in the synchronisation region regardless of Re . These are the $2S$ mode, with two single vortices shed per oscillation cycle, and the $P+S$ mode, with a single vortex and a vortex pair formed per oscillation cycle. The region of synchronisation is the area on the plots in figure 4.1 between the two “horns” emanating from $f/f_{St} = 1$. The $2S$ mode occurs at lower A^* , and the transition to the $P+S$ wake occurs as A^* is increased. For a given Re , the exact value of A^* at this transition shows some weak frequency dependence.

Outside of the synchronisation region, variants of the $2S$ mode are observed. However, these modes are not periodic, with the frequency of oscillation and the Strouhal frequency interacting. This causes a beating-type phenomenon, and the entire wake acquires a low-frequency wandering from one side to another, the frequency being equal to the difference

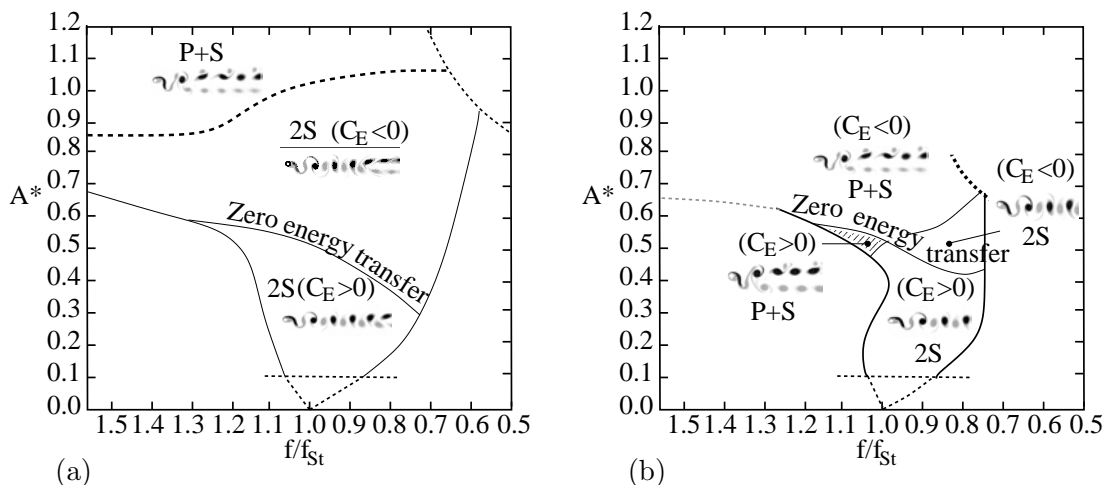


Figure 4.1: (a) Wake modes when $Re = 100$. (b) Wake modes when $Re = 300$. In both cases, only the $2S$ and $P + S$ modes are found in the primary synchronisation region. However, the transition between the modes is dependent on Re . When $Re = 300$, there is a region (hatched) where the $P + S$ mode occurs in the positive C_E region.

between the oscillation and Strouhal frequencies.

Comparison of the wake mode maps in figure 4.1 with the wake mode map produced at higher Re by Williamson & Roshko (1988) (reproduced in figure 2.8) shows a major difference; the higher- Re map has the $2S$ and the $2P$ wake in the synchronisation region. Therefore, it appears that the appearance of the $P + S$ wake is dependent of the flow being two-dimensional. This conclusion is supported by the two-dimensional simulations of Blackburn & Henderson (1999) that produced a $P + S$ wake mode for $Re = 556$, where the flow would naturally be three-dimensional. As well as this, it was briefly reported in Williamson & Roshko (1988) that the $P + S$ wake replaced the $2P$ wake when $Re < 200$. It could reasonably be expected that at such low Re the flow is two-dimensional.

Examples of flow visualisation from experiments (Williamson & Govardhan, 2004) of the $2S$ and $P + S$ wakes obtained at $Re < 200$ are compared with particle tracking simulation results in figure 4.2. The close comparison shows that the $P + S$ wake is not a numerical artifact, but is in fact physical, and dependent on the flow being two-dimensional.

Also shown on the maps in figure 4.1 is a line of zero energy transfer. Energy transfer



Figure 4.2: Experimental dye visualisation from Williamson & Govardhan (2004) (top) and results from particle tracking simulations (bottom) of the $2S$ mode (left) and the $P + S$ mode (right). The comparison between the two is very close, and indicates that the $P + S$ mode in particular is physical.

was quantified by C_E , defined by

$$C_E = \int_T C_L \mathbf{V}_{cyl} d\tau \quad (4.1)$$

which was the work done on the cylinder by the fluid over one period of oscillation. Here, $C_L = F_{lift}/(0.5 * \rho U^2 D)$ is the instantaneous lift coefficient per unit length of cylinder, $\mathbf{V}_{cyl} = \mathbf{v}_{cyl}/U$ is the normalised instantaneous transverse velocity of the cylinder, and T is the period of oscillation in non-dimensional time units τ , where $\tau = tU/D$. These non-dimensional quantities are defined in terms of the instantaneous lift force, F_{lift} , the fluid density, ρ , the freestream velocity U , the cylinder diameter D , the cylinder transverse velocity \mathbf{v}_{cyl} , and time t . C_E is only constant during synchronisation when the flow is completely periodic. A fuller description of energy transfer forms the basis of the following section.

What needs to be pointed out here is the change in relation of where $C_E = 0$ and the transition from the $2S$ and $P + S$ wake. For $Re = 100$, the transition occurs well above the $C_E = 0$ contour. Therefore, only the $2S$ mode results in positive energy transfer. However, for $Re = 300$, the transition to the $P + S$ wake occurs at much lower amplitudes. In fact, there is a region of the A^* , f/f_{St} plane where a $P + S$ wake mode results in positive energy transfer. This is an interesting result. It indicates that it is theoretically possible for vortex-induced vibration to occur with a asymmetric wake mode. An unstable $P + S$ mode was found during vortex-induced vibration simulations from Singh & Mittal (2005), for $Re = 325$. However, a stable $P + S$ wake mode has never been observed, numerically or experimentally, during vortex-induced vibration. The stability results of chapter 6 indicate that the flow may also be three-dimensional for $Re = 300$, which has been shown to destroy the $P + S$ wake (Williamson & Roshko, 1988). However, it is an interesting theoretical result that an asymmetric wake can lead to positive energy transfer.

It is also clear that the transition between the $2S$ and $P + S$ modes is not dependent on C_E changing sign, or on a particular value of C_E .

4.3 Energy transfer

As well as investigating the wake modes produced, the energy transfer to the cylinder was determined throughout the synchronisation region, quantified by C_E . This quantity is an

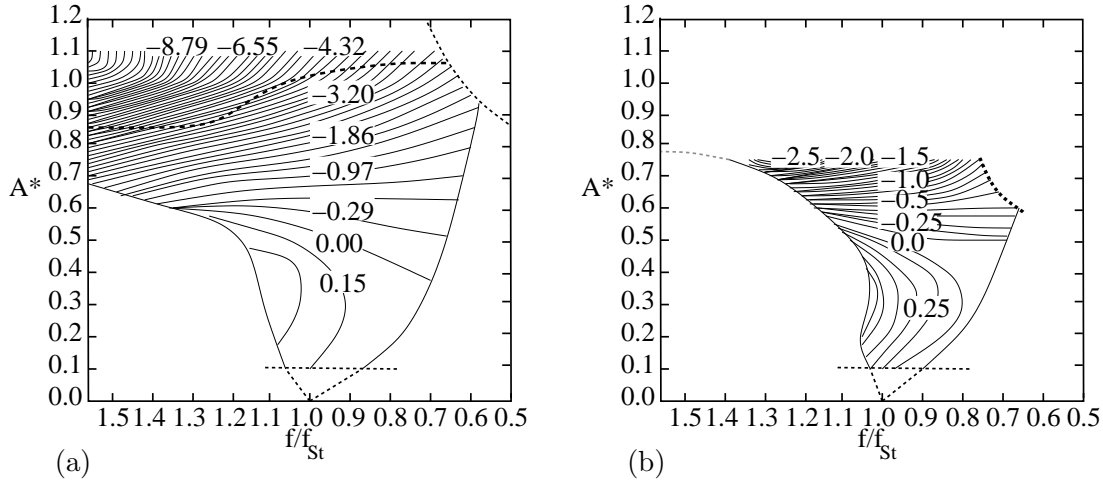


Figure 4.3: Contours of C_E in the synchronisation for (a) $Re = 100$, and (b) $Re = 200$. It is shown that for both Re , C_E is mainly dependent on the frequency of oscillation at low amplitude ($A^* \lesssim 0.35$), and is mainly dependent on amplitude at higher A^* .

important one when comparing driven oscillations with vortex-induced vibration. During vortex-induced vibration, C_E must be positive. If it is not, energy is transferred from the cylinder to the fluid, and the oscillation must die away.

C_E was mapped over the A^* , f/f_{St} plane. Again, this was done for a single Re for each map. Two of these maps, produced at $Re = 100$ and $Re = 200$ are shown in figure 4.3. Both of these maps show contours of C_E in the synchronisation region.

In both cases, the contours vary from being approximately vertical at $A^* \lesssim 0.35$, to being approximately horizontal at higher A^* . This shows that C_E is primarily determined by frequency at low amplitude, and by amplitude as the amplitude increases.

This phenomenon can be explained by the changing balance in the flow forces. In this flow, there are two major contributors to the pressure force on the cylinder; the shed vortices and the stagnation point at the front of the cylinder. As the amplitude of oscillation is increased, the stagnation point is moved further around towards the back of the cylinder, due to the increasing crossstream component of the velocity of the cylinder. This is most pronounced when the velocity is a maximum (also where the net displacement is close to zero). Additionally, as the overall relative peak velocity of the cylinder increases, the stagnation point pressure increases, as it scales with the square of the velocity of the incoming fluid relative to the cylinder. Therefore, as the amplitude of oscillation is increased, it can

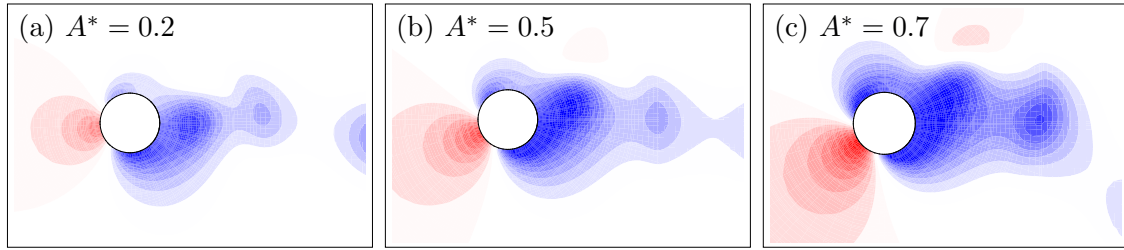


Figure 4.4: Contours of pressure for $f/f_{St} = 1.01$, $Re = 200$, and $A^* = 0.2, 0.5, 0.7$. Flow is from left to right. The amplitude A^* increases from left to right. It is clear that increasing the amplitude of oscillation increases the magnitude and the angle of action of the positive stagnation point pressure, shown here in red. Both of these facts lead it to make a larger and larger contribution to the overall lift force, where lift is the crossstream component of force.

be expected that this stagnation point pressure will come to dominate the force attributable to pressure. It should also come to dominate the overall lift force, due to the increased amplitude and the increased angle of action of the force relative to the freestream direction. Here, lift force refers to the transverse component of force.

This phenomenon is clearly demonstrated in figure 4.4. Plotted are instantaneous pressure contours $f/f_{St} = 1.01$, $Re = 200$, for values of $A^* = 0.2$, $A^* = 0.5$ and $A^* = 0.7$. It is clear that as the amplitude of oscillation is increased, the stagnation pressure region is strengthened, and moved further towards the back of the cylinder.

The angle of the stagnation point relative to the freestream is time-dependent, resulting from the oscillating vertical component of velocity due to the motion of the cylinder. Therefore, the instantaneous lift force attributable to the stagnation point pressure should oscillate in phase with the cylinder velocity. This velocity, by definition for a sinusoidal oscillation, is -90° out of phase with the cylinder displacement. Therefore, if the lift force, and therefore energy transfer, comes to be dominated by the effect of the stagnation point, the overall phase between lift force and displacement is expected to approach -90° .

This is in fact what is observed, and is demonstrated in figure 4.5. Plotted in this figure is the phase of the overall lift and the lift attributable to pressure with respect to cylinder displacement, against A^* for $f/f_{St} = 1.01$. These are referred to as ϕ and ϕ_p , respectively. It is clear that at high A^* the value of ϕ_p approaches -90° , and as a result, so does the

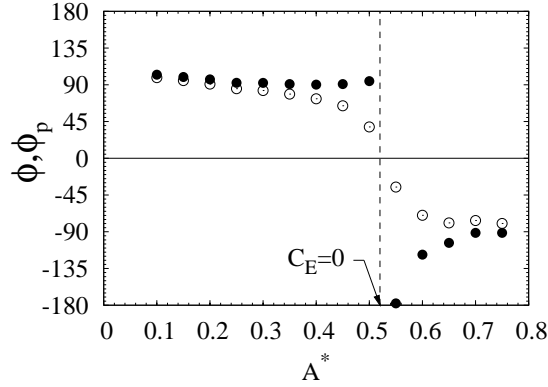


Figure 4.5: Pressure phase, ϕ_p (\bullet), and total phase, ϕ (\circ), plotted against A^* for $Re = 200$, $f/f_{St} = 1.01$. After a steep change in phase that coincides with the change in direction of energy transfer, ϕ_p approaches -90° with increasing A^* . The dominance of this term takes ϕ towards the same value. Also marked is the amplitude where $C_E = 0$, showing this occurs quite close to where the change in sign of the phase occurs.

overall phase ϕ .

Following the formulation of Carberry (2001), if it is assumed that the lift force and cylinder displacement can be modelled identically by sinusoidal functions; i.e.,

$$\begin{aligned} \frac{y_{cyl}}{D} &= A^* \cos(2\pi f^* \tau) , \\ C_L &= |C_L| \cos(2\pi f^* \tau + \phi) , \end{aligned} \quad (4.2)$$

then the integral of equation 4.1 defining C_E reduces to

$$C_E = A^* |C_L| \pi \sin(\phi) . \quad (4.3)$$

It should be noted that this equation has no direct dependence on frequency, and the effect of frequency can only be expressed as either a change in phase or a change in the magnitude of the lift force. Therefore, if the phase is fixed (as is the case for high values of A^*), then the frequency can only influence C_E through changing the magnitude of the lift force.

If it is assumed that the lift force is dominated by the stagnation pressure, it is assumed that the magnitude of the lift force is proportional to the square of the magnitude of the velocity. By differentiating the displacement function in equation 4.2, it can be shown that the magnitude of the velocity is linearly proportional to both A^* and f^* , resulting in the lift force being proportional to the square of A^* and the square of f^* . When included in

equation 4.3, this implies

$$C_E \propto A^{*3} f^{*2}, \quad (4.4)$$

showing a proportionality to the cube of A^* . This means that A^* will come to dominate C_E for higher values of A^* . The deviation of the contours in figure 4.3 could be attributed to the lift force not being purely sinusoidal at high A^* , especially with the onset of the $P + S$ wake.

4.4 Phase between lift and displacement

Due to the difficulty of directly measuring C_E during experiments, the direction of energy transfer has often been inferred from the sign of the phase between the lift force and cylinder displacement. It has been shown that if both the lift and displacement histories are assumed to be sinusoidal, that only phase angles $0^\circ < \phi \leq 180^\circ$ result in positive energy transfer (Carberry, 2001; Carberry *et al.*, 2003).

This approximation is not always true. Shown in figure 4.6 are plots of the stable periodic time histories of the lift coefficient, C_L , with cylinder displacement, y_{cyl}/D , for $Re = 200$, $f/f_{St} = 1.01$, for amplitudes $A^* = 0.2$, $A^* = 0.5$, and $A^* = 0.7$. Also shown are plots of C_L against y_{cyl}/D . Inspection of these plots shows that at low amplitudes ($A^* = 0.2$), the lift is very close to sinusoidal. However, as amplitude is increased, the lift force deviates significantly from a pure sinusoid, even though the cylinder motion is sinusoidal. This is reflected in the Lissajou figures of C_L against displacement, which deviate significantly from an ellipse, the shape generated when two sinusoidal functions of different amplitude and phase are plotted against each other.

For this Re and f/f_{St} , $C_E = 0$ at $A^* = 0.52$. Therefore, the plots in figure 4.6 at $A^* = 0.5$ are very close to the transition from positive to negative C_E . It should be noted that the magnitude of the overall lift is greatly reduced compared to that at lower amplitudes. This, along with the deviation from a pure sinusoid, indicates that there are at least two competing force components that contribute to the overall lift. Carberry *et al.* (2001) and Govardhan & Williamson (2000) have decomposed the overall lift into two components, an added mass component linked with accelerating the fluid at the cylinder surface, and a vortex component, due to the vorticity of the flow. A similar decomposition

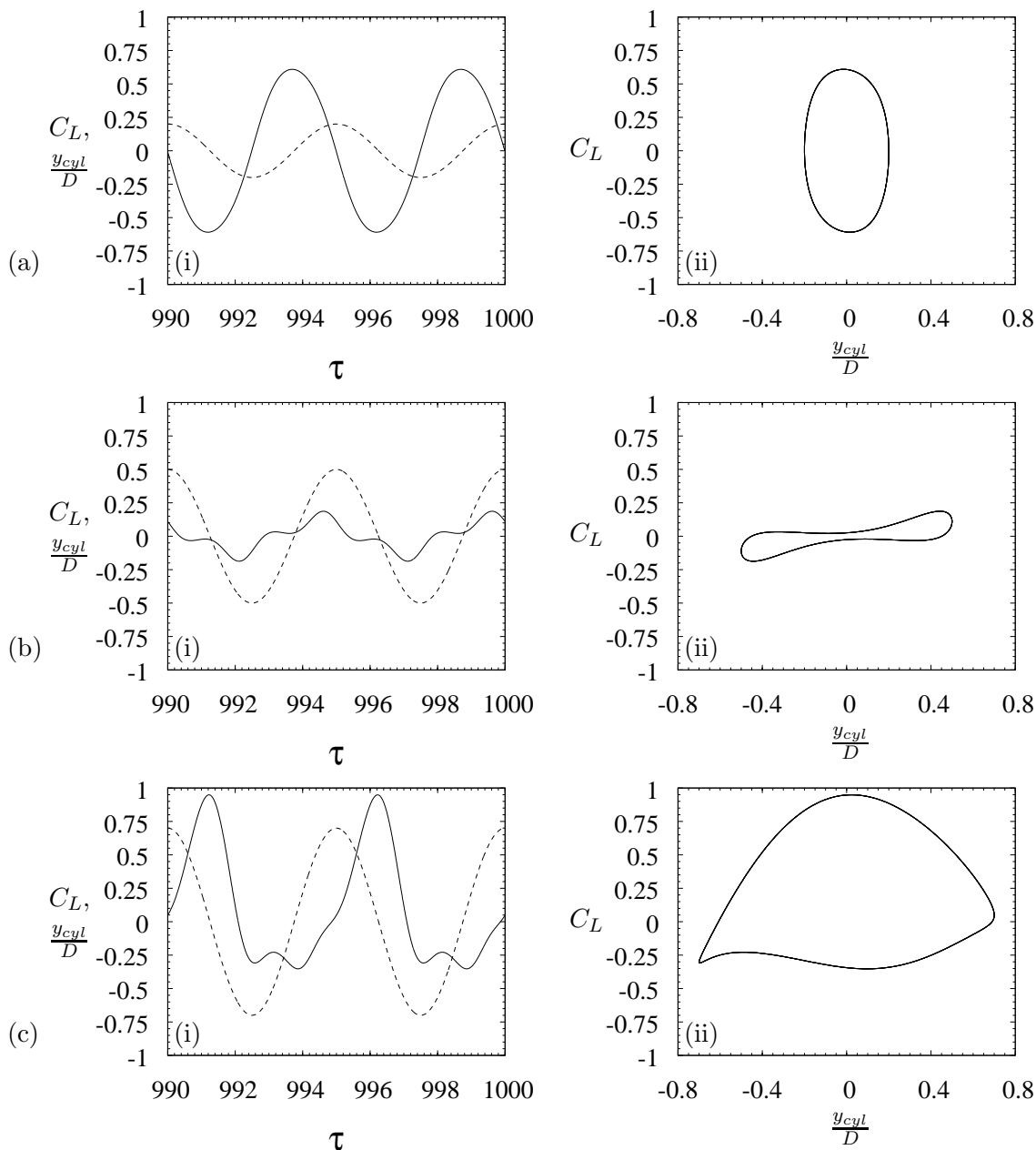


Figure 4.6: (i) Time histories of lift coefficient C_L (—) and cylinder displacement y_{cyl}/D (- - -), and (ii) Lissajou figures of C_L against displacement when $Re = 200$, $f/f_{St} = 1.01$, for (a) $A^* = 0.2$, (b) $A^* = 0.5$, and (c) $A^* = 0.7$. It is clear that increasing the amplitude of oscillation from $A^* = 0.2$ to $A^* = 0.5$ decreases the amplitude of C_L , and causes a significant deviation from a pure sinusoid. Increasing further to $A^* = 0.7$ sees transition to the $P+S$ wake, the asymmetry of which is reflected in the lift history and loss of symmetry axis in the Lissajou figure.

is performed below in section 4.5, that goes some way towards explaining this phenomena.

With a further increase in amplitude to $A^* = 0.7$, the wake undergoes a transition to the $P + S$ wake state. The asymmetry of this wake state is reflected in the non-zero mean lift in the plot in figure 4.6. The asymmetry is also represented by the loss of a symmetry axis in the Lissajou figure.

Even though the lift force is not universally sinusoidal, the transition from positive to negative energy transfer still coincides quite closely with a jump of the phase past 180° . This was shown in figure 4.5. Again, this can be somewhat explained by considering the added mass and vortex forces, the topic of the following section.

4.5 Added mass and vortex force

Carberry *et al.* (2001) showed that the total lift force could be decomposed into two components, the added mass force and the vortex force. The added mass force is attributable to the force required to accelerate the fluid at the cylinder surface from one instant to the next. It can be calculated following the formulation from Leonard & Roshko (2001), and is shown to be proportional to the potential velocity field generated by an incremental change in cylinder velocity $\Delta \mathbf{V}_{cyl}$. Expressed non-dimensionally as an added mass lift coefficient C_{L_a} , added mass force can be calculated from the relation

$$C_{L_a} = -\frac{1}{2} \frac{d\mathbf{V}_{cyl}}{d\tau} \quad (4.5)$$

where, for sinusoidal oscillation, $\frac{d\mathbf{V}_{cyl}}{d\tau}$ is defined and can be calculated analytically as

$$\frac{d\mathbf{V}_{cyl}}{d\tau} = -A^*(2\pi f^*)^2 \cos(2\pi f^* \tau). \quad (4.6)$$

As this quantity is attributable to an instantaneous potential velocity field (which is by definition irrotational), the remaining component of lift force can be thought of as being attributable to the rotation, or vorticity, of the flow. Therefore, subtracting the added mass lift from the total lift gives the vortex lift, expressed as the vortex lift coefficient, C_{L_v} .

From the definition of C_E in equation 4.1, it is shown that only the component of force in phase with the cylinder velocity contributes to the energy transfer. The definition of C_{L_a} in equation 4.5 shows that the added mass force is always in phase with the cylinder

displacement. Therefore, only the vortex force contributes to energy transfer, as it is only this force that has a component in phase with the cylinder velocity.

Because of this fact, if the vortex force can be represented by a pure sinusoid, the overall phase is only in the range $0^0 \leq \phi \leq 180^0$ when the vortex phase is such that $0^0 \leq \phi_v \leq 180^0$. Therefore, if the vortex force can be represented by a pure sinusoid, the direction of energy transfer will be determined by whether $0^0 \leq \phi_v \leq 180^0$, and therefore whether $0^0 \leq \phi \leq 180^0$.

Plotted in figure 4.7 are time histories and Lissajou figures of the vortex force when $Re = 200$, $f/f_{St} = 1.01$, for values of $A^* = 0.2$, $A^* = 0.5$, and $A^* = 0.7$.

Concentrating on the plots for $A^* = 0.5$, it is shown that there still appears to be at least two contributing factors to the vortex lift. The evidence of this is the deviation of the vortex lift from a pure sinusoid, with what appears to be a second component of twice the primary frequency occurring. This is thought to be due to two components of the same frequency, but of different phases, being superpositioned. This two-component behaviour may be the beginning of the mechanism that eventually leads to vortex splitting in the $P + S$ wake, as it is clear from the plot for $A^* = 0.7$ that there is a similar “bump” in the time trace that corresponds to the formation of two vortices per half cycle on one side of the wake.

The plots in figure 4.7 indicate that the vortex force magnitude has some dependence on A^* . This is shown explicitly in figure 4.8. Plotted is the peak magnitude of the periodic vortex lift coefficient, along with the total lift coefficient, against A^* for $Re = 200$ and $f/f_{St} = 1.01$. Also plotted is the overall phase and the vortex force phase against A^* for the same conditions. The phase angles were approximated for the non-sinusoidal waveforms by calculating the peak of the cross-correlation function between the lift force and displacement.

Comparison of the two plots in figure 4.8 show that when the total lift force coefficient is a minimum (close to $A^* = 0.55$), ϕ_v is close to 180^0 . This is to be expected, as it is the vector addition of the added mass and vortex force that leads to the total lift force. As C_{L_v} and C_{L_a} act in opposite directions when $\phi_v = 180^0$, they effectively cancel each other out, leading to a very small overall lift force coefficient.

Comparing figure 4.8b with figure 4.3 shows that the variation in ϕ_v with A^* starts to

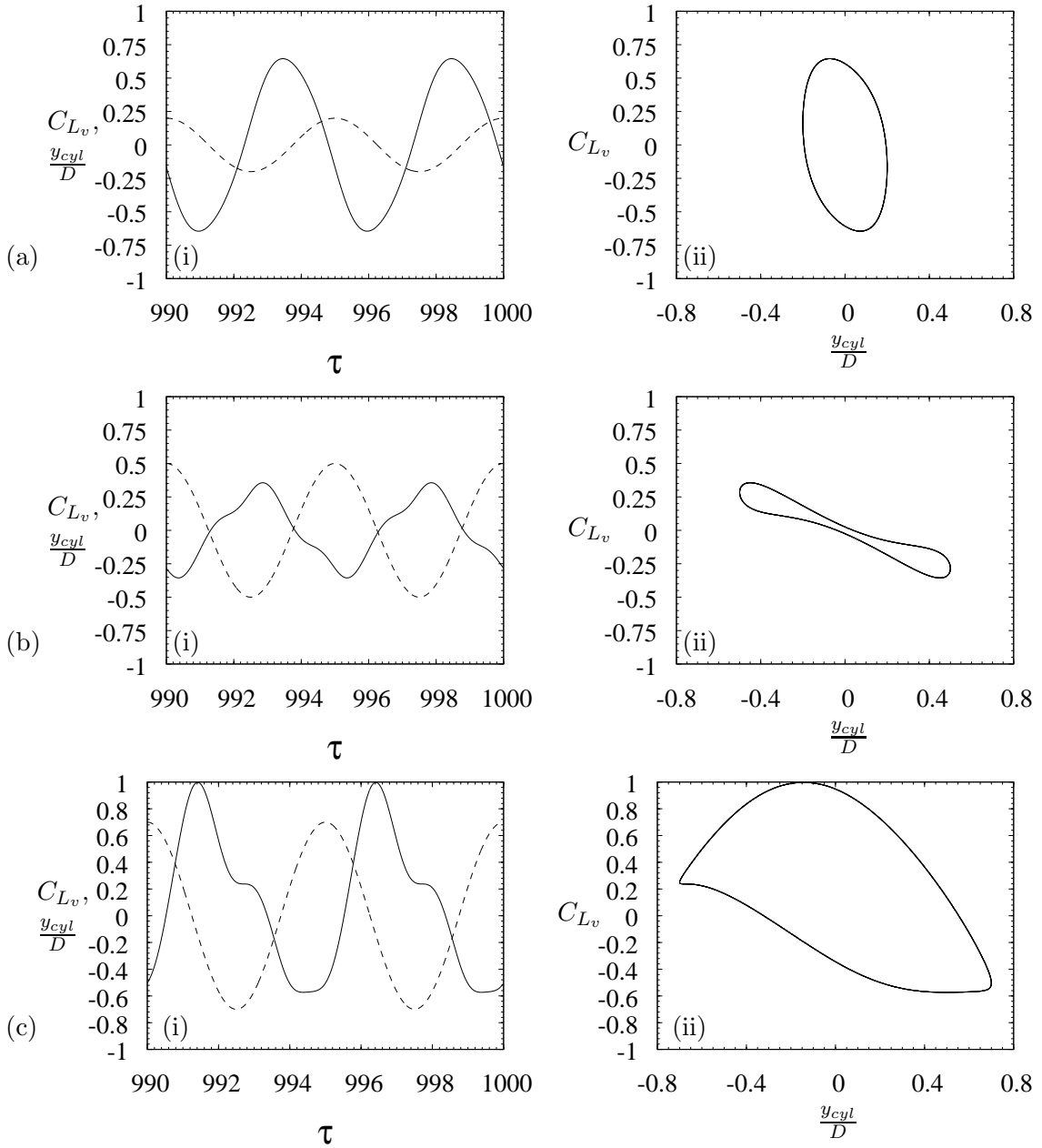


Figure 4.7: (i) Time histories of vortex lift coefficient C_{L_v} (—) and cylinder displacement y_{cyl}/D (---) and (ii) vortex lift C_{L_v} against cylinder displacement y_{cyl}/D , when $Re = 200$, $f/f_{St} = 1.01$, for (a) $A^* = 0.2$, (b) $A^* = 0.5$, and (c) $A^* = 0.7$. The vortex lift still deviates from a pure sinusoid. The deviation may be the genesis of the mechanism that eventually leads to the $P + S$ wake at higher A^* .

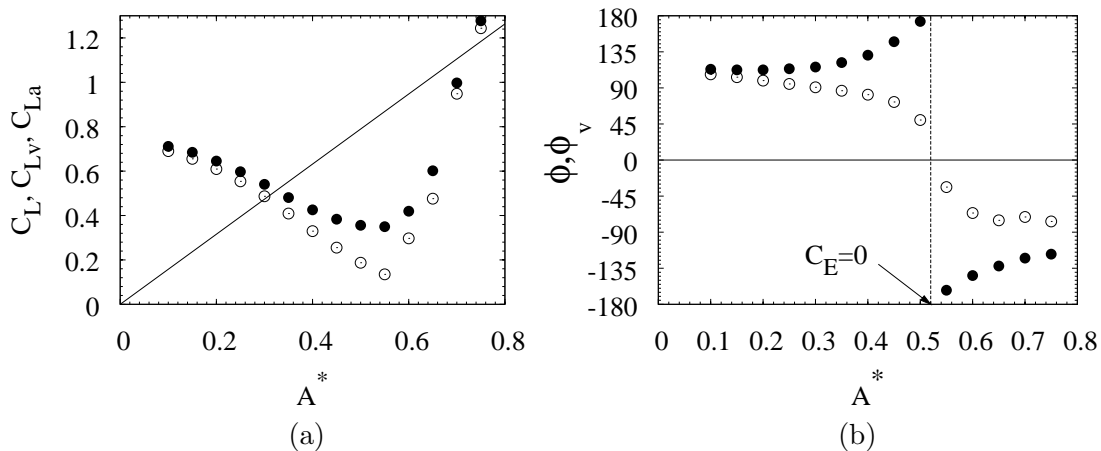


Figure 4.8: (a) Magnitude of the overall lift coefficient C_L (\circ), vortex lift coefficient C_{L_v} (\bullet), and the added mass lift coefficient C_{L_a} (—) against A^* for $Re = 200$, $f/f_{St} = 1.01$. (b) Total phase ϕ (\circ) and vortex phase ϕ_v (\bullet) for the same conditions. Comparison of the two plots shows that when the overall force is at its minimum, the vortex phase is close to 180° , and the vector addition of the vortex and added mass force effectively cancel each other.

increase at approximately the same amplitude of oscillation as that at which C_E begins to show a dependence on A^* . It also shows that the “jump” in ϕ , where ϕ_v reaches 180° , coincides very closely with where $C_E = 0$. What should be noted is that at this point, ϕ_v varies quite smoothly. This implies that C_E can change from positive to negative with only a very slight variation in wake configuration.

This is confirmed by the vorticity contour plots shown in figure 4.9 and 4.10. In figure 4.9, f/f_{St} was held constant at $f/f_{St} = 1.01$, and in figure 4.10, A^* was held constant at $A^* = 0.5$. These figures show the wake as amplitude, and then frequency, are slowly varied across the $C_E = 0$ boundary. In both cases, it is clear that as the $C_E = 0$ boundary is crossed (at $A^* \simeq 0.52$ in the case of amplitude variation, and at $f/f_{St} \simeq 0.95$ in the case of frequency variation) the wake configuration on either side is very similar. This further confirms the findings of section 4.2 that the change in sign of C_E is not linked to a change in wake configuration.

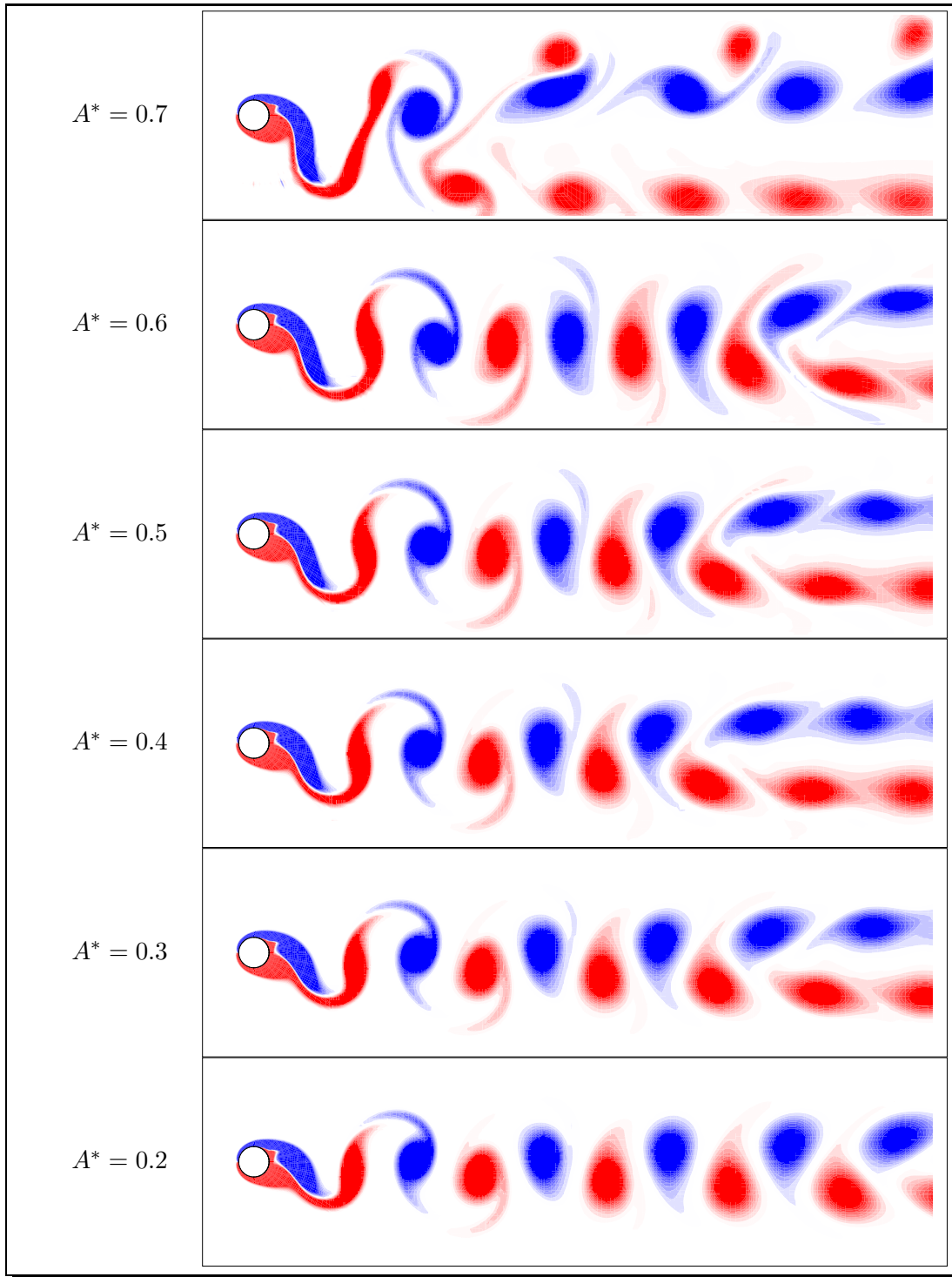


Figure 4.9: Variation of the wake with increasing A^* for $Re = 200$, $f/f_{St} = 1.01$. Images span the range $0.2 \leq A^* \leq 0.7$ in increments of $\Delta A^* = 0.1$, increasing up the page. Even though $C_E = 0$ is traversed at $A^* = 0.52$, the images at $A^* = 0.5$ and $A^* = 0.6$ appear very similar.

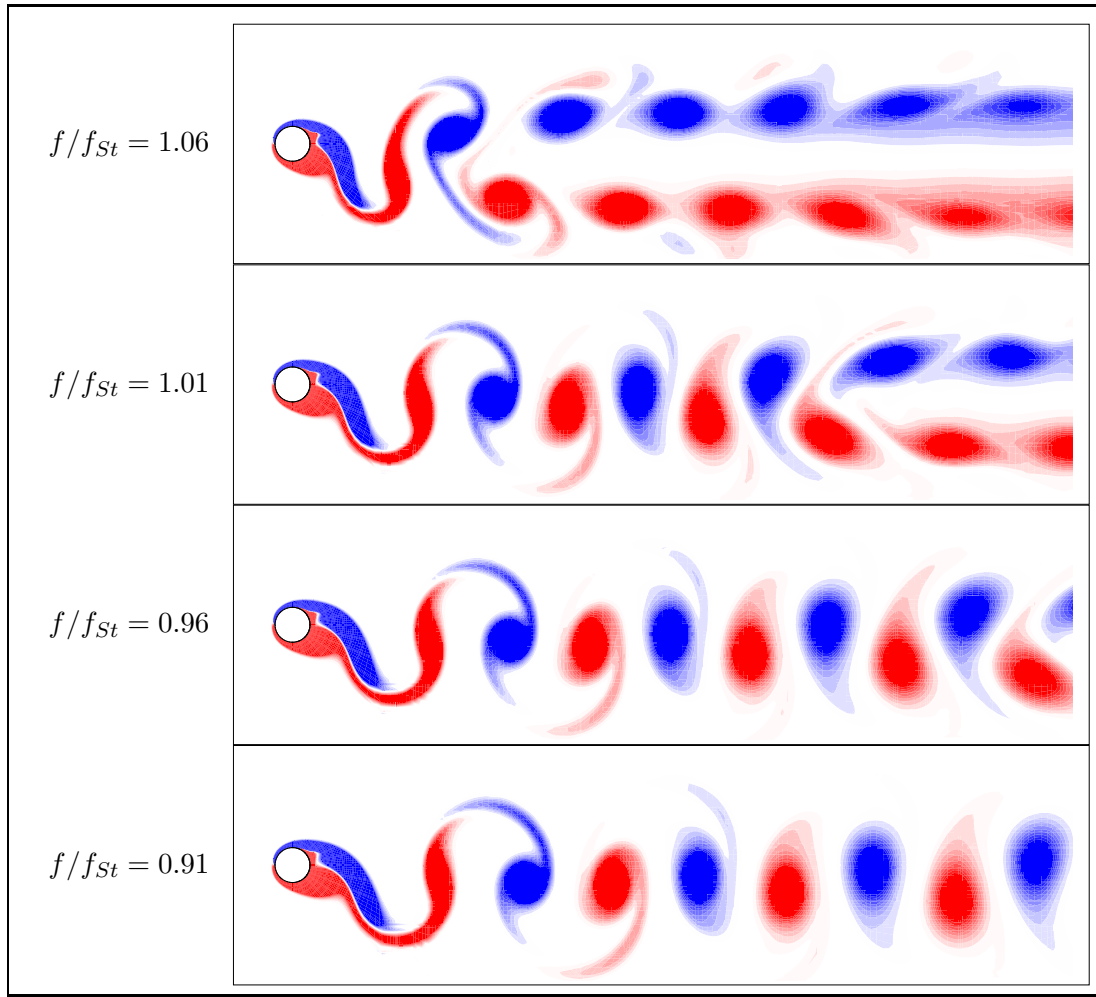


Figure 4.10: Variation of the wake with increasing f/f_{St} for $Re = 200$, $A^* = 0.5$. Images are for $f/f_{St} = 0.91, 0.96, 1.01, 1.06$, increasing up the page. Even though $C_E = 0$ is traversed at $f/f_{St} = 0.95$, no significant change is seen in the near wake over the first three images.

4.6 Explicit dependence on Reynolds number

As the wake mode and energy transfer maps produced for the previous sections were all produced for a single value of Re in the A^* , f/f_{St} plane, a direct comparison between maps at different Re could be made. The main parameters of interest to compare for a dependence on Re were the synchronisation boundaries, the contour of $C_E = 0$, and the transition point from the $2S$ to the $P + S$ wake mode. Shown in figure 4.11 are three plots comparing these three parameters over the range $50 \leq Re \leq 300$.

It is shown that the synchronisation region is narrowed with increasing Re . While the boundary defining the lower limit of f/f_{St} is almost fixed, increasing Re has a profound impact upon the upper f/f_{St} limit. At $Re = 50$, synchronisation is held almost indefinitely for $f/f_{St} > 1$ when $A^* > 0.2$. It is perhaps not surprising that the wake is so receptive to an external frequency at this Re , as it is only slightly above the Re for the transition to vortex shedding from a fixed cylinder of $Re = 46.7$ (Le Gal *et al.*, 2001).

Increasing to $Re = 100$ sees this upper f/f_{St} limit significantly reduced, and further increases in Re continue to lower the synchronisation limit. Also, from a lower limit of $Re = 200$, a range of A^* is found where increasing A^* actually decreases the upper limit of f/f_{St} for synchronisation. This appears as the deficit “bump” in the upper f/f_{St} limit synchronisation boundary for $Re = 200$ and $Re = 300$ in figure 4.11a.

Figure 4.11b shows that while there is some dependence on Re for the exact position of the $C_E = 0$ contour, the upper value of A^* for this contour remains essentially fixed at $A^* \simeq 0.6$. This has some important consequences when considering vortex-induced vibration. For vortex-induced vibration to occur, C_E must be positive.

The finding here predicts that, regardless of Re , two-dimensional vortex-induced vibration will not occur with amplitudes $A^* > 0.6$. This prediction relies on the assumption that vortex-induced vibration occurs with a sinusoidal displacement history. This prediction agrees with the low- Re experimental results of Anagnostopoulos & Bearman (1992), and the simulations of Blackburn & Henderson (1996) and those included in the results presented in the “Griffin” plot in Williamson & Govardhan (2004). However, this limit can be exceeded if the oscillation during vortex-induced vibration is not sinusoidal, as is demonstrated in chapter 5 of this thesis.

As previously commented on in section 4.2, increasing Re has the effect of lowering the

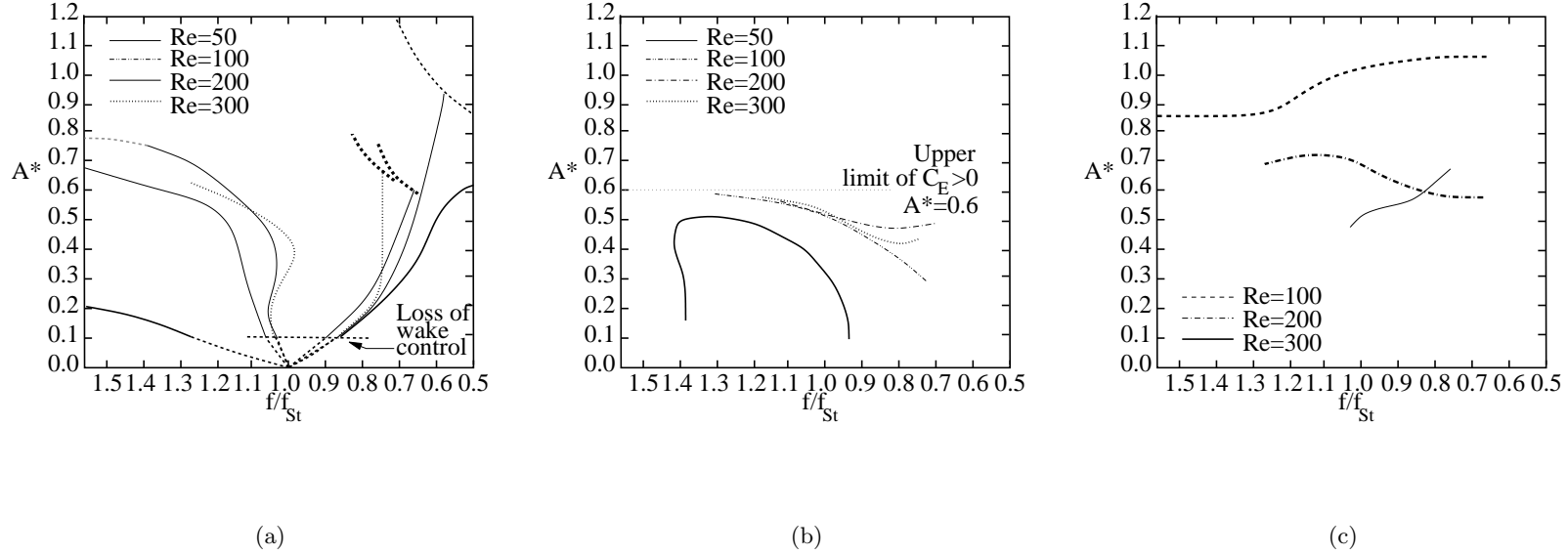


Figure 4.11: The dependence on Re is shown explicitly by comparing results compiled over the range $50 \leq Re \leq 300$. (a) Synchronisation boundaries. The dotted lines emanating from $f/f_{St} = 1$ indicate that the curves have been extrapolated, as the wake is not controlled and truly synchronised for these low values of A^* . The dotted lines in the upper right-hand corner indicate the loss of synchronisation to the primary frequency. The synchronisation region is shown to narrow with increasing Re . (b) Contours of $C_E = 0$. The upper limit of A^* for positive C_E is relatively fixed at ~ 0.6 . (c) Transition boundaries from the $2S$ to $P + S$ wake mode. The value of A^* for the $2S$ to $P + S$ transition is significantly reduced with increasing Re .

value of A^* at which the transition from the $2S$ to $P + S$ wake state occurs. This is shown in figure 4.11c. The reason for the reversal in the direction of frequency dependence at $Re = 200$ is not clear at this stage.

4.7 Sinusoidal oscillation summary

It has been shown that the general map of wake modes during sinusoidal driven oscillation of a circular cylinder in two-dimensional flow consists of two modes in the synchronisation region. These modes are the $2S$ mode, and the $P + S$ mode, and the latter always occurs at higher amplitudes than the $2S$ mode. For any value of Re , the $P + S$ mode occurs at higher A^* than the $2S$ mode for a given frequency of oscillation. However, the exact value of A^* that this transition occurs at is dependent on Re , with the value of A^* for the transition between the two modes decreasing with increasing Re .

With regard to energy transfer, it has been shown that the value of C_E is primarily dependent on frequency at low amplitudes ($A^* < 0.35$), while it is primarily dependent on amplitude at higher A^* . This is explained by the fact that at high amplitudes, the lift force is dominated by the force attributable to the stagnation point at the front of the cylinder. Energy transfer is primarily governed by the lift force and amplitude of oscillation. This results in a quadratic dependence on f/f_{St} , but a cubic dependence on A^* , resulting in A^* dominating at high amplitudes. It was found that the upper value of A^* for positive C_E remained fixed at $A^* \simeq 0.6$, regardless of Re .

As the sign of energy transfer was found to be relatively insensitive to Re , the transition between the wake modes was not. It can therefore be concluded that the value of C_E is not linked in any intrinsic way to the wake mode produced. Further, not even the sign of C_E is important, as a region of the parameter space was found for $Re = 300$ where the $P + S$ mode produced positive energy transfer.

The sign of the phase between the lift force and cylinder displacement (when the phase is expressed over the range $-180 < \phi \leq 180$) has often been linked to the sign of energy transfer. It was found that this phase underwent a change in sign that coincided quite closely with the change in sign of C_E .

Decomposing the lift force into added mass and vortex components shows that the sign

of the phase between the total lift force and cylinder displacement, ϕ , is dependent on the sign of the phase between the vortex lift and cylinder displacement, ϕ_v , if the vortex lift force is assumed to be sinusoidal. It was shown that the vortex lift force is not exactly sinusoidal in time when C_E changes sign, but the deviation from a pure sinusoid is not great. It therefore seems reasonable to conclude that the sign of C_E follows the sign of this phase, ϕ_v , and therefore the sign of ϕ .

It was also shown that when ϕ_v changes sign, it does so as part of a continuous, smooth change in the value of ϕ_v . This, and images of vorticity contours of the wake, are further evidence that C_E can change sign without a significant change in wake configuration.

Finally, the synchronisation boundaries, C_E and the transition between wake modes have been explicitly compared across a range of Re . In all cases, a dependence on Re was found, although the dependence does not affect the upper limit of A^* for positive C_E , which seems to be a dimensional effect. Therefore, the results presented here support the first hypothesis of this thesis, that a dependence on Re exists for the response of the wake during driven sinusoidal oscillation of a circular cylinder.

CHAPTER 5

VORTEX-INDUCED VIBRATION OF AN ELASTICALLY-MOUNTED CYLINDER

5.1 Introduction

Since the results of Feng (1968), much work has been done in the field of vortex-induced vibration in classifying different response regimes, and identifying and explaining the differences between these regimes. The state of knowledge, at the present time, is basically as follows.

For high- m^* cylinders, two “branches” of response exist. The term “branch” is slightly confusing here. It effectively means a regime of response over a particular range of reduced velocity $U^* = U/f_N D$, rather than a possible solution, which is the meaning the term “branch” takes on in bifurcation theory. For the reduced velocity, U is the freestream velocity, f_N is the natural frequency in fluid, and D is the cylinder diameter. For consistency with the literature, the term “branch” will be applied here to mean a response regime. The two branches in high- m^* vortex-induced vibration have been termed the initial and lower branch (Khalak & Williamson, 1996). The transition between these two branches has been shown to be hysteretic (Feng, 1968).

For low- m^* cylinders, a third branch emerges between the initial and lower branches. This is the upper branch (Khalak & Williamson, 1996), so-called because it consists of very high peak amplitudes of displacement. Plots of peak amplitude against U^* for both high-

and low- m^* cylinders were shown in figure 2.10.

However, it has been proposed that the upper branch does not emerge when the flow is two-dimensional, either through imposition or by virtue of a low Re (Williamson & Govardhan, 2004). This conclusion was reached from the inspection of Griffin plots (see those reproduced in figure 2.9) where laminar vortex-induced vibration settles to a maximum peak amplitude of $A_{max}^* \simeq 0.6$, whereas higher- Re flow can achieve amplitudes as high as $A_{max}^* \simeq 1.4$, where $A_{max}^* = y_{max}/D$, and y_{max} is the peak amplitude of displacement of the cylinder.

Considering the nature of the response, Hover *et al.* (1998, 2004) have shown experimental evidence that the wake and cylinder response on the upper branch is highly disordered. The fully three-dimensional simulations of Lucor *et al.* (2005) also show that a single wake configuration does not persist along the span of the cylinder, and there is little order in the organisation of the near wake. It therefore appears that the upper branch is not simply a high- A^* periodic mode, but that it is quite possibly a chaotic regime of response. Two-dimensional simulations from Blackburn & Henderson (1996) showed evidence of the existence of a similarly chaotic regime.

Therefore, it is hypothesised here that a chaotic regime of flow exists in two-dimensional flow, and that it has characteristics similar to the upper branch in higher- Re vortex-induced vibration. Evidence for this branch is shown in numerous parameters, and it is also clearly distinguished from the quasiperiodic initial branch, over a range of mass ratios $1 \leq m^* \leq 10$, for a Reynolds number $Re = 200$. Here, $m^* = 4m/\pi D^2 \rho$, where m is the mass of the cylinder per unit length, D is the cylinder diameter and ρ is the fluid density. For this chapter, the response is considered chaotic when it consists of at least three non-conformant frequencies, and appears to be bounded, but non-repetitive (Seydel, 1994).

Following from this, it is shown that the use of purely sinusoidal oscillation to model vortex-induced vibration in this chaotic branch is inadequate. However, modulating the oscillation amplitude leads to an improvement, especially in the prediction of peak lift forces. Sinusoidal oscillations, while not always an exact representation of vortex-induced vibration, do seem adequate in modelling vortex-induced vibration when the flow is completely periodic in the lower branch.

5.2 The existence of three response regimes

5.2.1 An overview

Traditionally, the parameter that has been used to identify branches during vortex-induced vibration has been the peak amplitude of displacement, $A_{max}^* = y_{max}/D$, where y_{max} is the magnitude of the largest displacement reached. On the upper branch, A_{max}^* can reach values up to 1.4 (Williamson & Govardhan, 2004). When A_{max}^* is plotted against U^* , this small regime of high- A_{max}^* response is quite clear, as was shown in figure 2.10.

Using A_{max}^* as a sole indicator, no upper branch is detected in the simulation results presented here at $Re = 200$, for any mass ratio. To achieve the highest possible amplitudes, the damping ratio for the simulations was kept low, and set at $\zeta = 0.01$, where $\zeta = c/c_{crit}$, c is the damping coefficient per unit length of the cylinder, and c_{crit} is the critical damping coefficient. Simulations were then conducted across a range of U^* for three different mass ratios, $m^* = 1$, $m^* = 5$ and $m^* = 10$.

A_{max}^* is plotted against U^* for these mass ratios in figures 5.1a(i), 5.1b(i) and 5.1c(i), respectively. All three show a single contiguous branch of high A_{max}^* , that slowly decreases with increasing U^* .

However, this does not mean that there is only one branch present in the two-dimensional flow. It is simply that the two branches are not delineated by their peak amplitudes, and other response parameters need to be considered. Figures 5.1a(ii), 5.1b(ii) and 5.1c(ii) show peak lift coefficient $C_{L_{max}}$ against U^* for the three mass ratios tested. Here, $C_{L_{max}} = F_{lift_{max}}/0.5\rho U^2 D$, where $F_{lift_{max}}$ is the peak lift force (the force transverse to the flow direction). It shows that there is a range of U^* , highlighted by the hatched and shaded boxes in each plot, where $C_{L_{max}}$ is significantly higher than for outside this range. There is also a relatively sudden drop in $C_{L_{max}}$ as U^* is increased beyond this regime. This change in $C_{L_{max}}$ indicates that while the peak amplitude may vary only slightly, there is a change in the nature of the flow, indicating the presence of two separate regimes.

In fact, three distinct regimes can be identified. With increasing U^* , the first regime is the quasiperiodic regime, and is indicated in figures 5.1a, b, and c by the narrow hatched box. This regime is characterised by moderate peak amplitudes, and by the fact that it is quasiperiodic, with contributions from only the Strouhal frequency for a fixed cylinder,

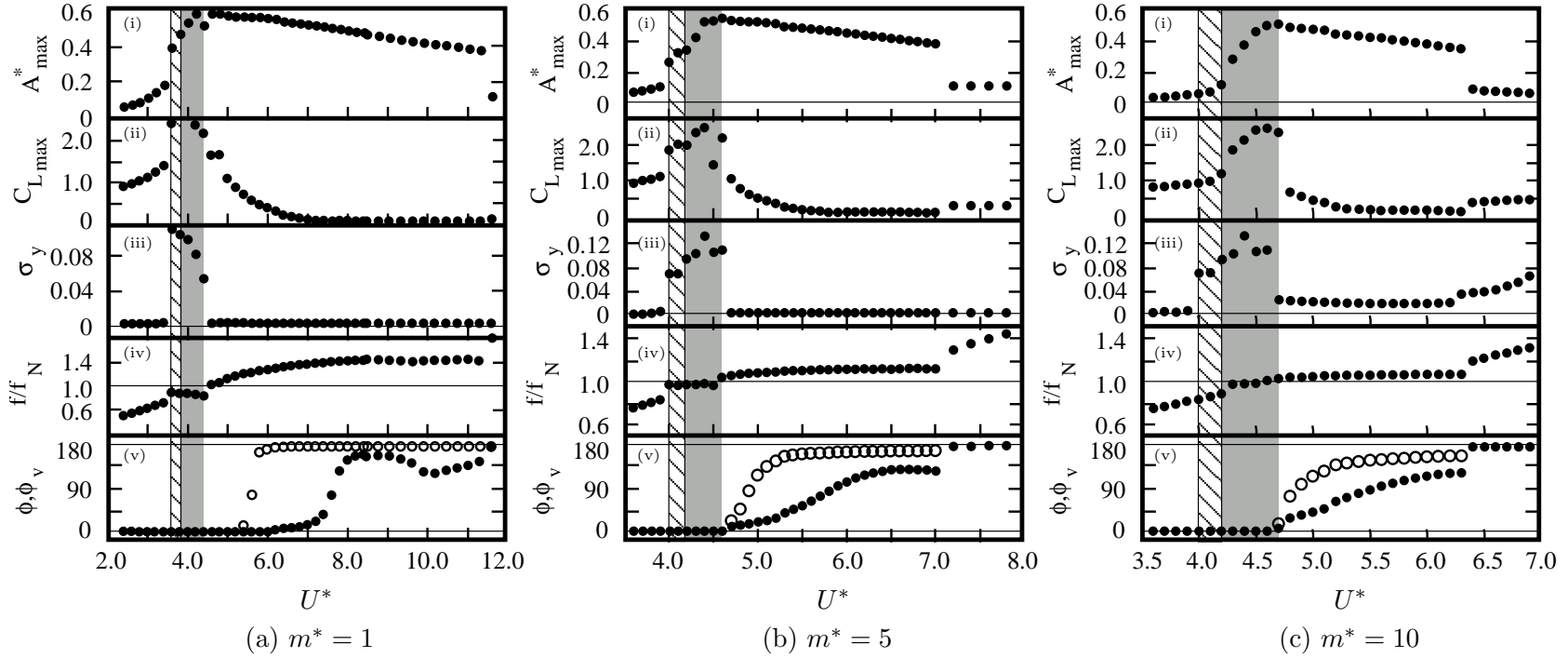


Figure 5.1: Wake and cylinder response as a function of U^* when $Re = 200$ for: (a) $m^* = 1$; (b) $m^* = 5$; (c) $m^* = 10$. The wake response is characterised in terms of: (i) A_{max}^* , the peak amplitude response; (ii) $C_{L,max}$, the peak lift coefficient; (iii) σ_y , the standard deviation of the amplitude response envelope; (iv) f/f_N , the ratio of the primary frequency response to the cylinder natural frequency; and (v) ϕ (\bullet), and ϕ_v (\circ), the phase lag between the overall and vortex lift force and cylinder displacement. All except the peak amplitude show evidence of the quasiperiodic, chaotic, and periodic regimes, regardless of mass ratio. The quasiperiodic regime is highlighted by the hatched box, and the chaotic regime by the grey box. Increasing the mass ratio has the effect of moving the U^* range of the quasiperiodic and chaotic regimes to higher values.

and a frequency close to the natural frequency of the cylinder.

Second, there is the chaotic regime. This regime has been defined as where the flow is non-periodic, and the amplitude modulation is more complicated than purely sinusoidal. At least three non-conformant frequencies are present in the cylinder response in this regime. It is in this regime that the largest peak amplitudes of oscillation occur.

Third, there is the periodic regime. Here, the cylinder oscillation and the wake are fully synchronised, generally to a frequency slightly higher than the cylinder natural frequency. The oscillations of the cylinder in this regime are essentially sinusoidal, with no secondary frequencies. A fuller picture of all of these regimes will be presented over the remainder of this chapter.

From the above discussion, it is obvious that the regimes are not only defined by $C_{L_{max}}$. Other parameters show distinct changes in behaviour, particularly with transition between the chaotic and periodic regime. Plotted in figure 5.1a(iii), 5.1b(iii) and 5.1c(iii) is σ_y against U^* , where σ_y is the standard deviation of the amplitude envelope of the cylinder displacement. The amplitude envelope was obtained using a Hilbert transform (Khalak & Williamson, 1999). High values of σ_y indicate a high level of variation over time of the cylinder displacement amplitude. As expected, σ_y deviates from zero in the quasiperiodic regime, and is often at its highest value in the chaotic regime. With transition to the periodic regime, it is seen to drop back to practically zero, as is expected for purely sinusoidal oscillation with constant amplitude.

Two other parameters that are important in characterising any oscillation are the frequency of oscillation, and the phase (or lag) between the lift force and displacement (a discussion of phase for signals that are not purely sinusoidal was given in chapter 4). Both the frequency and phase are addressed in figure 5.1.

Figure 5.1a(iv), 5.1b(iv) and 5.1c(iv) show the ratio of the primary frequency of response to the natural frequency, f/f_N , plotted against U^* . The primary frequency of response was found by taking the fast Fourier transform (FFT) of the cylinder displacement data and calculating the magnitude of the power spectral density for each frequency. The frequency with the largest power spectral density was determined to be the primary frequency, f . These plots show that with the beginning of the quasiperiodic regime, the primary frequency is shifted from the Strouhal frequency for a fixed cylinder, to a frequency close to, but

less than, the natural frequency of the cylinder. The effect is most pronounced in figure 5.1c(iv), for $m^* = 1$. By the end of the chaotic regime, the primary frequency is shown to be substantially less than the natural frequency. Transition to the fully synchronised periodic regime sees a distinct jump in the primary frequency.

For the highest mass ratio tested, $m^* = 10$, f/f_N quickly asymptotes to a constant value only slightly above unity. However, as the mass ratio is lowered, the value to which f/f_N asymptotes in the periodic regime increases. Interestingly, for all the values of m^* tested, if f was non-dimensionalised by the natural frequency *in vacuo*, $f_{N_{vac}}$, the value approached was $f/f_{N_{vac}} \simeq 1$. This implies that the fluid added mass is close to zero in this periodic regime. This is a deviation from the result for three-dimensional flow of a fluid added mass of close to -0.6 throughout the lower branch (Govardhan & Williamson, 2000) for similar mass ratios to those tested here.

Figure 5.1a(v), 5.1b(v) and 5.1c(v) show ϕ , the phase lag between the total lift and cylinder displacement, and ϕ_v , the phase lag between the vortex lift and cylinder displacement, plotted against U^* . It should be noted that throughout the chaotic regime, the phase could vary considerably over time. Therefore, the values presented in figure 5.1 should be treated as the average value of phase over time.

For all mass ratios, both ϕ and ϕ_v are shown to be approximately zero throughout the quasiperiodic and chaotic regime. Over the periodic regime, ϕ is observed to initially slowly increase from close to zero at the start of the branch, then more quickly increase over the middle of the branch, and finally asymptote towards a value approaching 180° at the end of the branch. The variation in the rate of change of ϕ with respect to U^* shows some dependence on m^* . For $m^* = 1$, the initial rate is quite low, whereas the rate in the middle of the branch is very high, with ϕ appearing to “jump” from 0° to 180° at $U^* = 7.5$. For $m^* = 5$, the jump is not as severe, with the plot of ϕ tracing out a smooth “S”-shape curve. Further increasing to $m^* = 10$ sees nearly all evidence of the jump disappear, and ϕ climbs approximately linearly over the range of U^* of the periodic regime.

This behaviour differs from that observed with transition to the lower branch in higher-*Re* three-dimensional flow. During such experiments, the phase is observed to jump suddenly from $\sim 0^\circ$ to $\sim 180^\circ$ at the transition. Also, it has been shown by previous research that the vortex phase, ϕ_v , undergoes a similar jump at the beginning of the upper branch,

while the total phase ϕ remains close to zero (Govardhan & Williamson, 2000). During the simulations conducted for this thesis, the average vortex phase (as presented in figure 5.1) was not observed to deviate from zero throughout the chaotic and quasiperiodic regimes. Following the treatment in chapter 4, vortex force was resolved by subtracting the added mass lift from the total lift (Leonard & Roshko, 2001). As the added mass force relies on the cylinder acceleration, a central-difference method was used to calculate cylinder acceleration from a time history of cylinder velocity.

For the two higher mass ratios, $m^* = 5$ and $m^* = 10$, ϕ_v appears to be another parameter that signifies the transition between the chaotic and periodic regimes. In both of these cases, ϕ_v is approximately zero throughout the chaotic regime, before suddenly beginning to increase at the transition, and quickly asymptoting towards a value close to 180° as U^* is increased. However, this behaviour is not carried over to the lowest mass ratio tested, $m^* = 1$. In this case, the sudden increase in ϕ_v does not occur until a value of U^* slightly higher than that for the chaotic-periodic transition.

To further evaluate the nature of the three response regimes (quasiperiodic, chaotic, and periodic), three values of U^* for $m^* = 1$ have been investigated in some detail. These values are $U^* = 3.6$, $U^* = 4.4$ and $U^* = 5.0$, each falling in one response regime as defined in figure 5.1a. The results of this investigation are presented in the following section.

5.2.2 Time history of cylinder response

The delineation of three separate regimes is clear on inspection of the time history of the cylinder displacement at values of U^* in each. Examples of these regimes are presented in figure 5.2. Plotted are the time histories of cylinder displacement for $U^* = 3.6$, $U^* = 4.4$ and $U^* = 5.0$. These fall in the quasi-periodic, chaotic and periodic regimes, respectively.

Figure 5.2a shows that the response for $U^* = 3.6$ is quasiperiodic, with the amplitude of oscillation simply being modulated over time. In general, this beating was the product of an interaction between the Strouhal frequency for a fixed cylinder, and a frequency close to the cylinder natural frequency.

The relatively simple behaviour observed in the quasiperiodic regime is destroyed in the chaotic regime, as is indicated by figure 5.2b for $U^* = 4.4$. More and more frequencies begin to become apparent in the response, resulting in oscillation that is close to, but not

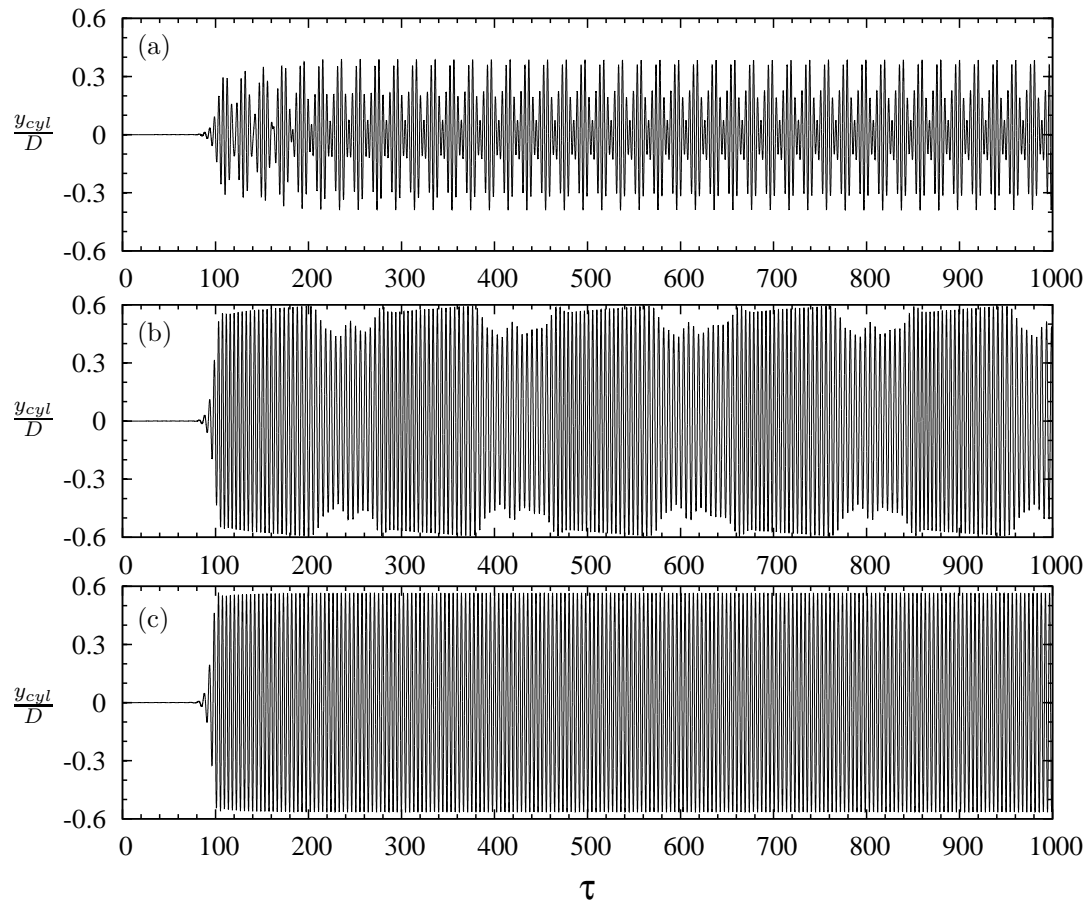


Figure 5.2: Time history of cylinder displacement when $Re = 200$, $m^* = 1$ for: (a) $U^* = 3.6$; (b) $U^* = 4.4$; (c) $U^* = 5.0$. The simple beating of the quasiperiodic regime is clear in (a), and has descended into a much more complicated and chaotic pattern in (b). This is in contrast to the constant-amplitude periodicity in (c).

quite, repetitive. The amplitude of oscillation varies considerably over time, and the flow at times can become quite disordered.

With transition to the periodic regime, the variation in amplitude over time vanishes, and the cylinder response reverts to an essentially sinusoidal periodic oscillation over time. All extra frequency content disappears, and the flow takes on a steady configuration.

5.2.3 Spectra of cylinder response

This difference in behaviour is also clear from inspection of frequency spectra of the cylinder response in each regime. The spectra for the time histories presented in figure 5.2 are shown in figure 5.3. These spectra were formed using a fast Fourier transform (FFT), and then calculating the power spectral density for each frequency component. The results are presented in terms of non-dimensional frequency, $f^* = fD/U$, where f is the response frequency of interest, and P_f , which is the power spectral density normalised by the maximum power spectral density of the given signal. In terms of this non-dimensional frequency, the FFT was calculated from data with a sample frequency of $f^* = 100$, resulting in a Nyquist frequency of $f^* = 50$. This was well above any frequency that contributed to the response, and as such the spectra presented in figure 5.3 have been truncated to focus on the bandwidth where significant frequency response occurred.

The spectrum presented in figure 5.3a is typical of the response in the quasiperiodic regime. It shows that the response in this regime consists of only two frequencies. These frequencies are the Strouhal frequency for a fixed cylinder, expressed as the Strouhal number, St , and a second frequency close to, but slightly below the cylinder natural frequency, f_N . The natural frequency has been non-dimensionalised in the same manner as the system response frequency, such that $f_N^* = f_N D/U$, or $1/U^*$.

Figure 5.3b shows that in the chaotic regime, the response contains components at many frequencies, even though the bandwidth occupied by these frequencies is quite narrow, and is grouped around the Strouhal and natural frequencies. The primary frequency of response during the chaotic regime can be shifted significantly below the cylinder natural frequency, as is apparent in figure 5.3b. This shifting effect becomes more pronounced as the cylinder mass ratio is lowered, as can be deduced from the plots of primary frequency against U^* in figure 5.1. The frequencies present in the spectrum with significant power spectral

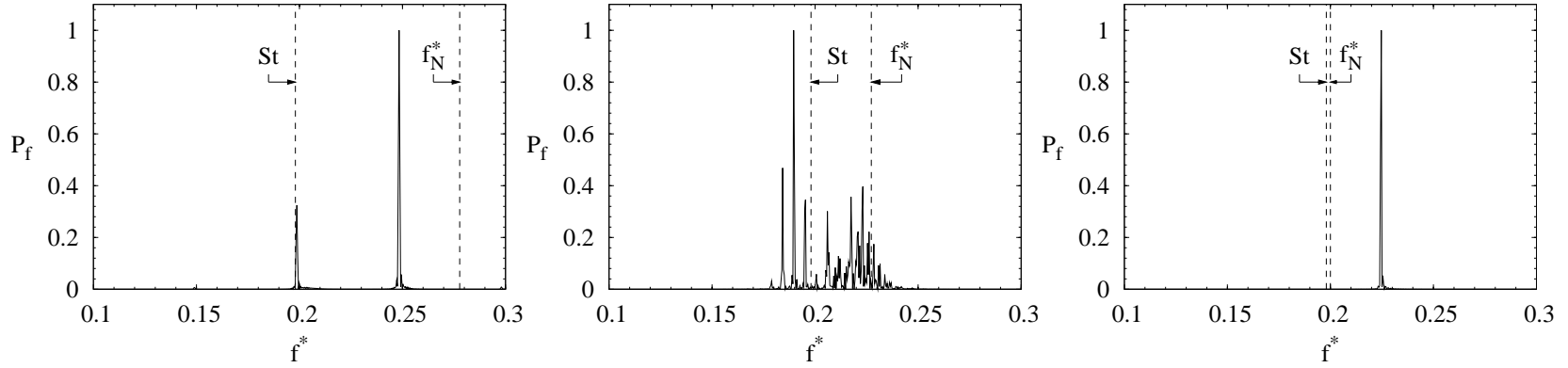


Figure 5.3: Normalised power spectra of the cylinder displacement response when $Re = 200$, $m^* = 1$ for: (a) $U^* = 3.6$; (b) $U^* = 4.4$; (c) $U^* = 5.0$. The spectrum in (a) shows that the quasiperiodic regime response consists of only two frequencies, which are the Strouhal frequency for a fixed cylinder, expressed as St , and a frequency close to, but below, the cylinder natural frequency. The spectrum in (b) shows that during the chaotic regime, the response can consist of a multitude of frequencies, and the primary frequency of response can be shifted significantly below the natural frequency. The spectrum in (c) shows that in the periodic regime, only a single frequency, slightly above the natural frequency, persists.

density are not just simply harmonics of the system characteristic frequencies (such as the Strouhal and natural frequencies). They are also not simply a harmonic series, but are incommensurate, further confirming that the response in this regime is in fact chaotic.

An example spectrum of the periodic branch at $U^* = 5.0$ is shown in figure 5.3c. It further confirms that the cylinder response in this regime is periodic, and very close to sinusoidal, with only a single frequency component present in the spectrum.

Expanding further on the frequency response in the chaotic regime, figure 5.4 shows the development of the frequency response with increasing U^* . Presented are spectra across the range of U^* that encompasses the chaotic regime. It is shown that with increasing U^* , more and more frequencies arise in the response. Therefore, the spectra containing the most frequencies are present towards the upper limit of U^* for the regime, which also coincides with the highest peak amplitudes of response.

5.2.4 Phase space of cylinder and wake response

To further characterise the differences in these response regimes, the relationship between the cylinder motion and the wake response has been investigated. This has been done by comparing the cylinder displacement with the lift force produced. Lift force has been chosen to characterise the wake response as it is a global, integrated quantity.

Plots of non-dimensional cylinder displacement, y_{cyl}/D , against the instantaneous lift force coefficient, C_L , have been produced from the cylinder response, again at $U^* = 3.6$, $U^* = 4.4$, and $U^* = 5.0$, to demonstrate the difference in the character of the response in each of the regimes, and to further demonstrate the non-repetitive nature of the chaotic regime. These phase plots, or Lissajou figures, are shown in figure 5.5.

The plot in figure 5.5a shows the repetition of the quasiperiodic regime over a series of cylinder oscillations. One cylinder oscillation is represented on the plot by one orbit about the origin in a counter-clockwise direction. It can be seen that a repeating spiral is traced out that is centred approximately at the origin.

This is contrasted with the plot at $U^* = 4.4$ in the chaotic regime, shown in figure 5.5b. Here, there is no repetition on any scale. Each orbit traces out a different path in the phase space. These orbits are very similar, and occur only within a bounded region, but it cannot be said that they repeat, or even appear to be converging to a repeating limit cycle. This

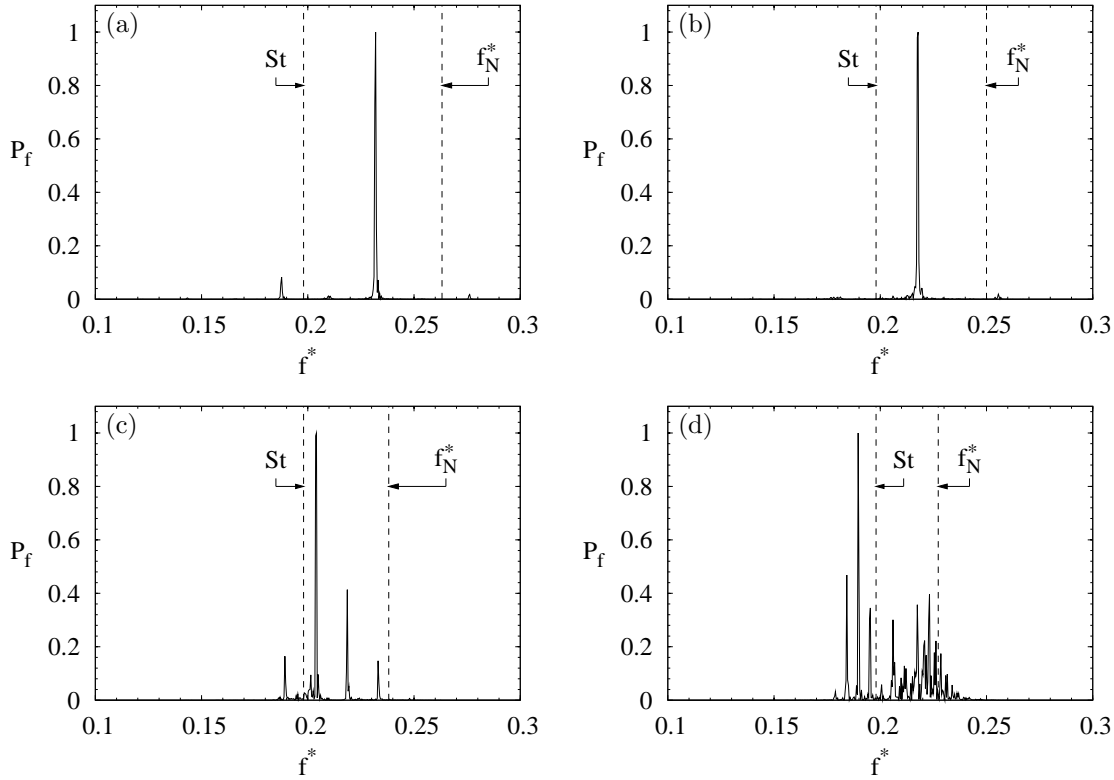


Figure 5.4: The development of frequency content in the chaotic regime with increasing U^* . The figures are the power spectral density against non-dimensional frequency when $Re = 200$, $m^* = 1$ for: (a) $U^* = 3.8$; (b) $U^* = 4.0$; (c) $U^* = 4.2$; (d) $U^* = 4.4$. This figure demonstrates that with increasing U^* , more and more frequencies arise in the response. Even though the secondary frequencies in (a) and (b) are very small, the primary frequency is significantly shifted from the Strouhal and natural frequencies.

type of behaviour in phase space is characteristic of a chaotic response.

In the periodic regime, each orbit in the phase plane is identical. This is demonstrated in figure 5.5c, constructed from the response when $U^* = 5.0$. Interestingly, the path traced crosses itself. As the energy transfer to the cylinder is the work done on the cylinder by the fluid, the energy transfer coefficient (the non-dimensional energy transfer per cycle) can be calculated by evaluating the cyclic integral

$$C_E = \frac{1}{D} \oint C_L dy_{cyl} , \quad (5.1)$$

which is related to the definition of C_E given in equation 4.1 through Green's theorem.

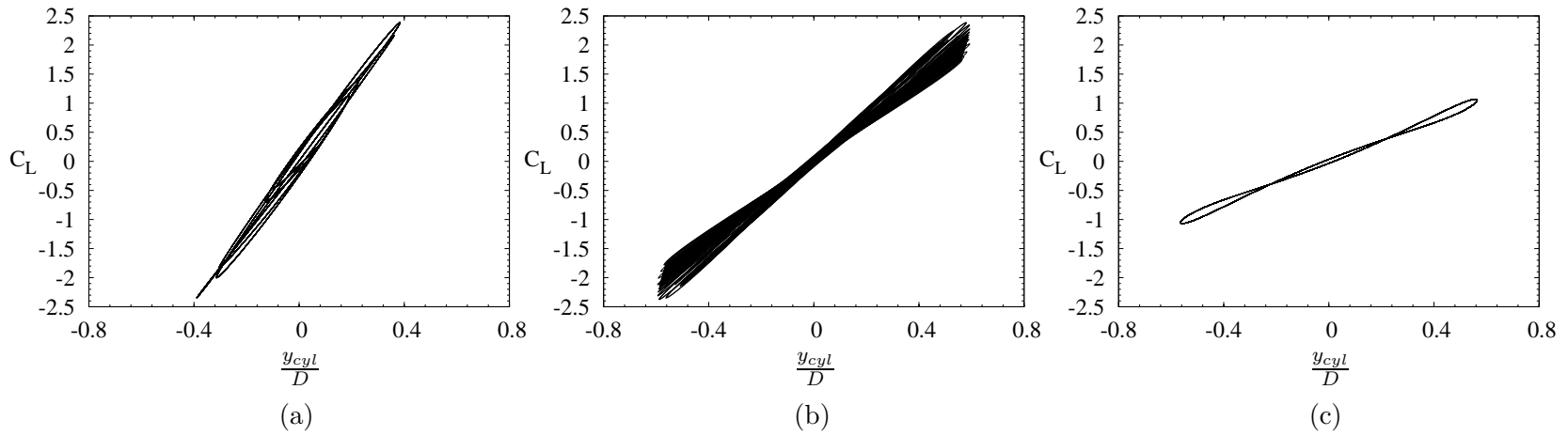


Figure 5.5: Lissajou, or phase space, plots of cylinder displacement against instantaneous lift coefficient when $Re = 200$, $m^* = 1$ for: (a) $U^* = 3.6$; (b) $U^* = 4.4$; (c) $U^* = 5.0$. The plots represent the history of the flow from $\tau = 600$ to $\tau = 1000$, which equates to around 80 oscillation cycles (or orbits in the phase plane). In (a), the quasiperiodic response manifests as a repeating spiral around the origin, whereas the chaotic response shown in (b) shows no repetition, but instead orbits non-repetitively in a bounded region. The periodic response in (c) traces out a single repetitive path each cycle of oscillation. Interestingly, this path crosses itself, indicating there are portions of the oscillation cycle where energy is transferred to the cylinder, and portions where energy is transferred from the cylinder.

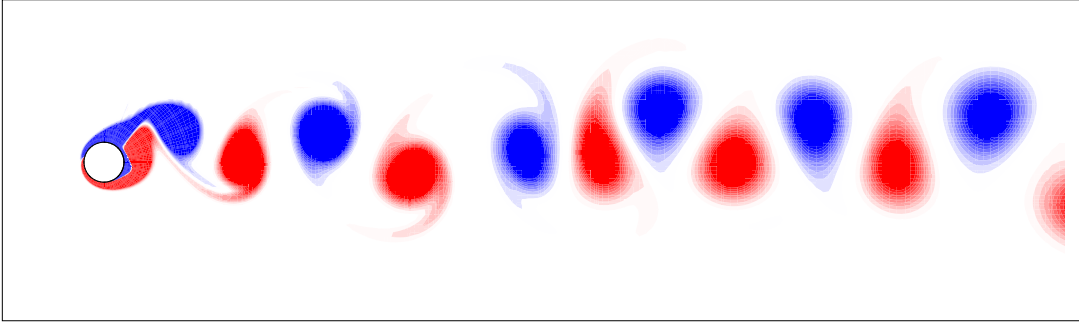


Figure 5.6: Instantaneous vorticity contours demonstrating the structure of the quasiperiodic wake when $Re = 200$, $m^* = 1$, for $U^* = 3.6$. The wake is essentially a standard von Kármán vortex street, or $2S$ mode, with a long wavelength wandering of the wake centreline attributable to the beating between the Strouhal and natural frequencies.

The definition given here says that the value of C_E is the positive area enclosed by the cycle in the phase space. A positive area is one which is enclosed by a cycle that proceeds in a counter-clockwise direction. As the cycle plotted in figure 5.5 crosses itself, there is a portion of the cycle that results in an area enclosed by a cycle which proceeds in a clockwise, or negative, direction. This behaviour can be interpreted as there being portions of the oscillation cycle where energy is in fact removed from the cylinder system, being transferred to the fluid. So, even though there is a net positive energy transfer over the cycle, the direction of energy transfer is not fixed throughout the oscillation.

5.2.5 Wake structure in the different regimes

The three different regimes of response are also differentiable from inspection of the organisation of vortices in the wake. Instantaneous images of the wake for each regime are shown in figures 5.6, 5.7, and 5.8.

The image in figure 5.6 shows that the quasiperiodic regime consists of an interaction between the Strouhal frequency, and a frequency close to the natural frequency of the cylinder. The “beating” of these two frequencies results in a wake similar to the standard Kármán vortex street or $2S$ mode, with an additional wandering of the wake centreline. The frequency of this wandering is well-predicted by the beat frequency, which is simply the difference between the two component frequencies. For instance, the two component

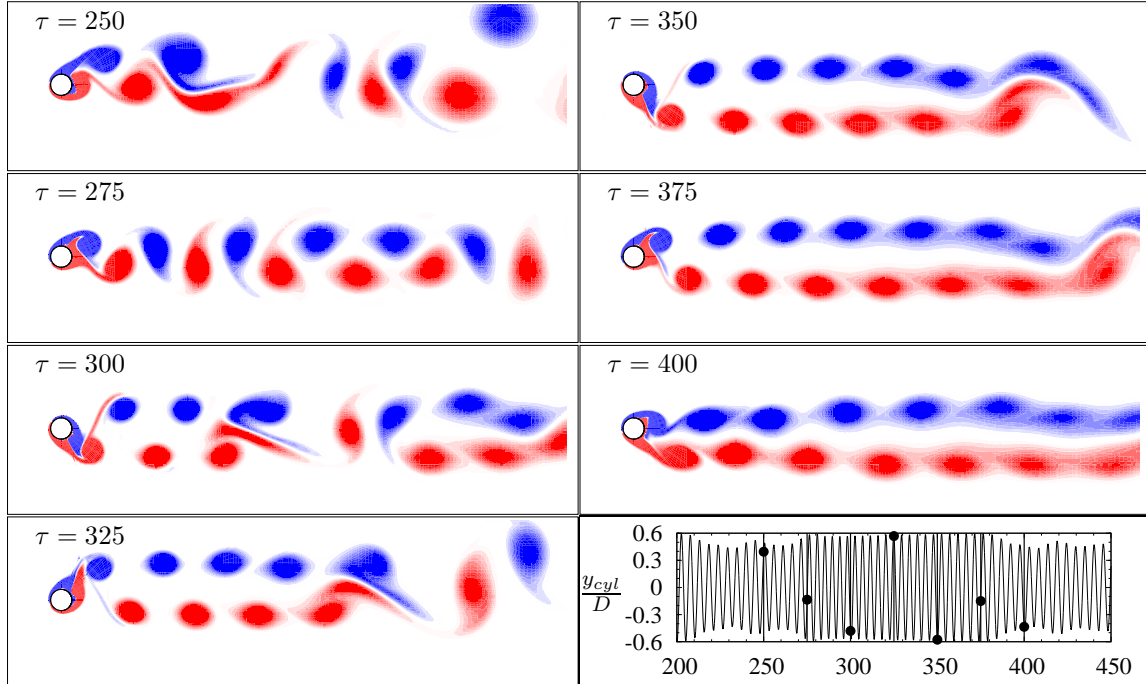


Figure 5.7: A series of images of instantaneous vorticity contours covering the growth and decay cycle of the chaotic regime when $Re = 200$, $m^* = 1$ for $U^* = 4.4$. The images cover the time history from $\tau = 225$ to $\tau = 400$, which is reproduced at the bottom of the figure, and the points in the time history that correspond to the images have been marked. The images progress in time starting from the top left image and progressing first down, then across the page. At low amplitudes, the wake approaches a stable single-row configuration, and it approaches a double-row configuration at high amplitudes. However, at times the wake can become highly disordered.

frequencies shown in the spectrum for $U^* = 3.6$ in figure 5.3a are separated by, and hence correspond to, a beat frequency of, $\Delta f^* \simeq 0.05$. This results in a period of approximately 20τ , or 4–5 shedding cycles. The image in figure 5.6 shows that the centreline wandering period occurs over around 8–9 half-cycles, each half-cycle resulting in one wake vortex. This corresponds to the same period as the beat period.

Figure 5.7 shows a series of images of the chaotic regime wake, covering one growth and decay episode of the cylinder oscillation amplitude for $U^* = 4.4$. This episode occurred over an interval of approximately 175τ , and the time history of cylinder displacement A^* is shown at the bottom of the figure. The images are separated in time by 25τ .

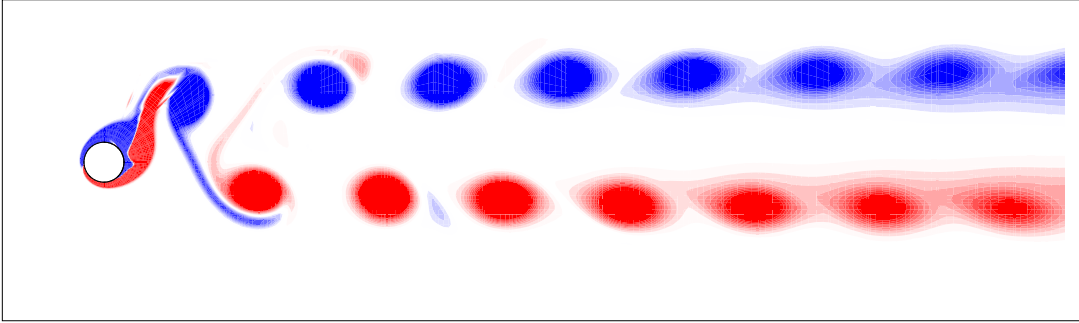


Figure 5.8: Instantaneous vorticity contours demonstrating the structure of the periodic wake when $Re = 200$, $m^* = 1$ for $U^* = 5.0$. Again, the shedding mode is $2S$, with two single vortices shed per oscillation cycle, that quickly organise themselves into a stable double-row configuration.

It is shown that the wake development over time in this regime is far more complex than that for the quasiperiodic regime. The wake varies from something resembling a $2S$ mode forming a single-row configuration of vortices when the oscillation amplitude is low, to a $2S$ mode forming a double-row configuration of vortices when the amplitude of oscillation is high. However, the growth in the amplitude of oscillation is limited, and it appears that when the amplitude “overshoots”, the high-amplitude oscillation cannot be sustained, the timing of vortex shedding rapidly changes, and the organisation of the near wake is upset. With this loss of organisation, the wake becomes highly disordered, resulting in the cylinder oscillation amplitude being reduced. Eventually, with the cylinder oscillation amplitude reduced to close to zero and the flow representing that of flow past a stationary cylinder, the process is free to repeat as the single-row configuration of shed vortices is reinstated. This growth and decay process is quite involved, and it is for this reason that the cylinder response is chaotic.

With transition to the periodic regime, all of this disorder disappears, and the wake takes on a stable double-row configuration, as shown for $U^* = 5.0$ in figure 5.8. Again, the shedding mode is $2S$.

5.2.6 Chaotic behaviour at higher mass ratio

All of the examples so far of the chaotic regime have come from the lowest mass ratio tested, $m^* = 1$. While it is conceded that no significant effort has been made to establish the mass ratio dependence of the chaotic regime, it is certainly detected over the range $1 \leq m^* \leq 10$.

Figure 5.9 shows the time history, phase history, spectrum, and Lissajou figure of the response when $Re = 200$, $m^* = 10$ and $U^* = 4.6$. The phase history was gained using a Hilbert transform. Here again, the variability of the response is clear. This figure shows that here, the amplitude undergoes the growth and decay cycle characteristic of this branch. The figure also shows that the phase is not necessarily fixed over the history of the response. This effect is more pronounced at the higher mass ratios tested, possibly because of the higher inertia of the heavier cylinder resulting in the cylinder not responding to fluctuations in the lift force. The phase results presented in figure 5.1 in the chaotic regime should therefore be treated as an average phase. Inspection of the spectrum in figure 5.9 shows that the main effect of the heavier cylinder is to reduce the bandwidth of frequencies involved in the response.

5.2.7 The dependence on Reynolds number of the chaotic regime

The results presented over the preceding sections have established that quasiperiodic, chaotic, and periodic regimes of response exist during two-dimensional vortex-induced vibration. Therefore, it appears that the possibly chaotic oscillations in the upper branch at higher- Re are not entirely dependent on the flow being three-dimensional.

This is not to say that these flow regimes appear universally when the flow is two-dimensional. The results from Mittal & Singh (2005) indicate that vortex-induced vibration can occur at values of Re below $Re = 46.7$, the value at which vortex shedding begins from a fixed cylinder (this result is confirmed and expanded upon as the subject of chapter 7). At these low values of Re , only one characteristic frequency of the system remains, the natural frequency of the cylinder. It is therefore difficult to envisage how the quasiperiodic regime could arise. This, coupled with the extra viscous damping at lower Re , suggests that the chaotic regime will not be observed.

If this conjecture is true, then it implies that there is some value of Re at which the

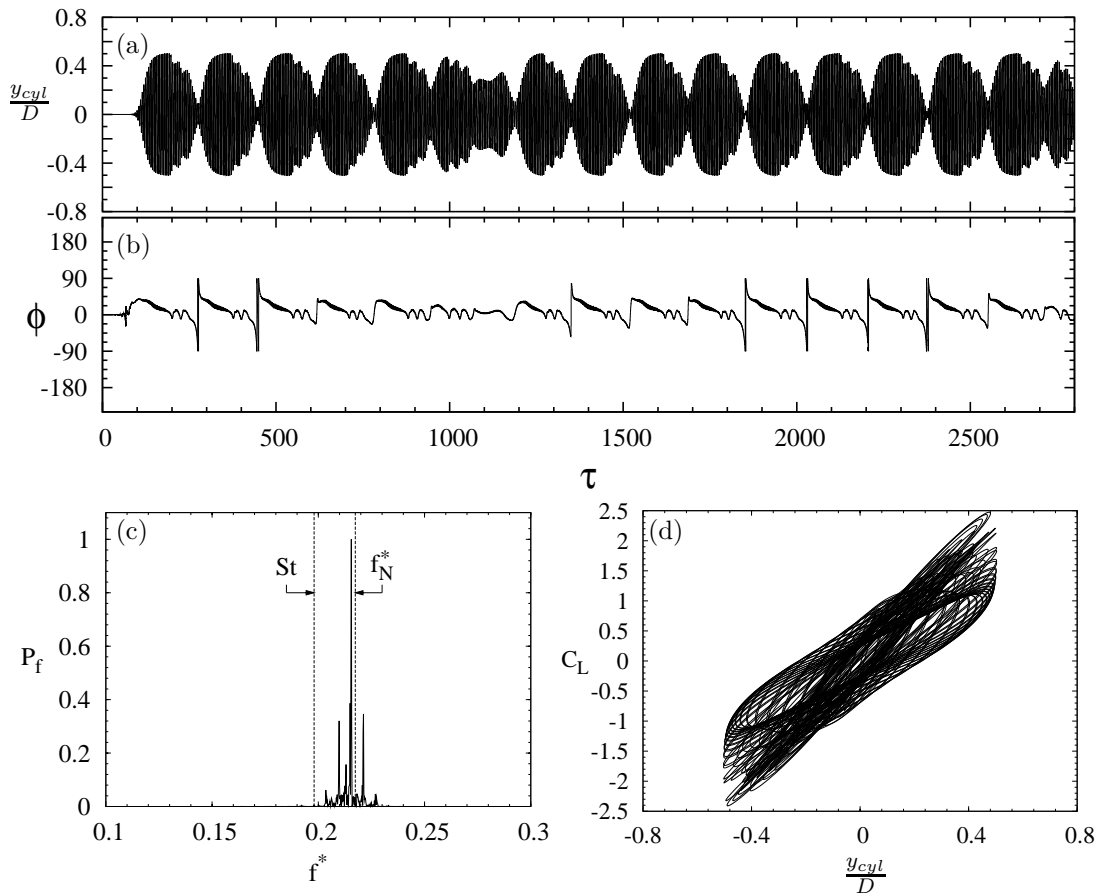


Figure 5.9: (a) Time history of cylinder response A^* , (b) time history of phase between lift force and cylinder displacement ϕ , (c) power spectral density P_f against non-dimensional frequency f^* and (d) Lissajou figure of lift coefficient C_L against cylinder displacement y_{cyl}/D , for $Re = 200$, $m^* = 10$, and $U^* = 4.6$. The growth and decay cycle is again present, and it is shown that the phase is not constant over the flow history. The spectrum contains non-conformant contributing frequencies over a narrow band, and the Lissajou figure shows the bounded, but non-repetitive nature of the response.

quasiperiodic and chaotic regimes emerge, and that value is somewhere between $Re = 46$ and the value of $Re = 200$ tested thus far. This has been tested by performing a series of simulations where $m^* = 1$, for a range of Re , to establish at what values of U^* the chaotic regime exists for. The results of these simulations are presented in figure 5.10.

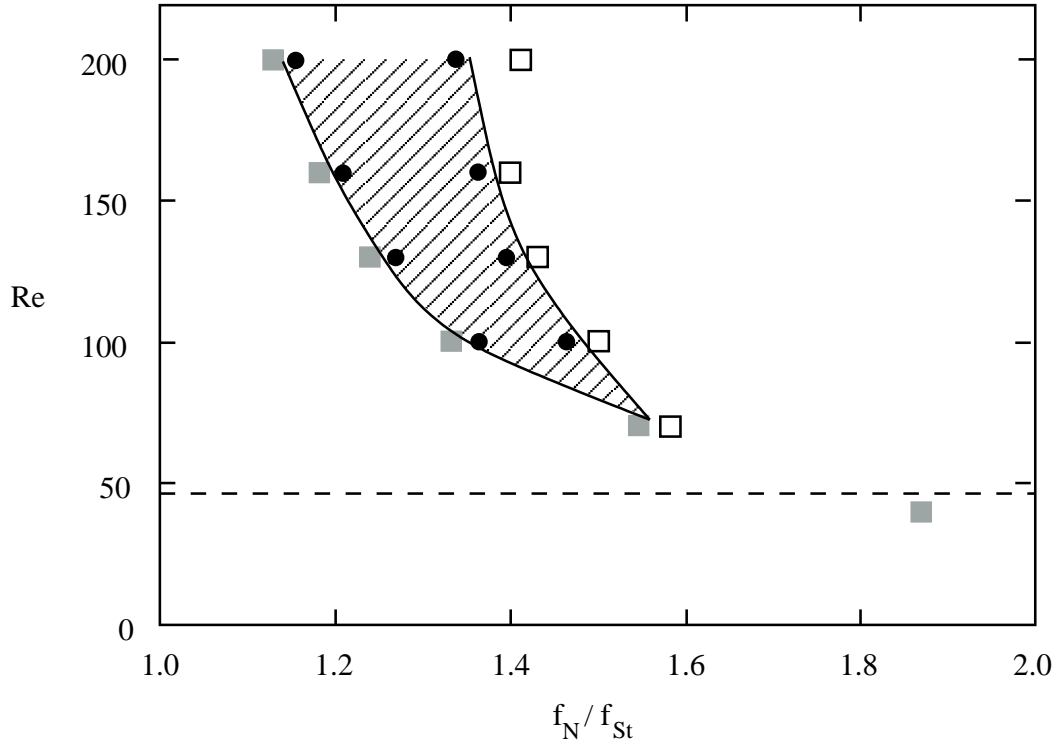


Figure 5.10: A map of the region in the $Re-f_N/f_{St}$ plane occupied by the chaotic branch when $m^* = 1$. Open squares (\square) represent quasiperiodic response, circles (\bullet) represent chaotic response, and grey squares (\blacksquare) represent periodic response. The broken line (- -) marks $Re = 46.7$, the value above which vortex shedding occurs for a fixed cylinder. The solid lines enclose a hatched region, indicating the region for which the chaotic regime occurs. The chaotic regime was not observed for $Re \leq 70$, and the quasiperiodic regime was not observed for $Re \leq 40$.

The results of figure 5.10 are presented in terms of f_N/f_{St} rather than U^* to allow a reasonable comparison across the range of Re , as f_{St} varies over this range. Regardless of the parameter used, the chaotic regime was not observed for $Re \leq 70$, and neither the quasiperiodic or chaotic regime was observed for $Re \leq 40$, below the fixed cylinder Re

required for vortex shedding.

Figure 5.10 also shows that there is a dependence on Re for the range of f_N/f_{St} that is occupied by the chaotic regime, with the range becoming wider with increasing Re . This range is also shifted to lower values of f_N/f_{St} . These results establish that a controlling parameter in whether the chaotic regime arises is the Reynolds number. They also establish that for $Re \leq 40$ (roughly coinciding with the range of Re for which steady flow persists for a fixed cylinder wake) the only oscillatory response is periodic and synchronised.

5.3 A comparison between elastically-mounted and driven oscillation

5.3.1 A comparison with sinusoidal driving

Following the establishment of distinct response regimes over the course of the previous section, and the quantification of sinusoidal driven oscillation in chapter 4, a natural extension is to compare the vortex-induced vibration and externally-driven systems. This is undertaken in this section, with focus on the ability of the sinusoidal driven oscillations to accurately model the vortex-induced vibration response over the different regimes.

The results gained from each system are directly compared in figure 5.11. Here, the primary frequency of response and the peak amplitude of response (as presented in figure 5.1) have been plotted on the A^* , f/f_{St} plane for $Re = 200$. The results presented are from the three mass ratios $m^* = 1$, $m^* = 5$, and $m^* = 10$. These freely oscillating results have been overlaid on the synchronisation boundaries and contours of the energy transfer coefficient, C_E , from the sinusoidal driven oscillation results at $Re = 200$. The freely oscillating results from each regime have been colour coded to distinguish them from each other.

Inspection of figure 5.11 shows that, in general, the elastically-mounted cylinder response in the periodic regime falls in a region of the parameter space where the driven oscillation results in synchronisation and $C_E \geq 0$. This is the region where driven oscillation predicts all vortex-induced vibration response should occur. The periodic regime points also follow reasonably closely the contours of C_E . As shown by Carberry (2001) and explained in chapter 4, if both the cylinder displacement and lift force can be approximated

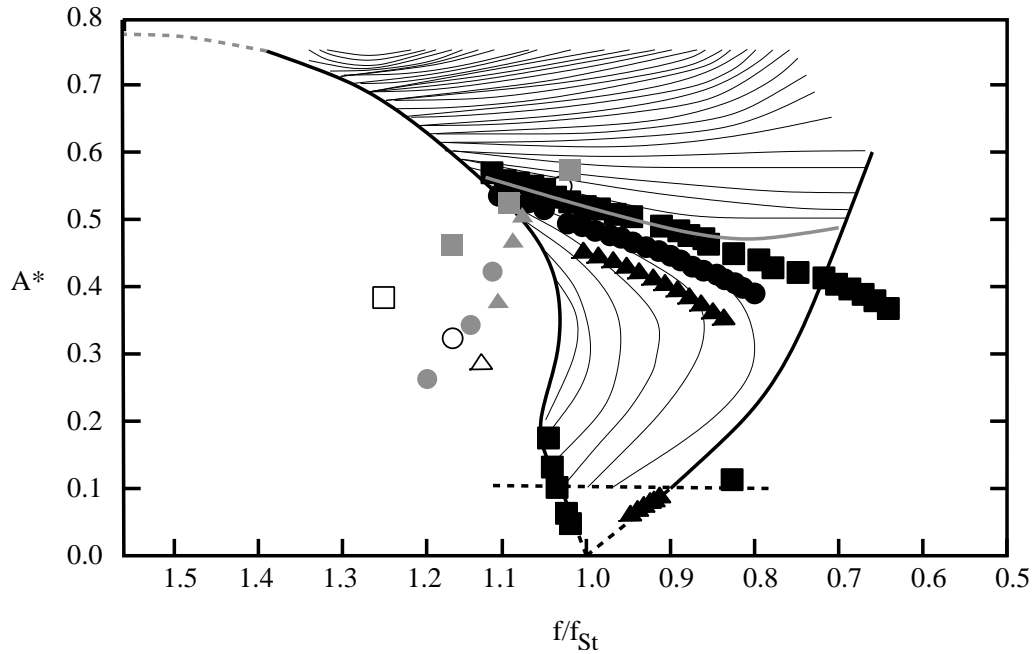


Figure 5.11: The elastically-mounted cylinder response overlaid on sinusoidal driven oscillation results when $Re = 200$ in both cases. Elastically-mounted results are for: $m^* = 1$ (\square , \blacksquare , \blacksquare); $m^* = 5$ (\circ , \bullet , \bullet); $m^* = 10$ (\triangle , \blacktriangle , \blacktriangle). Open symbols (\square , \circ , \triangle) represent points from the quasiperiodic regime, grey symbols (\blacksquare , \bullet , \blacktriangle) represent points from the chaotic regime, black symbols (\blacksquare , \bullet , \blacktriangle) represent points from outside these regimes, therefore including the periodic regime. Heavy, solid black lines represent synchronisation boundaries. The solid grey line represents $C_E = 0$, $C_E > 0$ below this line. Dotted lines represent regions where pure synchronisation is difficult to ascertain during driven oscillation. Light, solid black lines are contours of constant C_E . It is shown that the points in the periodic regime fall almost exclusively inside the positive C_E , synchronised region, and follow the contours of C_E reasonably closely. However, the chaotic regime response points fall either outside the synchronisation region, or inside the synchronisation region but where $C_E < 0$. The highest amplitudes achieved in the chaotic regime exceed that which is predicted to be a maximum by the sinusoidal driven oscillations, indicating these amplitudes cannot be supported by a periodic response.

by sinusoidal functions, C_E is dependent on the magnitude of the displacement and vortex lift force, and the phase between the two, ϕ_v . Therefore, as the results of figure 5.1 show that these three parameters are close to constant over the majority of the periodic regime, it is consistent to expect the elastically-mounted results to follow the contours of C_E the way they do in the periodic regime.

The only periodic regime results that do not fall in the positive C_E , synchronised region in figure 5.11 are those from high- U^* , and low frequency of response, for the lightest cylinder tested, i.e. $m^* = 1$. These results continue smoothly across the synchronisation boundary. The exact reason for this is unclear, but it does seem logical that if this behaviour occurs, that it should occur for low values of m^* .

The results in the quasiperiodic and chaotic regimes fall outside of the positive C_E , synchronised region, generally by being outside of the synchronisation region altogether. However, the elastically-mounted simulations of the chaotic regime that result in the largest peak oscillations present an interesting case. It can be deduced from figure 5.11 that they fall inside the synchronisation region, but where $C_E < 0$, and above the limit predicted by the driven oscillation simulations. This indicates that oscillations of this amplitude are unsustainable during fully-synchronised periodic vortex-induced vibration, and can only be achieved transiently by a regime such as the chaotic regime.

These results indicate that sinusoidal driven oscillation is generally adequate to model vortex-induced vibration in the periodic regime, but it does not adequately capture the behaviour in the chaotic regime, when the amplitudes of oscillation are greatest. This is made particularly clear by comparing the phase plots of lift coefficient against cylinder displacement for the elastically-mounted cylinder and a driven oscillation using the same frequency and peak amplitude. This comparison is presented in figure 5.12. The difference in character is quite clear, with the driven oscillation actually resulting in a synchronised response (albeit with a non-sinusoidal lift force). The negative energy transfer is indicated here by the large area in the middle of the plot that is circumnavigated in a clockwise direction. The elastically-mounted response results in a very different shape plot, and has a peak lift force that is of an order of magnitude larger than that for the sinusoidally driven cylinder.

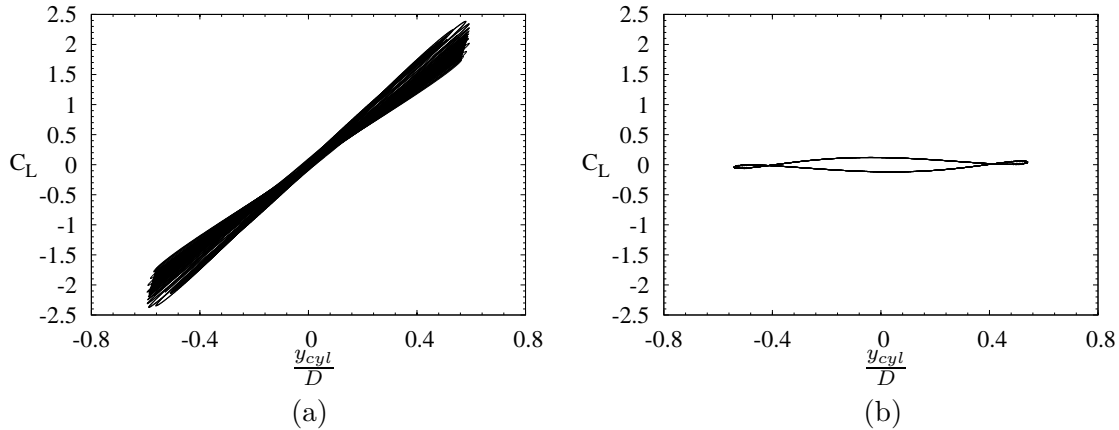


Figure 5.12: (a) Lift coefficient C_L against cylinder displacement y_{cyl}/D resulting from vortex-induced vibration when $m^* = 1$ and $U^* = 4.4$. (b) Lift coefficient C_L against cylinder displacement y_{cyl}/D during sinusoidal driven oscillation using the peak amplitude of displacement and primary frequency of response taken from the vortex-induced vibration response of (a). In both cases, $Re = 200$. The character of response is totally different, and the elastically-mounted cylinder experiences peak lift coefficients of an order of magnitude greater than the driven cylinder.

5.3.2 More complicated driving functions

With the conclusion that sinusoidal oscillation seems unable to adequately model vortex-induced vibration in the chaotic regime, other methods need to be sought that may still allow an uncoupled system to behave in a manner somewhat similar to the coupled, elastically-mounted cylinder. The simplest extension to the purely sinusoidal driving employed previously is to add extra frequency components, resulting in modulated driving.

This has been done for a case when $Re = 200$, $m^* = 10$ and $U^* = 4.6$. The time history and frequency response of this case were presented in figure 5.9. Inspection of the spectrum in this figure shows that amongst the many frequencies present, three main components are present. These three components were extracted and used to construct a quasiperiodic driving signal. The frequencies of each component were simply taken to be the frequencies resulting in the three largest values of P_f . The amplitude of each component was deduced by observing that the two lesser components had a power spectral density of 0.33 that of the primary component, and that the peak amplitude of the driving function should be the

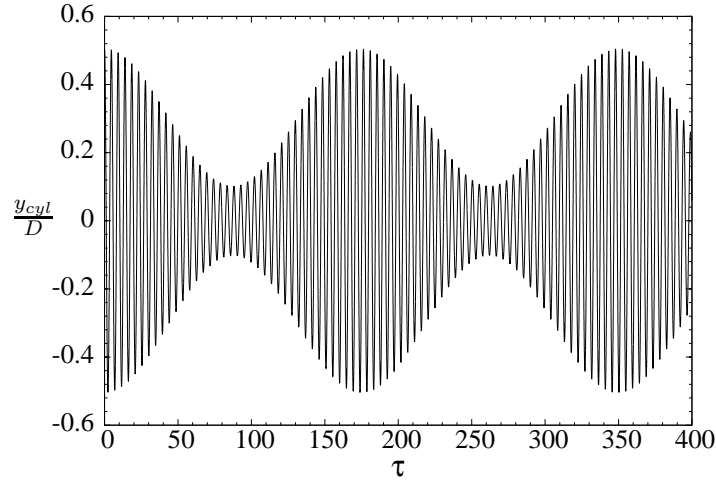


Figure 5.13: Time history of the driving function using the three major frequencies present in the response of the elastically-mounted cylinder when $Re = 200$, $m^* = 10$ and $U^* = 4.6$.

same as that achieved during vortex-induced vibration.

The resulting driving function, represented graphically as the displacement history, is presented in figure 5.13. The frequencies and relative amplitudes used to build this displacement history were $f_1^* = 0.210$, $f_2^* = 0.216$ and $f_3^* = 0.221$, with amplitudes $A_1^* = A_3^* = 0.101$ and $A_2^* = 0.302$.

Presented in figure 5.14 are plots of the time history of the lift coefficient for sinusoidal driven oscillation, driven oscillation using the three frequencies as presented in figure 5.13, and from the elastically-mounted cylinder response. The sinusoidal driven oscillation result shows that the wake is synchronised with the cylinder oscillation, resulting in a periodic, constant-amplitude lift coefficient. This lift coefficient is only approximately 25% of the peak lift coefficient obtained during vortex-induced vibration.

The modulated driving using three frequency components goes some way towards improving this situation. The peak lift coefficient is of a magnitude similar to that obtained during vortex-induced vibration, and the lift force undergoes a growth and decay cycle somewhat similar to the vortex-induced vibration case. While the wake response during the modulated oscillation and vortex-induced vibration are not identical, it does seem that the phase-disturbance introduced by the modulation goes some way towards modelling the physics of the flow in the chaotic regime.

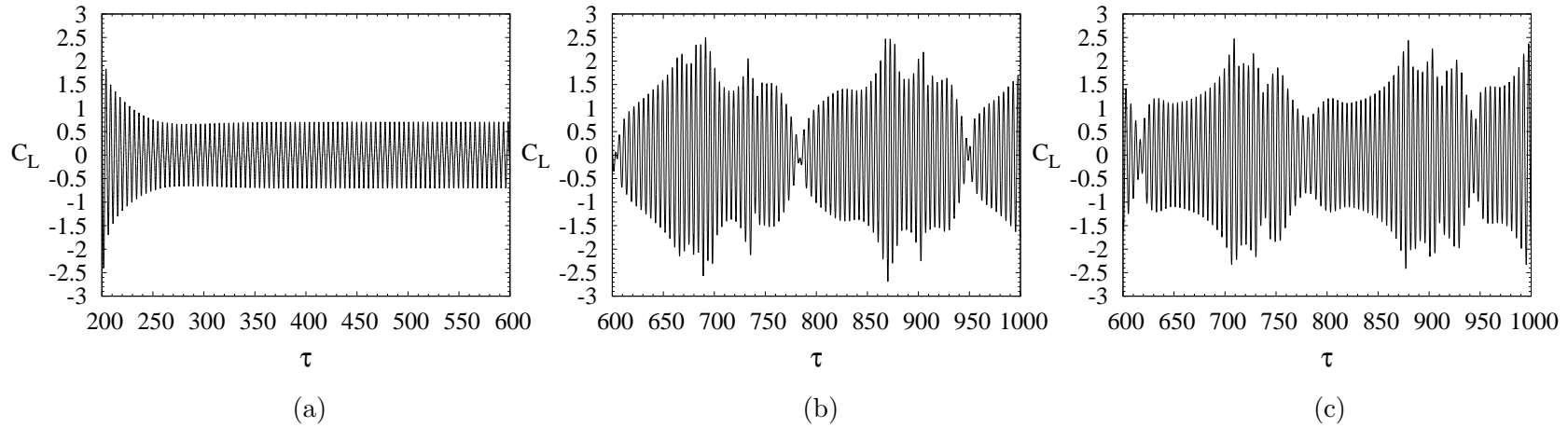


Figure 5.14: Portions of the time history of the lift coefficient C_L for: (a) Purely sinusoidal driven oscillation; (b) Modulated driven oscillation following the history presented in figure 5.13; (c) Vortex-induced vibration when $m^* = 10$, $U^* = 4.6$. $Re = 200$ in all cases. In all cases the primary frequency and peak amplitude of oscillation are the same. It is shown that the sinusoidal driving results in a synchronised and periodic wake with a significantly lower peak lift coefficient than that for the elastically-mounted cylinder. However, the modulating driving results in a similar magnitude of lift coefficient.

5.4 Comparison with the upper branch at higher Re

The results from the two-dimensional simulations of vortex-induced vibration presented in this chapter establish that three separate regimes exist in the response of the cylinder with respect to the reduced velocity, U^* . Of particular interest is the emergence of the chaotic regime, where the largest peak amplitudes of oscillation occur.

The behaviour during vortex-induced vibration at higher Re , where the flow is inherently three-dimensional, appears to exhibit some similar behaviours. When the mass ratio m^* is low, higher- Re vortex-induced vibration is characterised by the initial, upper and lower branches (for a more complete description, see section 2.2.4 of the literature review of chapter 2 and the references cited therein). There appears to be a body of evidence that the upper branch itself is chaotic, suggesting that it possibly arises from mechanisms similar to the chaotic regime during two-dimensional vortex-induced vibration.

The experimental results from Hover *et al.* (1998, 2004) indicate that during the upper branch response, the correlation between the lift force at either end of a three-dimensional cylinder is very low, approaching zero. This indicates that features of the flow such as vortex organisation and separation points vary considerably along the span of the cylinder. The three-dimensional simulations from Lucor *et al.* (2005) show this lack of spanwise organisation clearly, and also indicate that the separation point at a particular spanwise position is not fixed in time, further highlighting the variability of the flow in this regime.

The general description of the upper branch as a periodic branch of high amplitude has been given by Khalak & Williamson (1996, 1997, 1999) and Govardhan & Williamson (2000). It is described as occurring in bursts interspersed with regions of the lower branch over time. The recent results of Morse & Williamson (2006) show that using sinusoidal oscillations to match either of these portions works reasonably well. However, while the high-amplitude portions of the time history of displacement may well be approaching sinusoidal, the result that this high-amplitude response occurs only in intermittent bursts lends weight to the conclusion that the underlying solution is in fact chaotic. In fact, for very low values of m^* , Govardhan & Williamson (2000) state that “...it becomes unclear whether one is switching between two distinct frequencies (i.e. between distinct response branches) anymore”.

The spectra of cylinder response at high Re and low m^* presented by Branković &

Bearman (2006) also show that at values of U^* that cover the range of the upper branch, many frequencies are present, and the primary frequency of oscillation can be significantly shifted from either the natural or Strouhal frequencies. This is very similar to the behaviour described for the chaotic regime in this chapter, particularly that illustrated in figures 5.3 and 5.4.

The major difference between the upper branch and the chaotic regime presented in this thesis is the peak amplitude of response. This can reach $A^* = 1.4$ in the higher- Re flow, where it appears limited to somewhere around $A^* = 0.6$ in the two-dimensional flow. However, in both cases, the maximum amplitude obtained occurs in the chaotic regime or upper branch, and this peak is achieved when the amplitude is significantly modulated. It seems that the domain of attraction of any attractor in the phase space is altered, but the nature of this attractor is not varied by the introduction of three-dimensional flow.

5.5 Vortex-induced vibration summary

Results from simulations of an elastically-mounted cylinder, constrained to oscillate in the cross-flow direction, have been presented. The simulations have been conducted over a range of reduced velocities U^* , and mass ratios m^* .

The results indicate that for the low mass ratios tested ($1 \leq m^* \leq 10$), three distinct response branches exist with varying U^* . These are the quasiperiodic regime, chaotic regime, and periodic regime. The highest amplitudes of oscillation occur transiently in the chaotic regime.

A comparison with the sinusoidal oscillation results from chapter 4 shows that sinusoidal oscillation is an adequate model for vortex-induced vibration in the periodic regime. However, the chaotic regime is not adequately modelled in this fashion. Inclusion of other frequency components in the driving function goes some way towards improving this situation. It seems that the phase disturbance of vortex shedding introduced by the modulation of the driving function better represents the dynamics in the chaotic regime. These results confirm the third hypothesis of this thesis.

Comparison with results in the literature show that the chaotic regime has many similarities to the upper branch of response at higher Re . It therefore seems that the very

high peak amplitudes of response in this upper branch are not caused by the presence of three-dimensionality, but are significantly amplified by it.

CHAPTER 6

FLOQUET STABILITY ANALYSIS OF THE TRANSITION TO THREE-DIMENSIONAL FLOW FOR THE EXTERNALLY-DRIVEN OSCILLATING CYLINDER

6.1 Introduction

This chapter reports on results from a Floquet stability analysis of the wake of an externally-driven sinusoidally-oscillating cylinder. This was done to establish the modes present during the transition to three-dimensionality, and to establish the impact of oscillation amplitude on this transition.

It is known that the onset of three-dimensionality in a cylinder wake can be suppressed if the cylinder is forced to oscillate transverse to the freestream at moderate amplitudes. Experiments with an elongated cylinder by Berger (1967) showed that suitable transverse oscillations increased the upper limit of Reynolds number for the laminar shedding regime from the non-oscillating limit of $Re = 190$ to $Re = 300 \sim 350$. Koopman (1967) and Griffin (1971) both performed forced oscillation experiments at $Re \leq 300$ based on the assumption that a laminar shedding regime persisted over this Re range. The visualisations of vortex filaments shed from a transversely oscillating cylinder by Koopman (1967) at $Re = 200$

show no spanwise variation. This two-dimensionality is assumed to be attributable to the oscillation, as the more recent work of Williamson (1996*b*), and Barkley & Henderson (1996) has shown that the transition to three-dimensional flow occurs at Reynolds numbers below 200 for a stationary cylinder.

The obvious reference case for a study of three-dimensional transition in an oscillating cylinder wake is provided by the limiting case of a stationary cylinder. For a stationary cylinder, the transition from the two-dimensional Kármán vortex street to a three-dimensional flow occurs with the onset of the first three-dimensional mode, aptly named mode A, at $Re \simeq 190$, first described in detail by Williamson (1988). It has been shown that mode A breaks only the translational and span-invariant reflectional symmetry of the two-dimensional flow, but preserves the spatio-temporal symmetry of the two-dimensional base flow (Barkley & Henderson, 1996; Barkley *et al.*, 2000; Blackburn *et al.*, 2005).

Two other three-dimensional modes have been shown to be theoretically possible: the second three-dimensional mode, mode B, which has a much shorter spanwise wavelength than mode A and breaks the spatio-temporal symmetry as well as the spanwise symmetry of the flow; and finally mode QP, which is quasiperiodic (hence the designation QP) and can consist of modulated travelling or standing waves.

Mode B bifurcates from the two-dimensional base flow at $Re \simeq 260$, but experimentally it is observed at lower Re due to the modification of the two-dimensional base flow by mode A. As Re is further increased, the saturated (fully-developed) mode B state is seen to dominate the three-dimensional flow, with mode B vortical structures still present at $Re > 1000$ (Wu *et al.*, 1996). Mode QP has only recently been identified and classified as quasiperiodic by Blackburn & Lopez (2003). Floquet stability analysis has shown that this mode becomes unstable at $Re \simeq 377$. However, the experimental wake at this Re is already highly three-dimensional and has descended into spatio-temporal chaos (Henderson, 1997), and mode B continues to dominate. A more in-depth treatment of the background material relating to all three of these modes is given in section 2.1.3.

While the possible three-dimensional modes that can occur are now relatively well-defined, the physical nature of the instabilities that cause them are less well understood. Williamson (1996*a*) proposed that mode A was due to an elliptic instability of the primary vortex cores, and that mode B was due to an instability of the braid shear layers. Sub-

sequently, Leweke & Williamson (1998) showed that elliptic instability theory predicted the wavelength of mode A to within 25%, and hypothesised that mode B was caused by a hyperbolic instability of the braid shear layers. Floquet analysis and three-dimensional direct numerical simulations of Thompson *et al.* (2001) showed strong evidence that the transition to mode A could be interpreted as a cooperative elliptic instability. The results of this chapter support this theory.

Floquet stability analysis is well-suited to establishing the Reynolds number for transition to three-dimensional flow. Barkley & Henderson (1996) first used this method to predict the critical Re and the wavelengths of both modes A and B for a fixed cylinder wake. Other bluff body wakes have been investigated using this method, including square cylinders (Robichaux *et al.*, 1999), normal-to-flow flat plates (Julien *et al.*, 2004), elliptical leading-edge plates (Ryan *et al.*, 2005) and tori (Sheard *et al.*, 2003*b*). The same method is applied in the present study.

A primary difference between many other flows and that studied here is that most fixed bluff-body flows have only one independent parameter, Re , whereas the oscillating cylinder has up to three. They are the Reynolds number, $Re = UD/\nu$, non-dimensional oscillation amplitude, $A^* = y_{max}/D$, and non-dimensional oscillation frequency, $f^* = fU/D$, where U is the freestream velocity, D is the cylinder diameter, ν is the kinematic viscosity, y_{max} is the amplitude of oscillation and f is the frequency of oscillation. For the present study, $f^* = 0.2$ has been fixed and only the effect of Re and A^* have been considered.

The introduction of a second variable greatly increases the complexity of the bifurcation problem, as well as allowing other types of generic bifurcation (Blackburn *et al.*, 2005; Marques *et al.*, 2004). While different three-dimensional modes are highly unlikely if the two-dimensional wake configuration stays the same, different modes are possible if the two-dimensional wake symmetries change. Indeed, a change of the two-dimensional wake does occur in the wake of an oscillating cylinder, with the onset of the $P + S$ wake configuration as described in chapter 4; this breaks the spatio-temporal symmetry of the conventional Kármán wake (Williamson & Roshko, 1988). With the onset of this different two-dimensional wake, different three-dimensional modes, such as subharmonics, become possible.

In any bifurcation and stability analysis, symmetry and the symmetries broken by

bifurcation play a critical role (Iooss & Joseph, 1990). Therefore, it is important to know the symmetry group of the base flow when making the analysis. The two-dimensional vortex street behind a fixed cylinder possesses a translational and reflectional symmetry along the span, hence it possesses the $O(2)$ symmetry group. It also possesses a spatio-temporal symmetry, which consists of a reflection about the wake centreline plus a temporal evolution of half a period. This also gives it the Z_2 symmetry group. Therefore, the total symmetry group of the fixed cylinder wake is expressed as $Z_2 \times O(2)$.

At low amplitudes of oscillation, the oscillating cylinder wake has the same symmetry group for the base flow. Considering this, along with the fact that the extra variable of cylinder oscillation allows different bifurcations, the following questions arise:

- What three-dimensional modes occur?
- In what order, with respect to Re and A^* , do these modes occur?
- How does the loss of spatio-temporal symmetry (of the base flow) at higher amplitudes of oscillation affect the transition to three-dimensionality?
- As the base flow varies considerably with increasing amplitude of oscillation, does oscillation always suppress the transition?

Floquet stability analysis has been employed to answer these questions.

The results in this chapter are focused upon a map in the $Re-A^*$ plane that shows the modes present in the transition to three-dimensional flow, and where each of them is predicted by the analysis to become critical. Each of the modes involved in the transition is then described in more detail.

This chapter shows that transverse oscillations of the cylinder can suppress the three-dimensional transition for amplitudes of oscillation $A^* \lesssim 0.55$, increasing the critical value of Reynolds number to as high as $Re = 280$. However, for higher oscillation amplitudes, the oscillation is predicted by this study to excite the three-dimensional modes, meaning the transition Re is decreased with increasing amplitude of oscillation. It is also shown that the transverse cylinder oscillation can change the order of inception of the wake modes.

6.2 A definition of the problem studied

6.2.1 Geometry and oscillation history

The focus of this study was to determine the effect of the oscillation amplitude on the stability of a cylinder wake, for the case where the wake and applied oscillation are synchronised. The non-dimensional frequency, f^* , was fixed at $f^* = 0.20$ for all simulations. This value was chosen because it is close to the middle of the range of the Strouhal number for a fixed cylinder, over the range of Reynolds numbers where transition occurs. According to the three-term fit given by Williamson & Brown (1998), over the Reynolds number range $180 < Re < 350$, the Strouhal number, St , spans the range $0.193 < St < 0.215$. Therefore, the value of $f^* = 0.20$ is shown to be close to the fixed cylinder Strouhal number for all the simulations conducted.

Keeping the oscillation frequency close to the fixed cylinder Strouhal frequency ensures that the wake is synchronised with the cylinder oscillation. This synchronisation occurs over a wider range of frequencies as the amplitude is increased, as was shown in chapter 4. However, at amplitudes where $A^* < 0.1$, synchronisation does not occur and the wake is not periodic, with both the oscillation and Strouhal frequencies present. Since Floquet stability analysis requires a periodic base flow, no stability results are shown for amplitudes of $A^* < 0.1$ (except for $A^* = 0$, where the results correspond to a fixed cylinder shedding at the natural Strouhal frequency). All of the simulations conducted for this Floquet analysis fell in the synchronised region of the A^*-f/f_{St} plane, as defined in figure 4.11.

6.2.2 The identification of critical values

As stated in section 3.7, the parameter that needs to be evaluated to discern whether a Floquet mode is predicted to become critical is the Floquet multiplier, μ . This parameter is a measure of the growth of the mode from one period to the next. If $\mu > 1$, the Floquet mode is predicted to grow and therefore the flow is predicted to become three-dimensional. Floquet modes are referred to as “critical” when they return a value of $\mu = 1$.

To identify where the Floquet modes become critical, μ was calculated over a range of spanwise wavelengths, at a fixed value of Re and A^* . For each Reynolds number, the multipliers must vary quadratically about each local maximum. After identifying the

approximate location of a local maxima, a parabolic fit was used to determine the position of each local maximum. This process was repeated for a range of Re , and the local maxima calculated for each. Next, these maxima were used to determine the $\mu = 1$ crossing. In this way, the critical values of Re and λ were found for each Floquet mode, at a given value of A^* . For this study, steps of $\Delta Re = 5$ and a maximum $\Delta\lambda = 0.1$ were employed, where λ is the spanwise wavelength of the Floquet mode. This process was repeated for each value of A^* . Here, λ is a non-dimensional quantity, the wavelength being normalised by the cylinder diameter.

In the case of a fixed cylinder, only one variable governs the wake behaviour: Re . Stability and bifurcation analyses therefore proceed by slowly varying Re , and assessing when the two-dimensional base flow becomes unstable to the three-dimensional modes. However, in the case of the oscillating cylinder, at least a second variable exists, in this case the amplitude of oscillation, A^* . Therefore, instead of there existing one critical value of Re for a given mode, the critical Re becomes a function of A^* . To determine the functional variation, the critical Re for a given mode was first found for a set value of A^* . The amplitude was then incremented, and the critical Re again found. This process was repeated until the parameter space was spanned. By performing the analysis in this way, a map of criticality of all the modes and transitions present in the A^*, Re plane was constructed.

6.3 Wake modes and three-dimensional transitions

This map of criticality is presented in figure 6.1. This figure shows various lines defining the different transitions. A dotted line dividing the plane approximately vertically defines the transition from the $2S$ to $P + S$ base state. This line shows explicitly that this wake mode transition of the base flow has an dependence on Re , with the value of A^* at the transition varying inversely with Re . The transition to three-dimensional flow differs markedly for the two different base flows on either side of this transition.

The base flow to the left of this transition (at lower A^*) is the $2S$ wake. From this base flow, three three-dimensional modes are seen to bifurcate. These correspond to mode A, mode B, and the quasiperiodic mode QP. These three modes share similar features to

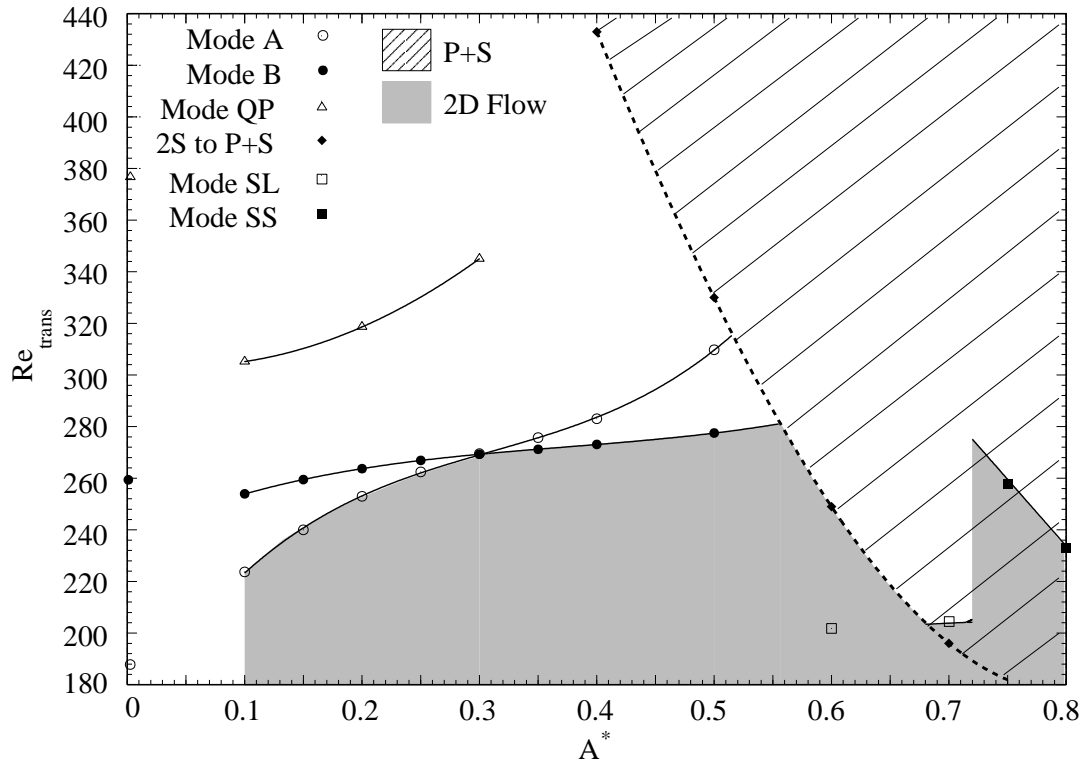


Figure 6.1: The diagram of transitions, showing the curves of criticality for mode A, mode B, mode QP, mode SL and mode SS in terms of A^* . Also shown with a dotted line is the boundary defining the transition from a $2S$ to $P + S$ wake configuration. The shaded grey area denotes that the flow is two-dimensional. The hatched area denotes where the $P + S$ base flow is present.

the corresponding modes in a fixed cylinder wake. The details of each of these modes are provided in section 6.4.

At low amplitudes of oscillation, for $A^* < 0.3$, the order of criticality of the three modes is the same as for a fixed cylinder. With respect to increasing Re , first mode A becomes critical, then mode B, and finally mode QP. Increasing A^* has the effect of increasing the critical Re for all the modes. However, this effect is much more pronounced for mode A than for mode B. The net result is that at $A^* \simeq 0.3$ the critical Re for mode A matches that of mode B, and, for $A^* > 0.3$, the order of inception of modes A and B with respect to Re is reversed, with mode B becoming critical *before* mode A.

Previous studies have also shown that by varying a second parameter, the order of onset of the modes can change. This was observed by Ryan *et al.* (2005). As the aspect ratio of elliptical leading-edge plates was varied, the order of inception of what were dubbed mode A and mode B', was reversed (the prime indicating that the spatio-temporal symmetry was the same as mode B as described here, but that features such as critical wavelength and near-wake structure were different). However, the results presented herein are the first time that a "pure" mode B has been observed to become critical before mode A, without explicitly suppressing mode A. It has been shown that if mode A is suppressed, for example by restricting the spanwise domain size in three-dimensional simulations, the nonlinear development of mode B can lead to a period-doubling cascade leading to turbulence (Karniadakis & Triantafyllou, 1992). This suggests that for the oscillating cylinder wake, the transition to turbulence may take a different route depending on the amplitude of oscillation. A similar observation was made for the elliptical leading-edge plate by Thompson *et al.* (2006).

For an oscillating cylinder, mode QP is found to always become critical at Reynolds numbers greater than those for both modes A and B, at least for the frequency of oscillation used here. This suggests that mode QP plays a minimal role in experimental flows, as the flow will already be strongly three-dimensional and chaotic at Reynolds numbers required for its positive growth. Like the fixed cylinder, this leaves modes A and B as the two most physically relevant.

To the right of the $2S$ to $P + S$ transition in figure 6.1 (at higher A^*), the base flow is the $P + S$ wake, indicated by the diagonal hatching. With the onset of the $P + S$

two-dimensional wake mode, modes A, B and QP cease to exist. Instead, two new three-dimensional modes, named here as mode SL and mode SS , are present. The first character, S, designates that the modes are true subharmonic modes, and the second character, L or S, designate long or short wavelengths, respectively.

It is reasonable to expect subharmonic modes to arise from a base flow that does not possess Z_2 symmetry. This modification of the base flow symmetry group is known to allow true subharmonic modes, as discovered in the wake of tori by Sheard *et al.* (2003b). In the case of tori, a subharmonic mode is the first to become critical with respect to increasing Re for diameter ratios $4 \leq Ar \leq 8$. For the case of the oscillating cylinder presented here, subharmonic modes are the first to reach criticality once the base flow takes on the $P + S$ configuration.

Focusing on the transition scenario when the base flow is in the $P + S$ configuration, some interesting observations can be made. For amplitudes where $A^* \lesssim 0.67$, mode SL is shown to grow for all Re where the $P + S$ wake exists. After $A^* \simeq 0.67$, there is a region where the base flow takes on the $P + S$ pattern, where three-dimensional modes do not grow. This finding predicts that a two-dimensional $P + S$ wake is physically realisable, as has been shown by the flow visualisation at low Re of Williamson & Govardhan (2004). However, it has also been stated (Williamson & Roshko, 1988) that the $P + S$ wake mode is not observed (until much higher A^*) at $Re > 300$ in experiments, where the flow has, until now, been assumed to be three-dimensional. Therefore, if mode SL relies on the $P + S$ wake mode to materialise, it is unlikely that it will be observed in a physical experiment, even though it may instigate the breakdown to three-dimensionality. It seems that the path to turbulence where mode SL is the first three-dimensional transition will be very complex.

The two-dimensional $P + S$ wake mode is observed to be *inherently* unstable to mode SL for $0.55 \lesssim A^* \lesssim 0.67$. As the Re at the $2S$ to $P + S$ transition varies inversely with A^* , this effectively means that the Re at transition to three-dimensionality also varies inversely with A^* . This is an important finding, as it had been thought that the oscillation of the cylinder should suppress the onset of three-dimensionality; yet here, for a range of A^* , the opposite is predicted to occur.

For amplitudes where $0.67 \lesssim A^* \lesssim 0.72$, there is a small region for low Reynolds

numbers where the $P + S$ mode exists without mode SL growing. For this range mode SL is still the first three-dimensional mode to become critical. Increasing the amplitude further, beyond $A^* \gtrsim 0.72$, sees mode SL cease to ever become critical. This phenomenon is elaborated on in section 6.5.3. This “dying-out” of mode SL leaves mode SS as the first three-dimensional transition, and hence there is a sudden jump in the critical Re . Further increases in A^* sees the critical Reynolds number again decrease.

How the behaviour of these subharmonic modes will be manifested physically is yet to be seen. The fact that the $P + S$ wake mode is not observed once the flow is three-dimensional suggests that there is a complex non-linear interaction between the Floquet mode and the two-dimensional base flow, to the point where the unstable three-dimensional mode modifies the two-dimensional topology that it itself depends on for growth. There may be strong hysteretic effects present. In short, it seems that three-dimensional simulations or carefully controlled experiments are required to complete the picture for the wake flow in this region of the parameter space.

However, this linear analysis clearly renders some interesting points that can be used to guide such an investigation. One such point is that, for the oscillating cylinder, there are four different three-dimensional modes that become critical first, over successive ranges of A^* . Mode A is the leading three-dimensional mode for $A^* < 0.3$ and mode B for $0.3 < A^* < 0.55$. Following the transition to the $P + S$ wake mode, mode SL is the first to become critical for $0.55 < A^* < 0.72$, and finally mode SS for $A^* > 0.72$. The order of inception of the different modes is summarised in table 6.1. This change in the mode that leads the three-dimensional transition suggests that multiple routes to turbulence may be possible in the wake of an oscillating cylinder, depending on A^* .

6.4 Three-dimensional instabilities of the $2S$ base state

In the following sections, details of each of the three-dimensional modes are presented. These include the symmetries of the modes, similarities and differences of the modes when compared to those of other bluff-body wakes, and some discussion of their physical causes and instability types.

A^* range	Mode inception order (with increasing Re)
$A^* < 0.3$	A – B – QP
$0.3 < A^* < 0.55$	B – A
$0.55 \lesssim A^* \lesssim 0.67$	$(P + S) - SL$
$0.67 \lesssim A^* \lesssim 0.72$	$P + S - SL$
$A^* > 0.72$	$P + S - SS$

Table 6.1: Mode inception order with increasing Re for successive ranges of A^* . For the ranges indicated, four different three-dimensional modes occur first. The brackets about $P + S$ denote that in this range, the $P + S$ two-dimensional mode is inherently unstable to three-dimensional perturbations.

6.4.1 Mode A

The mode A instability of the oscillating cylinder is very similar in character to mode A of a fixed cylinder. In particular, mode A retains the spatio-temporal symmetry of the base flow (in terms of the velocity field). Mode A still appears to be an instability of the primary vortex cores. This, along with the symmetry of the mode, is confirmed by inspection of figure 6.2, which shows the perturbation field streamwise and spanwise vorticity for mode A at $A^* = 0.3$, $Re = 280$ and $\lambda = 2.8D$, close to the fastest growing wavelength. The spanwise vorticity shows that the forming primary vortex at the rear of the cylinder contains both positive and negative regions of perturbation vorticity, and then a high amplitude of the perturbation field in the high-strain region between vortices. Further downstream, the perturbation is most concentrated in the primary vortex cores. This perturbation field is very similar to that for the wake of a fixed cylinder, as shown by Thompson *et al.* (2001). In that case, this perturbation field arrangement was interpreted as consisting of a cooperative elliptic instability close to the rear of the cylinder, and a downstream elliptic instability in the shed vortex cores. The similarity in the perturbation field here suggest the same mechanisms apply to mode A for the oscillating cylinder. The streamwise perturbation vorticity further highlights the spatio-temporal symmetry of mode A, with the streamwise vorticity changing sign every half period (which corresponds to the reflection of the velocity field, and therefore a change in sign of the y -component of velocity on opposite sides of the wake).

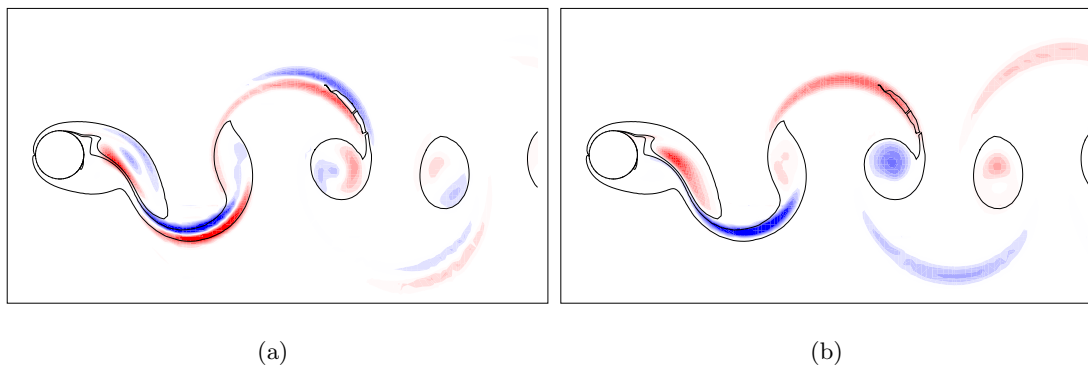


Figure 6.2: (a) Colour contours of spanwise perturbation vorticity for mode A, where $A^* = 0.3$, $Re = 280$, and $\lambda = 2.8$. Blue is negative, red is positive. Solid lines represent contours of vorticity of the base flow. This pattern is very similar to that for mode A for a fixed cylinder. (b) Contours of streamwise perturbation vorticity for the same conditions. The spatio-temporal symmetry is the same as mode A for the fixed cylinder.

Increasing the amplitude of oscillation also affects the fastest growing wavelength of mode A. The fastest growing wavelength at the critical Re versus amplitude of oscillation is plotted in figure 6.3. What is shown is that the critical λ decreases as A^* increases. This decrease is almost linear. One possible explanation is that as the amplitude increases, the vortices shed into the wake become increasingly stretched and narrowed, effectively reducing the diameter of the vortex cores. As the mode A wavelength presumably scales with the vortex core diameter (Lewke & Williamson, 1998), this wavelength is reduced by the narrower cores. This narrowing of the shed wake vortices is shown in figure 6.4. Vorticity plots of the base flow close to where mode A becomes critical are shown for $A^* = 0.1$ and $A^* = 0.5$. It is clear that the vortices are more strained, and narrower, for the higher amplitude of oscillation. In fact, the negative vortex about to be shed when $A^* = 0.5$ is 0.69 times as wide as the same vortex when $A^* = 0.1$. The critical λ when $A^* = 0.5$ is 0.73 times that at $A^* = 0.1$. This agreement is consistent with the hypothesis that the mode A wavelength scales with the vortex core width.

The elliptic instability theory developed by Landman & Saffman (1987) has been applied to fixed cylinder wakes by Lewke & Williamson (1998) and Thompson *et al.* (2001), and predicts a fastest growing wavelength for mode A of $\lambda \simeq 3D$. From Lewke & Williamson

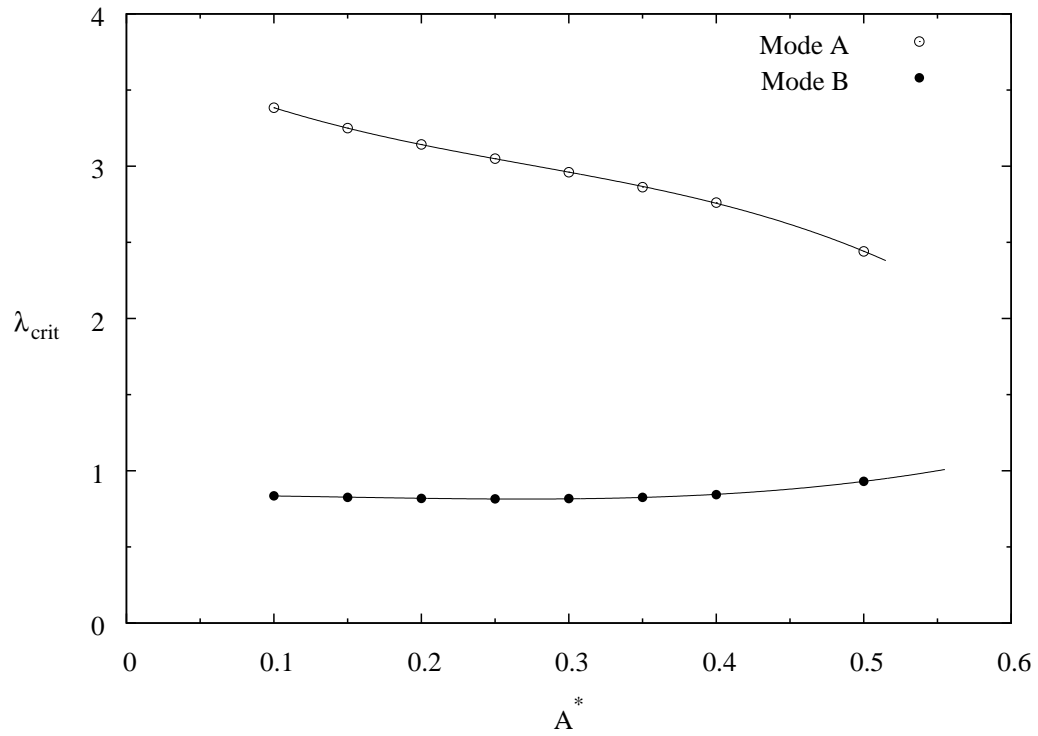


Figure 6.3: Fastest-growing wavelengths for modes A and B at criticality against A^* . Mode A has its wavelength shortened by the increasing amplitude, whereas the mode B wavelength is effectively unchanged.

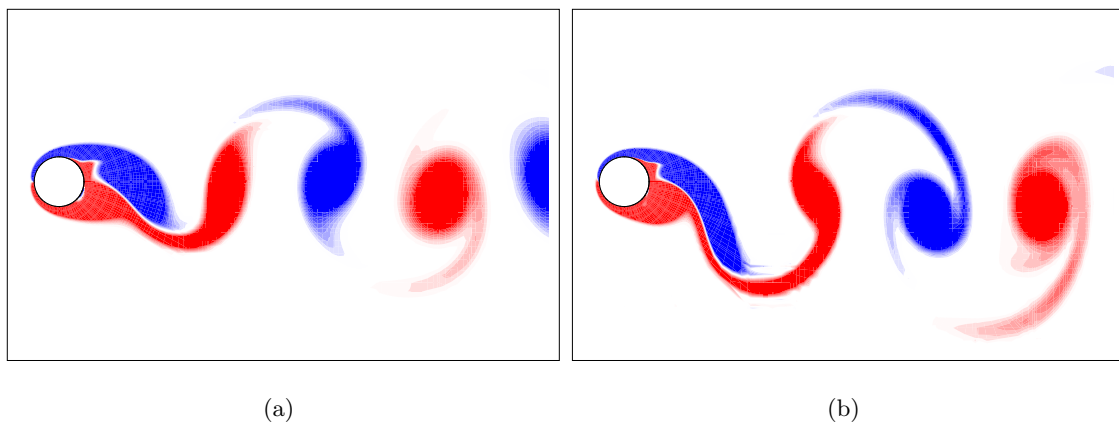


Figure 6.4: The base flow vorticity when mode A becomes critical for (a) $A^* = 0.1$, and (b) $A^* = 0.5$. It is clear that the shed vortices narrow with increasing A^* .

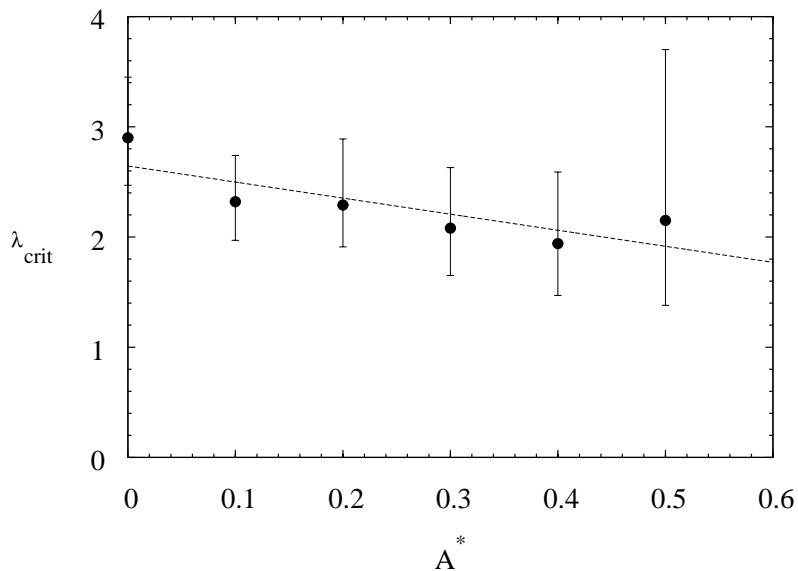


Figure 6.5: Critical wavelength variation with amplitude, as predicted by elliptic instability theory. The theory predicts shorter wavelengths as the oscillation amplitude is increased.

(1998), the fastest growing wavelength can be predicted using the relation

$$\lambda = D \left(\frac{2}{1 - \beta} \right)^{\frac{1}{2}} \tan \theta, \quad (6.1)$$

where β is the eccentricity parameter at the centre of the vortex, and θ is the angle of the wave vector to the z -axis. Values of θ were found from the numerical results presented in Landman & Saffman (1987). For validation, the method was employed on the wake of a fixed cylinder at $Re = 190$, and a wavelength of $\lambda = 2.9D$ was recovered, in close agreement with the $\sim 3D$ found in Leweke & Williamson (1998).

The results for the wavelength prediction for the oscillating cylinder at a series of amplitudes are shown in figure 6.5. It is shown that the theory predicts shorter wavelengths for the oscillating cylinder than for the fixed cylinder. It also predicts that, on the whole, the critical wavelength should decrease with increasing amplitude, as indicated by the least-squares line fit. This has been predicted to occur by the Floquet analysis, as shown in figure 6.3.

The predicted wavelength at $A^* = 0.5$ seems to break the trend of decreasing critical λ with increasing A^* . However, it should be noted that as the eccentricity becomes high (i.e. where the vortices become more elliptical), the predicted wavelength becomes very

sensitive to the value of β , as is clear from inspection of equation 6.1. For $A^* = 0.5$, the value of β calculated was $\beta = 0.95$, near the upper limit of $\beta = 1$ for elliptical flow. This accounts for the large error bars at this point. The error bars at all points were estimated by assuming an accuracy of ± 0.025 for the eccentricity, β , and an accuracy of $\pm \pi/48$ for θ . Even so, the overall trend of the theory shows a reduced wavelength with increasing amplitude, that is consistent with the present Floquet analysis. This is further evidence that mode A is (primarily) caused by an elliptic instability (Leweke & Williamson, 1998; Thompson *et al.*, 2001).

6.4.2 Mode B

As with the mode A instability, mode B was found to be analogous in structure to mode B for a fixed cylinder. The symmetry of the mode in both cases (fixed and oscillating) is the same, with the streamwise vorticity repeating every half base period, rather than every period as occurs for mode A. This results in what appears to be a continuous tube of streamwise vorticity being formed that connects the successive, but opposite-signed, base flow vortices. A plot of streamwise vorticity is shown in figure 6.6. This clearly shows the connecting “tube” of vorticity between the base flow vortices.

Also shown in figure 6.6 is a plot of the spanwise perturbation vorticity for mode B. Leweke & Williamson (1998) presented results that indicated mode B for a fixed cylinder was a hyperbolic instability of the braid shear layers between the primary vortices, partly because of the high amplitude of the instability in these regions. Evidence has also been presented by Ryan *et al.* (2005) that a centrifugal instability plays a role. Comparison of the spanwise perturbation vorticity presented in figure 6.6 with that for mode B of a fixed cylinder (Barkley & Henderson (1996), Ryan *et al.* (2005) and figure 3.5) shows that the two are very similar. It is therefore proposed that the same mechanism causes mode B for an oscillating cylinder as for a fixed cylinder.

Unlike mode A, the critical wavelength of mode B is hardly affected by the oscillation amplitude, maintaining a nearly-constant value of $\lambda \simeq 0.8$. This effect is illustrated by plotting the fastest-growing wavelength for mode B at criticality versus amplitude of oscillation as in figure 6.3. Interestingly, Sheard *et al.* (2003b) also observed an almost constant value for the fastest-growing mode B wavelength in the wake of different tori. This finding

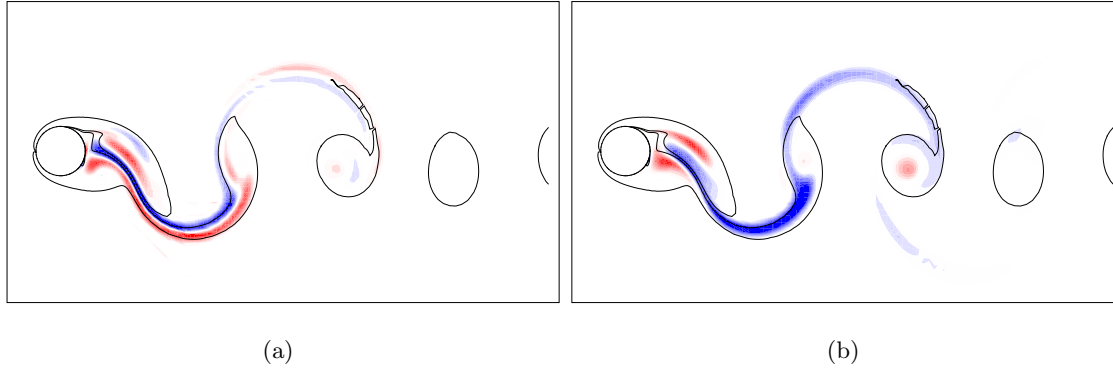


Figure 6.6: (a) Spanwise perturbation vorticity for mode B, where $A^* = 0.3$, $Re = 280$, and $\lambda = 0.85$. This pattern is very similar to that for mode B for a fixed cylinder. (b) Streamwise perturbation vorticity for the same conditions. The spatio-temporal symmetry is the same as mode B for the fixed cylinder.

is consistent with the fact that the mode B wavelength appears to scale with the thickness of the braid shear layer between the shed vortices. This shear layer thickness is not significantly affected by the amplitude of oscillation, hence the wavelength of mode B remains relatively constant.

6.4.3 Mode QP

Mode QP is influenced by the amplitude of oscillation in two different ways, as can be deduced from inspection of figure 6.1. It has previously been established that mode QP for a fixed cylinder becomes critical at $Re \simeq 377$ (Blackburn *et al.*, 2005). This result is confirmed by the validation study reported in section 3.8.4.

The first effect of the oscillation is to reduce this critical Re quite significantly, to $Re \simeq 305$ for an amplitude of oscillation of $A^* = 0.1$, close to the lowest amplitude at which synchronisation of the base wake flow and cylinder oscillation can be obtained (Koopman, 1967). However, this trend is not continued as A^* is further increased. For $A^* > 0.1$, increasing the amplitude of oscillation sees the critical Re for mode QP increase, until it has reached $Re \simeq 345$ for $A^* = 0.3$. Note that the sudden drop in the critical Reynolds number from $A^* = 0$ to $A^* = 0.1$ may be due to the shift in wake frequency from the natural Strouhal shedding frequency of the two-dimensional base flow to the applied frequency of $f^* = 0.2$.

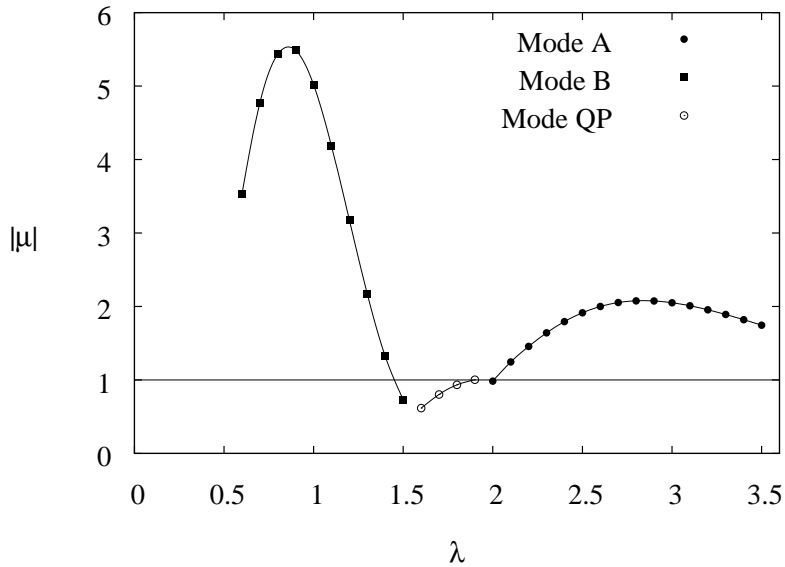


Figure 6.7: Floquet multiplier versus wavelength when $A^* = 0.3$, $Re = 350$. Mode QP is close to critical, but the growth rates of both mode A and mode B are much higher. The range of wavelengths covered by mode A encroaches on that of mode QP, meaning no turning point can be defined for mode QP with interpolation.

At amplitudes higher than $A^* \geq 0.3$, the critical values of Re and λ for mode QP become harder to determine. This is because the method employed to detect the Floquet modes returns only the fastest growing mode, and at these higher amplitudes, mode A becomes the fastest growing mode at increasingly shorter wavelengths, that intrude upon the range of wavelengths that mode QP covers. This is illustrated in figure 6.7. Plotted is the magnitude of the Floquet multiplier for the fastest growing mode over a range of wavelengths that encompass modes A, B and QP. The amplitude and Reynolds number are fixed at $A^* = 0.3$ and $Re = 350$, respectively. It is shown that the data points representing mode QP have no turning point that can be identified for the fastest growing wavelength. Therefore, the point presented as critical at $A^* = 0.3$ in figure 6.1 was obtained by extrapolating a quadratic function fitted to the data with the least-squares method.

Figure 6.7 shows that while mode QP is close to critical for these conditions, mode B and mode A both have far higher growth rates, which suggests again that it is these two modes that are the most physically relevant.

The existence of mode QP was deduced from the oscillation of the growth rate over

successive base flow periods and observation of the perturbation fields. The magnitude of the complex Floquet multiplier was deduced by taking the mean value of the periodic oscillation of the Floquet multiplier (Blackburn & Lopez, 2003).

Shown in figure 6.8 is a series of images of the perturbation field, taken one base flow period apart, for $A^* = 0.3$ and $Re = 350$. The series of images spans approximately one period of the oscillation of the Floquet multiplier. It is shown that the perturbation field almost repeats over two base periods. That it is not quite periodic is confirmed by the gradual growth and decay of the perturbation field on a much longer timescale.

This is highlighted, for instance, by comparing the initially positive region (shown in red) of perturbation vorticity inside the vortex at the immediate rear of the cylinder in the first image. Scanning down the page, comparing images two base periods apart, shows that this region gradually weakens, and eventually changes sign (appearing in blue). This illustrates that the mode is truly quasiperiodic and as such it repeats with a period incommensurate with the base flow.

As the mode is quasiperiodic, the Floquet multiplier is seen to oscillate over time when it is calculated as the growth rate from one base flow period to the next. This period was found to be relatively stable with respect to the amplitude of oscillation and Re , but it varies over a band of wavelengths. This is illustrated in figure 6.9a. The time history for a series of wavelengths is plotted for $A^* = 0.3$ and $Re = 350$. It appears that the period of oscillation is increasing with increasing wavelength, and the amplitude of the oscillation about a mean value is decreasing. This variation makes it difficult to hypothesise about the possible physical mechanisms behind this instability, due to the fact that it grows with a maximum at different places at different times. Approximating the full complex multiplier by including frequency information from a point in the wake shows that the mode crosses the critical value of $\mu = 1$ with a complex-conjugate pair of multipliers in the vicinity of the negative real axis. This again reinforces that the mode is close to, but not, subharmonic.

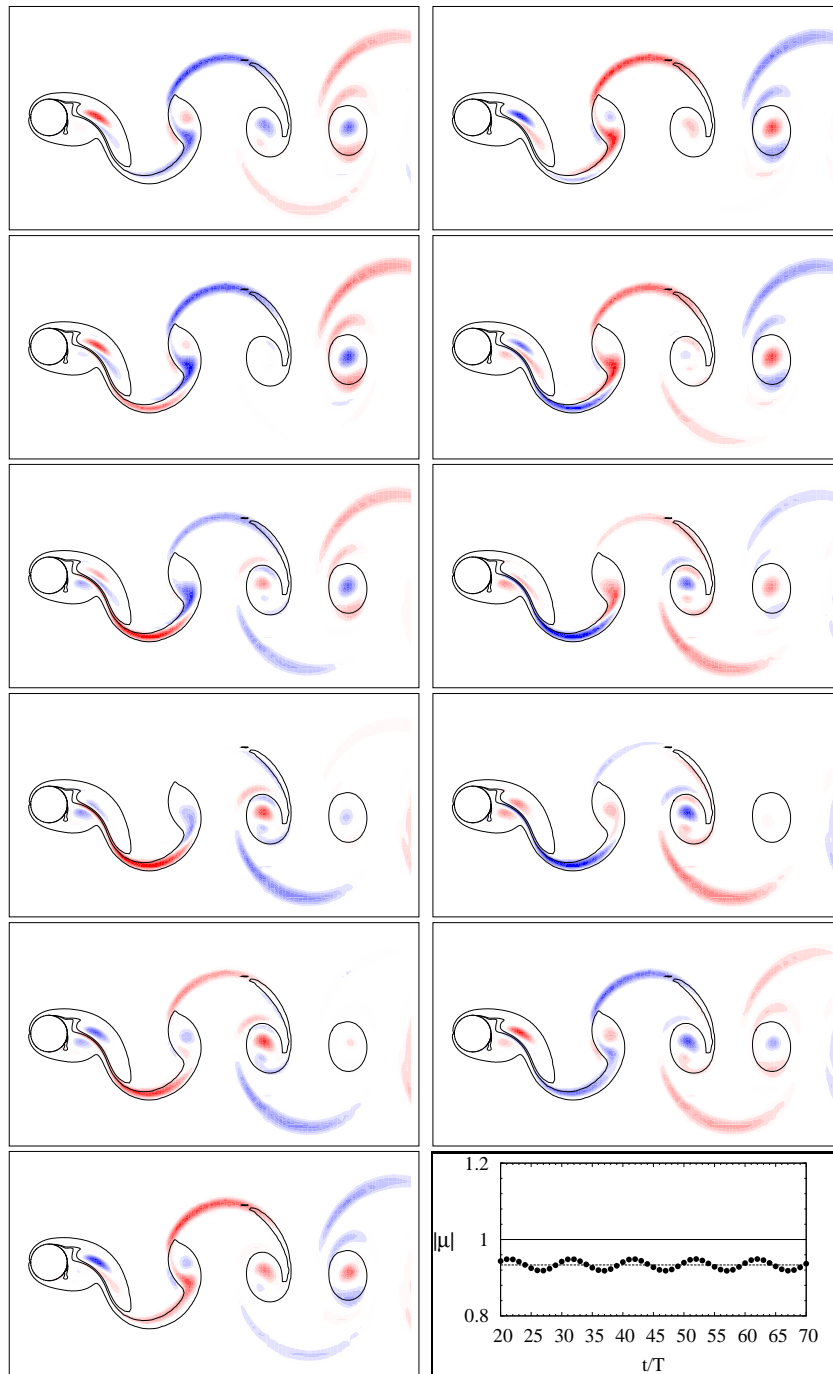


Figure 6.8: Streamwise vorticity of the quasiperiodic mode, when $A^* = 0.3$, $Re = 350$, and $\lambda = 1.8$. Images are set at one base flow period apart, and read left to right, bottom to top. It is shown that the mode almost repeats every two base periods, except for the growth and decay of the modes in the free shear layers connecting the base flow vortices. The plot in the bottom right-hand corner shows the oscillation of the Floquet multiplier over time. The series of images covers approximately one period of this oscillation.

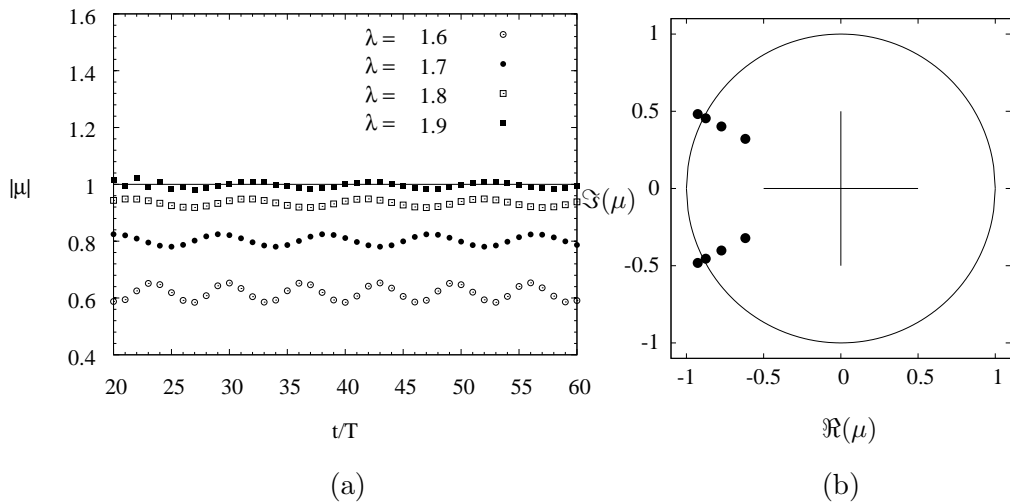


Figure 6.9: (a) The history of the Floquet multiplier for the quasiperiodic mode, when $A^* = 0.3$, $Re = 350$. The period of the oscillation becomes slightly longer with increasing λ and the amplitude of the oscillation about the mean decreases, until at $\lambda \simeq 1.9$, it appears that the oscillation has almost disappeared. (b) The same data with the complex multiplier reconstructed from a measured perturbation frequency in the wake, presented on the complex plane. The circle denotes the unit circle. The proximity of the complex-conjugate pairs of multipliers to -1 on the real axis again reveal the mode is close to, but not, subharmonic.

6.5 Three-dimensional instabilities of the $P + S$ base state

6.5.1 Mode SL : The first subharmonic mode

The first subharmonic mode detected after the transition to the $P + S$ shedding mode has been dubbed mode SL . Here the “S” designates that the mode is subharmonic, and “L” indicates that this mode has a longer wavelength than the second subharmonic mode, which is discussed in section 6.5.2. An example of the spanwise perturbation vorticity of this mode is shown in figure 6.10. Four images are shown, taken at half-period intervals (the cylinder is at its zero displacement position in each image). As well as illustrating where the mode grows, the subharmonic nature of the mode is highlighted by comparing the images that are separated by a full period; i.e., by comparing the top images to the bottom images. It is shown that over one period, the structure of the mode is the same except for a sign change of the perturbation field (expressed as a change of colour).

Inspection of figure 6.10 shows that the mode originates in the region between the forming vortices in the near wake. However, this does not happen every half-cycle, but instead occurs only in the half during which the strong vortex of the pair of vortices in the $P + S$ wake (the vortex that does not split) is shed. This coincides with the “up”-stroke in the images of figure 6.10, and is demonstrated by the high levels of perturbation vorticity in this vortex in the leftmost images in this figure. As this vortex proceeds to roll up and is shed into the wake, the perturbation is transferred to the vortex core, as demonstrated by the perturbation vorticity distribution in the rightmost images of figure 6.10. The mode appears to be quickly dissipated downstream.

A true subharmonic mode was found in the wake of tori by Sheard *et al.* (2003b), that was later demonstrated to lead to a period-doubling bifurcation (Sheard *et al.*, 2005). While even the two-dimensional wake topology is different in the ring wake compared to the oscillating cylinder, comparison of the perturbation fields seems to indicate that mode C in the wake of the torus and mode SL in the wake of an oscillating cylinder are similar in some respects. However, this similarity is not enough to deduce that they are attributable to the same or a similar physical mechanism at this stage. This is despite a fairly close agreement in the fastest growing wavelength of the two modes, with mode C in the torus wake growing fastest around $\lambda = 1.6$, and mode SL described here growing fastest around

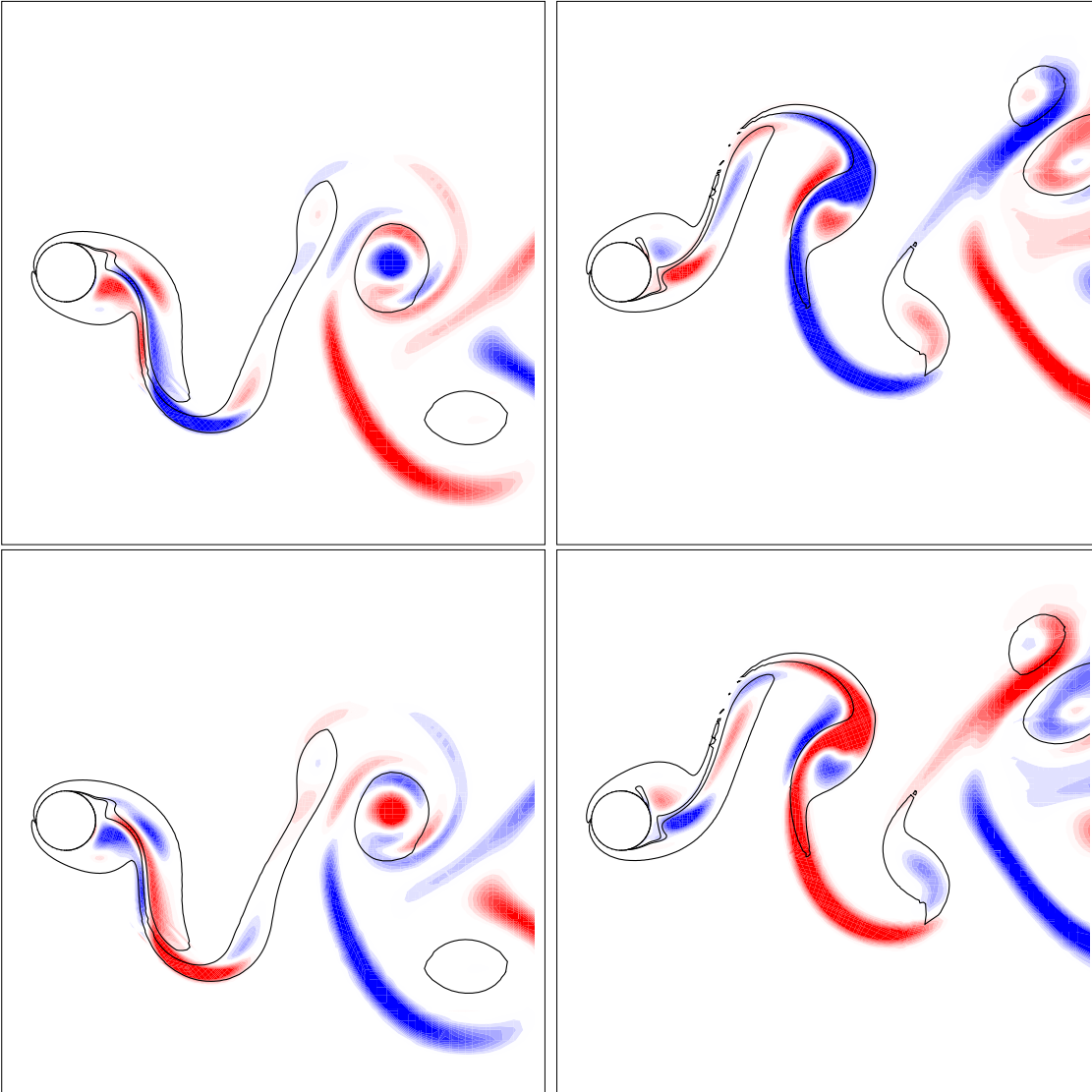


Figure 6.10: Streamwise perturbation vorticity for mode SL , when $A^* = 0.70$, $Re = 205$ and $\lambda = 1.4$. The images are taken half a period apart, reading left to right.

$\lambda = 1.4$.

6.5.2 Mode SS : The second subharmonic mode

The second subharmonic mode has been dubbed mode SS . Here, the first “S” designates that the mode is subharmonic, and the second “S” signifies that the mode has a shorter wavelength than mode SL , discussed previously in section 6.5.1. Its near wake structure, in terms of perturbation spanwise vorticity, is shown in figure 6.11. The spanwise vorticity clearly shows where the mode is at its strongest. Again, the subharmonic nature of the mode is illustrated by comparing the top images to the bottom images, and observing that over one period, the mode structure is the same except for a change in sign.

Figure 6.11 shows that mode SS appears to originate in the forming stronger vortex of the pair of vortices in the $P + S$ configuration (the vortex that does not split), during the “up”-stroke of the examples shown in figure 6.11. However, the mode does not remain focused in this vortex. It is stretched out and transferred to the forming vortex of the next half-cycle (the vortex that does split), during the “down”-stroke. During the splitting process, the vortex becomes highly strained and very narrow. It is in this region of the flow that the mode is strongest, as can be deduced from the high levels of perturbation vorticity in this region in all of the images of figure 6.11.

This is a distinguishing feature between the two subharmonic modes, mode SL and mode SS . Mode SL is supported primarily by the vortex that does not split, whereas mode SS is supported by the vortex that does split. The critical wavelength of mode SS is quite short, around $\lambda = 0.75$. This wavelength can be associated with the very narrow, highly strained vortex structure of this splitting vortex in the $P + S$ wake.

6.5.3 Behaviour of the subharmonic modes with increasing A^*

From amplitudes where the $2S$ to $P + S$ transition occurs, until $A^* \simeq 0.72$, mode SL is the first three-dimensional mode to become critical. In fact, for values of $A^* \lesssim 0.67$, mode SL is predicted to grow for all values of Re where the $P + S$ shedding mode is observed. In other words, it is predicted that for $A^* \lesssim 0.67$, the $P + S$ shedding mode will never be observed as a pure two-dimensional shedding mode experimentally, regardless of Re . It is expected that as soon as the $P + S$ mode of shedding develops, mode SL will begin to

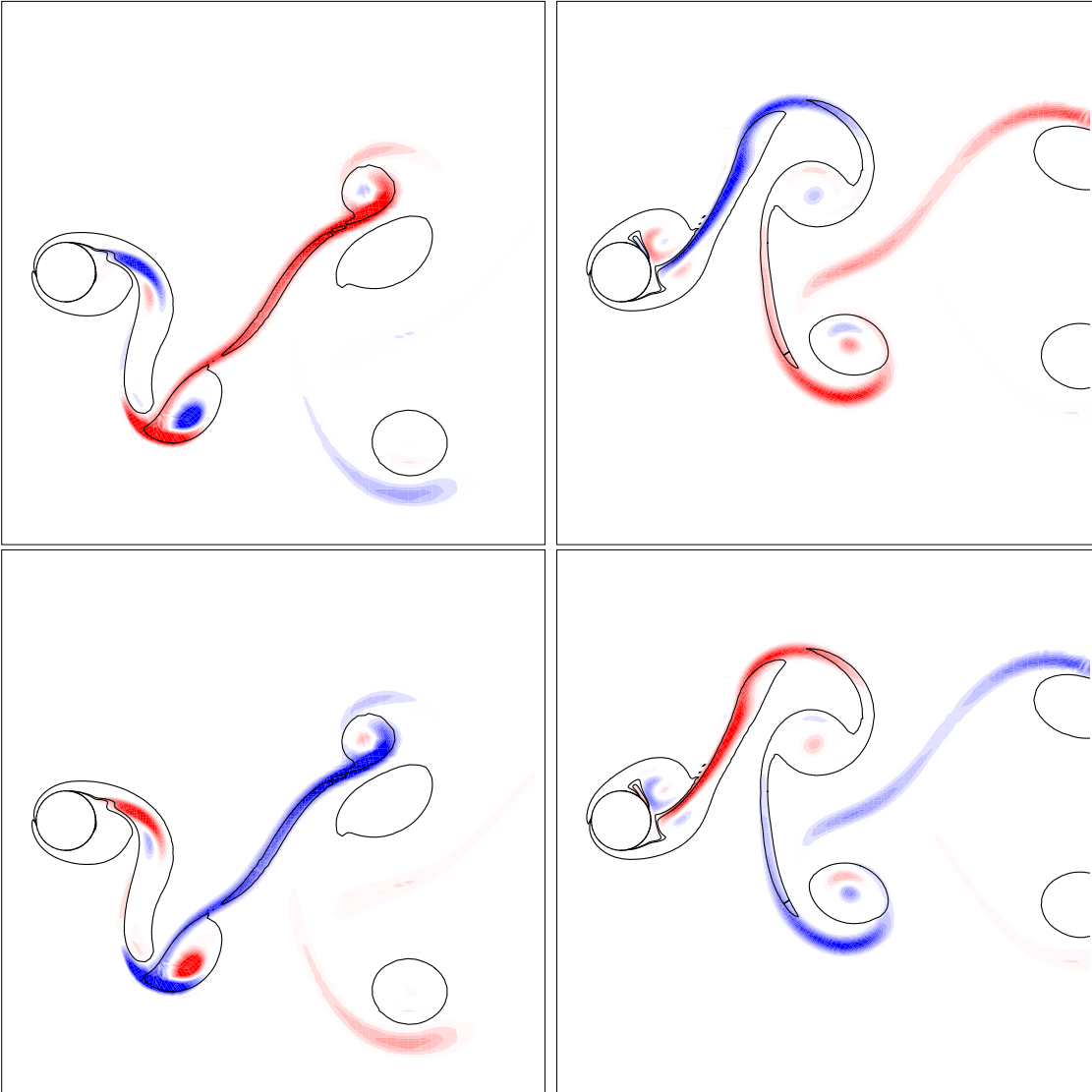


Figure 6.11: Streamwise perturbation vorticity for mode SS when $A^* = 0.75$, $Re = 260$ and $\lambda = 0.70$. The images are taken half a period apart, reading left to right.

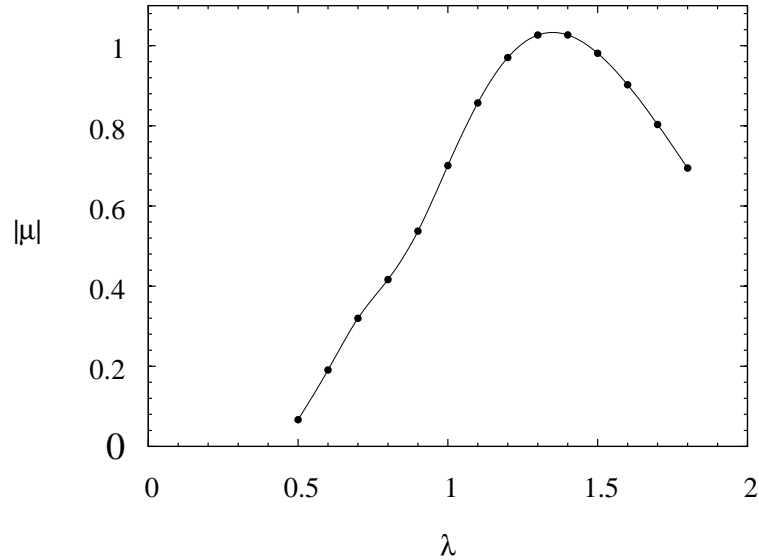


Figure 6.12: Floquet multiplier versus wavelength when $A^* = 0.7$, $Re = 205$. One continuous curve is resolved over the range $0.5 < \lambda < 2.0$. This curve is representative of mode SL . For $\lambda > 2.0$, another quasiperiodic mode is resolved.

grow, introducing three-dimensionality into the flow.

For $A^* \leq 0.72$, mode SL is the only subharmonic mode resolved using the current method, as it is faster growing than mode SS over all wavelengths tested (see section 3.7 for an explanation of how modes are resolved for a particular wavelength). This effect is highlighted in figure 6.12. It is shown that one continuous curve of multipliers is returned over the wavelength domain $0.5 < \lambda < 2.0$ when $A^* = 0.70$. This fact, along with careful inspection of the perturbation field at the shorter wavelengths where mode SS might be expected to be observed, confirms that mode SL is the fastest growing over this entire range of λ . An example perturbation field at $\lambda = 0.7$ is shown in figure 6.13. Comparison of this figure with figure 6.10 shows that it is indeed mode SL , and not mode SS , dominating even at these low values of λ .

For $\lambda > 2.0$, a seemingly quasiperiodic mode exists. This mode has a highly variable period, that is dependent on A^* , Re , and λ . However, like mode QP emanating from the $2S$ wake mode, it seems to play a secondary role physically, and never becomes critical before either mode SL or mode SS . It is possible that the role this mode plays increases in importance for other oscillation frequencies.

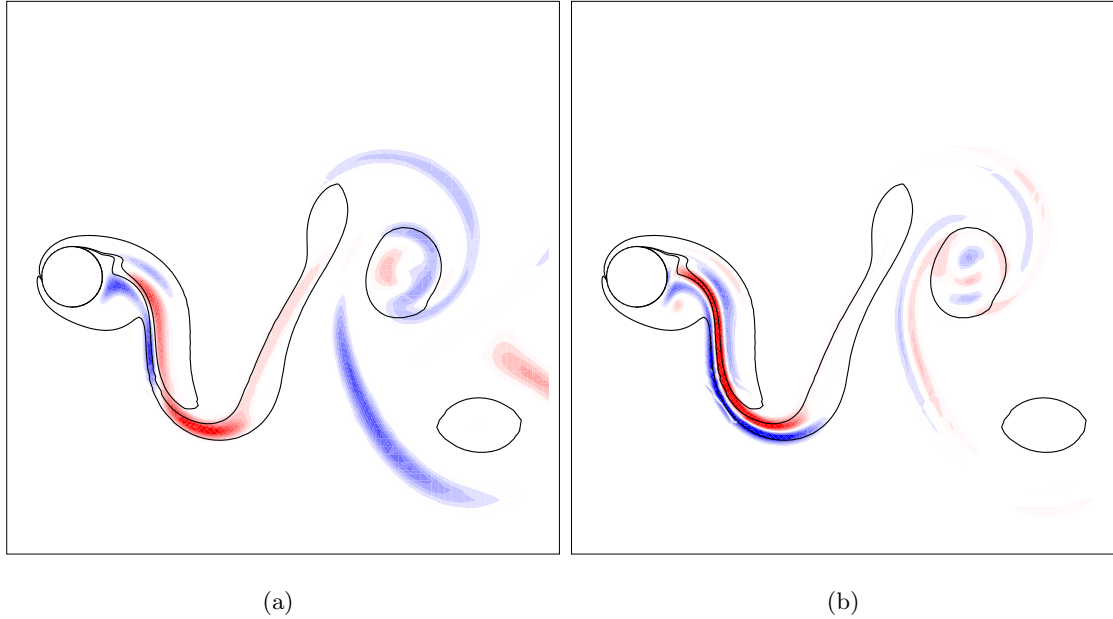


Figure 6.13: (a) Streamwise and (b) spanwise perturbation vorticity when $A^* = 0.7$, $Re = 205$ and $\lambda = 0.70$. Comparison with figures 6.10 and 6.11 show that this is in fact mode SL .

Increasing the amplitude to $A^* = 0.75$ sees the growth rate of mode SL decrease enough to allow the resolution of mode SS over the short wavelength range $0.5 < \lambda < 0.9$. Mode SS is clearly present, with the relevant change in perturbation field structure occurring over this wavelength range. The magnitude of the Floquet multiplier is plotted for all wavelengths for this amplitude at $Re = 260$ in figure 6.14. Comparison with figure 6.12 clearly shows the emergence of mode SS at this slightly higher amplitude.

The development of each of the subharmonic modes progresses rapidly over a very small amplitude range from $A^* = 0.7$ to the point where by $A^* = 0.75$, the situation has changed dramatically. The major change is that, whilst mode SL was previously completely dominant, it now ceases to reach a critical state, and is therefore predicted to never grow. This suggests that, physically, mode SL will have no effect for amplitudes where $A^* > 0.75$. Also, while mode SS continues to become critical, this happens at a significantly higher Re than mode SL , at amplitudes only slightly smaller. This effect is made clear through reference to figure 6.1. A sudden jump in the curve defining the transition from two-dimensional to three-dimensional flow is seen to occur at $A^* \simeq 0.72$.

The observation that mode SL never becomes critical at $A^* = 0.75$ is demonstrated

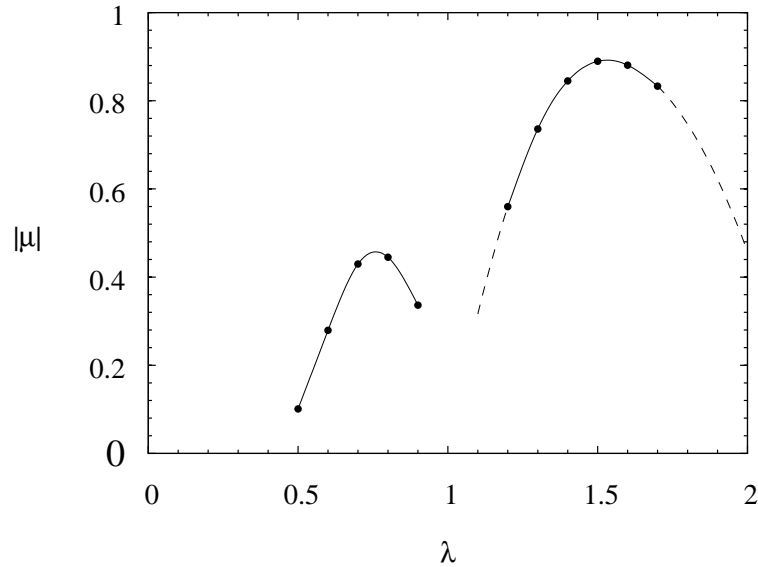


Figure 6.14: Floquet multiplier versus wavelength when $A^* = 0.75$, $Re = 230$. Two subharmonic modes are clear, with mode SS occupying the bandwidth $0.5 < \lambda < 0.9$, and mode SL occupying $1.0 < \lambda < 2.2$.

by plotting the highest value of μ returned for a given Re for mode SL at this amplitude. Such a plot is shown in figure 6.15. This shows that initially, the growth rate of mode SL increases with increasing Re . However, this trend slows, and eventually reverses. For $Re > 225$, the growth rate of mode SL decreases with increasing Re . This trend continues so that, at much higher values of Re , mode SL is not resolved at all.

Further increases in the amplitude of oscillation see mode SL continue to weaken, leaving mode SS as the only mode that becomes critical. However, increasing A^* has the effect of decreasing the critical Re of mode SS . This is a somewhat unintuitive result; it seems natural to think that an increased amplitude of oscillation should have the effect of aligning the wake vortices with the span of the cylinder, strengthening the wake vortices and therefore suppressing the onset of three-dimensionality. This has been shown to be the case for the $2S$ shedding mode. However, this does not hold for the $P + S$ shedding mode, and mode SS is seen to become critical at a lower Re as A^* is increased, at least over the range of amplitudes investigated here.

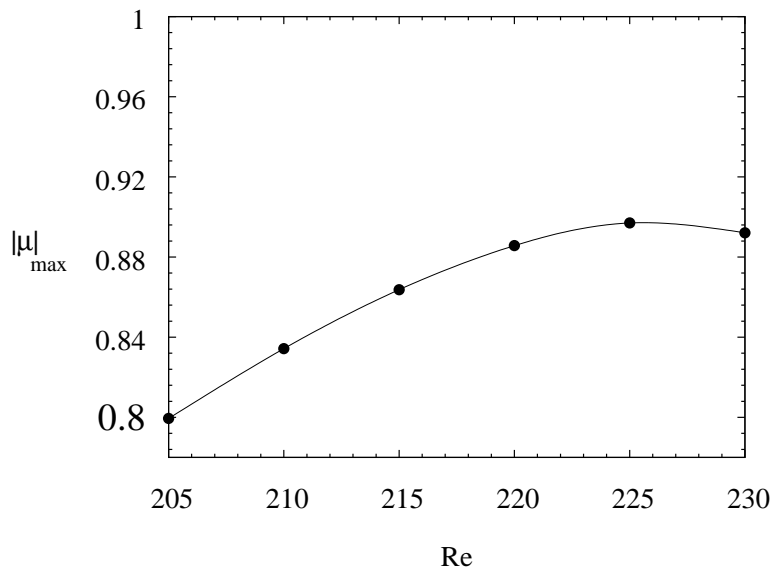


Figure 6.15: Maximum growth rate for mode SL versus Re when $A^* = 0.75$. It is clear that for $Re > 225$, the growth rate decreases with increasing Re . It is also clear that the mode never becomes critical.

6.6 Floquet stability analysis summary

Several important contributions towards an improved understanding of wakes from oscillating bodies have been presented. Most importantly, the effect of transverse oscillation on the transition to three-dimensionality in the wake of a cylinder has been quantified. It was found that synchronised oscillation at close to the natural shedding frequency can delay the onset of three-dimensionality until the Reynolds number reaches $Re = 280$. Furthermore for $A^* > 0.3$, the transition occurs through a different linear mode (mode B) than for the fixed cylinder (mode A), possibly strongly affecting the transition to fully turbulent flow. This change occurs due to a damping effect on the initial linear mode due to changes in the scale of the wake vortices.

At higher oscillation amplitudes ($A^* > 0.55$) the two-dimensional base flow changes from a $2S$ to a $P+S$ wake. This alters the three-dimensional transition completely, since modes A and B are bifurcations from the $2S$ state. In fact, two new three-dimensional modes arise, modes SL and SS , both of which are subharmonic. For amplitudes where $A^* \lesssim 0.67$, the $P+S$ wake is inherently unstable to mode SL , implying that a *two-dimensional* $P+S$ wake mode cannot be physically realised over this amplitude range without artificially imposing

the restriction to two dimensions. For amplitudes up to $A^* \lesssim 0.72$, mode SL becomes critical first. However, mode SL ceases to become critical for $A^* > 0.72$, leaving mode SS as the first-appearing three-dimensional mode.

Thus, four three-dimensional modes have been shown to lead the transition to three-dimensionality, including two previously unidentified modes, depending of the amplitude of oscillation over the range of amplitudes tested. These results therefore support the fourth hypothesis of this thesis. This may have a profound influence on the routes to turbulence in the different regimes.

CHAPTER 7

THE PRIMARY HOPF BIFURCATION OF AN ELASTICALLY-MOUNTED CYLINDER

7.1 Introduction

This chapter reports on results investigating the primary Hopf bifurcation in the wake of an elastically-mounted cylinder. Put simply, the Hopf bifurcation is where a periodic, time-dependent state first becomes possible. Often, when this occurs, the periodic state becomes the only stable state, so that the Hopf bifurcation coincides with a transition from steady to periodic flow.

This model has been used with some success to model Hopf bifurcations in bluff-body wakes before. Provansal *et al.* (1987) and Dušek *et al.* (1994) used this approach to model the transition in the wake of a fixed cylinder, and Le Gal *et al.* (2001) and Thompson & Le Gal (2004) employed it to model the oscillating wake behind a driven oscillating cylinder. In their driven oscillation model, a forcing term was incorporated into the system, effectively treating the cylinder oscillation as a forcing term on a wake oscillator.

The Stuart–Landau model is effectively an equation describing the growth of the amplitude of a periodic solution. It can be expressed as

$$\frac{dA}{d\tau} = \sigma_l A + l_c |A|^2 A + \gamma |A|^4 A \dots \quad (7.1)$$

where A is some parameter that characterises the amplitude of the arising periodic mode, and σ_l , l_c , and γ are, when considering the model as an amplitude equation, real constants.

In fact, when this equation is truncated to only include terms of up to third order, it represents the normal form equation for the supercritical Hopf bifurcation (Seydel, 1994). A normal form is the simplest equation that still describes the behaviour of the bifurcation, namely an exchange of stability from a fixed point equilibrium (a steady-state solution) to a stable limit cycle, or periodic oscillation.

If the bifurcation being modelled is subcritical, equation 7.1 must include up to at least quintic terms (as presented in equation 7.1) to capture the nature of the transition. An explanation of what it means for a mode to be supercritical or subcritical, and why higher-order terms are required to model the subcritical case, is given below.

In the context of bifurcation theory, the term “critical” takes on a specific meaning. A supercritical Hopf bifurcation is one in which the original, steady-state solution becomes unstable, and the new periodic solution suddenly arises at the same value of some control parameter, known as the bifurcation point. In this way, there is only ever one stable solution for any given value of the control parameter. Conversely, a subcritical transition is one in which two solutions can be simultaneously stable. Which solution is settled on by the system can depend on aspects of the problem such as initial conditions, or the direction of approach of the control parameter to the bifurcation point (whether the control parameter is increased or decreased). Often in fluid dynamics problems, and particularly in bluff-body flows, the control parameter governing this bifurcation is the Reynolds number, Re .

The concept of subcritical and supercritical transitions is more easily understood when bifurcation diagrams are introduced. For a single control parameter problem, these diagrams consist of plots of a measure of the amplitude of the solution (or mode), against the control parameter. For a bluff-body wake flow such as that considered here, a suitable measure of amplitude may be either the maximum transverse velocity of the flow at a point on the wake centreline, or the lift force on the body. While, in general, it is best to use a global quantity when investigating global transitions (such as the Hopf bifurcation investigated here), it has been previously established by Thompson & Le Gal (2004) that this transition is in fact global, and that if the wake is found at any point to undergo the transition, the transition will occur everywhere (albeit with phase differences). Therefore, if the purpose of the investigation is to establish at which Re the Hopf bifurcation occurs, or whether it is subcritical or supercritical, it is adequate to use transverse velocity measurements on the

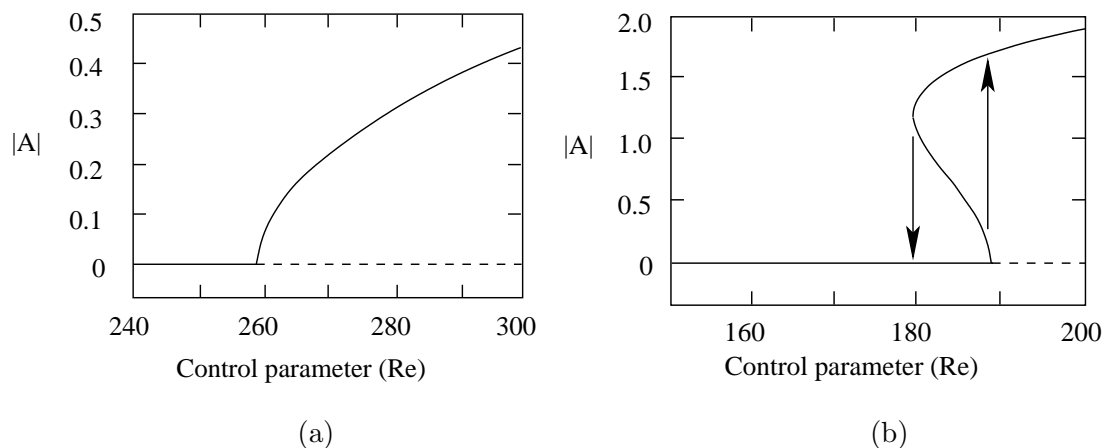


Figure 7.1: Examples of bifurcation diagrams for Hopf bifurcations. (a) Supercritical bifurcation, where there is a simple exchange of stability between modes at the bifurcation point, and the periodic mode has only one possible amplitude for each value of the control parameter. This requires only two terms to be described. (b) Subcritical bifurcation, where there is a range of the control parameter over which both modes are stable, and the periodic mode exhibits two possible magnitudes of amplitude where it is stable. This type of behaviour requires at least three terms to be described, and forms the basis of hysteresis, as indicated by the arrows. The two examples shown are for the mode B and mode A three-dimensional transitions in the wake of a fixed cylinder, reproduced from data in Barkley *et al.* (2000).

wake centreline as a measure of amplitude, or norm, of the bifurcating mode.

Example sketches of bifurcation diagrams for a supercritical and subcritical bifurcation are shown in figure 7.1. The supercritical transition is shown first, as it is the simpler of the two. In the case of the supercritical transition, it is shown that there is simply an exchange of stability from the steady-state, zero-amplitude mode, to the periodic, finite-amplitude mode at the bifurcation point. However, the situation is more complicated for the subcritical transition. Not only is there a range of the control parameter where both modes are stable, but over this range there are two theoretically possible magnitudes of amplitude for the periodic mode.

Consideration of the bistable amplitude behaviour of the subcritical bifurcation, and some manipulation of equation 7.1, shows the necessity of retaining higher-order (up to quintic) terms when modelling such bifurcations. The manipulation required is to divide

equation 7.1 through by a factor of A , and then to simplify the expression of the resulting left-hand side. This leads to equation 7.1 being expressed as

$$\frac{d \ln A}{d\tau} = \sigma_l + l_c |A|^2 + \gamma |A|^4 \dots \quad (7.2)$$

which is simply a polynomial in $|A|^2$. At saturation, the periodic mode must reach a stable amplitude, resulting in the left-hand side of equation 7.2 being zero. In the case of subcritical transition, there must be two values of $|A|^2$, and therefore two values of $|A|$, that satisfy this equation in the neighbourhood of the bifurcation, as shown in figure 7.1. For this to be possible, equation 7.2, and therefore equation 7.1, must have at least three terms (therefore truncating only after the quintic term) to admit a quadratic solution possible of two real roots.

In the case of a supercritical transition, two roots are not required, as the magnitude of amplitude can only take on one value for a given value of the control parameter. Therefore, only a linear solution with a single root is needed. A linear solution is possible with only two terms, and equation 7.1 can be truncated after the cubic term.

Regardless of the nature of the bifurcation, σ_l represents the initial linear growth. This coefficient must be positive if the mode is to grow from infinitesimal perturbations. Because of this fact, the coefficient of at least the highest-order term remaining in equation 7.1 after truncation must be negative, if the amplitude is to eventually saturate to a constant, non-zero value.

This leads to a robust way of identifying the nature of a given bifurcation. If the bifurcation is supercritical, $\frac{d \ln A}{d\tau}$ must be a linear function of $|A|^2$, and the value of l_c must be negative. Because of this fact, l_c is often referred to as the Landau constant.

The study here has measured the growth and eventual amplitude of the periodic wake behind an elastically-mounted cylinder constrained to oscillate transverse to the freestream direction. Even though it may appear that the elastically-mounted cylinder and the wake should be considered as two separate, but coupled oscillators, the single equation represented in equation 7.1 was deemed sufficient for three major reasons. First, the work of Le Gal *et al.* (2001) and Thompson & Le Gal (2004) showed that for a driven cylinder, the global bifurcation is supercritical, and as such is non-hysteretic, indicating there should be only a single mode amplitude that the wake can “lock” to. Second, the results presented earlier in section 5.2.7 showed that for low values of Re , only periodic oscillation occurs,

with no evidence of the quasiperiodic or chaotic regimes. Third, the results of Mittal & Singh (2005), and to some extent Singh & Mittal (2005), show that bifurcation appears to occur at values of Re lower than that for a fixed cylinder. All of these factors indicate that the elastically-mounted cylinder and wake act as a single system, with a single synchronised frequency of response, justifying the use of a single equation model. The quantity used to characterise the mode amplitudes is the transverse velocity at a point on the wake centreline.

This study has used the Stuart–Landau model to investigate the nature of the primary Hopf bifurcation of the elastically-mounted cylinder wake. It was found that while the critical value of Re for this transition was significantly lowered by the presence of the elastic mounting (when compared to a rigidly-mounted cylinder wake), the bifurcation remains supercritical. It is conjectured that the lowering of the critical value of Re is due to a feedback effect between a local absolute instability and the elastically-mounted cylinder.

7.2 A definition of the problem studied

While the major control parameter when considering the primary Hopf bifurcation in bluff-body wakes is the Reynolds number, the elastically-mounted cylinder presents a problem with multiple variables. As well as the Reynolds number, Re , the mass ratio m^* , mechanical damping ratio ζ and the spring stiffness in the form of natural frequency f_N need to be considered. The following steps were taken to determine the effect of the major control parameter, Re .

The mass ratio was kept constant at $m^* = 1$. This value was shown in chapter 5 to result in high-amplitude oscillations for $Re = 200$. While the low value of m^* admits high-amplitude oscillations, it has not been set at the limit of $m^* = 0$, so as to retain an inertial term in the cylinder equation of motion. This implies that a natural frequency can be defined for the system, and therefore to retain the possibility of a finite parameter range for synchronisation to occur.

To admit the highest possible oscillations in the synchronised region, all mechanical damping was removed from the system, so that $\zeta = 0$. Very low values of ζ have little effect on the response characteristics of the cylinder during vortex-induced vibration, except

to slightly reduce the amplitude of oscillation. Damping was completely removed for these simulations as the focus was on identifying where self-sustaining oscillations first occur, and it was envisaged this would occur for most vigorously for zero damping.

For each value of Re tested, the spring stiffness was set such that the ratio of the natural frequency of the cylinder system in fluid to the predicted Strouhal frequency was unity, i.e. $f_N/f_{St} = 1$. A predicted value of Strouhal frequency was required as a true Strouhal frequency is not defined for the fixed cylinder when $Re < 46.7$, the value at which the Hopf bifurcation occurs in that situation. A predicted value was calculated by employing the three-term fit of Williamson & Brown (1998), effectively extrapolating the Strouhal curve presented previously in figure 3.2 back to lower values of Re .

The normalised transverse velocity of the flow, $v^* = v/D$, where v is the transverse velocity at a point on the wake centreline was used to characterise the amplitude of the modes involved. The measurement point was located approximately $10D$ downstream of the cylinder centre.

7.3 The nature of the Hopf bifurcation

As set out in the introduction to this chapter, whether the bifurcation is subcritical or supercritical in nature can be deduced from two factors. First, from inspection of equation 7.2, there should be only a single value of magnitude, or $|v^*|$ (as v^* is the amplitude parameter for this system), where $\frac{d \ln v^*}{d\tau} = 0$, if the bifurcation is supercritical. Further, if the bifurcation is supercritical, $\frac{d \ln v^*}{d\tau}$ should vary linearly with $|v^*|^2$. Second, as the mode must saturate to a stable amplitude from initially exponential growth, the value of the Landau coefficient, l_c , must be negative.

All of these characteristics can be checked by plotting $\frac{d \ln v^*}{d\tau}$ against $|v^*|^2$ for a given time series where the flow settles into a periodic oscillation. When started from rest, because the steady-state solution becomes unstable, the periodic mode must grow from any small perturbation, and computational noise (such as truncation error) is sufficient to act as this perturbation. This growth can be monitored, and $\frac{d \ln v^*}{d\tau}$ determined at all values of $|v^*|^2$ between zero and the eventual saturation amplitude. A typical time series of v^* is shown in figure 7.2a. From this time series, $|v^*|$ was determined by identifying the local maxima of

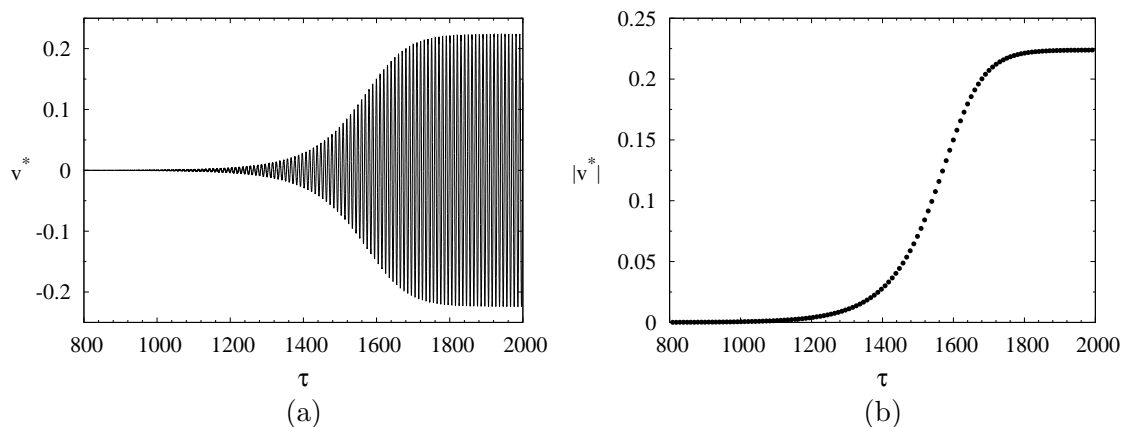


Figure 7.2: (a) The time history of v^* for $m^* = 1$, $f_N/f_{St} = 1$, and $Re = 28$. Initially, the periodic mode grows exponentially from close to zero out of the computational noise, before the higher-order terms begin to dominate, causing the amplitude of the mode to saturate. (b) The series of points extracted from the local maxima of the time history in (a). These points define $|v^*|$, and $\ln v^*$ was calculated at these points. $\frac{d \ln v^*}{d\tau}$ was derived from these points using a central-difference method.

v^* using quadratic interpolation, also allowing $\ln v^*$ to be calculated at these points. The extracted points from the time series of figure 7.2a are shown in figure 7.2b. From these points, $\frac{d \ln v^*}{d\tau}$ was derived using a central-difference method.

A crude estimate of the critical value of Re for the Hopf bifurcation to occur was found by simply performing simulations across a series of Re , and identifying which values resulted in non-zero $|v^*|$. This was done to ensure the Stuart–Landau model was only initially applied in the neighbourhood of the bifurcation, as Dušek *et al.* (1994) showed the model was applicable for values of Re within around 10% of the critical value (although Zielinska & Wesfreid (1995) showed a suitable scaling could extend this limit). The critical value was found to be close to $Re = 27$. Therefore, plots of $\frac{d \ln v^*}{d\tau}$ against $|v^*|^2$ for $28 < Re < 31$ are presented in figure 7.3. For all values of Re , a linear trend is clear. A linear least-squares fit to the data from each value of Re was performed, and the results are shown as the solid lines in figure 7.3. The data deviate slightly from being perfectly linear, with the deviation increasing with increasing Re . This is representative of the fact that the bifurcation is not perfectly modelled by the two-term Landau equation. However, the fact that the Landau constant is negative for all values is clearly apparent from the negative slope of the curves

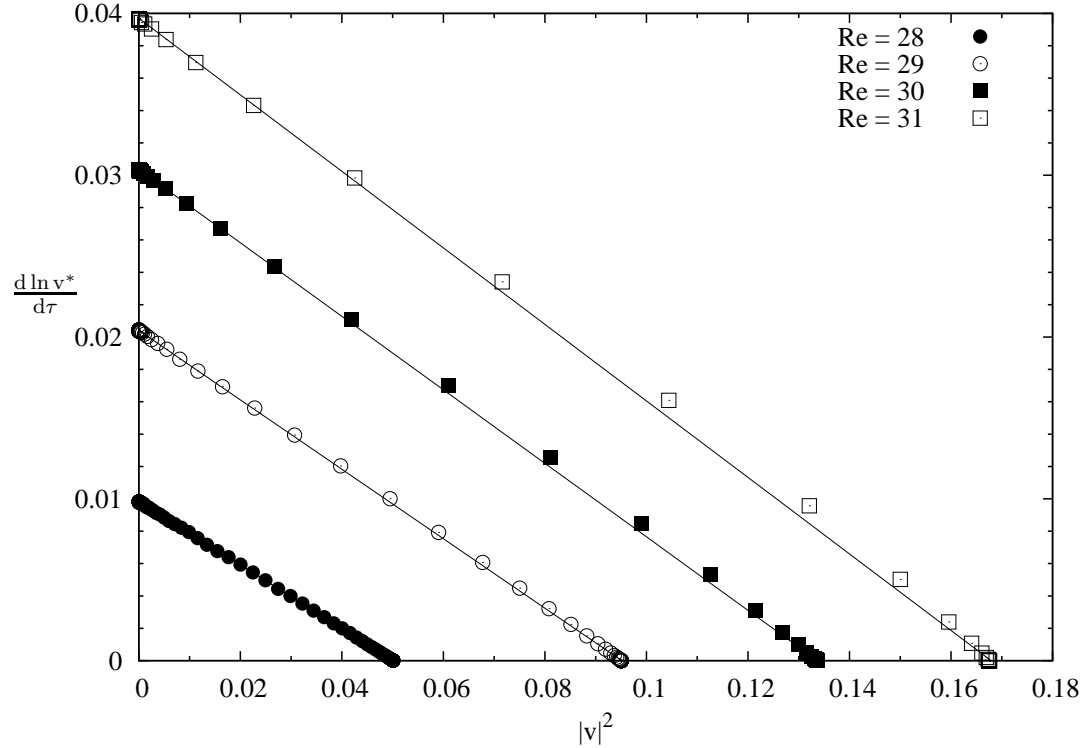


Figure 7.3: $\frac{d \ln v^*}{d \tau}$ against $|v^*|^2$ for $m^* = 1$, $f_N/f_{St} = 1$, and $Re = 28$ (\bullet), $Re = 29$ (\circ), $Re = 30$ (\blacksquare) and $Re = 31$ (\square). The solid lines are from a linear least-squares fit to the data at each value of Re . In all cases, the variation is close to linear with a negative slope, indicating that the bifurcation is supercritical. There is some slight deviation in the data from being purely linear as Re increases, which would not occur if the two-term Landau model was a perfect representation of the bifurcation.

fitted to the data. These findings indicate that the bifurcation is supercritical. The fact that the bifurcation is supercritical implies that the transition between the steady-state and periodic flow is non-hysteretic.

7.4 Determination of the critical Reynolds number

The results gained from these simulations were then used to get a more accurate estimate of the critical value of Re for the bifurcation. Provansal *et al.* (1987) stated that, according to the Landau model, the saturated amplitude of the periodic mode in the neighbourhood

of the bifurcation should vary with $Re^{1/2}$. For the problem considered here, this can be expressed as

$$|v^*| = \alpha(Re - Re_{crit})^{\frac{1}{2}} \quad (7.3)$$

where Re_{crit} is the value of Re at which the bifurcation occurs.

From this relationship, α and Re_{crit} could be found from the saturated amplitudes over a series of Re , by simply fitting a curve of the form of equation 7.3 to the data. Such a curve is presented in figure 7.4, fitted in a least squares sense to the saturated amplitudes over the range $28 < Re < 31$. It was also imposed that this curve should be normal to the x -axis at $|v^*| = 0$, to satisfy the supercritical condition of only a single amplitude corresponding to each value of Re . It is clear that the amplitudes follow the curve quite closely. From this curve, it is deduced that the critical Reynolds number is $Re_{crit} = 26.7 \pm 0.1$. Estimates of the error were gained by first only using the two closest points to the bifurcation in the curve fit, and successively including more points.

Mittal & Singh (2005), using a natural frequency of $f_N = 3.875/Re$, showed that oscillation of an elastically-mounted cylinder could occur for values of Re as low as $Re = 20$. However, no comment was made on the nature of the bifurcation leading to the oscillation. It is also difficult to analyse the data from that study for any sort of frequency information, as their natural frequency varied inversely proportionally to Re , whereas the Strouhal frequency varies proportionally with Re . Also, no explanation was given as to why the elastically-mounted cylinder undergoes this bifurcation at lower values of Re than the rigidly-mounted cylinder.

It is conjectured here that the critical Re is lower due to a feedback mechanism between an area of local absolute instability in the near wake and the cylinder. The work of Chomaz *et al.* (1988) showed that, in the wake of a fixed cylinder, it was possible to have a bifurcation to a locally absolutely unstable flow before the bifurcation to the global mode that led to Kármán shedding. It was stated that this area of local absolute instability was “necessary but not sufficient” for the onset of the global mode.

Extending this idea, Monkewitz (1988) analysed a series of idealised parallel wake profiles for their stability characteristics. It was found that for profiles representative of those found in the cylinder wake, a bifurcation to a local absolute instability occurred at around $Re = 25$. The frequency of the leading local mode found was approximately 1.34 times the

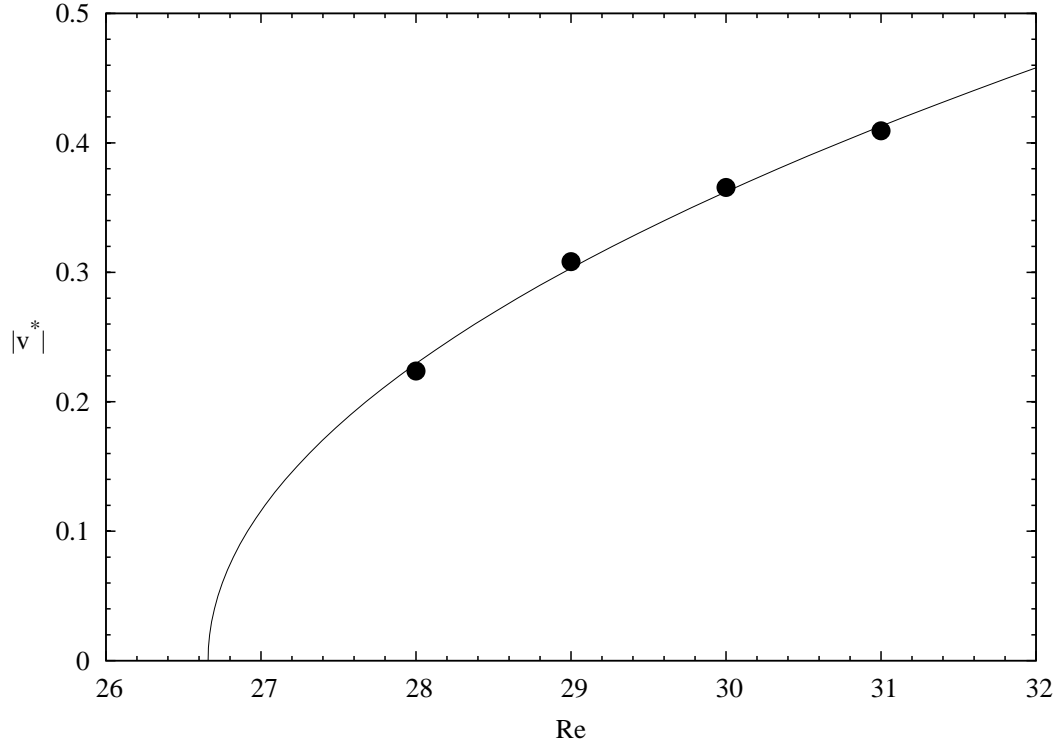


Figure 7.4: Saturated amplitude as a function of Re in the neighbourhood of the Hopf bifurcation. The line represents a least-squares fit to the data of a curve of the form of equation 7.3. From this curve, the critical value of Re where the bifurcation occurs is calculated as $Re_{crit} = 26.7 \pm 0.1$.

predicted Strouhal frequency at this value of Re .

If it is this local mode acting through a feedback mechanism that leads to the global Hopf bifurcation, it might be expected to see a resonant-type effect. This in fact does occur, as is clear from the data presented in figure 7.5. Shown here is the saturated amplitude $|v^*|$ as a function of the frequency ratio f_N/f_{St} , when $Re = 28$. It is clear that there is a dependence on frequency, which peaks at around $f_N/f_{St} = 1.4$. The dependence of $|v^*|$ on f_N/f_{St} is close to quadratic. A quadratic polynomial was fitted to the data over the range $1.0 \leq f_N/f_{St} \leq 1.6$ in a least-squares sense. It was found to represent the data well, as is shown by the solid curve in figure 7.5.

There is an obvious similarity in the natural frequency where the peak amplitude occurs, and the frequency of the local mode at onset. However, it is difficult to discern exactly what the “natural” frequency of the cylinder is, due to the variability of the added mass effect.

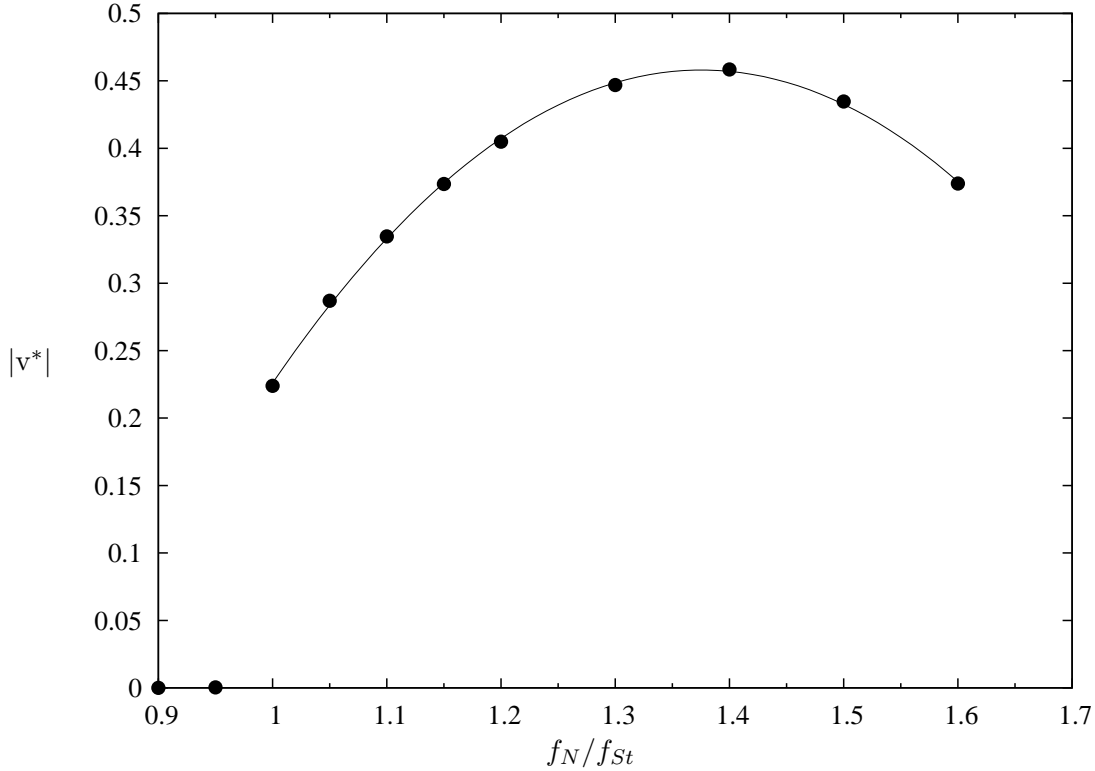


Figure 7.5: The dependence of the saturated amplitude on f_N/f_{St} , when $Re = 28$. The highest amplitude occurs at close to $f_N/f_{St} = 1.4$, similar to the ratio of the local instability frequency to the Strouhal frequency at onset, as discovered by Monkewitz (1988). Over the range $1.0 \leq f_N/f_{St} \leq 1.6$, the saturated amplitude varies close to quadratically, as indicated by the solid line obtained by fitting a quadratic in a least-squares sense.

Even for these low values of Re , the frequency of oscillation did not exactly match f_N , for the mass ratio $m^* = 1$, instead varying from a ratio of $f/f_N \simeq 1.4$ down to $f/f_N \simeq 1$ across the range of f_N/f_{St} tested. This is very similar to the behaviour exhibited at higher values of Re reported in chapter 5.

There are definite similarities between the findings of a local absolute instability of Chomaz *et al.* (1988) and Monkewitz (1988), and the onset of the global instability in the wake of an elastically-mounted cylinder. The first test of the hypothesis that it is a feedback mechanism between the local mode and the elastically-mounted cylinder would be to break the coupling, expecting the critical value of Re to rise. If the cylinder is fixed, this is obviously what happens, somewhat confirming this hypothesis. However, while the

results presented here represent a first step towards clarifying this theory, a more in-depth investigation is required before feedback as a causal mechanism for the lower critical Re can be stated with any certainty.

7.5 Hopf bifurcation summary

A Stuart–Landau model has been applied to the primary Hopf bifurcation in the wake of an elastically-mounted cylinder. The single-equation model was found to accurately capture the nature of the bifurcation, and show that the bifurcation is supercritical, confirming the fifth hypothesis of this thesis.

The critical value of Re at which the bifurcation occurs was found to be significantly lower than that for the bifurcation in the wake of a fixed cylinder. Inspection of the frequencies involved and saturated amplitudes leads to the preliminary conclusion that this lowering is possibly due to a feedback mechanism between an area of local absolute instability in the near wake and the elastically-mounted cylinder. This feedback possibly leads to the triggering of the global mode, resulting in vortex shedding and periodic cylinder oscillation.

CHAPTER 8

CONCLUSIONS

Simulations of an externally-driven cylinder, following a sinusoidal trajectory, have been conducted over a range of amplitudes and frequencies of oscillation, and Reynolds numbers. It was found that when the wake is synchronised with the cylinder oscillation, two wake modes exist, either the $2S$ mode at lower amplitudes, or the $P + S$ mode at higher amplitudes. The amplitude of oscillation at which the transition between these two modes occurs is primarily dependent on Reynolds number.

Conversely, while the value of amplitude at which the energy transfer switches from positive to negative (from the cylinder to the fluid) shows some frequency and Reynolds number dependence, the maximum amplitude for positive energy transfer is relatively independent of Reynolds number. This demonstrates that the wake mode transition is not dependent on a change of direction of energy transfer. The results also demonstrate that the $P + S$ mode can exist with a positive energy transfer for higher Reynolds numbers.

It was found that the energy transfer is primarily dependent on the frequency of oscillation at low amplitudes of oscillation, and primarily dependent on amplitude at higher amplitudes. This appears to be a direct consequence of the increasing impact of stagnation pressure with increasing amplitude.

The range of frequencies for synchronisation was also found to be dependent on Reynolds number. These findings confirm the first hypothesis of this thesis, that *wake modes, transitions and energy transfer characteristics are dependent on Re for Re where the wake of an oscillating cylinder is two-dimensional.*

Simulations of an elastically-mounted cylinder, constrained to oscillate transverse to the freestream direction have been performed. Clear evidence of three separate response regimes, in terms of the reduced velocity, was found. These three regimes consist of a quasiperiodic response, a chaotic response, and a periodic response. It has also been shown these three regimes arise when $Re > 70$. The largest peak oscillations occur in the chaotic regime, and can exceed the amplitude where energy transfer switches from positive to negative during externally-driven sinusoidal oscillation.

The evidence for these response regimes, particularly the chaotic regime, is found in the magnitude of the peak lift force, the frequency of response, the phase between lift force and cylinder displacement, and the phase space consisting of the lift force and cylinder displacement. While the branches are not immediately obvious from inspection of only the peak amplitude of displacement, there are many shared characteristics between the chaotic regime and the upper branch in higher Reynolds number flow. The findings therefore confirm the second hypothesis of this thesis, that *the origin of branching behaviour for three-dimensional vortex-induced vibration has its genesis in two-dimensional flow*.

The results from the externally-driven sinusoidal oscillation simulations and elastically-mounted simulations have been directly compared. While the periodic regime elastically-mounted simulation results compare well with the driven oscillation results, the chaotic regime results occur in regions of the parameter space that the driven oscillation predicts should not be possible. In particular, the chaotic regime can occur in regions of the parameter space that are synchronised, but with negative energy transfer. It seems that the process in the chaotic regime is more complicated than a switching between two essentially sinusoidal modes.

Further confirmation of this conclusion is found in the results using a non-sinusoidal forcing. Using a modulated driving function with the same peak amplitude as the pure sinusoidal driving saw a marked increase in peak lift force, close to that seen in the chaotic regime. These results confirm the third hypotheses of this thesis, that *pure sinusoidal oscillation is a valid approximation in the lower branch, and modulated oscillation can capture major flow features relating to force in the upper branch*.

Floquet stability analysis has been conducted to investigate the transition to three-dimensional flow in the wake of a externally-driven cylinder, following a sinusoidal trajec-

tory. It was found that while the two-dimensional base state remained in the $2S$ configuration, the three-dimensional modes that arise are the same as those for a fixed cylinder wake, namely modes A, B, and QP. However, the order of inception with respect to increasing Reynolds number is dependent on the amplitude of oscillation. For amplitudes $A^* > 0.3$, mode B becomes critical before mode A. While the two-dimensional base state remains in the $2S$ configuration, increasing the amplitude of oscillation suppresses the transition to three-dimensional flow, to a maximum Reynolds number of $Re = 280$.

With transition of the two-dimensional base state to the $P + S$ mode, the three-dimensional modes A, B, and QP cease to exist. Two previously undocumented modes, referred to here as modes SL and SS , arise, both of which are subharmonic. For amplitudes $0.55 \leq A^* \leq 0.72$, mode SL is the first to become critical. Over most of this range, the $P + S$ base state is inherently unstable to this mode, and the critical Reynolds number decreases with increasing amplitude of oscillation. For amplitudes $A^* > 0.72$, mode SL ceases to ever become critical, and mode SS leads the transition to three-dimensionality.

Four separate three-dimensional modes can lead the transition to three-dimensional flow, depending of the amplitude of oscillation, making this system a good candidate for investigating the ramifications of initial transition characteristics on the path to fully-developed turbulence. The results of this investigation confirm the fourth hypothesis of this thesis, namely that *transverse oscillation will change the nature of the transition to three-dimensionality in the wake of a cylinder*.

The initial transition to unsteady flow in the wake of the elastically-mounted cylinder has also been investigated, using a Stuart-Landau model. A single-equation model was applied to the coupled cylinder-wake system, as the simulations showed that a single frequency, periodic oscillation was the only unsteady state to arise for $Re < 40$.

It was found that the critical Reynolds number for this transition is significantly lower than that in the wake of a rigidly-mounted cylinder, confirming the findings of previous studies. Application of the Stuart-Landau model shows that the transition remains supercritical. The results also indicate that the lowering of the critical Reynolds number may be due to a feedback mechanism between the cylinder and a local absolute instability in the near wake.

The results of this investigation therefore confirm the fifth hypothesis of this thesis,

8. CONCLUSIONS

that regardless of the lowering of Re at transition, the transition to unsteady flow in the wake of an elastically-mounted cylinder remains supercritical.

BIBLIOGRAPHY

- ANAGNOSTOPOULOS, P. 1989 Numerical solution for laminar two-dimensional flow about a fixed and transversely oscillating cylinder in a uniform stream. *J. Comp. Phys.* **85**, 434–456.
- ANAGNOSTOPOULOS, P. & BEARMAN, P. W. 1992 Response characteristics of a vortex-excited cylinder at low Reynolds numbers. *J. Fluids & Structures* **6**, 39–50.
- BARKLEY, D. & HENDERSON, R. D. 1996 Three-dimensional Floquet stability analysis of the wake of a circular cylinder. *J. Fluid Mech.* **322**, 215–241.
- BARKLEY, D., TUCKERMAN, L. & GOLUBITSKY, M. 2000 Bifurcation theory for three-dimensional flow in the wake of a circular cylinder. *Physical Review E* **61**, no. 5, 5247–5252.
- BEARMAN, P. W. 1984 Vortex shedding from oscillating bluff bodies. *Annu. Rev. Fluid Mech.* **16**, 195–222.
- BENARD, H. 1908 Formation de centres de giration a l’arriere d’un obstacle en mouvement. *C.R. Acad. Sci. Paris* **147**, 839.
- BERGER, E. 1967 Suppression of vortex shedding and turbulence behind oscillating cylinders. *Phys. Fluids* **10**, No. 9, Part 2, S191–193.
- BISHOP, R. E. D. & HASSAN, A. Y. 1964 The lift and drag forces on a circular cylinder oscillating in a flowing fluid. *Proceedings of the Royal Society of London, series A* **277**, n1368, 51–75.

- BLACKBURN, H. M., GOVARDHAN, R. N. & WILLIAMSON, C. H. K. 2000 A complementary numerical and physical investigation of vortex-induced vibration. *J. Fluids & Structures* **15**, 481–488.
- BLACKBURN, H. M. & HENDERSON, R. 1996 Lock-in behaviour in simulated vortex-induced vibration. *Exp. Therm. Fluid Sci.* **12**, 184–189.
- BLACKBURN, H. M. & HENDERSON, R. 1999 A study of two-dimensional flow past an oscillating cylinder. *J. Fluid Mech.* **385**, 255–286.
- BLACKBURN, H. M. & KARNIADAKIS, G. E. 1993 Two- and three-dimensional simulations of vortex-induced vibration of a circular cylinder. In *Proceedings of the Third International offshore and polar engineering conference*. Singapore.
- BLACKBURN, H. M. & LOPEZ, J. M. 2003 On three-dimensional quasiperiodic Floquet instabilities of two-dimensional bluff body wakes. *Phys. Fluids* **15**, n8, L57–L60.
- BLACKBURN, H. M., MARQUES, F. & LOPEZ, J. M. 2005 Symmetry breaking of two-dimensional time-periodic wakes. *J. Fluid Mech.* **522**, 395–411.
- BLACKBURN, H. M. & MELBOURNE, W. H. 1997 Sectional lift forces for an oscillating circular cylinder in smooth and turbulent flows. *J. Fluids & Structures* **11**, 413–431.
- BLEVINS, R. D. 1977 *Flow-induced vibration*. Van Nostrand Reinhold Company, New York.
- BLOOR, S. 1964 The transition to turbulence in the wake of a circular cylinder. *J. Fluid Mech.* **19**, no. 2, 290–304.
- BRANKOVIĆ, M. 2004 Vortex-induced vibration attenuation of circular cylinders with low mass and damping. PhD thesis, Imperial College, University of London.
- BRANKOVIĆ, M. & BEARMAN, P. 2006 Measurements of transverse forces on circular cylinders undergoing vortex-induced vibration. *J. Fluids & Structures* **22**, 829–836.
- BRIKA, D. & LANEVILLE, A. 1993 Vortex-induced vibration of a long flexible circular cylinder. *J. Fluid Mech.* **250**, 481–508.
- CANUTO, C. 1988 *Spectral methods in fluid dynamics*. Springer-Verlag, New York.

- CARBERRY, J. 2001 Wake states of a submerged oscillating cylinder and of a cylinder beneath a free surface. PhD thesis, Monash University.
- CARBERRY, J., GOVARDHAN, R., SHERIDAN, J., ROCKWELL, D. & WILLIAMSON, C. H. K. 2002a Wake states and response branches of forced and freely oscillating cylinders. In *Proceedings of the conference on bluff body wakes and vortex-induced vibrations (BBVIV3), Port Douglas, Australia*, pp. 45–48.
- CARBERRY, J., SHERIDAN, J. & ROCKWELL, D. 2001 Forces and wake modes of an oscillating cylinder. *J. Fluids & Structures* **15**, 523–532.
- CARBERRY, J., SHERIDAN, J. & ROCKWELL, D. 2002b Vortex forces on an oscillating cylinder. In *Proceedings of IMECE: ASME International Mechanical Engineering Congress and Exposition*, pp. 1–7.
- CARBERRY, J., SHERIDAN, J. & ROCKWELL, D. 2003 Controlled oscillations of a cylinder: A new wake state. *J. Fluids & Structures* **17**, 337–343.
- CHOMAZ, J., HUERRE, P. & REDEKOPP, L. 1988 Bifurcations to local and global modes in spatially developing flows. *Physical Review Letters* **60**, no. 1, 25–28.
- CHOPRA, K. & HUBERT, L. 1964 Kármán vortex-streets in earth's atmosphere. *Nature* **203**, 1341–1343.
- DEN HARTOG, J. 1932 The vibration problems in engineering. In *Proceedings of the 4th international congress of applied mathematics*, pp. 36–53.
- DUŠEK, J., LE GAL, P. & FRAUNIÉ, P. 1994 A numerical and theoretical study of the first Hopf bifurcation in a cylinder wake. *J. Fluid Mech.* **264**, 59–80.
- FACCHINETTI, M. L., DE LANGRE, E. & BIOLLEY, F. 2004 Coupling of structure and wake oscillators in vortex-induced vibration. *J. Fluids & Structures* **19**, 123–140.
- FENG, C. C. 1968 The measurement of vortex-induced effects in flow past stationary and oscillating circular and D-section cylinders. Master's thesis, University of British Columbia.
- FLETCHER, C. A. J. 1984 *Computational Galerkin methods*. Springer-Verlag, New York.

- FLETCHER, C. A. J. 1991 *Computational techniques for fluid dynamics, vol. 1*. Springer-Verlag, New York.
- GABBAI, R. D. & BENAROYA, H. 2005 An overview of modeling and experiments of vortex-induced vibration of circular cylinders. *J. Sound & Vib.* **282**, 575–616.
- GASTER, M. 1969 Vortex shedding from slender cones at low Reynolds numbers. *J. Fluid Mech.* **38**, 565–576.
- GOPALKRISHNAN, R. 1993 Vortex-induced forces on oscillating bluff cylinders. PhD thesis, MIT.
- GOVARDHAN, R. & WILLIAMSON, C. H. K. 2000 Modes of vortex formation and frequency response of a freely vibrating cylinder. *J. Fluid Mech.* **420**, 85–130.
- GOVARDHAN, R. & WILLIAMSON, C. H. K. 2001 Mean and fluctuating velocity fields in the wake of a freely-vibrating cylinder. *J. Fluids & Structures* **15**, 489–501.
- GOVARDHAN, R. & WILLIAMSON, C. H. K. 2002 Resonance forever: existence of a critical mass and an infinite regime of resonance in vortex-induced vibration. *J. Fluid Mech.* **473**, 147–166.
- GRIFFIN, O. M. 1971 The unsteady wake of an oscillating cylinder at low Reynolds number. *J. Applied Mech.* **38 no. 4**, 729–737.
- GRIFFIN, O. M. 1980 Vortex-excited cross-flow vibrations of a single cylindrical tube. *Transactions of the ASME: Pressure vessels and Piping Division (Publ.)* pp. 158–166.
- GRIFFIN, O. M. & RAMBERG, S. E. 1974 The vortex-street wakes of vibrating cylinders. *J. Fluid Mech.* **66, p3**, 553–576.
- HARTLEN, R. & CURRIE, I. 1970 Lift-oscillator model of vortex-induced vibration. *Journal of the engineering mechanics division: Proceedings of the ASME* pp. 577–591.
- HENDERSON, R. D. 1997 Nonlinear dynamics and pattern formation in turbulent wake transition. *J. Fluid Mech.* **352**, 65–112.

- HOPF, E. 1942 Abzweigung einer periodischen Lösung von einer stationären Lösung eines differentialsystems. *Bericht der Math.-Phys. Klasse der Sächsischen Akademie der Wissenschaften zu Leipzig* **94**, 3–22.
- HOVER, F. S., DAVIS, J. & TRIANTAFYLLOU, M. S. 2004 Three-dimensionality of mode transition in vortex-induced vibrations of a circular cylinder. *Eur. J Mech B/Fluids* **23**, 29–40.
- HOVER, F. S., TECHET, A. H. & TRIANTAFYLLOU, M. S. 1998 Forces on oscillating uniform and tapered cylinders in crossflow. *J. Fluid Mech.* **363**, 97–114.
- HOVER, F. S., TVEDT, H. & TRIANTAFYLLOU, M. S. 2001 Vortex-induced vibrations of a cylinder with tripping wires. *J. Fluid Mech.* **448**, 175–195.
- HURLOUT, S., SPAULDING, M. & WHITE, F. 1982 Numerical solution for laminar two-dimensional flow about a cylinder oscillating in a uniform stream. *J. Fluids Eng.* **104**, 214–222.
- IOOSS, G. & JOSEPH, D. D. 1990 *Elementary stability and bifurcation theory*. Springer-Verlag, New York.
- JULIEN, S., ORTIZ, S. & CHOMAZ, J.-M. 2004 Secondary instability mechanisms in the wake of a flat plate. *Eur. J. Mech B/Fluids* **23**, 157–165.
- VON KÁRMÁN, T. 1911 Über den mechanismus des widerstands, den ein bewegter Körper in einer Flüssigkeit erfährt. *Göttingen Nach. Math. Phys. Kl.* pp. 509–519.
- KARNIADAKIS, G. E., ISRAELI, M. & ORSZAG, S. A. 1991 High-order splitting methods of the incompressible Navier–Stokes equations. *J. Comp. Phys.* **97**, 414–443.
- KARNIADAKIS, G. E. & SHERWIN, S. J. 2005 *Spectral/hp methods for computational fluid dynamics*. Oxford University Press, Oxford.
- KARNIADAKIS, G. E. & TRIANTAFYLLOU, G. S. 1992 Three-dimensional dynamics and transition to turbulence in the wake of bluff objects. *J. Fluid Mech.* **238**, 1–30.
- KHALAK, A. & WILLIAMSON, C. H. K. 1996 Dynamics of a hydroelastic cylinder with very low mass and damping. *J. Fluids & Structures* **10**, 455–472.

- KHALAK, A. & WILLIAMSON, C. H. K. 1997 Fluid forces and dynamics of a hydroelastic structure with very low mass and damping. *J. Fluids & Structures* **11**, 973–982.
- KHALAK, A. & WILLIAMSON, C. H. K. 1999 Motions, forces and mode transitions in vortex-induced vibrations at low mass-damping. *J. Fluids & Structures* **13**, 813–851.
- KOOPMAN, G. H. 1967 The vortex wakes of vibrating cylinders at low Reynolds numbers. *J. Fluid Mech.* **28**, 501–512.
- KRENK, S. & NIELSEN, S. 1999 Energy balanced double oscillator model for vortex-induced vibrations. *J. Eng. Mech.* **125**, 263–271.
- KREYZIG, E. 1999 *Advanced engineering mathematics (8th ed)*. John Wiley & Sons, New York.
- LANDMAN, M. J. & SAFFMAN, P. G. 1987 The three-dimensional instability of strained vortices in a viscous fluid. *Phys. Fluids* **30**, no. 8, 2339–2342.
- LE GAL, P., NADIM, A. & THOMPSON, M. 2001 Hysteresis in the forced Stuart-Landau equation: Application to vortex shedding from an oscillating cylinder. *J. Fluids & Structures* **15**, 445–457.
- LEONARD, A. & ROSHKO, A. 2001 Aspects of flow-induced vibration. *J. Fluids & Structures* **15**, 415–425.
- LEWEKE, T. & WILLIAMSON, C. H. K. 1998 Three-dimensional instabilities in wake transition. *Eur. J. Mech. B/Fluids* **17**, n4, 571–586.
- LUCOR, D., FOO, G. & KARNIADAKIS, G. 2005 Vortex mode selection of a rigid cylinder subject to VIV at low mass-damping. *J. Fluids & Structures* **20**, 483–503.
- MARQUES, F., LOPEZ, J. M. & BLACKBURN, H. M. 2004 Bifurcations in systems with Z_2 spatio-temporal and $O(2)$ spatial symmetry. *Physica D* **189**, 247–276.
- MENEGHINI, J. R. & BEARMAN, P. W. 1993 Numerical simulation of high amplitude oscillatory flow about a circular cylinder using a discrete vortex method. In *Shear Flow Conf. AIAA Pap. 93-3288, Orlando, FL, Jul. 6-9*.

- MENEHINI, J. R. & BEARMAN, P. W. 1995 Numerical simulation of high amplitude oscillatory flow about a circular cylinder. *J. Fluids & Structures* **9**, 435–455.
- MITTAL, S. & SINGH, S. 2005 Vortex-induced vibrations at subcritical Re. *J. Fluid Mech.* **534**, 185–194.
- MONKEWITZ, P. 1988 The absolute and convective nature of instability in two-dimensional wakes at low Reynolds numbers. *Phys. Fluids* **31**, no. 5, 999–1006.
- MONKEWITZ, P. 1996 Modeling of self-excited wake oscillations by amplitude equations. *Exp. Therm. Fluid Sci.* **12**, 175–183.
- MORSE, T. & WILLIAMSON, C. 2006 Employing controlled vibration to predict fluid forces on a cylinder undergoing vortex-induced vibration. *J. Fluids & Structures* **22**, 877–884.
- NAKANO, M. & ROCKWELL, D. 1993 The wake from a cylinder subjected to amplitude-modulated excitation. *J. Fluid Mech.* **247**, 79–110.
- NAUDASCHER, E. & ROCKWELL, D. 1994 *Flow-induced vibrations: An engineering guide*. A.A. Balkema, Rotterdam.
- PONCET, P. 2002 Vanishing of mode B in the wake behind a rotationally oscillating circular cylinder. *Phys. Fluids* pp. 2021–2023.
- PONTA, F. L. & AREF, H. 2006 Numerical experiments on vortex shedding from an oscillating cylinder. *J. Fluids & Structures* **22**, 327–344.
- PREGNATALO, C. 2003 Flow-induced vibrations of a tethered sphere. PhD thesis, Monash University.
- PROVANSAL, M., MATHIS, C. & BOYER, L. 1987 Bénard-von Kármán instability: transient and forced regimes. *J. Fluid Mech.* **182**, 1–22.
- RAO, S. 1995 *Mechanical vibrations, 3rd ed.*. Addison-Wesley, Massachusetts.
- RAYLEIGH, L. 1879 Acoustical observations II. *Philosophical Magazine* **VII**, 149–162.
- ROBICHAUX, J., BALACHANDAR, S. & VANKA, S. P. 1999 Three-dimensional Floquet instability of the wake of a square cylinder. *Phys. Fluids* **11**, n3, 560–578.

- ROBINSON, A. & SAFFMAN, P. 1982 Three-dimensional stability of vortex arrays. *J. Fluid Mech.* **125**, 411–427.
- ROSEN, J. 1995 *Symmetry in science: An introduction to the general theory*. Springer-Verlag, New York.
- ROSHKO, A. 1954 On the development of turbulent wakes from vortex streets. *NACA Report 1191* .
- ROSHKO, A. 1955 On the wake and drag of bluff bodies. *J. Aero. Sci.* **22**, 124–132.
- ROSHKO, A. 1993 Perspectives on bluff body aerodynamics. *J. Wind Engineering and Industrial Aerodynamics* **49**, 79–100.
- RYAN, K., THOMPSON, M. C. & HOURIGAN, K. 2005 Three-dimensional transition in the wake of bluff elongated cylinders. *J. Fluid Mech.* **538**, 1–29.
- SARPKAYA, T. 1978 Fluid forces on oscillating cylinders. *Journal of the waterways, port, coastal and ocean division of ASCE* **104**, 275–290.
- SARPKAYA, T. 1979 Vortex-induced oscillations: A selective review. *J. App. Mech.* **46**, 241–258.
- SARPKAYA, T. 2004 A critical review of the intrinsic nature of vortex-induced vibrations. *J. Fluids & Structures* **19**, 389–447.
- SEYDEL, R. 1994 *Practical Bifurcation and Stability Analysis*. Springer-Verlag, New York.
- SHEARD, G., THOMPSON, M. C. & HOURIGAN, K. 2003a A coupled Landau model describing the Strouhal-Reynolds number profile of a three-dimensional circular cylinder wake. *Phys. Fluids* **15**, no. 9, L68–L71.
- SHEARD, G., THOMPSON, M. C. & HOURIGAN, K. 2003b From spheres to circular cylinders: the stability and flow structures of bluff ring wakes. *J. Fluid Mech.* **492**, 147–180.
- SHEARD, G., THOMPSON, M. C., HOURIGAN, K. & LEWEKE, T. 2005 The evolution of a subharmonic mode in a vortex street. *J. Fluid Mech.* **534**, 23–38.

- SHIELS, D., LEONARD, A. & ROSHKO, A. 2001 Flow-induced vibration of a circular cylinder at limiting structural parameters. *J. Fluids & Structures* **15**, 3–21.
- SINGH, S. & MITTAL, S. 2005 Vortex-induced oscillations at low Reynolds numbers: Hysteresis and vortex-shedding modes. *J. Fluids & Structures* **20**, 1085–1104.
- STANSBY, P. K. 1976 The locking-on of vortex shedding due to the cross-stream vibration of circular cylinders in uniform and shear flows. *J. Fluid Mech.* **74**, 641–665.
- STAUBLI, T. 1983 Calculation of the vibration of an elastically mounted cylinder using experimental data from forced oscillation. *J. Fluids Eng.* **105**, 225–229.
- STOKES, G. S. 1851 On the effect of the internal friction of fluids on the motion of pendulums. *Transactions of the Cambridge Philosophical Society* **9**, 8–106.
- STROUHAL, V. 1878 Über eine besondere art der tonerregung. *Ann. Phys. und Chemie.* **5** (New Series), 216–251.
- STUART, J. 1958 On the non-linear mechanics of hydrodynamic instability. *J. Fluid Mech.* **4**, 1–21.
- STUART, J. 1960 On the non-linear mechanics of wave disturbances in stable and unstable parallel flows. Part 1: The basic behaviour in plane Poiseuille flow. *J. Fluid Mech.* **9**, 353–370.
- TANEDA, S. 1956 Experimental investigation of the wakes behind cylinders and plates at low Reynolds numbers. *J. Phys. Soc. Japan* **11**, 302–307.
- THOMANN, H. 1959 Measurements of the recovery temperature in the wake of a cylinder and of a wedge at mach numbers between 0.5 and 3. *Aeronautical Research Institute of Sweden (FFA) Report no. 84* .
- THOMPSON, M. C., HOURIGAN, K., RYAN, K. & SHEARD, G. 2006 Wake transition of two-dimensional cylinders and axisymmetric bluff bodies. *J. Fluids & Structures* **22**, 793–806.
- THOMPSON, M. C., HOURIGAN, K. & SHERIDAN, J. 1996 Three-dimensional instabilities in the wake of a circular cylinder. *Exp. Therm. Fluid Sci.* **12**, 190–196.

- THOMPSON, M. C. & LE GAL, P. 2004 The Stuart-Landau model applied to wake transition revisited. *Eur. J. Mech B/Fluids* **23**, 219–228.
- THOMPSON, M. C., LEWEKE, T. & WILLIAMSON, C. H. K. 2001 The physical mechanism of transition in bluff body wakes. *J. Fluids & Structures* **15**, 607–616.
- TRITTON, D. 1959 Experiments on the flow past a circular cylinder at low Reynolds numbers. *J. Fluid Mech.* **6**, 547–567.
- TRITTON, D. 1970 A note on vortex streets behind circular cylinders at low Reynolds numbers. *J. Fluid Mech.* **45**, 203–208.
- VAN DYKE, M. 1982 *An Album of fluid motion*. Parabolic press, Stanford.
- WALEFFE, F. 1990 On the three-dimensional instability of strained vortices. *Phys. Fluids A* **2** (1), 76–80.
- WHITE, F. 1999 *Fluid Mechanics, 4th ed.*. WCB / McGraw-Hill, Boston.
- WILLIAMSON, C. H. K. 1988 The existence of two stages in the transition to three-dimensionality of a cylinder wake. *Phys. Fluids* **31** (11), 3165–3168.
- WILLIAMSON, C. H. K. 1989 Oblique and parallel modes of vortex shedding in the wake of a circular cylinder at low Reynolds numbers. *J. Fluid Mech.* **206**, 579–627.
- WILLIAMSON, C. H. K. 1992 The natural and forced formation of spot-like ‘vortex dislocations’ in the transition of a wake. *J. Fluid Mech.* **243**, 393–441.
- WILLIAMSON, C. H. K. 1996a Three-dimensional wake transition. *J. Fluid Mech.* **328**, 345–407.
- WILLIAMSON, C. H. K. 1996b Vortex dynamics in the cylinder wake. *Annu. Rev. Fluid Mech* **28**, 477–539.
- WILLIAMSON, C. H. K. 1997 Advances in our understanding of vortex dynamics in bluff body wakes. *J. Wind Engineering and Industrial Aerodynamics* **69-71**, 3–32.
- WILLIAMSON, C. H. K. & BROWN, G. L. 1998 A series in $1/\sqrt{(Re)}$ to represent the Strouhal–Reynolds number relationship of the cylinder wake. *J. Fluids & Structures* **12**, 1073–1085.

- WILLIAMSON, C. H. K. & GOVARDHAN, R. 2004 Vortex-induced vibrations. *Annu. Rev. Fluid Mech.* **36**, 413–455.
- WILLIAMSON, C. H. K. & ROSHKO, A. 1988 Vortex formation in the wake of an oscillating cylinder. *J. Fluids & Structures* **2**, 355–381.
- WU, J., SHERIDAN, J., WELSH, M. C. & HOURIGAN, K. 1996 Three-dimensional vortex structures in a cylinder wake. *J. Fluid Mech.* **312**, 201–222.
- ZDRAVKOVICH, M. M. 1982 Modification of vortex shedding in the synchronization range. *J. Fluids Eng.* **104**, 513–517.
- ZHANG, H.-Q., FEY, U., NOACK, B. R., KÖNIG, M. & ECKELMANN, H. 1995 On the transition of the cylinder wake. *Phys. Fluids* **7**, no. 4, 779–794.
- ZIELINSKA, B. & WESFREID, J. 1995 On the spatial structure of global modes in wake flow. *Phys. Fluids* **7**, 1418–1424.